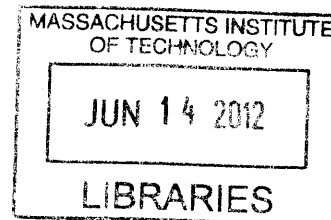# Tumor-Penetrating Delivery of Small Interfering RNA Therapeutics

By

Yin Ren

S.B. Electrical Engineering and Computer Science
Massachusetts Institute of Technology, 2006

SUBMITTED TO THE HARVARD-MIT DIVISION HEALTH SCIENCES AND
TECHNOLOGY IN PARTIAL FULFILLMENT OF THE REQUIREMENTS FOR THE
DEGREE OF

ARCHIVES

DOCTOR OF PHILOSOPHY IN MEDICAL ENGINEERING
AT THE
MASSACHUSETTS INSTITUTE OF TECHNOLOGY

JUNE 2012

Signature of Author:_____

Harvard-MIT Division of Health Sciences and Technology
May 4, 2012

Certified by:_____

Sangeeta N. Bhatia, M.D., Ph.D.
John and Dorothy Wilson Professor of Health Sciences & Technology and Electrical
Engineering & Computer Science, MIT
Thesis Supervisor

Accepted by:_____

Ram Sasisekharan, Ph.D.
Edward Hood Taplin Professor of Health Sciences & Technology and Biological Engineering,
MIT
Director, Harvard-MIT Division of Health Sciences and Technology

1

Tumor-Penetrating Delivery of Small Interfering RNA Therapeutics

by

Yin Ren

Submitted to the Harvard-MIT Division of Health Sciences and Technology on May 4, 2012 in Partial Fulfillment of the Requirements for the Degree of Doctor of Philosophy in Medical Engineering

ABSTRACT

Efforts to sequence cancer genomes have begun to uncover comprehensive lists of genes altered in cancer. Unfortunately, the number and complexity of identified alterations has made dissecting the underlying biology of cancer difficult, as many genes are not amenable to manipulation by small molecules or antibodies. RNA interference (RNAi) provides a direct way to assess and act on putative cancer targets. However, the translation of RNAi into the clinic has been thwarted by the "delivery" challenge, as small interfering RNA (siRNA) therapeutics must overcome clearance mechanisms and penetrate into tumor tissues to access cancer cells.

This thesis sought to develop nanotechnology-based platforms to rapidly discover and validate cancer targets *in vivo*. First, we developed versatile surface chemistries for nanoparticle tumor targeting. Leveraging new discoveries in amplified transvascular transport, we designed a siRNA delivery system that integrates the tumor specificity and tissue-penetrating ability of tumor-penetrating peptides with membrane penetration properties of protein transduction domains to direct siRNA to tumors *in vivo*.

Second, we utilized this delivery system to bridge the gap between cancer genomic discovery and *in vivo* target validation. Comprehensive analysis of ovarian cancer genomes identified candidate targets that are undruggable by traditional approaches. Tumor-penetrating delivery of siRNA against these genes potently impeded the growth of ovarian tumors in mice and improved survival, thereby credentialing their roles in tumor initiation and maintenance.

Lastly, we described efforts extending this platform for clinical translation. Mechanistic studies identified functional properties that favored receptor-specific siRNA delivery. We also explored a strategy to improve the microdistribution of successively dosed siRNA therapeutics through modulating the tumor microenvironment. Finally, we investigated the utility of the system in primary human tumors derived from patients with ovarian cancer.

Together, these findings illustrate that the combination of cancer genomics with the engineering of siRNA delivery nanomaterials establishes a platform for discovering genes amenable to RNAi therapies. As efforts in genome sequencing accelerate, this platform illustrates a path to clinical translation in humans.

Thesis Supervisor: Sangeeta N. Bhatia
Title: John and Dorothy Wilson Professor of Health Sciences & Technology and Electrical Engineering & Computer Science

ACKNOWLEDGEMENTS

TABLE OF CONTENTS

LIST OF FIGURES

8

9

1. Background and Significance

1.0 Overall goals

Efforts in genome sequencing have begun to uncover comprehensive lists of genes altered in cancer [1-2]. Unfortunately, the complexity and sheer volume of data that emerges from these efforts has made dissecting the underlying biology of cancer extremely difficult. To utilize genomic discoveries as a starting point for therapeutic development programs, one needs to rapidly interrogate the functional importance of genes *in vitro* and *in vivo* to identify the subset of genes that can be targeted by therapeutics. However, the number and types of candidate genes preclude high-throughput functional validation, as many genes do not represent targets amenable to inhibition by traditional small molecule or antibody-based approaches [1].

RNA interference (RNAi) provides a means to assess and act on candidate genes by suppressing their expression with high specificity and potency [2-4]. However, the translation of RNAi into the clinic has been thwarted by the so-called "delivery" challenge since small interfering RNA (siRNA) molecules have poor *in vivo* pharmacokinetic properties [5-6]. Nonetheless, existing nanoparticle-based delivery methods do not provide a reliable means to deliver siRNA, partially due to the requirements that siRNA must traverse through the tumor interstitium, cross the cell membrane and enter the cytosol of cancer cells to act [7]. Thus, tumor-targeted and tissue-penetrating delivery of siRNA therapeutics is yet to be achieved.

The overall goal of this thesis is to engineer a nanotechnology-based platform that overcomes the delivery barrier and enables the rapid *in vivo* evaluation of oncogenomic targets. Leveraging new discoveries in amplified transvascular transport, the delivery system described herein penetrates into the tumor and targets specific tumor cells, delivers siRNA therapeutics

against essential genes identified from comprehensive analysis of cancer genomes, and establishes an integrated platform for identifying and credentialing genes involved in cancer.

1.1 Ovarian cancer

1.1.1 Incidence and diagnosis

Ovarian cancer is the second most common gynecologic malignancy and the most lethal of all gynecologic cancers. There are an approximately 21,500 new cases and nearly 15,000 cancer-related deaths annually in the United States, making it the fifth leading cause of cancer deaths in women [8]. Worldwide, over 220,000 women were diagnosed with ovarian cancer in 2008 and over 140,000 died from this deadly disease [9].

One of the main causes of the relatively high mortality rate is the lack of tools available to detect ovarian cancer at the earliest stage. Only 25% of epithelial ovarian cancers (EOC) are diagnosed at Stage I; most patients who present have advanced Stage III-IV disease. This is thought to be due to a lack of specific, pathognomonic signs of early stage disease – symptoms reported by patients with ovarian cancer include bloating, increased abdominal girth, difficulty swallowing, urinary changes, or abdominal pain. To complicate matters further, there is a lack of blood or urinary biomarkers that can detect early events in carcinogenesis with high sensitivity and specificity. The circulating blood biomarker CA-125, a serum glycoprotein that is elevated in a subset of patients with EOC, is only 50% sensitive for Stage I disease [10] and is not detected in over 20% of ovarian cancer tissues studied [11]. Anatomical imaging techniques such as x-ray, computed tomography (CT) or magnetic resonance imaging (MRI) are poor at detecting small pelvic masses or predicting if an anatomic adnexal mass found on imaging is malignant.

Transvaginal ultrasound examination is typically employed in combination with CA-125 monitoring to achieve greater sensitivity. However, in patients with early-stage disease, biochemical alterations that arise due to genetic insults typically occur before gross anatomical changes. As a result, existing screening methods that are aimed toward detecting structural abnormalities often fail to provide molecular insights into the process of cancer initiation and progression, and are therefore inherently limited in detecting early-stage disease.

1.1.2 Management

Unlike many types of abdominal cancers that metastasize *via* extravasation into the bloodstream and seeding in distal extra-abdominal organs, ovarian cancer is typically restricted to the peritoneal cavity and intraperitoneal organs such as the uterus, small and large intestines, and the peritoneal membrane. Maximal surgical cytoreduction remains to be the optimal initial clinical management for ovarian disease, even when complete removal of the tumor is not possible [12-13]. Indeed, retrospective studies have shown that the size of tumor nodules remaining after initial cytoreduction surgery is inversely correlated with patient survival [14-15].

In cases where the disease has begun to metastasize to other peritoneal organs or where complete resection is impossible, combination chemotherapy is typically used to eradicate residual cancer cells. Of note, since a majority of ovarian cancers localize to the peritoneum and abdominal organs, intraperitoneal (i.p.) administration of chemotherapy has been shown to achieve >10-fold increase in drug concentration near the tumor [16-17]. However, i.p. treatment is often associated with higher rates of complications than intravenous (i.v.) chemotherapy due to side-effects such as GI toxicity, neuropathy, and myelotoxicity. Nevertheless, for both intraperitoneal and intravenous chemotherapy, a combination of microtubule-inhibiting taxane-based drugs (such as docetaxel and paclitaxel) and platinum-based DNA alkylating compounds

(such as cisplatin and carboplatin) are utilized [18]. First introduced in the late 1970's,

taxane/platinum-based therapy remains as the standard of care today. These agents act *via*

exploiting general biochemical differences between quiescent normal cells and rapidly

proliferating tumor cells; they do not target specific molecular abnormalities found in ovarian

cancer cells from individual patients. As a result, many patients re-present with recurrent and

progressively more drug-resistant disease [19]. Currently, overall 5-year survival for women

with ovarian cancer of all stages is 50%, but only 20-30% for women with advanced-stage

disease. This is significantly lower than that of other malignancies such as breast cancer, whereas

the 5-year overall survival is well over 80% (**Figure 1.1**). Therefore, there is a desperate need to

develop "personalized" therapeutic strategies that target ovarian-specific lesions and is tailored

towards the specific genotype of each patient.
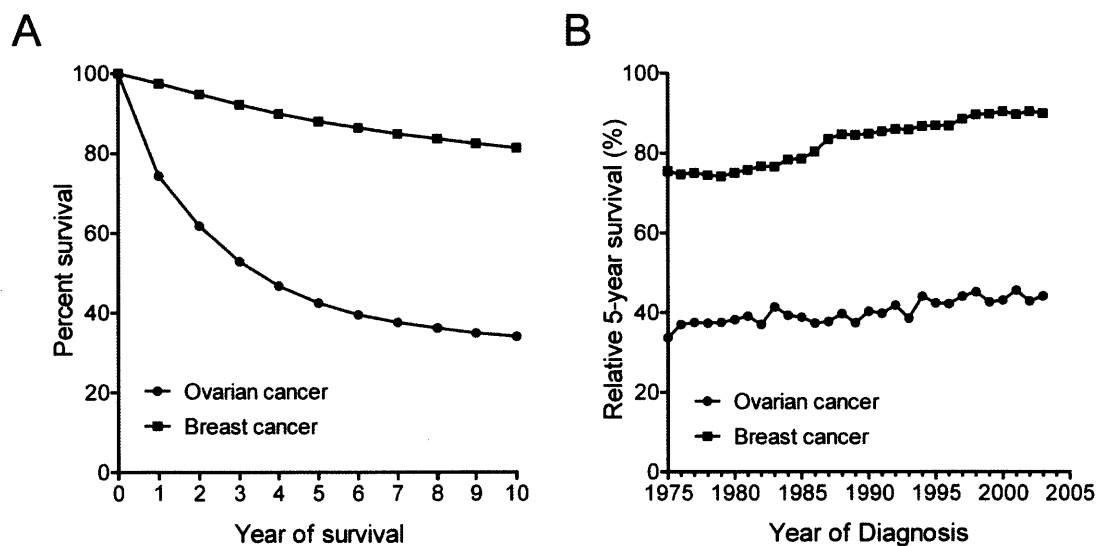
Figure 1.1. Clinical outcomes of women with ovarian and breast cancers. (A) Relative survival by survival time for women of all ages and all races between 1988-2007. (B) 5-Year relative survival by year of diagnosis with ovarian cancer and breast cancer between 1975-2003. The 5-year survival estimates are calculated using monthly intervals. From: Fast Stats: An interactive tool for access to SEER cancer statistics. Surveillance Research Program, National Cancer Institute. http://seer.cancer.gov/faststats. (Accessed on 3-14-2012)

Despite advancement over the last few decades in our understanding of the biology

underlying cancer initiation, progression, and metastasis, we have not seen equal progress in the

clinical management of cancer patients. Two main bottlenecks exist between translating discoveries made at the bench into therapeutic regimens used in the clinic. The first barrier lies in the development of new drugs based on the newfound knowledge of genes and signaling pathways underlying oncogenesis. With efforts from high-throughput sequencing and functional genomics, we have recently begun to enumerate all genetic alterations that could have functional consequences within a particular tumor. Therefore, the next generation of drugs will likely target these newly identified genetic mutations. Novel "personalized" therapies will be designed for each individual patient by taking into account the tremendous genotypic and phenotypic heterogeneity within cancers. While a number of personalized therapies currently exist in our drug armamentarium against cancer, more targeted agents should be identified and rapidly tested in the pipeline as our understanding of tumor biology becomes more comprehensive. In *Section 1.2* of the thesis, advancements in high-throughput sequencing of cancer genomes and development of personalized cancer medicine are discussed in more detail, with a special focus on personalizing the management of ovarian cancer.

The second, and arguably more critical, barrier lies in the delivery of therapeutics to the parenchyma of bulky tumors. In systemic disease processes such as cancer where localized drug delivery is generally ineffective to target every tumor cell, intravenously or intraperitoneally administered therapeutics must stably traverse the blood stream and overcome several major transport hurdles before reaching the tumor cell [20]. This is a significant problem that not only affects conventional chemotherapies, but also novel targeted agents including monoclonal antibodies and nucleic acid therapeutics, where their relative large size can further hinder drug diffusion and intratumoral transport. Specifically, these barriers include distribution to blood vessels that supply the tumor, extravasation from the vasculature and into the tumor parenchyma,

and penetration through the dense tumor interstitial matrix to reach cancer cells of interest. For

macromolecules such as DNA and siRNA, there is also the added requirement of translocation

across cellular membranes and entry into the cytosol where the molecule would become active.

In *Sections 1.3 through 1.5*, challenges in delivering drugs to cancer cells *in vivo* and approaches

to overcome them are discussed.

1.2 Personalizing cancer therapy

1.2.1 Targeted therapy

With recent advances in high-throughput genome sequencing technologies and methods

to identify genetic alterations associated with malignant phenotypes, there has been an explosion

of molecularly-targeted therapeutics for many different types of cancers. In contrast to

conventional genotoxic chemotherapeutics that exploit general differences in cellular

proliferation, targeted agents have higher therapeutic indices because they can be exquisitely

specific towards cancer cells harboring particular genetic alterations, thereby alleviating

toxicities due to off-target effects on normal cells. For example, in patients with chronic myeloid

leukemia (CML) harboring the *BCR-ABL* translocation, the selective Abl kinase small-molecule

inhibitor imatinib (Gleevec) is superior over conventional chemotherapy in inducing a

therapeutic response [21]. Elsewhere, in 10% to 20% of patients with non-small-cell lung cancer

(NSCLC) who also have activating mutations within the kinase domain of the epidermal growth

factor receptor (EGFR), treatment with small molecule tyrosine kinase inhibitors such as

erlotinib and gefitnib has led to dramatic responses [22]. Such findings highlight the critical

importance of utilizing genomic tools to analyze individual tumors, identifying the subset of

patients who harbor genetic mutations that drive oncogenesis that are also druggable, and ultimately treating them with the appropriate personalized therapy to maximize clinical response.

In contrast, one has not seen the same advancement in the development of personalized therapies for ovarian cancer. Clinical trials to date have employed conventional chemotherapeutics or combinations thereof to treat large cohorts of patients; however, improvements in progression-free or overall survival have been moderate. Currently, more clinical trials have been gearing towards smaller subsets of patients with new agents that target cancer-specific genetic and epigenetic alterations. Nonetheless, a more concerted and accelerated effort is needed to identify genetic abnormalities for earlier screening, stratify patients based on better biomarkers, and develop molecularly-targeted therapeutics.

Towards this goal, progress has been made at the bench over the past two decades in advancing our understanding of the molecular biology of ovarian cancer. Like many other neoplastic processes, ovarian cancer cells promote neoangiogenesis by producing factors and cytokines such as vascular endothelial growth factor (VEGF) and interleukin-8 (IL-8) [23]. Treatment of ovarian cancer patients with bevacizumab, a monoclonal antibody that inhibits VEGF-mediated signaling, prolonged median progression-free survival both as a first-line therapy and as an adjuvant therapy in recurrent disease [24-25]. Elsewhere, novel tyrosine kinase inhibitors such as vandetanib that target VEGF and growth factor receptors on pericytes is currently being tested in combination with docetaxel in patients with persistent or recurrent peritoneal malignancies, including cancers of the ovary and the fallopian tube [26-27].

Genomic sequencing studies have provided unprecedented insight into the genetic basis for ovarian tumorigenesis. While a significant fraction of ovarian cancers are clonal [28] and arise from the progeny of a single cell type, there is also great heterogeneity both in the

histopathological and genetic makeup amongst ovarian cancers. Many subtypes of ovarian

cancer do not share molecular similarities and therefore, respond differently to chemotherapy.

Only a fraction (10%-15%) of ovarian cancer is hereditary and associated with germline

mutations in the breast/ovarian cancer susceptibility genes, *BRCA1* or *BRCA2*. In contrast, in

patients who do not have significant family history but develop sporadic high-grade serous

ovarian cancers (HGSOC), one of the most common and lethal subtypes of ovarian cancer,

genome-wide analyses failed to yield a significant number genes that are also amenable to drug

intervention. To unbiasedly enumerate all genetic alterations found in ovarian cancer, recent

'omics' efforts led by The Cancer Genome Atlas (TCGA) research network have sequenced over

300 HGSOC tumor specimens. About 50% of which show germline or somatic mutations

involving the homologous recombination repair pathway, and over 90% have somatic mutations

in *TP53* [29]. Moreover, ovarian cancer exhibits a high degree of genomic instability as

evidenced by the large numbers of regions of recurrent amplification events [63] and focal

deletion events [55]. Amongst genes that are amplified in ovarian cancer are known oncogenes

such as *MYC, KRAS, AKT1,* and *HER2;* as well as novel candidates such as the p53 target gene

IRFBP2, the DNA-binding protein inhibitor *ID4*, and the embryonic development protein *PAX8*.

This genomic heterogeneity suggests that most cases of ovarian cancer have accumulated

amplified copies of oncogenes and tumor suppressor deletions, and have therefore likely evolved

redundant survival pathways. Therefore, agents that target a single mutation or signaling

pathway is unlikely to be curative.

Over the last decade, new evidence has emerged to suggest that epithelial cells of the

fallopian tube fimbriae are the primary cells-of-origin in HGSOC [30-32]. A recent study further

validated the "fallopian tube hypothesis" in *Dicer-Pten* double knockout mice that developed

HGSOC from primary fallopian tube tumors [33]. Thus, new cell lines and animal models can now serve as better paradigms and more accurate *in vitro* and *in vivo* models in recapitulating the initiation and progression of ovarian cancer. Moreover, together with integrated genomics efforts that comprehensively characterizes ovarian cancer genomes, it is now possible to systematically annotate the genome to identify cancer drivers, distill them down to ones amenable to therapeutic intervention, and develop personalized therapies based on small-molecules or RNA interference.

1.2.2 Functional genomics

Advances in high-throughput genome sequencing such as single nucleotide polymorphism (SNP) arrays and massively parallel sequencing have made it possible to enumerate all possible genetic alterations that exist in glioblastomas (GBM) and ovarian cancers [29, 34]. However, the sheer complexity and volume of data that emerges from these efforts make translation of genomic discoveries into targeted therapeutics extremely difficult. While a comprehensive inventory of genetic mutations in a given tumor is an essential first step, little is known about the functions of candidate genes that emerge from these efforts. To accelerate clinical translation, one also needs high-throughput approaches in parallel to functionally annotate genes and determine the phenotypic consequences of their perturbations. This will enable the distillation of cancer targets from structural characterizations and dissection of the underlying biology of ovarian cancer. Therefore, the next key challenge is to identify which of the myriad of genes implicated in genome sequencing efforts are true cancer drivers – whose protein products have causal roles in tumor initiation, maintenance, and metastasis.

To decipher the functional role of genetic alterations, one approach is to over-express genes of interest and determine the phenotypic consequences. In these gain-of-function approaches, libraries of human cDNAs and open reading frames (ORFs) have been utilized to

uncover candidate gene loci that when overexpressed, permits cell transformation [35-37]. More recently, many have investigated the role of microRNAs (miRNA) in cellular transformation. miRNAs are endogeneous small RNAs that represses the expression of numerous downstream target genes, either through post-transcriptional regulation via imperfect base-pairing or degradation of the mRNA transcript [38-40]. Many candidate miRNAs and their downstream target genes have been implicated in oncogenesis. Croce et al. identified the loss of miR-15a and miR-16 in chronic lymphocytic leukemias (CLL) [41]. Overexpression of the miR-17-92 cluster has been associated with oncogenic activity in diverse tumor subtypes such as B cell lymphomas [37]. The under-expression of miR-34a, a downstream target of p53 with tumor suppressing activity, is found in prostate cancer [42]. In the future, the further elucidation of miRNA targets will enable the identification of gene networks that drive carcinogenesis.

1.2.3 RNA interference

A complementary approach to probe gene function is through loss-of-function assays. However, traditional techniques to create gene knockouts are labor-intensive and require specific genetic manipulations that are not amenable for high-throughput applications. Fortunately, with the advent of genome-scale RNA interference (RNAi) libraries, large scale loss-of-function screens are now possible [4]. RNAi is a conserved mechanism in eukaryotic cells for defense against double-stranded RNA (dsRNA) introduced into cells by viruses and/or transposons [2-3, 43]. Briefly, the dsRNA is first recognized by a ribonuclease III enzyme, Dicer, and cleaved into small fragments of 21-23 nucleotides [44-45]. These dsRNA fragments, also known as short interfering RNAs (siRNA), contain two-nucleotide 3' overhangs, 5' phosphate and 3' hydroxyl termini. The sequences form a sense (passenger) strand and an antisense (guide) strand that will subsequently direct the post-transcriptional degradation of mRNA. The siRNA is incorporated

29

into a protein complex known as RNA-induced silencing complex (RISC), and the sense strand

is cleaved by a cleavage enzyme Argonaute 2 within RISC as dictated by the decreased

thermodynamic instability at its 3' terminus [46]. The remaining antisense (guide) strand of the

siRNA is then directed to the complementary mRNA sequence to initiate post-transcriptional

gene suppression by either transcript degradation or translational suppression (**Figure 1.2**) [47].
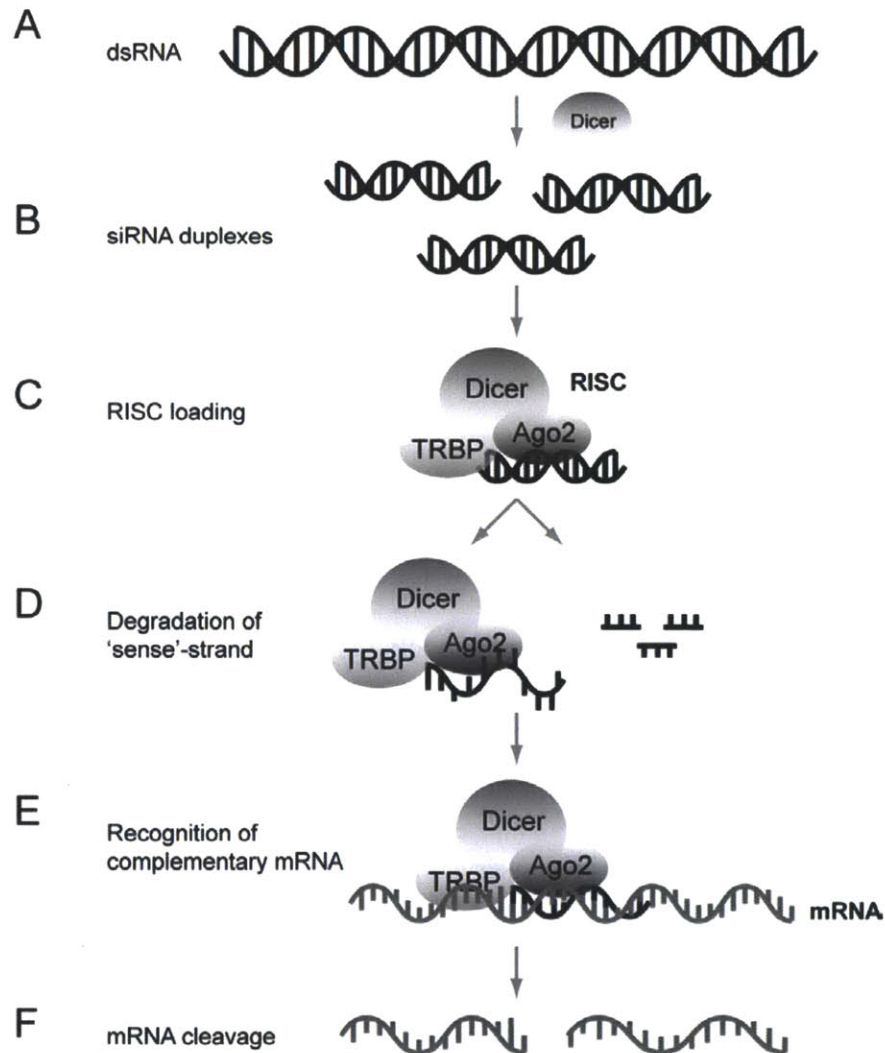
Figure 1.2. Mechanism of RNA interference mediated by short, double-stranded RNAs. (A) Upon introduction to the cytosol, dsRNA molecules are cleaved by Dicer into 21-23 nt dsRNA fragments known as siRNAs. **(B,C)** siRNA duplexes are subsequently loaded into the RNA-induced silencing complex (RISC). **(D)** The sense (passenger) strand is degraded by Ago2 protein within RISC. **(E)** The remaining antisense (guide) strand mediates recognition of complementary mRNA sequences. **(F)** Post-transcriptional gene silencing is achieved through cleavage of the complementary mRNA.

RNAi is highly effective in inducing post-transcriptional gene suppression. Since siRNA and shRNA can be synthesized in large quantities at relatively low cost, genome-wide RNAi libraries have been utilized to identify genes whose suppression induces a particular phenotype, such as changes in viability, apoptosis, or anchorage-independent growth. One such approach, termed Project Achilles, integrated genome-wide loss-of-function studies using pooled shRNA libraries with structural analyses of cancer genomes to identify genes that are amplified and essential for the survival of cancer cell lines. Specifically, by performing highly parallel RNAi screens against 11,194 genes in 102 established human cancer cell lines *in vitro*, Cheung *et al.* found 54 putative oncogenes that are essential for the proliferation of ovarian cancer cells and are also amplified in copy number in primary ovarian tumors [48].

Taken together, as our understanding of the cancer genome continues to evolve, the future development of both gain-of-function and loss-of-function approaches will provide powerful tools to identify new gene targets, dissect pathways that drive cancer growth and survival, and understand new cancer biology. Furthermore, the integration of structural genomics and functional genomics will accelerate the identification of new genes that have functional roles in cancer initiation, progression, and metastasis.

1.2.4 RNA-based therapeutics

RNA interference has enormous potential to become clinical therapeutics themselves, since exogenous siRNA can directly inhibit the function of candidate oncogenes, thereby perturbing the viability of cancer cells whose survival depend on the activity of those genes. This approach is particularly attractive for cancers that have a complex and mobile genotype, since multiple siRNA sequences can be applied to suppress distinct genes that are essential but "undruggable" by conventional approaches [1]. In contrast to small molecule drugs that function

at defined molar ratios by binding to specific locations on the target protein, RNAi is inherently self-catalytic: the incorporation of one siRNA molecule into RISC can degrade multiple complementary mRNA transcripts. Furthermore, while small molecules often cannot distinguish isoforms of the same protein, siRNAs can target any gene of interest since RNAi-mediated degradation mRNA is specific to the nucleotide sequence.

Additionally, RNAi is more attractive than antibody-based approaches. This is because monoclonal antibodies only bind to targets that are either membrane-bound receptors or secreted proteins localized to the extracellular milieu. By contrast, siRNA can theoretically degrade the mRNA transcript of any protein regardless of its intra-/extra-cellular localization. Finally, owing to the rapid advances in genome sequencing, new siRNA molecules can be identified and synthesized at large quantities with a quick turn-around time, enabling high-throughput drug discovery and development.

Indeed, RNA-based therapeutics has been employed in clinical trials for a variety of indications including neoplastic, cardiovascular, and infectious diseases. More recently, siRNA therapeutics have been tested in clinical trials to inhibit aberrantly functioning genes in diseases not limited to cancer, including age-related macular degeneration, viral infections from respiratory syncytial virus (RSV) and Hepatitis C , and dermatological illnesses [49-51]. The majority of these trials involved localized injections of naked, unmodified siRNAs. For example, siRNAs directed against the gene that encodes vascular endothelial growth factor (VEGF) and its receptor (VEGF-R) were administered into the eyes of patients with age-related macular degeneration (AMD), resulting in improved vision with minimal toxic side effects [52].

1.3 Tumor drug delivery

1.3.1 Challenges in siRNA delivery

Small molecule drugs are typically structurally lipophilic and low in molecular weight, properties that impart favorable ADME pharmacokinetic properties [53]. According to the Lipinski's Rule of "drug-likeness", the compound should have a molecular mass of less than 500 daltons, no more than 5 hydrogen bond donors, no more than 10 hydrogen bond acceptors, and an octanol-water partition coefficient $\log P$ less than 5 [54]. A drug that obeys a majority of these rules can typically maintain high circulating levels upon systemic administration. By contrast, siRNA molecules do not obey Lipinski's rules. They are relatively large with a molecular weight between 13,000 and 15,000 Da; they contain a large number (typically > 40) of anionic charges due to the negatively-charged phosphodiester backbone; and they are hydrophilic due to the presence of sugar moieties [7]. As a result, intravenously administered unmodified siRNAs are immediately chaperoned with opsonins and cleared from circulation within minutes after i.v. injection [55]. Furthermore, nucleic acids are unstable in serum due to degradation by RNase A-type nucleases, thereby limiting their bioavailability to tissues of interest [6]. To circumvent the poor pharmacokinetic properties, localized delivery has been utilized for indications where the affected organ is directly accessible and isolated from the other organs. These include the eye, dermis and vaginal epithelium [56-58]. In particular, intranasal or intratracheal inhalation of siRNA directed against genes essential for replication of RSV and SARS coronavirus has been efficacious in controlling infections [59-60]. siRNA targeting the nucleocapsid N gene of RSV showed low toxicity in Phase I and significant efficacy in phase II trials [50].

siRNA inevitably end up entrapped in endosomes subsequent to cellular uptake [61]. Endosomes undergo maturation where the interior compartment is gradually acidified ($pH \sim 5.5$-

6.5) by H+ ATPases. Subsequently, the endosomes fuse with lysomal compartments into endolysosomes [62]. The acidic *pH* ($\sim$ 4-5) will also activate special lysosomal enzymes that degrade entrapped siRNA, which results in little release into the cytoplasm [63]. Subsequent to endolysosomal escape, the siRNA molecule must readily dissociate from its carrier to be loaded into the RNA-induced silencing complex (RISC). Carriers such as PEI that contain a large number of positively charged tertiary amines may retard the dissociation of siRNA. Indeed, studies have shown that carrier dissociation rates can significantly impact the efficiency of DNA transfection [64]. Moreover, it has been demonstrated that steric hindrance from quantum dots in close proximity to siRNA can impact the magnitude of RNAi [65].

The immune system has natural defense mechanisms against dsRNA in the setting of viral infections [66-67]. Unsurprisingly, the introduction of siRNA can trigger immune responses [68-69]. Toll-like receptors including TLR3, TLR7, and TLR8 are activated when they encounter RNA duplexes in endolysosomes [70]. These TLRs belong to a class of pattern recognition receptors that respond to single stranded and double stranded RNAs from viral pathogens. Following endocytosis of siRNA, TLRs located on the endosomes are engaged and induces nuclear translocation of NF-κB and initiates transcription of genes such as interferon-α (*IFN-α*) and other inflammatory cytokines [71]. In addition, cytoplasmic RNA sensors such as dsRNA-binding protein kinase (*PKR*) and cytoplasmic RNA sensor (*RIG-I*) can also activate innate immune responses [71]. Fortunately, the magnitude of immunostimulatory effects can be modulated by optimizing the siRNA sequence and properties of the nanoparticle carrier. Known immunostimulatory sequences such as GU-rich motifs have been rationally excluded in various design algorithms [69, 72]. Moreover, backbone modifications with 2'-OMe and 2'-deoxy have improved the "stealth" nature of siRNA and evasion of immune recognition [73].

Much like the mechanism of miRNA-mediated translational repression, siRNA could suppress the expression of genes whose mRNA transcripts only share partial sequence homology [74-76]. The off-target silencing can introduce a host of transcript level changes in genes distinct from the expected target, thereby confounding the results [77]. Moreover, since endogenous microRNAs regulate gene expression *via* a shared pathway, the over-introduction of exogenous siRNA can have undesired off-target effects through saturation of the RISC machinery, de-repress miRNA-regulated genes, and cause phenotypic changes due to alterations in genes unrelated to the target [78].

1.3.2 Transport barriers for drug delivery
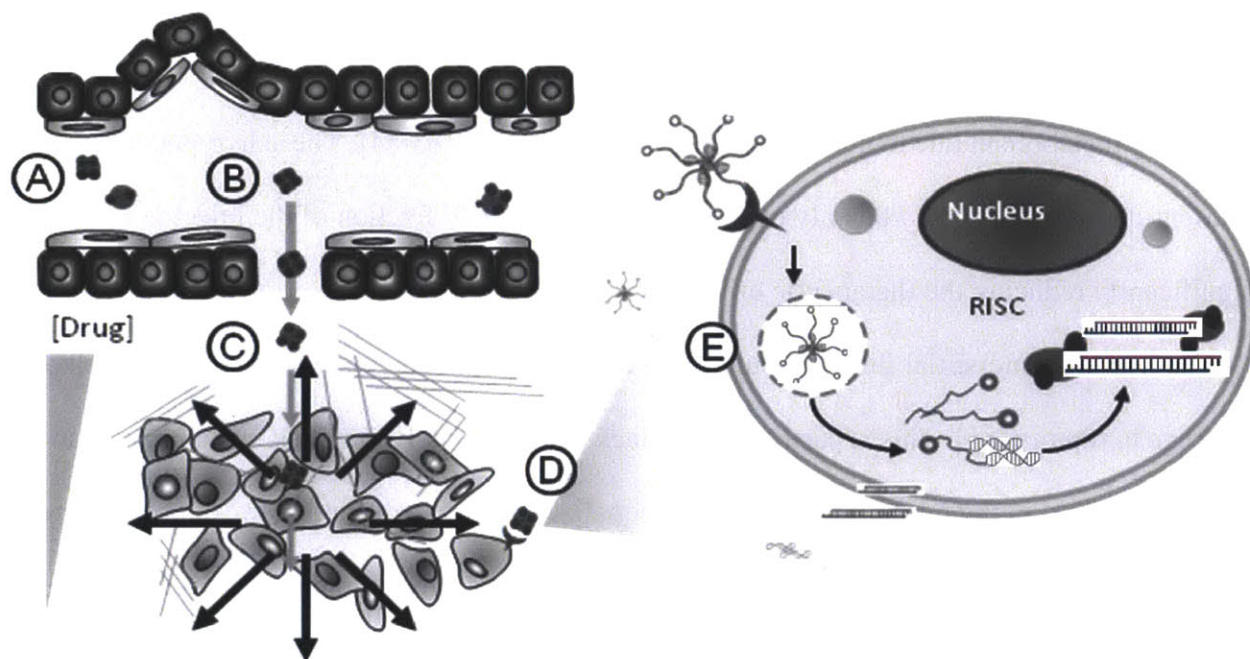
Figure 1.3. Barriers to systemic delivery of siRNA. Naked siRNA and nanoparticle carriers with siRNA payloads must negotiate several transport barriers before reaching the target cell. Namely, **(A)** Upon systemic administration, siRNA should stably circulate in blood until reaching the site of disease. **(B)** Once the siRNA cargo is distributed to blood vessels supplying the tumor, it must extravasate from the bloodstream via either passive diffusion or active transvascular transport. **(C)** After extravasation, the siRNA therapeutic should overcome high interstitial pressures and penetrate into the tumor parenchyma. **(D)** siRNA payloads are taken up by tumor cells via endocytosis. **(E)** Escape from endosomal entrapment by siRNAs is necessary to ensure localization to the cytosol and incorporation into RISC.

For widespread clinical translation, however, systemic delivery of siRNA therapeutics is required for diseases such as cancer where the affected tissue(s) cannot be locally accessible. An ideal siRNA carrier must successfully negotiate several transport barriers after systemic administration (**Figure 1.3**). Solid tumors exhibit tremendous disorganization in their vascular supply. Due to uncontrolled proliferation of tumor cells that is not matched by the accompanying growth of endothelial cells, tumor blood supply is typically heterogeneous and sparse compared to normal tissue counterparts [79-80]. In addition, other features unique to the tumor such as abnormal blood flow, variations in blood flow resistance due to disrupted vessel architecture, and physical pressure from the presence of hyper-proliferating tumor cells can all contribute to perfusion heterogeneity [81-82]. Consequently, subpopulations of tumor cells, especially ones located in the avascular and necrotic core of the tumor, are poorly perfused and undergo anaerobic metabolism due to nutrient and oxygen deprivation [83-84]. These hypoxic and nutrient-deprived cells may be only exposed to a sub-threshold fraction of the injected drug, significantly reducing the therapeutic efficacy.

Elevated interstitial fluid pressure (IFP) can also contribute to the poor systemic delivery of drugs to tumors [85]. This is partly due to a lack of functional lymphatics, which results in the build-up of fluid in the tumor interstitium and equalization of oncotic and hydrostatic pressures across the intravascular and extravascular spaces [86-87]. As a result, convection is negligible within the tumor parenchyma except at the tumor periphery. Nevertheless, once the drug has extravasated from the blood vessel into the tumor mostly via diffusion, it must now traverse through the dense interstitial matrix to reach epithelial tumor cells. The tumor extracellular matrix (ECM) is composed of a network of connective tissue such as collagen, proteoglycans, glycosaminoglycans, various proteins such as clotted proteins, fibrin and fibronectin, and stromal

cells including fibroblasts and tumor-associated inflammatory cells [88]. Together, they provide a significant barrier for fluid flow and drug transport. Indeed, it has been demonstrated that the diffusion coefficient of IgG measured in several tumors *in vivo* correlated with collagen content within the tumor; tumors with favorable transport characteristics typically displayed well-organized collagen architecture [89]. Furthermore, as tumors progress, the ECM undergoes extensive remodeling accompanied by an infiltration of inflammatory cells and concomitant activation of enzymes such as matrix metalloproteases (MMPs) [90].

1.3.3 Strategies for tumor targeting

The *in vivo* therapeutic index of anticancer drugs is dependent on its ability to affect tumor cells while minimally impacting normal tissues. This tissue specificity is especially critical for drugs that target features that are shared between hyperproliferating cancer cells and normal proliferative cells, as many chemotherapeutics fail due to dose-limiting toxicities in off-target tissues. Therefore, an optimal strategy to maximize therapeutic efficacy involves simultaneously enhancing drug delivery to tumors while minimizing delivery to normal tissues.

The recent advent of nanotechnology has sparked an explosion of nanoparticle formulations to accomplish this task. Nanoparticles, broadly defined as materials on the order of tens to hundreds of nanometers in size, represent a promising approach to overcome the delivery barrier [91]. Currently, several nanoparticle-based chemotherapies have been approved for clinical use owing to their superior pharmacokinetic properties and fewer side-effects compared to small molecule counterparts. These include Abraxane (albumin nanoparticle-bound paclitaxel) and Doxil (liposomal doxorubicin), both distribute to tumors *via* the enhanced permeability and retention (EPR) effect by exploiting structural abnormalities in the tumor vasculature such as disrupted endothelial linings [92-93]. Nevertheless, EPR can be highly variable and is not a

constant feature of all tumor subtypes [94], thereby limiting the potential for clinical translation. Furthermore, blood vessel fenestrations could be insignificant and passive targeting may be ultimately ineffective, as the high IFP in tumors would counteract convective flow. As a consequence, the diffusion of large macromolecular therapeutics such as proteins and nanoparticles into the tumor parenchyma can be too slow to be effective [95].

To precisely direct therapeutics to tumors, an alternative strategy is through exploiting the differential expression of molecular markers between cancer cells and normal cells. Nanoparticles can be engineered to display affinity ligands such as small molecules, peptides, and antibodies directed at tumor-specific markers. These markers include vascular surface proteins such as $\alpha v\beta3$ and $\alpha v\beta5$ integrins on the tumor endothelium, overexpressed or mal-expressed cell-surface proteins such as transferring receptor and epidermal growth factor receptor (EGFR), membrane lipids such as phosphatidylserine, and overactive proteases such as matrix-metalloproteases (MMPs) [96-99]. Screening technologies using libraries of small molecules, aptamers, and bacteroiophage-displayed peptides can unbiasedly select ligands with high affinity and specificity towards a molecular target [100-103].

While tumor blood vessel delivery and macroscopic accumulation may be sufficient for applications such as tumor detection by imaging, delivery to epithelial tumor cells deep in the tumor parenchyma is often required to eradicate disease. Indeed, the efficacy of chemotherapeutics is determined by how well the drug can leave tumor blood vessels, penetrate into the tumor tissue, and reach all cancer cells [104]. Treatments with macromolecular drugs such as antibodies that target tumor cells would be minimally effective if only delivered to blood vessels, since a fraction of tumor cells are not located near perfusing vasculature. Moreover, for

nucleic-acid based therapeutics such as DNA and siRNA, delivery to specific intracellular compartments within a tumor cell such as the cytosol is required for function.

1.3.4 Strategies for tumor penetration

In tumors with extensive stromal involvement, the response rate to chemotherapy is poor and development of drug resistance is common [105-106]. To improve tumor interstitial transport, approaches have been developed to reduce blood flow resistance, increase permeability, or both. Treatment with antiangiogenic agents showed normalization of vasculature, reduction of interstitial pressure, and improvement in drug penetration [107-109]. In patients with lymphoma or melanoma, an improved response to chemotherapy is seen with lower interstitial fluid pressure [110]. Bevacizumab (Avastin), a monoclonal antibody that inhibits VEGF, is the first clinically approved angiogenesis inhibitor for treatment of metastatic colon cancers. Elsewhere, vascular disrupting agents (VDA) such as tumor necrosis factor (TNF) and combretastatin A4 have been shown to shut down vessels supplying the tumor [111]. However, systemic administration of VDAs can have toxic side effects due to non-specificity towards normal blood vessels [112]. Alternatively, ECM-modifying molecules such as collagenase and hyaluronidase have been used to increase the transport of model drugs [113-114]. Modulation of the pancreatic tumor stroma *via* inhibition of hedgehog signaling or degradation by pegylated hyaluronidase enzyme can enhance the delivery of gemcitabine chemotherapy into the tumor and significantly improve survival [115-116]. However, these approaches are not tumor-specific; systemic administration of these agents can lead to the undesired degradation of normal connective tissue and toxicity. Moreover, remodeling of extracellular matrix could potentially increase the probability of metastasis.

One promising solution, recently described by Ruoslahti *et al.*, utilizes a newly discovered class of peptides that are both tumor-specific and tissue-penetrating to enhance the delivery of drugs to tumors [117-118]. One such peptide, iRGD (internalizing RGD; CRGDKGPDC), contains two features that endow tumor-specificity and tumor-penetration abilities. Namely, the RGD motif directs to integrins expressed on the surface of angiogenic endothelial cells, thereby conferring tumor-specificity. Additionally, the presence of the arginine/lysine-X-X-argine/lysine (RXXR) motif at the *C*-terminus (CendR motif) enables binding to neuropilin-1 (NRP1) and subsequent increase in tumor vascular permeability. Importantly, activation of NRP1 is dependent on the proteolytic processing of cyclic iRGD on the tumor cell surface, thereby unveiling the RXXR motif in a tumor-specific manner. In xenografts and genetically-engineered mouse models of cancer, iRGD enhances the co-delivery of small molecules, monoclonal antibodies, and nanoparticles into the tumor [119].

The precise mechanism by which CendR peptides enhance tumor penetration is still under investigation. Similar to vasoreactive agents such as bradykinin and endothelin that promote drug delivery through increasing vessel pore size, the effects of iRGD could be also attributed to the "stimulated permeability and retention" effects [120-122]. In addition, a VEGF-like effect is possible since $VEGF_{165}$ is a natural ligand for NRP1 [123-124]. Finally, the antiangiogenic properties of iRGD could lead to the normalization of tumor vasculature *via* blockade of NRP1- and integrin-mediated signaling [125].

1.4 Tools for siRNA delivery

While RNA interference is an extremely powerful discovery tool to interrogate gene function and identify novel pathways in mammalian systems, the development of RNAi-based

clinical therapeutics is fraught with challenges in delivery [5]. Over the years, a large array of tools has been developed to improve the drug-likeness of siRNA, either through chemical modifications or the deployment of carrier systems that chaperone siRNA payloads to their *in vivo* destinations. To date, a diverse set of biomaterials have been investigated including liposomes, proteins, polymers, and peptides [126-129] (**Figure 1.4**). This section will focus on the design of chemically-modified siRNAs and development of siRNA delivery systems.
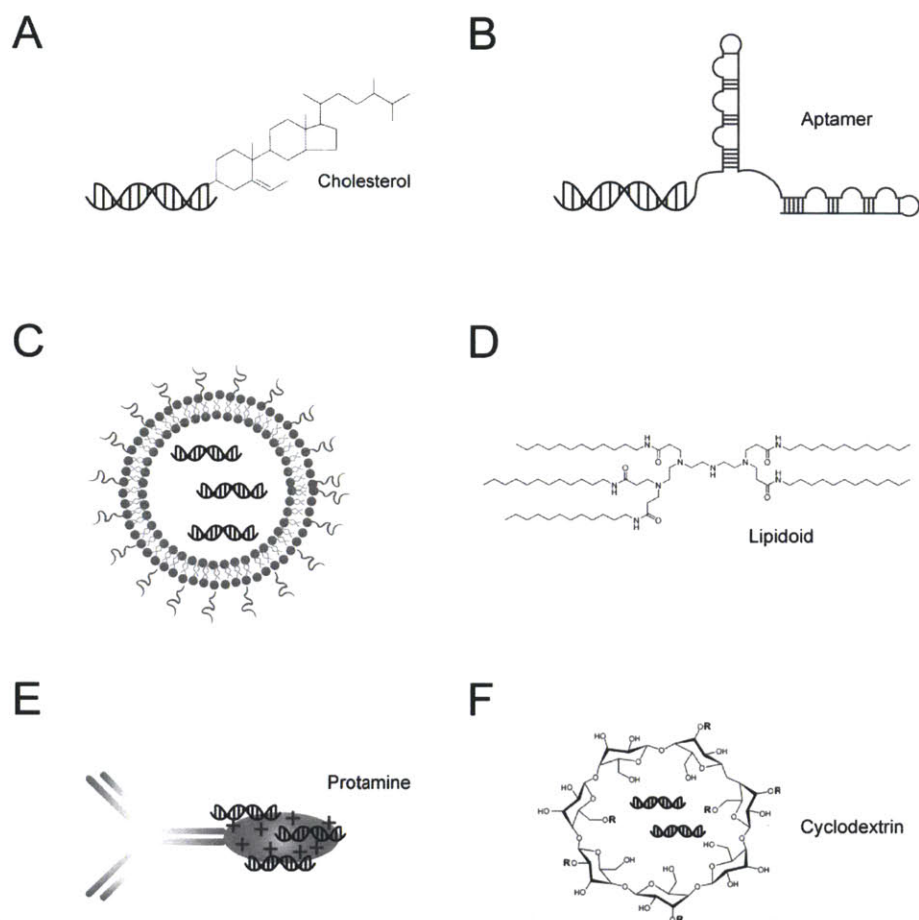
Figure 1.4. Tools for siRNA delivery. (A) siRNA molecules are modified with lipohilic moieties such as cholesterol to extend *in vivo* stability and half-life. **(B)** siRNA chemically linked to aptamers (blue) that target specific molecular targets allows cell type-selective delivery. **(C)** PEGylated liposomes made of cationic or neutral lipid bilayers can encapsulate siRNAs in the interior. **(D)** Lipid-like molecules, such as the 98N12-5 lipidoid, can form nanoparticles with siRNA. **(E)** Antibodies fused to positively-charged proteins such as protamine can target cells expressing specific receptors and deliver siRNA into the cytosol. **(F)** Polymers such as cyclodextrin-containing polymer (CDP) can be formulated with PEG, targeting moieties, and siRNA payloads via self-assembly for cancer-targeted delivery.

1.4.1 Chemical modifications

Chemical modifications of siRNA have been employed to improve stability and sequence-specificity. siRNAs are susceptible to degradation by endo- and exo-nucleases that are present in the serum. To improve serum stability, 2'-modifications have been applied to the sugar moieties to confer resistance against endonuclease activity [75]. Moreover, phosphorothioate backbone linkages in the 3'-end of the guide strand reduced susceptibility to exonuclease-mediated degradation [130]. To extend the *in vivo* half-life and improve tissue biodistribution, conjugation of lipophilic moieties to the termini of the passenger strand of RNA duplexes have been reported. Cholesterol-conjugated siRNAs can associate with LDL and hijack lipid trafficking pathways to target hepatocytes [131]. Delivery of siRNA targeting apolipoprotein B (*apoB*) in mice reduced circulating levels of apoB by up to 70% and total cholesterol levels by 40% [132]. Extending on these results, it has been demonstrated that diverse lipophilic moieties including long saturated fatty acids (stearoyl, C_{18}; and docosanyl, C_{22}), but not short chain fatty acids, can be conjugated to siRNA to enhance the knockdown of apoB *in vivo*.

While this discovery represents an important step forward, the large dose (50 mg siRNA/kg) required makes it too costly for clinical translation. One approach to reduce the dose of siRNA is by *targeting* the delivery of siRNA to the diseased organ. Aptamers, oligonucleotides composed of either ssDNA or ssRNA (20-40), recognize specific proteins owing to its unique three-dimensional structure and can be incorporated into the siRNA sequence. Using a screening process known as systematic evolution of ligands by exponential enrichment (SELEX), aptamers with exquisite specificity and high binding affinity to a select molecule can be isolated [133]. Aptamer-siRNA chimeras targeting the prostate-specific membrane antigen (PSMA) suppressed the growth of prostate tumor xenografts in mice [102,

127]. Elsewhere, siRNA-conjugated aptamers targeting either HIV proteins or CD4 cells inhibited HIV viral replication and disease transmission in humanized mice [134].

1.4.2 Lipids

Nanomaterials made of lipids and/or lipid-like molecules have been employed as drug delivery vehicles in the clinic [135]. Liposomes are attractive delivery vehicles because they are biocompatible, non-immunogenic, and versatile in encapsulating both hydrophilic and hydrophobic drugs [136]. The liposomal doxorubicin (Doxil) showed significantly reduced cardiotoxicity and has been approved for clinical treatment of ovarian cancer, multiple myeloma, and AIDS-related Kaposi sarcoma. Liposomes have been utilized to delivery nucleic acids in mouse models as well as in humans [137-138]. Stable nucleic acid-lipid particles (SNALPs) carrying siRNA against *apoB* suppressed ApoB expression in the liver of primates [139]. Toxicity studies indicated little to no toxicity observed in the animals, and Tekmira Pharmaceuticals is conducting Phase I trials using SNALPs in patients with primary liver cancers or liver metastases. To expand the chemical diversity of lipids, high-throughput combinatorial methods have been developed to synthesize structurally-diverse lipid-like materials ("lipidoids") [126]. Lipidoids provide a promising approach to knock down target genes in hepatocytes, such as factor VII, in the liver of mice, rats, and primates. More recently, lipidoid-mediated silencing of the chemokine receptor 2 (*CCR2*) in inflammatory monocytes was efficacious in controlling inflammation in diverse pathological processes ranging from atherosclerosis to cancer-associated inflammation [140]. Elsewhere, liposomes have been endowed with targeting moieties to direct them to specific cells. Liposomes coated with antibodies targeting β_7 integrins suppressed inflammation in an animal model of colitis [141]. Furthermore, targeting with vitamin A was able to target activated stellate cells in the liver to reverse liver fibrosis [142].

While initial preclinical results have been promising, evidence suggested that cationic lipids can stimulate the immune system [143]. For example, while SNALPs carrying siRNAs targeting the polymerase gene of Ebola protected guinea pigs against viraemia, activation of interferon-α and interferon-β was also observed [144]. To minimize charge-mediated immunostimulatory effects, neutral 1,2-dioleoyl-sn-glycero-3-phosphatidylcholine (DOPC) liposomes have been employed for tumor-targeted siRNA delivery [145-146]. Compared to conventional cationic systems, neutral liposomes deliver 10- to 30-fold higher siRNA payloads into target cells likely owing to improved biodistribution. Systemic delivery of DOPC liposomes carrying siRNAs targeting genes overexpressed in melanoma, such as the thrombin receptor protease-activated receptor-1 (*PAR-1*), led to significant reductions in tumor growth and metastasis [147]. Elsewhere, liposome-mediated delivery of siRNA suppressed genes involved in ovarian tumorigenesis (*IL-8, SIK2* and *EphA2*) in human ovarian cancer xenografts [147-150].

1.4.3 Proteins

Since the backbone of the RNA duplex is negatively charged, a cationic protein can condense siRNAs into nanoparticles. Several realizations using naturally-occurring and engineered proteins have been achieved. Antibodies targeting the HIV envelope protein gp160 were fused to the protamine, a class of arginine-rich nuclear proteins, and resulted in gene silencing in a cell type-selective manner in mouse models of HIV and melanoma [128]. More recently, RNA-binding proteins known as dsRNA Binding Domains (DRBD) has been utilized in conjunction with the TAT protein transduction domain for siRNA delivery. TAT-DRBD chimeras induced potent RNAi response in difficult-to-transfect cell lines such as T cells, primary human umbilical vein endothelial cells (HUVECs) and human embryonic stem cells (hESCs), with minimal innate immune response and no detectable cytotoxicity [151]. Separately,

efforts in protein engineering have led to the development of novel proteins tailored for gene delivery applications. One approach applied protein resurfacing techniques to mutate non-conserved residues on GFP without abolishing structure or function. The resulting "supercharged" GFP contained a +36 net positive charge, avidly complexed with nucleic acids, and delivered payloads to suppress gene expression in a variety of mammalian cell lines [152].

1.4.4 Polymers

Cationic polymers can also bind nucleic acids and form nanometer-sized particles amenable for transfection. Chitosans are attractive due to their cationic charge, biodegradability, biocompatibility, and permeability-enhancing properties. By optimizing the formulation conditions and polymer structure, chitosan was effective in delivering siRNA *via* intranasal or intravenous administration in animal models [153-154]. Separately, atelocollagen, a type I collagen from trypsin-digested bovine dermis, has been used to deliver siRNA with low toxicity and immunogenicity [155].

While naturally occurring polymers have shown promise, synthetic polymers offer the advantage that they can be precisely engineered for specific applications. Poly (ehyleneimine) (PEI) has been utilized to delivery nucleic acid-based drugs [156]. The excess tertiary amines on the PEI side chains can act as proton sponges while inside the endosomal compartment, thereby increasing the influx of chloride and water that ultimately ruptures the endosome. Additionally, PEI can be modified with targeting ligands such as RGD peptides to enhance its affinity for the tumor vasculature [157]. Unfortunately, PEI bearing a high degree of branched amines is non-biodegradable and has high cytotoxicity, thereby limiting its clinical utilization.

Cyclodextrins are polymers bearing a cyclic backbone based on glucose moieties that spontaneously assemble with siRNA into sub-100nm nanoparticles. Cyclodextrin-containing

polycation (CDP) systems bearing transferrin-coupled PEG have been shown to be efficacious in a mouse model of metastatic Ewing's sarcoma by delivering siRNAs against the *EWS-FLI1* fusion gene [158]. A similar system containing siRNAs against ribonucleotide reductase M2 subunit (*RRM2*) is currently being tested in patients with refractory solid tumors. Preliminary results indicated that the treatment is well-tolerated and knockdown is observed in tumor biopsies [159]. However, preclinical biodistribution data for CDP-based systems is poor and efforts to improve the intratumoral accumulation of siRNA payloads are needed.

1.4.5 Cell-penetrating peptides

Cell-penetrating peptides (CPPs, also known as Protein Transduction Domains) are short cationic or amphipathic peptides that can cross the cell membrane. Well-characterized CPPs include the peptide fragment derived from the 48-60 amino acid residues of the HIV TAT protein, antennapedia homeotic transcription factor derived peptide Penetratin, Herpes simplex virus protein VP22, a fusion of the neuropeptide galanin and mastoparan (Transportan), and synthetic poly-Arginines [160-161]. CPPs can be chemically linked to 5' thiol-containing siRNA via a disulfide linkage. Penetratin and transportan conjugated to siRNAs using this method have shown *in vitro* efficacy [162]. However, it is unclear whether the active component of siRNA delivery is indeed CPP-siRNA conjugates, since charge-neutralization by siRNA could theoretically abrogate cell internalization [163].

Alternatively, CPPs can complex with siRNA non-covalently to form stable nanoparticles. For example, TAT-derivatized proteins have been shown to deliver siRNA into primary and transformed cells, with minimal off-target effects and low cytotoxicity [151]. Poly-Arginine derivatives, such as cholesteryl oligo-D-nonaarginine (Chol-R9), are capable of simultaneously binding siRNAs and interacting with hydrophobic membrane lipids. Chol-R9

mediated delivery of *VEGF*-siRNA decreased the growth of tumor xenografts after intratumoral injection [164]. Recently, a rabies virus glycoprotein-derived peptide modified with poly-Arginine's was able to cross the blood-brain barrier, deliver siRNA to neurons *in vivo*, and protect mice from lethal encephalitis infection [165-166]. Elsewhere, amphipathic CPPs containing pH-titratable moieties, such as CADY and PepFect6 [167-168], have been shown to package siRNA into stable nanoparticles and trigger proton-sponge effects to aid in endosomal escape. However, all CPPs share the common feature of ubiquitous cell internalization: they are not cell-selective and translocate across the membrane of nearly all cell types *in vitro* and *in vivo* [151]. As a result, their translational potential for tumor-specific delivery is inherently limited.

In sum, since the discovery of RNA interference in mammalian cells in 2002, a wide array of systems for delivering siRNA have been developed [43]. The power of inhibiting the function of any gene using systemically administered siRNAs, especially ones that are undruggable by small molecule- or antibody-based approaches, will represent a paradigm shifting advancement in medicine. Furthermore, the added ability to amplify tumor parenchymal delivery of therapeutics using CendR peptides such as iRGD and LyP-1 could further enhance drug efficacy. With the explosion of genomics data and identification of novel oncogenes, a tumor-penetrating platform to target those lesions would be tremendously powerful. In this thesis, we develop a modular siRNA delivery system that overcomes the challenge of transporting therapeutics into the tumor parenchyma. Specifically, the system integrates the tumor specificity and tissue-penetrating abilities of CendR peptides with membrane penetration properties of canonical protein transduction domains. Using this system, siRNA therapeutics extravasated into the tumor interstitium, induced potent gene silencing, and suppressed the growth of disseminated ovarian tumors in mice.

1.5 Thesis Aims

The overall goal of the thesis is to develop an integrated platform for the *in vivo* discovery and validation of cancer targets, by combining novel nanomaterials for siRNA delivery with systematic efforts to identify essential genes in cancer cells. First, we developed versatile surface chemistries to target nanoparticles *in vivo*. We designed tandem peptides bearing membrane-translocation and CendR tumor-penetration motifs to act as tumor-specific siRNA carriers. We investigated the utility of the delivery system through the integrated interrogation of essential genes identified from whole-genome studies of human cancers. Finally, we extended the system to primary samples from ovarian cancer patients for clinical translation.
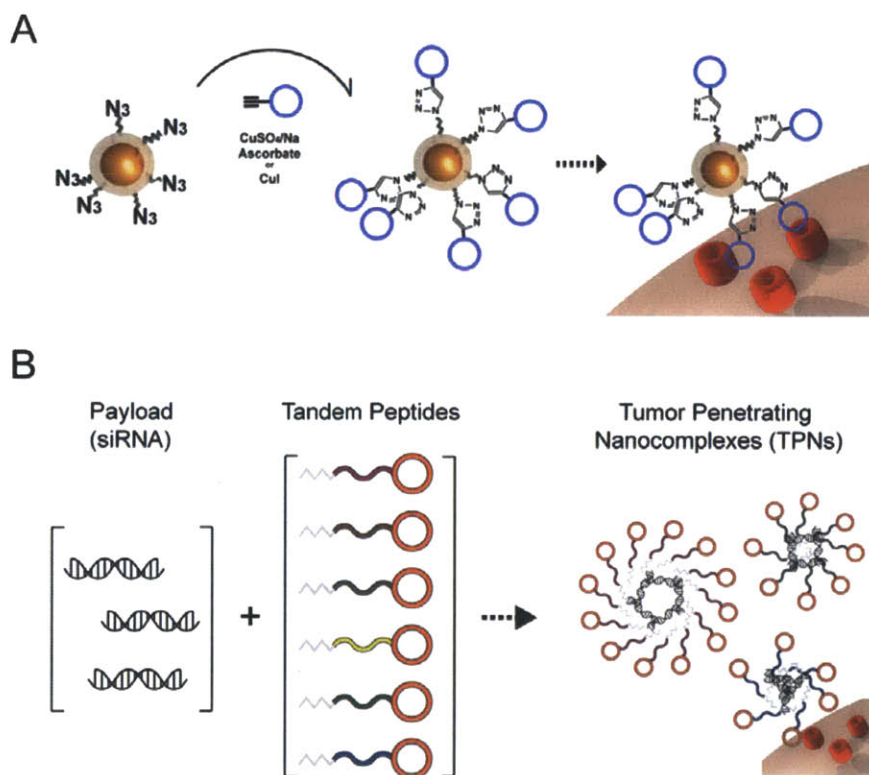
Figure 1.5. Schematic for Aim 1. (A) 'Click' attachment of LyP-1 onto iron-oxide nanoparticles for tumor targeting *in vivo*. **(B)** Screening of tandem peptides bearing cell-penetrating domains and a fixed cyclic tumor-penetrating domain (LyP-1, red) for delivery of siRNA in a cell type-specific fashion.

In **Aim 1**, we described the development of tumor-targeted and tissue-penetrating nanomaterials (**Figure 1.5**). We developed conjugation chemistries based on the "Click" reaction for attachment of LyP-1 peptides onto the surface of nanoparticles. To develop a system for siRNA delivery, we designed a library of tandem peptides bearing distinct cell-penetrating domains and LyP-1 as the tumor-penetrating domain. Upon complexation with siRNA, the resulting tumor-penetrating nanocomplexes (TPN) were taken up by tumor cells in a receptor-specific manner. TPN extended the circulation time of siRNA, protected them from degradation, and improved their tumor accumulation and tissue parenchymal targeting.
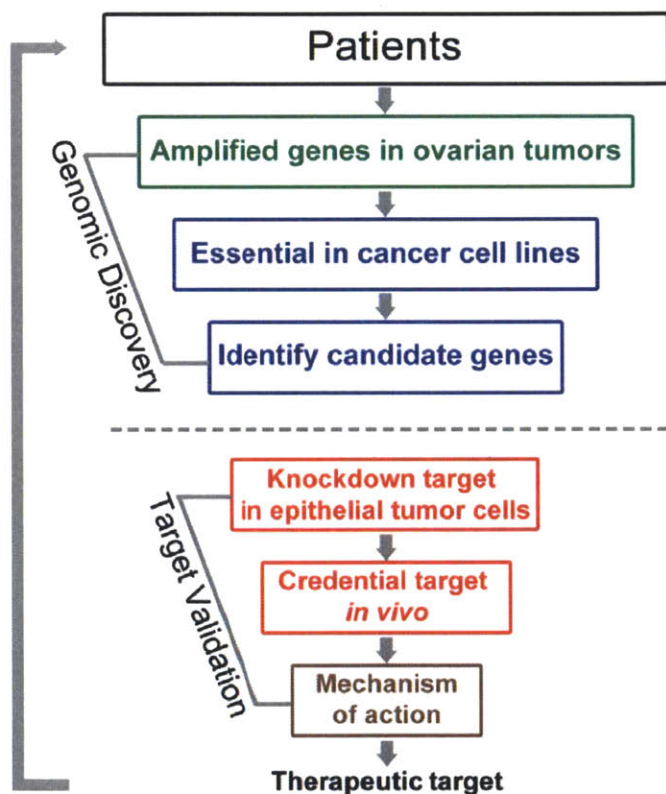
Figure 1.6. Schematic of Aim 2. An integrated platform enables high-throughput genomic discovery and rapid *in vivo* credentialing of cancer genes. Analyses of cancer genomes nominate candidate genes that are amplified and essential. The application of TPN for siRNA delivery overcomes the *in vivo* validation barrier (dotted line) by credentialing candidate genes and discover their mechanism of transformation. This will establish novel therapeutic targets to ultimately benefit patients.

In **Aim 2** of the thesis, we explored the utility of the TPN system as a platform for credentialing cancer targets (**Figure 1.6**). Integration of approaches that enumerate the structural

alterations in ovarian cancer genomes with technologies that identify genes essential for cancer provided a list of genes that are amplified and essential in ovarian cancer. In particular, the helix-loop-helix transcriptional regulator, *ID4*, was recurrently amplified in over 30% of primary ovarian tumors and essential for ovarian cancer cell lines. To validate *ID4* as a target amenable to therapeutic intervention *in vivo*, we applied TPN carrying siRNA targeting *ID4* to mouse models of ovarian cancer. Knockdown of ID4 suppressed the growth of aggressive tumors and improvement in overall survival. The versatility and modularity of the TPN system was investigated by targeting additional undruggable genes in ovarian cancer, including the tight-junction protein Claudin-3 (CLDN3), and the 19S proteasome regulatory complex PSMC2.
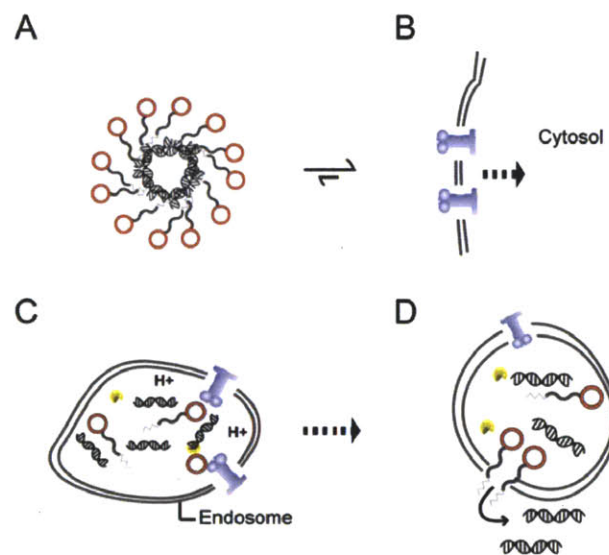
Figure 1.7. Schematic of Aim 3. Mechanistic studies to characterize pathways by which TPNs deliver siRNA payloads into select cancer cells. **(A)** Biophysical structural characterization of TPNs. **(B)** Quantitative analysis of TPN uptake in cancer cells expressing the cognate receptor, p32. **(C)** Measurement of rates of siRNA escape from endosomal entrapment. **(D)** Quantification of siRNA dissociation from the carrier and release into the cytosol.

In **Aim 3** of the thesis, we describe the mechanism and trafficking pathways by which TPN undertake to deliver siRNA in a cell type-specific manner (**Figure 1.7**). We characterized the physiochemical and functional properties of TPN including the valence of the tumor-penetrating ligand, the rate of endocytosis and endosomal escape, and dissociation of siRNA

from the carrier. We employed least square regression to derive structure-activity relationships and identified properties that favored receptor-specific siRNA delivery.

In **Aim 4** of the thesis, we apply the integrated platform developed in *Aims 1&2* in clinical translational studies (**Figure 1.8**). First, we explored a novel strategy to achieve sustained, high intratumoral accumulation of therapeutics by modulation of p32 receptor expression in the tumor microenvironment. We studied the effect of localized p32 suppression on TPN distribution *in vivo*. The utility of TPN delivery of *p32*-specific siRNA for tumor imaging by positron-emission tomography (PET) was also examined. Finally, the therapeutic activity of TPN-mediated siRNA delivery is investigated in primary cells derived from the ascites fluids of ovarian cancer patients. The generalizability of TPN targeting was also examined in a human tissue microarray containing tumor samples from ovarian cancer patients.
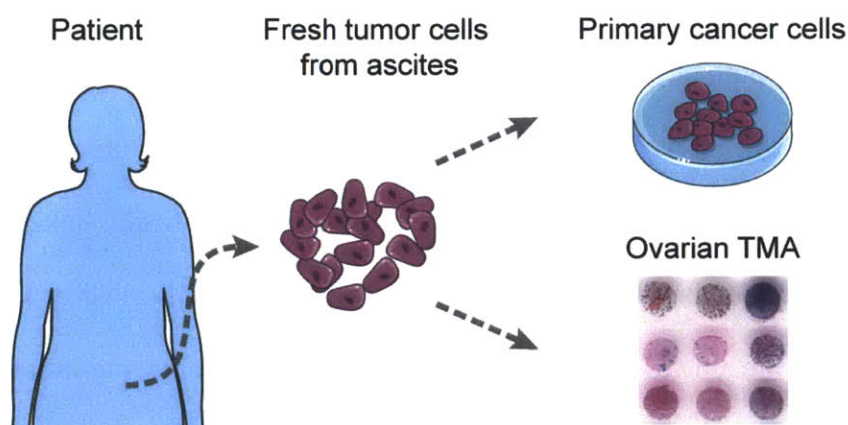
Figure 1.8. Schematic for Aim 4. Translational applications of the TPN system. The clinical feasibility of TPN-mediated siRNA delivery is examined in primary patient-derived ovarian cancer cells and ovarian tissue microarrays (TMA).

2 A versatile surface chemistry – *In vivo* tumor cell targeting with 'Click' nanoparticles

2.0 Abstract

The *in vivo* fate of nanomaterials strongly determines their biomedical efficacy. Accordingly, much effort has been invested into the development of library screening methods to select targeting ligands for a diversity of sites *in vivo*. Still, broad application of chemical and biological screens to the *in vivo* targeting of nanomaterials requires ligand attachment chemistries that are generalizable, efficient, covalent, orthogonal to diverse biochemical libraries, applicable under aqueous conditions, and stable in *in vivo* environments. To date, the copper(I)-catalyzed Huisgen 1,3-dipolar cycloaddition or "click" reaction has shown considerable promise as a method for developing targeted nanomaterials *in vitro*. Here, we investigate the utility of "click" chemistry for the *in vivo* targeting of inorganic nanoparticles to tumors. We find that "click" chemistry allows cyclic LyP-1 targeting peptides to be specifically linked to azido-nanoparticles and to direct their binding to p32-expressing tumor cells *in vitro*. Moreover, "click" nanoparticles are able to stably circulate for hours *in vivo* following intravenous administration (> 5h circulation time), extravasate into tumors, and penetrate the tumor interstitium to specifically bind p32-expressing cells in tumors. In the future, *in vivo* use of "click" nanomaterials should expedite the progression from ligand discovery to *in vivo* evaluation and diversify approaches toward multifunctional nanoparticle development.

(Reprinted (adapted) with permission from [169]. Copyright (2008) American Chemical Society)

2.1 Introduction

The ability to target nanomaterials to precise biological locations would have wide-ranging impact in medicine. In living systems, highly controlled transportation networks continually shuttle payloads to and from specific molecular addresses. The efficiency of these systems provides strong motivation for the advancement of targeted nanoparticle technologies, particularly for the diagnosis and treatment of human diseases. Towards this goal, high throughput strategies for ligand discovery have generated a multitude of chemical and biological motifs with the potential to direct nanomaterials to specific biomolecular targets. However, translation of these ligands towards *in vivo* nanoparticle targeting has been limited by the number of nanoparticle attachment methods that are efficient, generalizable, aqueous-compatible, chemically orthogonal to broad ranges of functional groups, and suitable for *in vivo* applications.

Previous work has demonstrated that *in vivo* bacteriophage display may be used to select for peptide sequences that mimic the ability of endogenous shuttles to target vascular and parenchymal tissue addresses [101, 170-173]. Already, linear peptide candidates of phage screens, as well as small molecule targeting candidates, have been translated towards nanomaterial targeting [103, 174-176], primarily via use of exogenous or non-essential thiols, carboxylic acids, or amines. Still, some of the most powerful targeting motifs developed to date are those that contain essential thiol, amine, and carboxyl groups, thereby prohibiting their specific attachment via traditional methods. In particular, conformationally-constrained, disulfide-cyclized targeting peptides are desirable for their enhanced affinity to biological receptors [177-178], and resistance to proteolytic degradation *in vivo* relative to their linear counterparts [179-180]. However, specific intramolecular cyclization makes it difficult to add exogenous cysteine residues, while essential amines and carboxyl groups prohibit selective

conjugation via exogenous lysine, aspartic acid, or glutamic acid residues. Additionally, non-covalent methods of ligand attachment relying on hydrophobic or electrostatic effects, although widely used *in vitro* [181-183], are unlikely to remain stable in blood or to resist rapid clearance *in vivo*.

Recently, the copper(I)-catalyzed Huisgen 1,3-dipolar cycloaddition or "click" chemistry has emerged as an extraordinarily selective chemistry and an attractive solution in applications where commonly used thiol-reactive (maleimide, 2-pyridyldithio, iodoacetyl) or amine-reactive (NHS, epoxy, aldehyde, EDC) chemistries are not suitable [184]. *In vitro*, "click" chemistry has been utilized to generate functionalized polymers [185-187], surfaces [188-190], and nanoparticles [191-199], and meets the criteria for broad utility in nanoparticle functionalization (chemical orthogonality, aqueous efficiency, applicability for diverse substrates). However the use of "click" nanoparticles for *in vivo* applications has not been investigated. Particularly, as opposed to small molecule reagents with circulation times on the order of minutes [176], ligand attachments on long circulating nanomaterials must remain stable against *in vivo* degradation for hours while nanoparticles circulate systemically and identify molecular targets.

Here, we find that alkyne-azide "click" chemistry provides a facile, single-step method for specifically linking the cyclic tumor-targeting peptide LyP-1 (CGNKRTRGC; [101, 200]), which contains essential thiol and amine groups, to polymer-coated magneto-fluorescent nanoparticles. LyP-1 binds to p32, a mitochondrial proteins that is both overexpressed and aberrantly localized at the cell surface of tumor cells, macrophages and lymphatic endothelial cells in certain experimental tumors and in human cancers [201-202]. We find that "click" LyP-1 nanoparticles are able stably traverse the systemic circulation, extravasate into tumors, and penetrate the tumor interstitium to specifically bind to receptors on p32-expressing cells in the

tumors. Together, these results provide strong motivation for future use of "click" functionalization as a strategy for developing nanoparticles for *in vivo* biomedical applications (**Figure 2.1**).
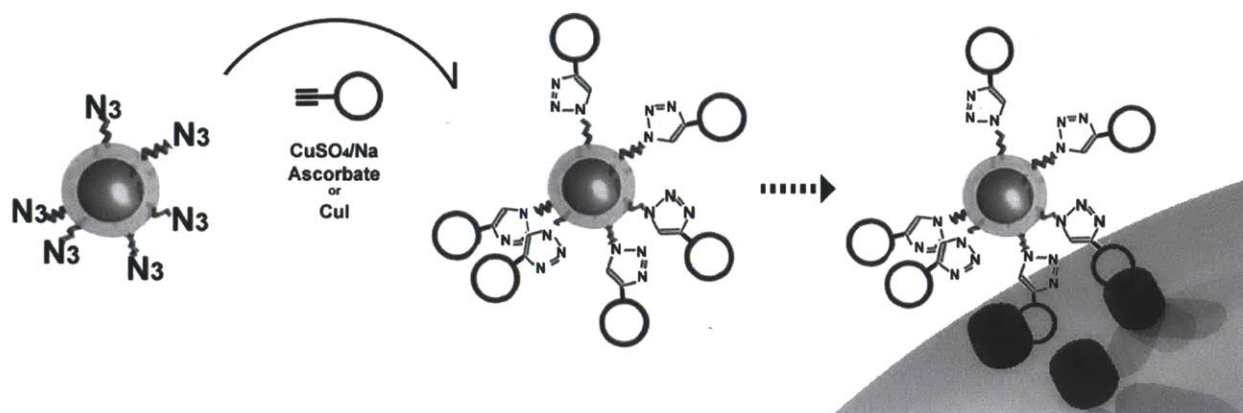
Figure 2.1. Design of a "click" nanoparticle that targets tumor cells *in vitro* and *in vivo*. Cross-linked, fluorescent, superparamagnetic iron oxide nanoparticles are modified to display azido-PEG groups. Conjugation of cyclic targeting peptides (purple circles) bearing pendant alkynes to azido-PEG nanoparticles via the copper(I)-catalyzed Huisgen 1,3-dipolar cycloaddition ("click" reaction) allows specific targeting of the nanoparticles to cells expressing the receptor (red).

2.2 Results and Discussion

In order for "click" chemistry to be applied to the development of peptide-targeted nanomaterials, peptides must be able to harbor pendant alkyne or azide moieties without abating peptide activity. To investigate the efficacy of targeting peptides harboring pendant alkyne moieties, LyP-1 peptide and untargeted cyclic control peptide, LyP-1CTL (CRVRTRSGC) in which the essential NKRTR motif is replaced with RVRTR to maintain net charge but abate p32 targeting [200], were synthesized to incorporate either of two alkyne moieties (the unnatural amino acid propargylglycine or 6-heptynoic acid) and a 5,6-carboxytetramethylrhodamine fluorophore (TAMRA) (**Figure 2.2**).
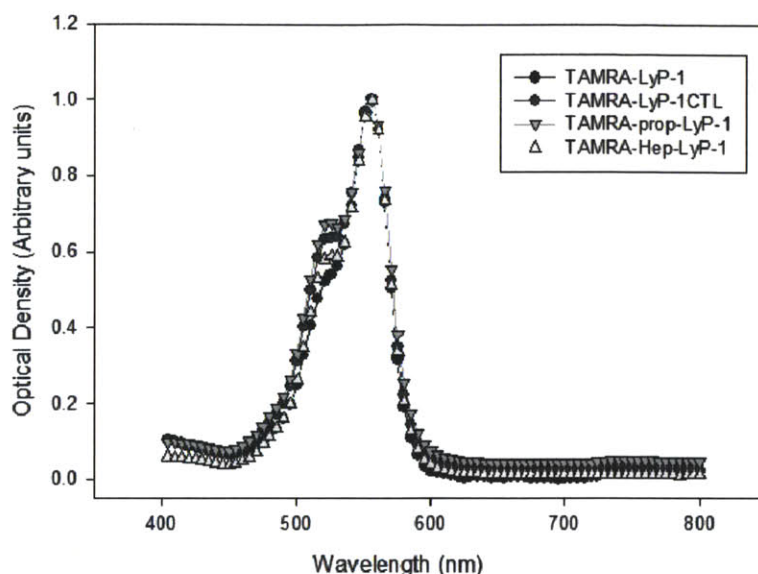
Figure 2.2. Fluorophore-labeled LyP-1 Peptide Spectra. UV-Vis spectra forLyP-1 and LyP-1CTL peptides synthesized with varying pendant alkyne groups (prop= propargylglycine; Hep=heptynoic acid)

Because the alkyne moieties provide molecularly small chemical handles that may be incorporated in FMOC synthesis to either the N- or C-terminal of essential peptide sequences, we hypothesized their presence could be tailored to allow chemical attachment to azido-nanomaterials without interfering with LyP-1 peptide activity. In previous investigations, we found that N-terminal addition of visible and near-infrared fluorophores do not disrupt peptide binding to its receptors [101, 200]. Accordingly, we reasoned alkyne moieties located near the N-terminus would be well-tolerated by the peptide.

To verify the specificity and efficacy of alkyne-LyP-1 targeting, 10 μM of LyP-1, bearing either propargylglycine, heptynoic, or no alkyne group were incubated for 45 minutes on monolayers of MDA-MB-435 human tumor cells, which have been shown to bind and internalize LyP-1 and express p32 at the cell surface [200-201], LyP-1CTL peptides were included as a control sequence to verify targeted enhancement of uptake over non-specific cyclic peptide structures. Cellular uptake of LyP-1 was quantified via flow cytometry and plotted as the populational fluorescent intensity, relative to cells incubated with vehicle alone. *In vitro* targeting

of LyP-1 peptides bearing either propargylglycine or 6-heptyoic acid was similar to that of native

LyP-1 and control peptides, indicating that alkyne modifications N-terminal to targeting

sequences were innocuously chaperoned by peptides and did not affect cell binding (**Figure 2.3**).
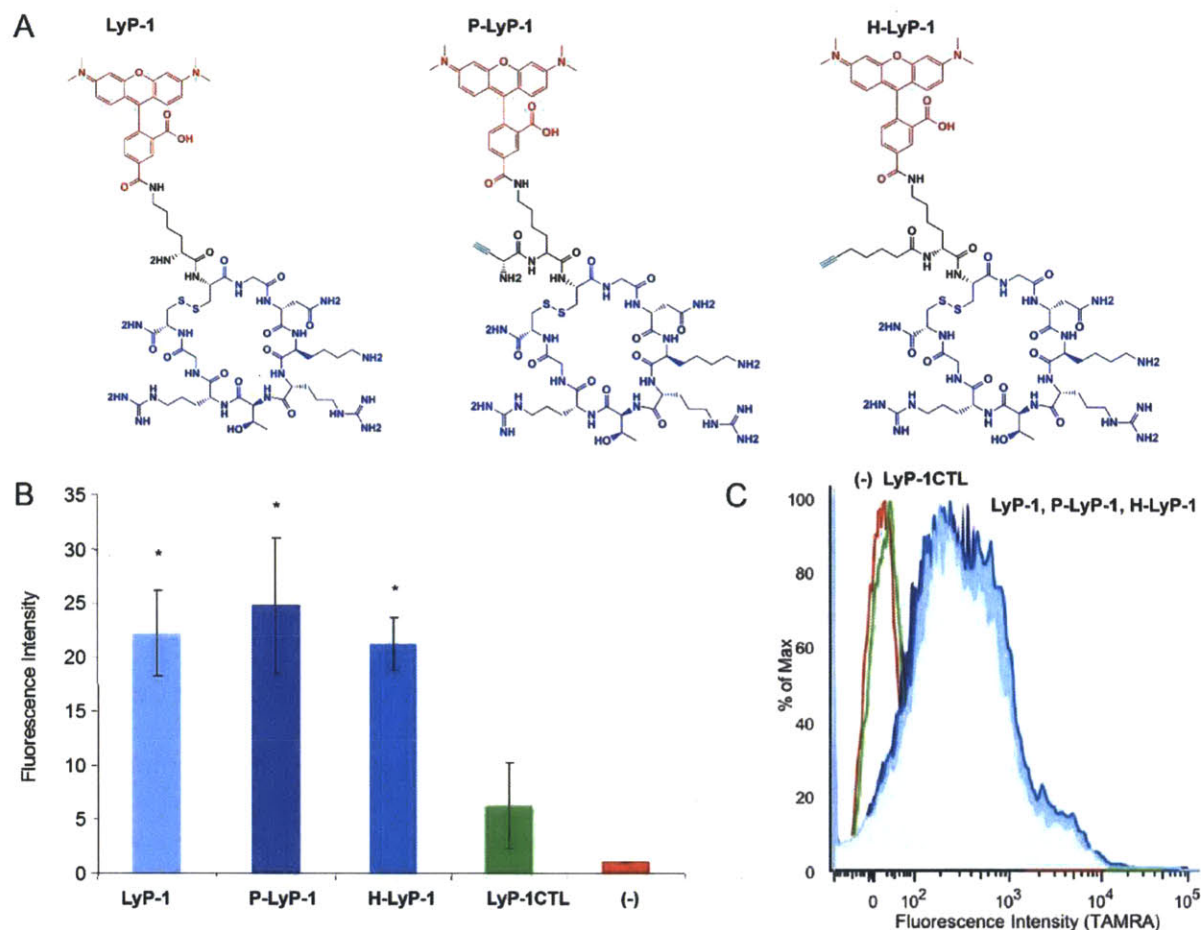
Figure 2.3. Native and alkyne-bearing LyP-1 peptides target p32-expressing MDA-MB-435 cells in vitro.(A) Structures of LyP-1, propargylglycine-LyP-1, and Heptynoic acid-LyP-1, all labeled with a TAMRA fluorophore (red). The cyclic nonapeptide is in blue. The pendant alkyne moieties were conjugated to the N-terminus of the peptide during standard FMOC peptide synthesis. **(B)** Flow cytometry shows that peptides bearing different alkyne groups target MDA-MB-435 cancer cells similarly, while a scrambled control (LyP-1CTL) do not target (P=propargylglycine, H=6-heptynoic acid, *$p<0.01$, unpaired Student's *t*-test).**(C)** Flow cytometry histogram shows LyP-1, P-LyP-1, and H-LyP-1 peptides (in different shades of blue) target MDA-MB-435 cells *in vitro*, while LyP-1CTL peptide (green) did not show targeting relative to peptide-free control cells (red).

We next probed the effect of three variables on "click" reaction conditions between our

peptides and an azido-PEG-amine (catalyst, catalyst concentration, and reaction time). Azido-

PEG-amine was chosen to emulate the azido-PEG surface of the nanoparticles to be used

subsequently and to provide a model reaction amenable to HPLC quantitation of product formation. Copper(I) catalyst was added either directly as an iodinated salt (Cu(I)I), or indirectly as soluble copper sulfate (Cu(II)SO$_4$) and reduced by sodium ascorbate *in situ*. The degree of product formation was measured via HPLC with mass spectrometric verification of product identity. The addition of the azido-PEO-amine rendered peptides more hydrophilic and decreased retention times compared to unconjugated peptides. Product formation proceeded more completely in the tested reaction conditions for the heptynoic acid-LyP-1, likely due to reduced steric hindrance provided by the extended hydrocarbon chain (**Table 2.1**). Optimal reaction conditions were found to be either: 1 mM CuSO$_4$ / 5 mM Na ascorbate or 1 mM -100 mM CuI for 72 h. Notably, the reaction yields with 10 mM CuSO$_4$ levels were dramatically lower than 1mM, likely due to global precipitation of reduced Cu(I) in solution. Nevertheless, we found 1mM CuSO$_4$ reactions to yield more reliable conjugations than 1 to100 mM CuI reactions, possibly because the insolubility of CuI in aqueous solutions produced variations in the amount of available catalyst. Therefore, the optimal conditions for subsequent nanoparticle modification were determined to be 1 mM CuSO$_4$ and 5 mM Na ascorbate. Under these conditions we did not observe any reduction of peptide disulfide bonds due to copper catalyst or Na ascorbate reduction as determined by MALDI mass spectrometry and HPLC analysis.

Table 2.1. Optimization of the "click" reaction. The rate of product conversion in the "click" reaction is measured as a function of product formation in HPLC. The reaction is performed in various catalysts (CuSO4 or CuI) and concentrations, in 24h or 72h reactions, using LyP-1 peptides bearing either propargylglycine or 6-heptynoic-acid.

Catalyst type [mM]	Click reaction time (h)	Propargylglycine-LyP-1	Heptynoic Acid-LyP-1
CuSO4 [1 mM]	24	44%	48%
CuSO4 [1 mM]	72	80%	82%
CuSO4 [10 mM]	24	0%	0.5%
CuSO4 [10 mM]	72	0%	13%
CuI [1 mM]	24	70%	70%
CuI [1 mM]	72	76%	95%
CuI [10 mM]	24	68%	76%
CuI [10 mM]	72	77%	100%
CuI [100 mM]	24	75%	83%
CuI [100 mM]	24	79%	89%
No Catalyst	72	0%	0%

Having verified that alkyne-bearing LyP-1 peptides could effectively target p32-expressing MDA-MB-435 cancer cells and become linked to azido-bearing PEG polymers, we next developed a protocol for linking these peptides onto azido-PEG bearing, near-infrared fluorochrome-labeled (VivoTag 680) iron oxide nanoparticles. Dextran-caged iron oxide nanoparticles were used as the parent formulation to provide a highly stable, relatively non-cytotoxic, and *in vivo*-tested nanoparticle scaffold. Briefly, a heterobifunctional linker bearing an azide on one end an N-hydroxysuccinimide leaving group on the other was synthesized and attached to an amine-PEG-thiol polymer (MW 50000 Da) via its terminal amine.

Azido-PEG-thiol polymers were subsequently linked to surface of cross-linked, aminated, fluorochrome-labeled, and dextran-coated iron oxide nanoparticles via the linker N-[γ-maleimidobutyryloxy] succinimide ester (GMBS) (**Figure 2.4**). Long PEG polymers were utilized to carry pendant azide groups in order to enhance particle circulation time *in vivo* and to provide a generalizable nanoparticle surface, whereby optimized "click" attachment conditions might be applicable to other PEG-coated organic and inorganic nanomaterials in the future. Azido-PEG particles were purified from excess polymer and linked to alkyne-bearing peptides in 1 mM CuSO$_4$, 5 mM Na ascorbate. Finally, the conjugated nanoparticles were purified and sterile filtered for*in vitro* and *in vivo* applications.

A

B

C
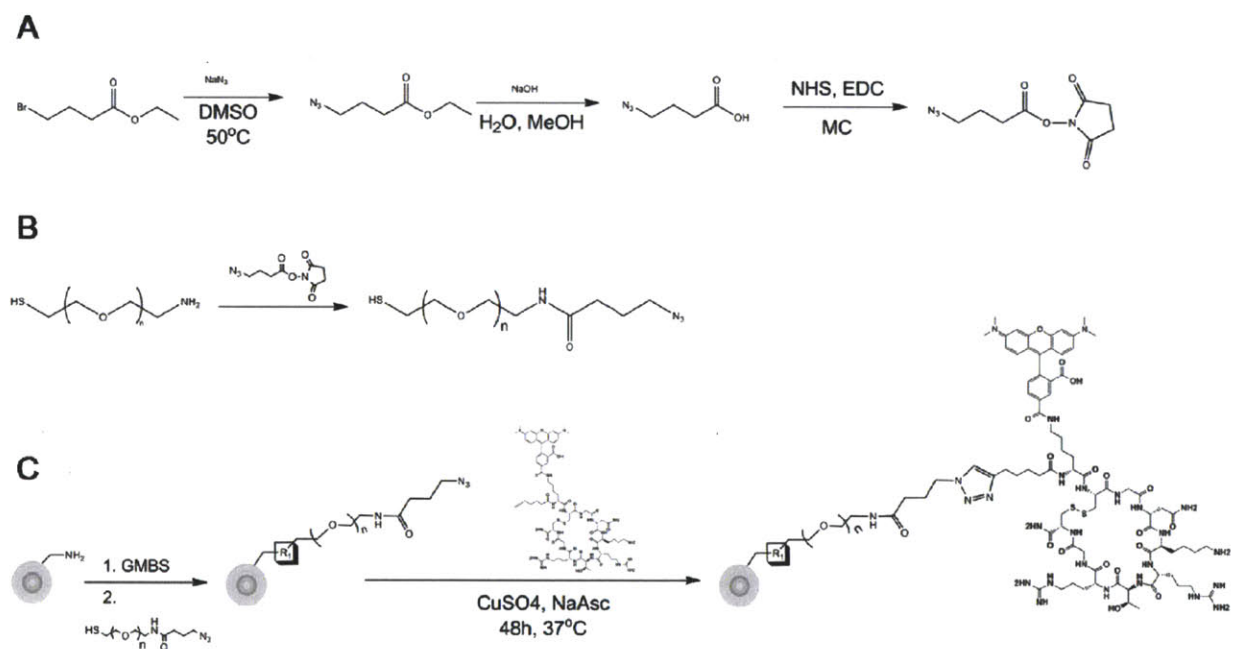
Figure 2.4. Synthesis of LyP-1-coated nanoparticles using "click" chemistry. (A) Synthesis of Succinimidyl 4-azidobutyrate. **(B)** Synthesis of azide-PEG-thiol by linking Succinimidyl 4-azidobutyrate to a 5kDa thiol-PEG-amine. **(C)** Aminated, cross-linked, fluorochrome-labeled superparamagnetic iron-oxide nanoparticles are activated with GMBS, filtered, and then reacted with the thiol-PEG-azide from (B) to yield azido-PEG bearing nanoparticles. After purification, the particle solutions were reacted with alkyne-bearing LyP-1 peptides with CuSO$_4$/Na Ascorbate as catalysts to yield LyP-1-coated nanoparticles for *in vitro* and *in vivo* use.

Peptide valency on nanoparticles was assessed spectrophotometrically by quantifying the number of TAMRA dyes added onto nanoparticles following "click" reaction (**Figure 2.5**). In the presence of catalyst, approximately 30 peptides were added per nanoparticle for both LyP-1 and LyP-1CTL peptides, whereas no addition was observed in the absence of catalyst. LyP-1 nanoparticles, LyP-1CTL nanoparticles, or azide nanoparticles were incubated over MDA-MB-435 tumor cells for 2 hours and nanoparticle accumulation was quantified using flow cytometry. LyP-1-nanoparticles showed significant tumor cell accumulation, while LyP-1CTL-nanoparticles or azide-nanoparticles displayed minimal cell uptake (**Figure 2.6**). The effect of serum on nanoparticle uptake was also studied, as low serum levels enhance the stress-induced expression of the p32 receptor [200]. The slight increase in LyP-1-nanoparticle targeting in lower serum levels provided further validation of receptor-specific targeting, as decreased serum protein concentrations lowers the likelihood of non-specific serum protein mediated uptake (**Figure 2.6**).
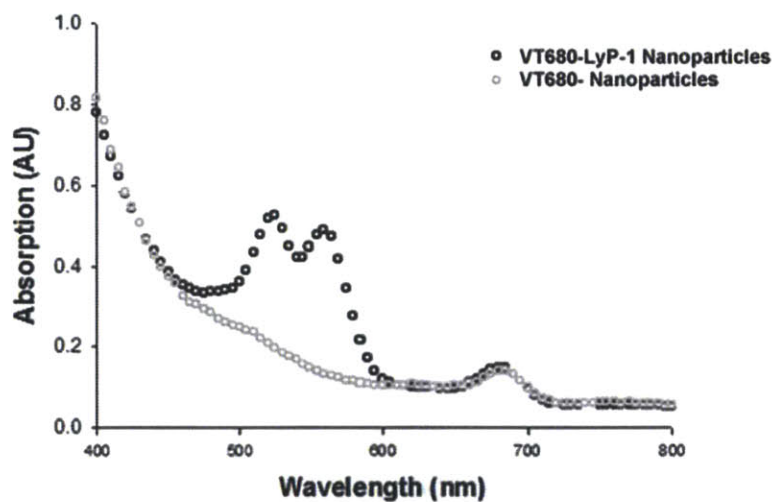
Figure 2.5. Spectrophotometric characterization of Click nanoparticles. The amount of peptide bound per particle was quantified spectrophotometrically by measuring the absorbance of the TAMRA dyes added following the click reaction. With the addition of catalyst $CuSO_4$/Na ascorbate (dark circles), the TAMRA absorbance at 555nm was quantified to equal approximately 30 peptides per particle, whereas no TAMRA signal was observed without catalyst (light circles).
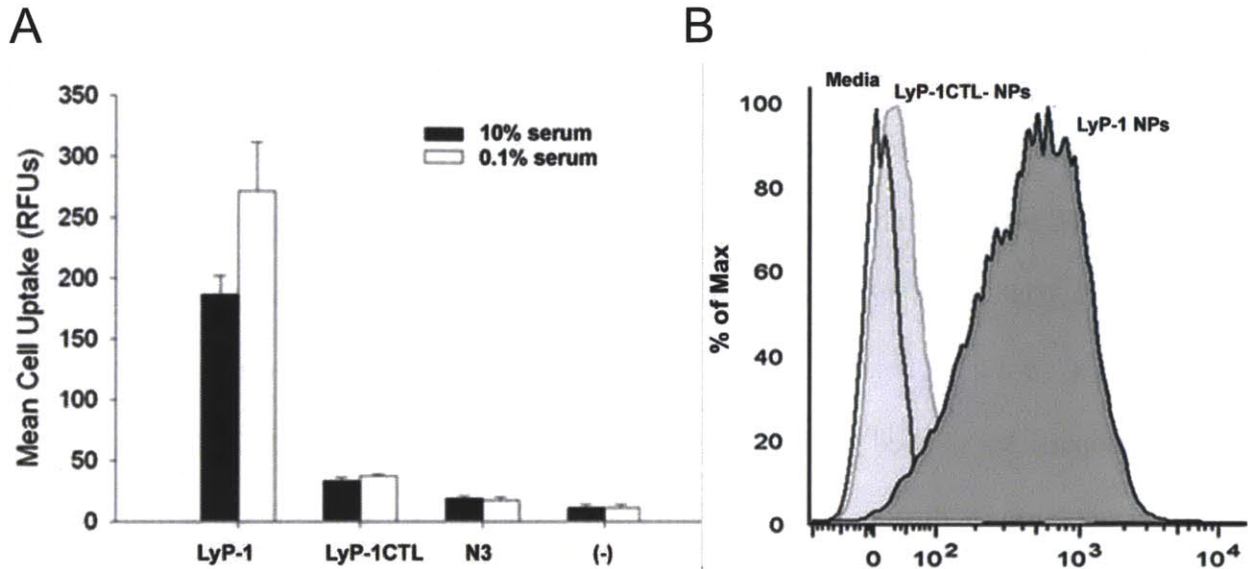
Figure 2.6. LyP-1-conjugated nanoparticles target p32-expressing MDA-MB-435 cells in vitro, while nanoparticles conjugated to control cyclic peptides (LyP-1CTL) do not target. (A) LyP-1-nanoparticles or control LyP-1CTL-nanoparticles (both at ~30 peptides per particle), or parent azido-bearing particles (N3), were added to MDA-435-MB cancer cells in normal 10% serum (dark green) and 0.1% serum-starved (light green) conditions. **(B)** Flow cytometry histogram shows marked increase in uptake of LyP-1-nanoparticles (blue) vs. LyP-1CTL-nanoparticles (green) and particle-free control cells (red). Each error bar represents 6 parallel experiments.
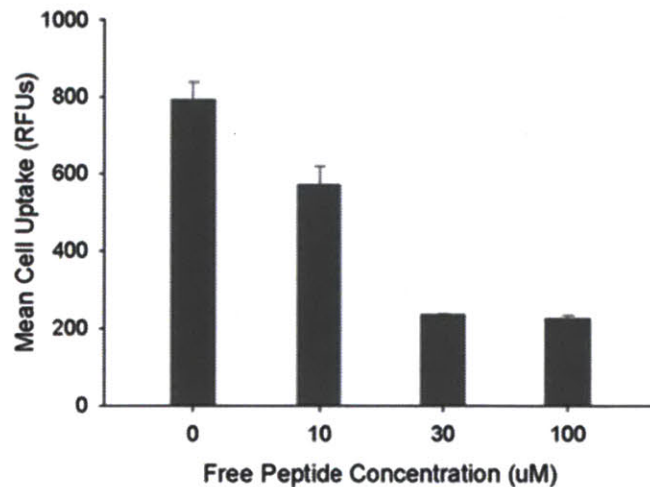
Figure 2.7. Effects of LyP-1 peptide on the cellular uptake of Click nanoparticles. Addition of free LyP-1 peptides at concentrations from 10 to 100 uM inhibited cellular uptake of LyP-1-coated nanoparticles, suggesting that the LyP-1 peptide and LyP-1-labeled particles target the same receptor.

To further confirm the uptake specificity of LyP-1-nanoparticles, free LyP-1 peptide was

added to cells along with LyP-1-particles. Dose-dependent inhibition of uptake was observed

with LyP-1 peptide concentrations from 10 to 100 μM, suggesting the free LyP-1 and LyP-1-labeled particles share common cellular receptors (**Figure 2.7**). We attribute the large excess of free peptide required for inhibition compared to the concentration of nanoparticles used (100 nM) to the presence of multiple copies of the LyP-1 peptide on each nanoparticle, thus improving nanoparticle avidity to receptors through polyvalent binding [203].

In order to visualize LyP-1 peptide-mediated cell uptake, nanoparticles bearing LyP-1 peptides, control LyP-1CTL peptides, or azides were incubated over MDA-MB-435 cells and imaged via epifluorescence microscopy (**Figure 2.8**). LyP-1-nanoparticles were seen associated with cells, while markedly less binding of azide-bearing or control peptide-bearing nanoparticles was not observed. If the same staining procedure was instead performed at 24 hrs post incubation, LyP-1-nanoparticles were seen in punctate locations consistent with sequestration in endosome-like compartments (**Figure 2.9**). To assess the cytotoxicity of "click" nanoparticles, NH_2-PEG-, azido-PEG- and peptide-conjugated nanoparticles were incubated for 24hrs of incubation above HeLa cell cultures. In all three formulations, the TC_{50} is >7mM Fe, or over 16 times higher than maximal blood concentrations during *in vivo* experiments performed here and 32 times higher than concentrations used *in vitro* here (**Figure 2.10**).

N3-Nanoparticles   **LyP-1CTL-Nanoparticles**   **LyP-1-Nanoparticles**
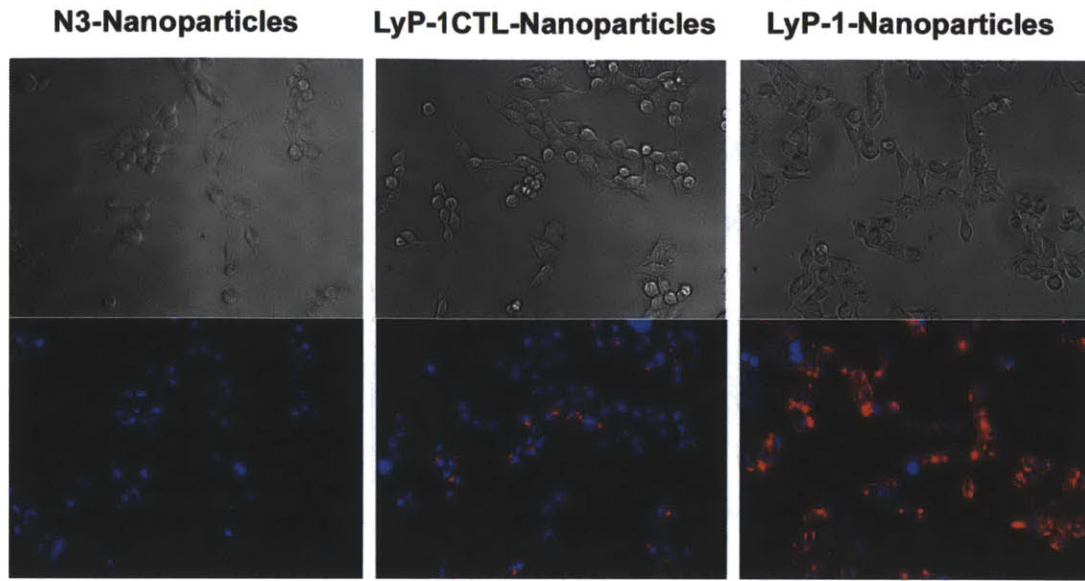
Figure 2.8. Tumor cell targeting with LyP-1 nanoparticles. LyP-1-nanoparticles target MDA-MB-435 cancer cells (right). Fluorescence imaging of cells incubated with LyP-1-nanoparticles showed increased near-infrared fluorescence (red). Uptake of azido-bearing or scrambled control peptide (LyP-1CTL)-bearing nanoparticles are not visible or show minor background (left and middle).
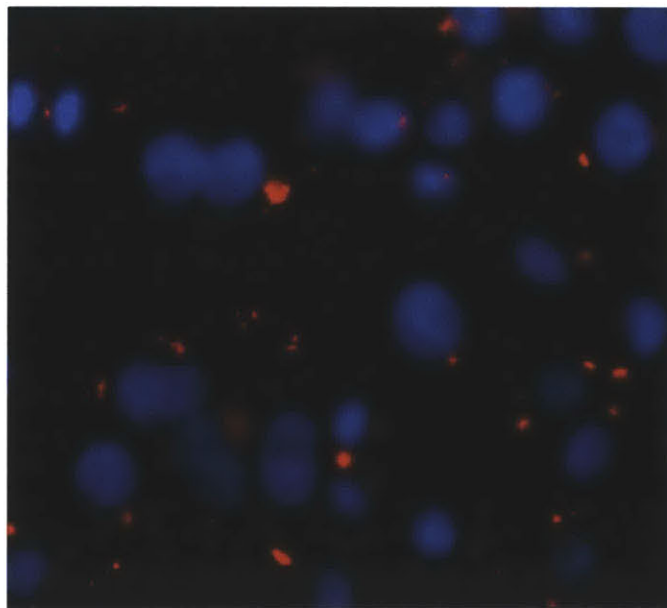
Figure 2.9. LyP-1-nanoparticles target MDA-MB-435 cancer cells and become localized in endosome-like compartments. Cells were incubated with LyP-1-nanoparticles for 30min, washed, and incubated for 24hrs before nuclear staining and imaging. PEG-LyP-1 nanoparticles no longer show diffuse membranous staining, but have become localized into punctuate compartments, implying endosomal sequestration away from cell surface
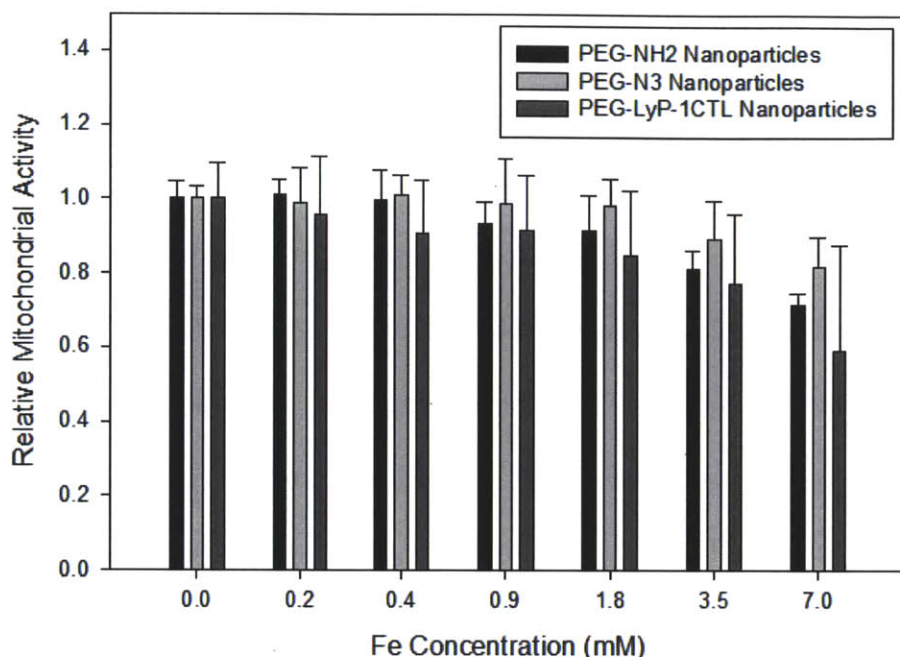
Figure 2.10. Probing "Click" Nanoparticle Cytotoxicity to Human Cell Cultures. Human HeLa cervical cancer cells were incubated with parent NH2-PEG-NPs, PEG-N3-NPs, or PEG-LyP-1CTL-NPs at varying concentrations for 24 hrs. Quantitaion of cellular viability showed that all three NP peparations have TC_{50} values of greater than 7mM, which is over 35-times that used *in vitro* here and greater than sixteen times the maximum blood concentrations during *in vivo* experiments.

Having found that "click" attachment of homing peptides mediated nanoparticle targeting *in vitro*, we evaluated the ability of "click" chemistry to direct nanoparticles to specific tumor cells *in vivo*. Again, near-infrared fluorochrome-labeled (VivoTag 680) nanoparticles were "clicked" to LyP-1 peptides, resulting on average of ~30 LyP-1 peptides per particle, while the parent azido-PEG nanoparticles were used as a negative control. Each population of nanoparticles was injected i.v. into mice bearing MDA-MB-435 melanoma xenografts. Nanoparticles were allowed to circulate in mice for 24 hrs, after which the mice were sacrificed and organs collected for immunohistochemical or whole organ fluorescence analysis. Vascular staining with anti-CD31 antibodies showed that azide nanoparticles in tumors remained localized within the immediate periphery of blood vessels. This perivascular distribution of untargeted nanomaterials is in agreement with previous histological and intravital observations of passive

liposomal accumulation in tumors [204-205]. By contrast, LyP-1 "click" nanoparticles appeared to have extravasated from the tumor vasculature, penetrated into the interstitial space of the tumor, and bound to p32-expressing cells (**Figure 2.11**).

As a result, the fraction of LyP-1 nanoparticles that get sequestered beyond the perivascular space was significantly higher than that of azido-nanoparticles (**Figure 2.12**) ($P<0.005$). This pattern was observed in all injected mice and is characteristic of LyP-1 peptide and phage homing observed previously [101]. Interestingly, previous LyP-1 bacteriophage experiments showed that the LyP-1-expressing phage concentrate in non-vascularized sites of tumors within minutes after injection while insertless phage do not reach these regions [101]. Thus, there may be unique transportation pathways within tumors that are exploited by this ligand after extravasation that are not available to untargeted materials. In the future, the localization of LyP-1 nanoparticles in avascular tumor regions may be of use for directing therapeutics into hypoxic regions of tumors, where most nanoparticle therapies do not reach.

Whole organ assessment of near-infrared tumor fluorescence demonstrated that, despite the distinct microscopic behavior of LyP-1 nanoparticles, the macroscopic tumor accumulation of LyP-1 nanoparticles and PEG-azide nanoparticles was similar (**Figure 2.13**), indicating that the targeted accumulation of LyP-1-nanoparticles was on par with passive delivery, whereby long-circulating materials accumulate in tumors via their hyper-porous vasculature over time [206-207]. These results are in accordance with data showing that the development of targeted nanoparticle formulations that amplify the macroscopic accumulation in tumors requires systematic *in vivo* optimization of multiple material parameters, including target avidity, circulation time, and particle size [129, 208]. Experiments of this kind are ongoing in order to probe the power of the LyP-1 targeting ligand for amplifying the accumulation and efficacy of

nanoparticle-based imaging and therapeutic agents.
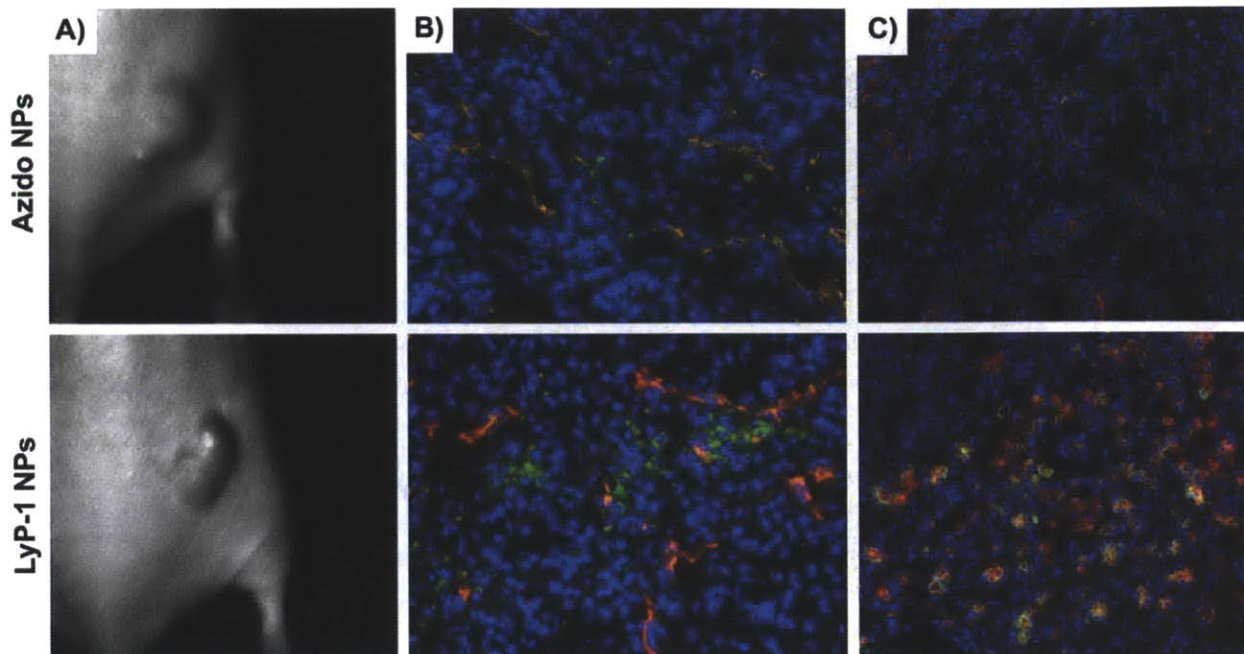
Figure 2.11. "Click" LyP-1-nanoparticle targeting to tumor cells *in vivo*. Nanoparticles bearing only azide groups (top) or labeled with LyP-1 peptides (bottom) that are matched in circulation time were injected intravenously via the tail vein into mice bearing human MDA-MB-435 cancer xenografts. Histological sections were obtained 24 hours post injection. **(A)** Light reflectance images of tumor xenografts. **(B)** Fluorescent LyP-1-nanoparticles (green) did not co-localize with CD31, a blood vessel marker (red) while untargeted azide-PEG nanoparticles remained localized to the blood vessels or their immediate periphery. **(C)** LyP-1-nanoparticles (green) accumulated in regions of high p32 expression (red), whereas untargeted, azido-bearing nanoparticles did not accumulate in these areas.
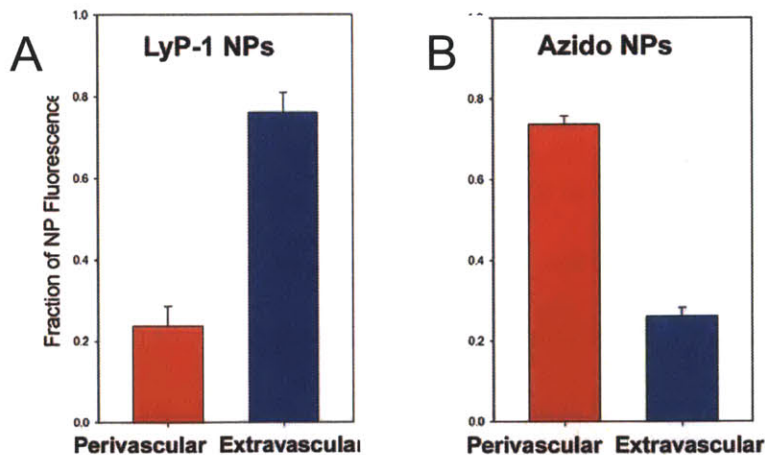
Figure 2.12. Quantification of "Click" LyP-1-nanoparticle targeting to tumor cells *in vivo*. Histological quantitation using CD31 stain to assess nanoparticle localization to immediate periphery of blood vessels. **(A)** The fraction of LyP-1 nanoparticles outside of the perivascular space of CD31-stained blood vessels is significantly higher than **(B)** azido-nanoparticles ($P<0.005$) as assessed from 3 randomly chosen views in each set of mice (n=3).
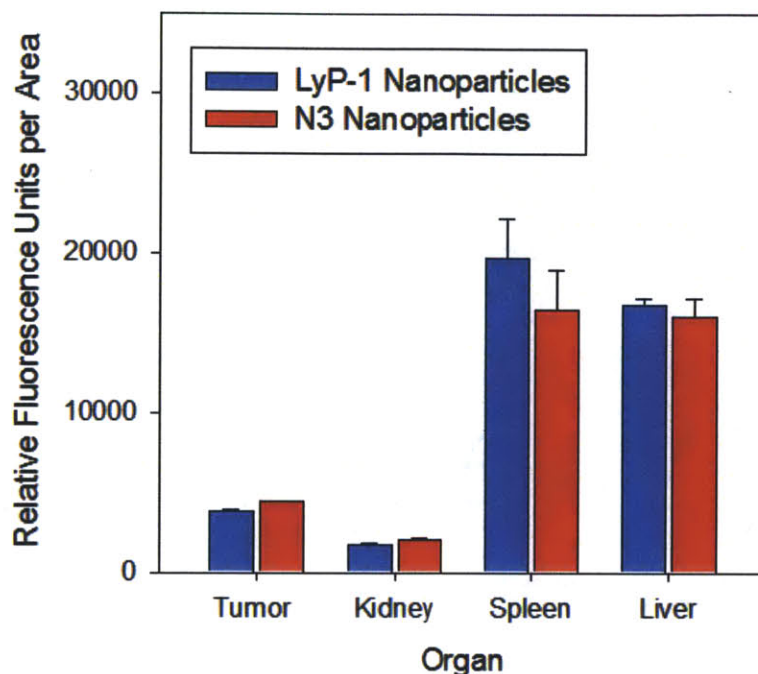
Figure 2.13. Near-Infrared Fluorescence Analysis of Nanoparticle Accumulation. Near-infrared fluorochrome-labeled nanoparticles bearing terminal azide (red) or LyP-1 (blue) were injected i.v. into mice bearing MDA-MB-435 melanoma xenografts. After 24 h, tumor, liver, spleen, and kidneys were fluorescently imaged for nanoparticle accumulation.

2.3 Conclusions

In this work, we have demonstrated that "click" chemistry may be used to develop nanoparticles that seek out specific cells *in vivo* based on their surface expression of protein markers. Ultimately, these findings suggest that "click" chemistry meets the criteria of being applicable under aqueous conditions, efficient, orthogonal to thiol- and amine-containing targeting motifs, and stable in the complex *in vivo* environments of the blood and tumor milieu. In the future, this work may empower the development of "click" nanomaterials that seek out specific tumor cell types, including tumor stem cells and angiogenic endothelial cells, or amplify the macroscopic accumulation of imaging agents or therapeutics in tumors. Further, the modularity of this "click" attachment strategy should allow it to be adapted to a diversity of *in*

vivo nanoparticle platforms and both biological and synthetic ligands, potentially empowering

novel on-nanoparticle screen approaches to targeted nanomaterial development.

2.4 Materials and Methods

Unless otherwise stated all reagents were purchased from Sigma-Aldrich and all reactions were performed at room temperature.

Iron-oxide nanoparticle synthesis. Cross-linked, aminated, fluorescent, superparamagnetic iron oxide nanoparticles were synthesized according to the published protocol [209-210]. Briefly, dextran-coated iron oxide nanoparticles were synthesized, purified, and subsequently cross-linked using epichlorohydrin. After exhaustive dialysis, particles were aminated by adding 1:10 v/v ammonium hydroxide (30%) and incubated on a shaker overnight. Aminated-nanoparticles were subsequently purified from excess ammonia using a Sephadex G-50 column and concentrated using a high-gradient magnetic-field filtration column (Miltenyi Biotec). The near infrared-fluorochrome VivoTag 680 was added to remotely detect particle accumulation *in vitro* and *in vivo* by reacting in 0.1M HEPES buffer with 0.15M NaCl at pH 7.2. DMSO-solubilized fluorochromes were added into particle solutions at 4°C under mixing and allowed to warm to room temperature to react for 2 hours. The yield was approximately 10 fluorochromes per nanoparticle for all experiments.

Succinimidyl 4-azidobutyratesynthesis.
Ethyl 4-azidobutyrate (1). To a solution of ethyl 4-bromobutyrate (5.85 g, 30 mmol) in dimethyl sulfoxide (DMSO, 20 ml), sodium azide (2.925 g, 45 mmol) was added with stirring. The reaction mixture was stirred for 22 h at 55 °C, and cooled to room temperature. Water was added to the reaction mixture and extracted with ethyl ether (3 x 30 ml). Combined organic layer was washed with water and brine, and reduced *in vacuuo* to afford 3.80 g of the azido compound 1.
4-Azidobutyric acid (2). Ethyl 4-azidobutyrate 1 (3.14 g, 20 mmol) was dissolved in aqueous sodium hydroxide solution (1 N, 24 ml) with minimum amount of methanol to make the solution homogeneous. The reaction mixture was stirred for 3 hrs at room temperature. After removal of methanol *in vacuo*, the aqueous solution was acidified to pH 0 with HCl and extracted with ethyl ether (3 x 50 ml). The ether layer was then dried over sodium sulfate and filtered. Removal of solvent gave the acid 2 (2.25 g).
Succinimidyl 4-azidobutyrate (3). To a solution of N-hydroxyl succinimide (1.65 g, 14.3 mmol) in methylene chloride (100 ml) was added acid 2 (1.68 g, 13 mmol) followed by 1-Ethyl-3-[3-dimethylaminopropyl] carbodiimide hydrochloride (EDAC, 2.74 g, 14.3 mmol). After stirring for 4 h at room temperature, the mixture was washed with water and brine, dried over sodium sulfate, and filtered. Solvent was removed under reduced pressure to yield 1.15 g of the succinimidyl 4-azidobutyrate 3.

Peptide synthesis. Peptides were synthesized in the MIT Biopolymers Lab and their composition was confirmed via HPLC and mass spectrometry. The LyP-1 and LyP-1CTL peptides were synthesized with either heptynoic acid or propargylglycine at the N-terminus for conjugation. Each peptide is also labeled with a TAMRA fluorophore (Anaspec) via a lysine residue separated by an aminohexanoic acid (Ahx) spacer. (LyP-1: Heptynoic acid or propargylglycine – K(Tamra)[Ahx] – CGNKRTRGC; LyP-1CTL: Heptynoic acid or propargylglycine – K(Tamra)[Ahx] – CRVRTRSGC). Peptides were cyclized by bubbling air into 10 μM aqueous peptide solutions overnight and lyophilized for subsequent use.

"Click" attachment of peptides to nanoparticles. Succinimidyl 4-azidobutyrate was linked to 5kDa thiol-PEG-amine polymers in 0.1M HEPES 0.15M NaCl pH 7.2 for 1 hour at a 2:1 molar ratio between linker and polymer. Simultaneously, amino-modified, fluorochrome-labeled nanoparticles were activated with N-[γ-maleimidobutyryloxy] succinimide ester (GMBS) (dissolved in DMSO) cross-linker under similar conditions at a 200:1 molar ratio between cross-linker and nanoparticles. To remove excess GMBS, nanoparticle samples were filtered on a G50 column into 50mM Na Phosphate buffer at pH 7.2 supplemented with 10mM EDTA. Purified nanoparticles were then combined with the polymer reaction mixture and allowed to react at room temperature overnight. Azido-PEG-nanoparticles were then purified from excess polymer and succinimidyl 4-azidobutyrateon a size exclusion column (ACA-44 media: Pall) into 0.1M HEPES pH 7.2 buffer. Finally, the azide-PEG-bearing particles were concentrated using Amicon Ultra-4 (Millipore) filters and stored at 4°C.

To optimize catalyst concentrations for the "click" reaction by HPLC, a 10-fold excess of azido-PEG-NH$_2$ or O-(2-Aminoethyl)-O'-(2-azidoethyl) pentaethylene glycol (Polypure) was added to a 100 µM peptide solution. CuSO$_4$ and Na ascorbate were dissolved in H$_2$O and added to the reaction mixture to final concentrations of 1 mM/5 mM and 10 mM/50 mM CuSO$_4$/Na Ascorbate. This mixture was shaken at 37°C for various times (1 day to 3 days), after which it was characterized via HPLC.

Alkyne-bearing peptides (35:1 peptide:nanoparticle molar ratio), CuSO$_4$ (1 mM), and sodium ascorbate (5 mM) in H$_2$O were added to a solution of particles and the mixture was shaken at 37°C for 48 h. Following the reaction, nanoparticles were purified from copper catalyst and excess peptides by filtration in ACA-44 size exclusion media into 0.1M HEPES 0.15M NaCl pH 7.2 buffer.

Cell culture. Cell uptake experiments were performed using a human MDA-MB-435 cancer cell line. Grow media was minimum essential medium eagle (Invitrogen) with fetal bovine serum (10%; Invitrogen). Cells were passaged into 96-well plates and used at 60-80% confluency.
For peptide uptake experiments, LyP-1 or LyP-1CTL peptides were added to cell monolayers in serum-containing media at a final concentration of 10 µM. After 45 minutes of incubation at 37 °C, cells were washed for flow cytometry (BD LSRII). Fluorescence data on 10,000 cells was collected for each sample.

For nanoparticle uptake, particles bearing LyP-1, LyP-1CTL, or terminal azides were added to the cells. After 2 h of incubation, cells were trypsinized and assayed for particle fluorescence by flow cytometry. For peptide inhibition experiments, free LyP-1 peptides (10 µM to 100 µM) were first incubated with the cells for 1 h. The cells were then washed and 100 nM of LyP-1-coated nanoparticles were added to the cell culture. For imaging, cells were observed using a 20x objective. Images were captured with a CCD camera mounted on a Nikon TE200 inverted epifluorescence microscope.

In vivo **studies of nanoparticle targeting.** Nude athymic mice were inoculated subcutaneously with human cancer cells (MDA-MB-435). After tumors had reached ~.5 cm^3 in size, LyP-1- and azide-bearing nanoparticles were injected intravenously in the tail vein (1mgFe/kg). Twenty-four hours after the injection, tumor tissues were excised, snap frozen, and cut into 15 µm histological sections. Rat anti-mouse CD-31 (1:50, BD Pharmingen) and polyclonal anti-p32 antibody (1:200; [201]) were used for immunohistochemical staining of frozen tissue sections. The corresponding secondary antibodies were added and incubated for 1 hour at room temperature: Alexa Fluor 594 goat anti-rat IgG (1:500, Invitrogen) for CD-31 and Alexa Fluor 594 goat anti-rabbit IgG (1:500, Invitrogen) for p32 antibody. The slides were washed three times with PBS and mounted in Vectashield Mounting Medium with DAPI (Vector Labs). The stained tumor sections were observed with a fluorescence microscope (Nikon, Tokyo, Japan). Histological quantitation of nanoparticles localization was done using ImageJ software. Stacks of CD31-stained sections and nanoparticle fluorescence images were utilized for intra- and extravascular particle distribution quantitation. Regions with CD31-staining were selected to denote intravascular accumulation of nanoparticles and surrounding areas were classified as extravascular. The net nanoparticle fluorescence signal above background was quantified for each of these regions to determine the approximate percent of nanoparticle fluorescence localized to the vasculature vs the extravascular space. Three sections from each set of mice were randomly chosen for analysis.

3 Development of targeted tumor-penetrating nanomaterials for siRNA delivery

3.0 Abstract

Targeted delivery of therapeutics such as siRNA may improve tumor treatment by increasing efficacy and minimizing side effects [211]. To date, siRNA targeting to the tumor parenchyma *in vivo* has been challenging due to siRNA's rapid clearance, susceptibility to serum nucleases, endosomal entrapment, and potential for innate immune stimulation [5]. Furthermore, nanoparticle- and antibody-based approaches have suffered from low tumor penetration and transvascular transit, thereby limiting the applicability to tumor parenchymal targets [128, 212]. Here, we provide a unifying technology that enables the precise homing of siRNA therapeutics deep into regions of the tumor parenchyma that express specific receptors *in vivo*. We report a siRNA delivery platform that is comprised of a tandem peptide structure, linking a cyclic tumor-penetrating homing peptide identified via *in vivo* phage display to a membrane-penetrating and siRNA-binding domain. Upon non-covalent complexation with siRNA, the resulting nanocomplex is stable, non-immunostimulatory, displays homing peptides in a multivalent fashion, and delivers siRNA payloads to the cytosol of tumor cells expressing p32 on the surface. Upon systemic administration into mice bearing orthotopic ovarian tumors, the nanocomplex penetrates into the tumor parenchyma to achieve gene silencing in a receptor-specific manner. *(Adapted with permission from [213])*

3.1 Introduction

RNA interference offers an attractive means to silence gene expression with extraordinary specificity, particularly for the subset of "undruggable" gene targets [1]. This capability is particularly appealing for diseases with complex genotypic and phenotypic alterations such as cancer. Still, the translation of new insights on mechanisms underlying cancer survival into new RNA-based therapeutics has been thwarted by an inability to efficiently reach extravascular cancer cells *in vivo*. Among the fundamental transport challenges that hinder the advancement of siRNA therapeutics are the requirements that intravenously-administered siRNA delivery vehicles extravasate in tumor blood vessels, penetrate into the tumor interstitium, and subsequently translocate into specific intracellular compartments such as the cytosol in order to be active. To date, approaches to target the delivery of siRNA in vivo have focused on development of carriers such as antibodies [128], lipids [126], and peptides [166, 212] which passively escape blood vessels in order to reach target cells. These advances have illustrated the potential of siRNA delivery in filtration organs, tumor endothelial cells, and cells in close proximity to tumor vessels *in vivo*, yet have shown limited capacities to efficiently deliver therapeutics to extravascular cancer cells located throughout the tumor parenchyma *in vivo*.

Recent work has identified new classes of peptides using in vivo phage display that are capable of rapidly accessing sites deep in the tumor parenchyma following intravenous injection. Two such tumor-penetrating ligands, LyP-1 (CGNKRTRGC) and iRGD (CRGDKGPDC), have demonstrated the ability to deliver large macromolecules and nanoparticles with diagnostic and therapeutic potential deep into the tumor parenchyma within minutes after intravenous injection [117, 169]. In some cases, tumor-penetrating peptides leverage consensus R/KXXR/K *C*-terminal peptide motifs (CendR) as mediators of cell and tissue penetration [117-118, 214]. This

process has been described as 'stimulated penetration' and involves neuropilin-1 binding that stimulates vascular permeability in a VEGF-like manner, thereby enabling rapid extravasation of therapeutics beyond the vascular barrier and through the tumor parenchyma. Separately, *in vitro* evidence has emerged that cell penetrating peptide sequences, such as TAT and poly-Arg domains, are capable of binding siRNA and penetrating the membrane of multiple cell types to access the cytosol [151, 215].

Here, we hypothesized that the unique functions of tumor-penetrating and cell-penetrating peptides could be integrated into tandem peptide sequences to direct siRNAs into the tumor parenchyma and subsequently into the cytosol of tumor cells *in vivo*. We report the design of a peptide-siRNA nanocomplex containing siRNA non-covalently bound to a tandem peptide comprised of a cyclic homing domain and a membrane-translocating domain, which targets tumors and efficiently delivers siRNA into the tumor parenchyma *in vivo* (**Figure 3.1**).
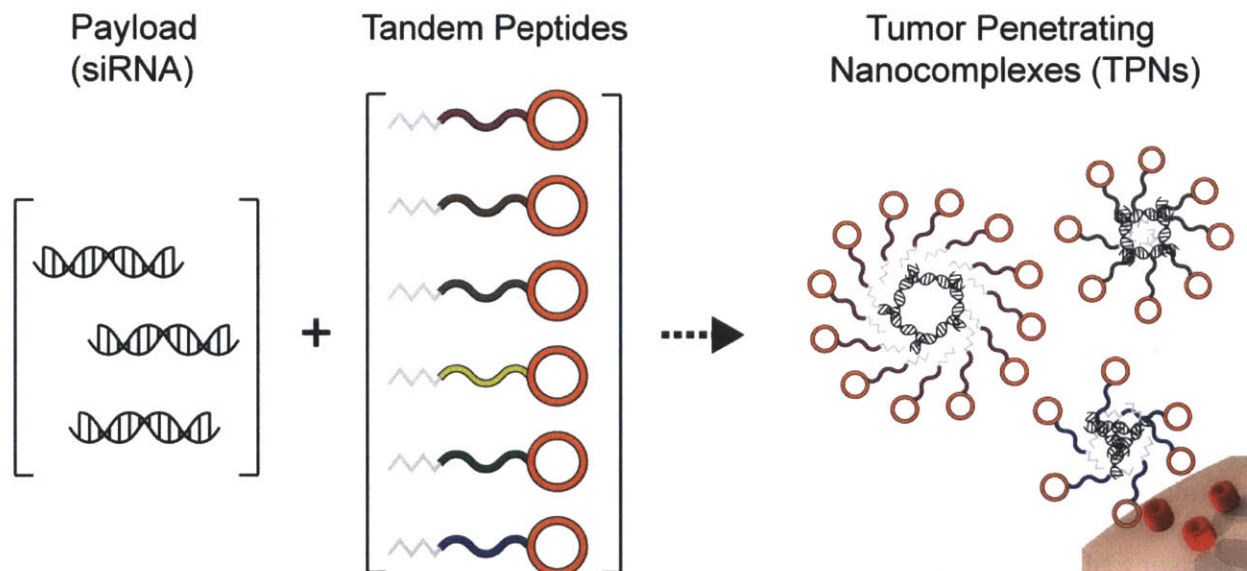
Figure 3.1. Design of tumor-penetrating nanocomplexes for siRNA delivery. Screening of tandem peptides bearing distinct cell-penetrating domains and a fixed cyclic tumor-penetrating domain (LyP-1, red) for ability to form tumor penetrating nanocomplexes (TPN) and deliver siRNA payloads in a cell type-specific fashion

3.2 Results and Discussion

3.2.1 Development of tumor-penetrating nanocomplexes

To begin, we synthesized a library of tandem peptides with a fixed cyclic domain for tumor homing and penetration and variable linear domains to electrostatically bind siRNA and cross cell membranes (**Figure 3.2**). Ideally, the resulting peptide-siRNA nanocomplex should not only target receptors that are differentially expressed on tumor cells, but also overcome the transport permeability barrier by penetrating into the tumor tissue. We selected the cyclic nonapeptide, LyP-1, as the tumor-penetrating domain because: (1) it binds p32, a mitochondrial protein whose expression is aberrantly elevated on the surface of stressed tumor cells in a variety of tumor types, thus conferring its tumor homing properties [202, 216-217]; (2) once bound, it is proteolytically processed by proteases to reveal a CendR motif that activates tissue penetration of associated payloads [218]; and (3) LyP-1 peptide causes extravasation of phage, albumin, and nanoparticles into tumors, and results in higher therapeutic accumulation [101, 169, 218-219].

In addition to receptor-specific binding, an effective siRNA delivery system must transfer its payload into the cell cytoplasm. Cell penetrating peptides (CPP), such as TAT and poly-Arginine, are short cationic peptide sequences capable of transducing macromolecular cargos into cells. However, CPPs have no inherent cell type specificity; they are internalized ubiquitously likely *via* binding to cell surface glycans [220]. We postulated that a tandem peptide consisting of an *N*-terminal CPP with a *C*-terminal LyP-1 separated by a 4-glycine linker domain would retain membrane translocation and tissue penetrating properties, condense siRNA into nanoparticles, and selectively target p32-expressing tumor cells. We created a library of 18 linear membrane-translocation domains that contained both polycationic (oligoarginines, TAT (48-60),

and the HSV-1 tegument protein VP22) and amphipathic sequences (penetratin derived from the Antennapedia homeotic transcription factor and transportan). Inspired by the myristoylated switch found in RNA viruses, we added a myristoyl group to the *N*-terminus to further stabilize the nanocomplex and facilitate interactions with membrane lipids [221-222]. The homing and membrane penetrating domains are separated by a four-glycine spacer to ensure that complexation with siRNA does not interfere with tumor targeting.

We generated tandem peptides that conformed to these design principles and examined their ability to condense siRNA into nanocomplexes that specifically target cells expressing surface p32. We confirmed that peptides from the library bound siRNA electrostatically to form stable nanocomplexes in water (diameter ~ 50nm), in phosphate-buffered saline (PBS, diameter ~ 200-400nm), and in mouse serum (diameter ~ 200-400nm) (**Figure 3.3**). The majority of peptides were non-cytotoxic (**Figure 3.4**). A gel-shift assay was used to determine an optimal complexation ratio of 1:20 (siRNA to peptide) and showed that 70% of the peptide-bound siRNA remained intact after 24 h incubation in murine serum (**Figure 3.5**).

Poly-(d)Arg: (dR) 3, 6, 9, 12, 15
TAT (48-60): GRKKRRQRRRGYK
Transportan: GWTLNSAGYLLGKINLKALAALAKKIL
Penetratin: RQIKIWFQNRRMKWKK
VP22: DAATATRGRSAASRPTERPRAPARSASRPRRPVD
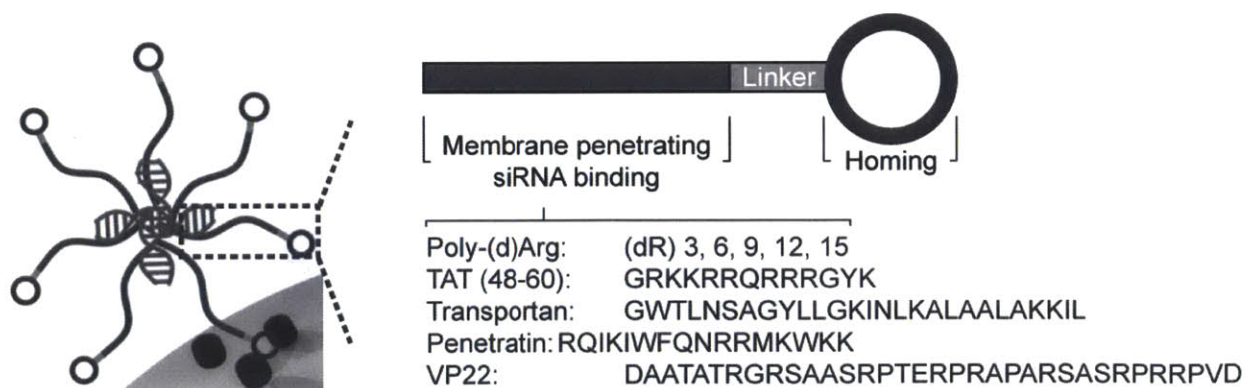
Figure 3.2. Schematic of tumor-penetrating nanocomplexes with tandem peptides and siRNA payloads. Schematic representation of a tandem peptide bearing a cyclic homing domain, a cell penetrating domain, and a linker (gray).
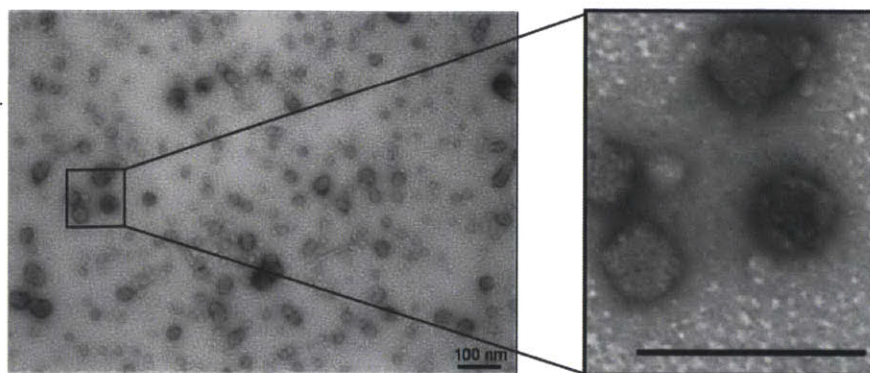
Figure 3.3. *In vitro* **size characterization of nanocomplexes.** Transmission electron micrograph (TEM) of TPN in water. A higher magnification view is shown on the right. Scale bar, 100 nm.
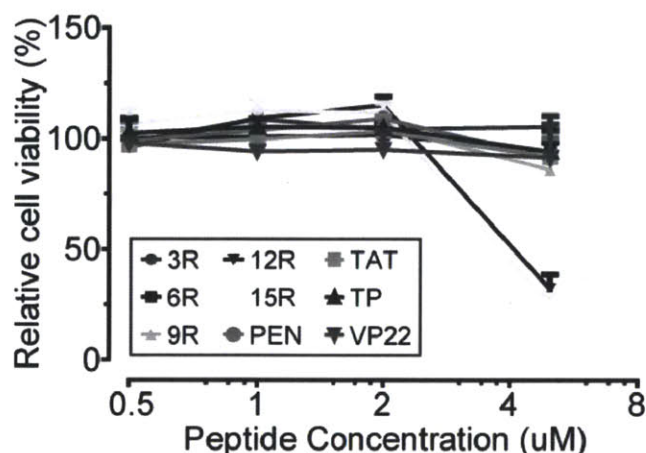
Figure 3.4. Cytotoxicity of nanocomplexes *in vitro*. Cytotoxicity assessments of TPN 48 h after transfection in HeLa cells. Error bars indicate s.d. from 3 independent experiments. Total viability was normalized to untreated cells.
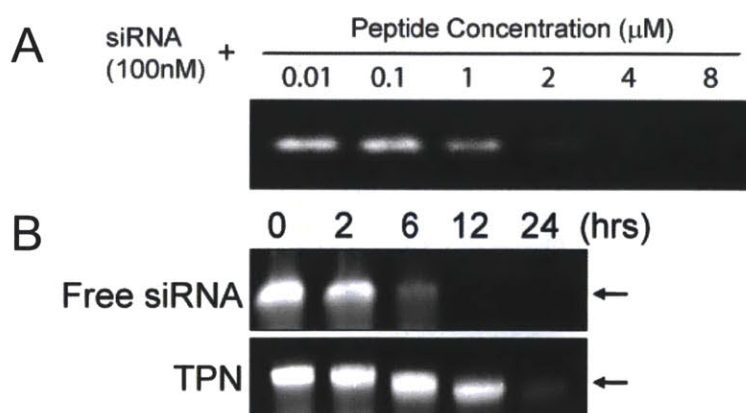
Figure 3.5. Characterization of nanocomplex formation and stability *in vitro*. **(A)** Agarose gel analysis of free siRNA complexed to tandem peptide at various molar ratios. **(B)** Agarose gel analysis of free or peptide-complexed siRNA in mouse serum at 37°C for up to 24 h. Naked, unmodified siRNA is completed degraded by 12 h.

3.2.2 Delivery of siRNA by nanocomplexes *in vitro*

We screened the library of nanocomplexes for uptake by p32-expressing HeLa cells and found that nanocomplex uptake was dependent on the homing domain, as quantified by monitoring tetramethylrhodamine-labeled peptides by flow cytometry. Internalization of nanocomplexes occurred after 1 h. After 4 h, cells efficiently incorporated all targeted nanocomplexes, whereas no uptake was seen with nanocomplexes formed from tandem peptides harboring a control homing domain (**Figure 3.6; Figure 3.7**).

To evaluate TPN-mediated gene silencing, we treated HeLa cells expressing destabilized green fluorescent protein (GFP) with GFP-specific siRNA bound to either tandem peptides or lipofectamine. Three carriers: 6R, 9R, and Transportan (TP), silenced GFP expression by ~40-60% (**Figure 3.8**). Flow cytometry analysis indicated that gene suppression was dose-dependent and heterogeneous across the cell population (50-70% of cells exhibiting near-complete gene suppression), likely due to the heterogeneity in surface p32 expression (**Figure 3.9**). In our experience, GFP suppression can underreport the magnitude of silencing endogenous gene targets, such as amplified oncogenes, thus we use this assay to compare TPNs but not as a quantitative measure of efficiency in evaluation of oncogenes [223].

Next, we examined the specificity of receptor targeting and gene suppression. We failed to detect altered GFP expression in HeLa cells exposed to untargeted TPNs carrying GFP-specific siRNA or TP-LyP-1 carrying a scrambled siRNA sequence. In contrast, when we used TP-LyP-1 carrying GFP siRNA, we observed over 40% suppression of GFP expression (**Figure 3.10**). In addition, we explored p32-receptor specificity by observing that MDA-MB-435 cells expressing a p32-directed shRNA showed significantly reduced binding of TP-LyP-1 nanocomplexes compared to cells expressing a control shRNA, whereas binding of

nanocomplexes bearing a control homing domain (TP-ARAL) was unaffected (**Figure 3.11**).

Similar results were obtained with 6R-LyP-1 (data not shown).

To further confirm the uptake specificity of those nanocomplex candidates that showed efficient GFP knockdown, free LyP-1 peptide was added to HeLa cells along with nanocomplexes in a competitive binding assay. Dose-dependent inhibition of GFP silencing was observed for TP-LyP-1 and 6R-LyP-1, suggesting that LyP-1 and the nanocomplexes compete for binding to the common p32 receptor (**Figure 3.12**). By contrast, the addition of LyP-1 did not interfere with lipofectamine. In addition, competition with a control peptide that has the same net charge as LyP-1, ARAL (ARALPSQRSR), had no effect. We attribute the excess of free peptide required for inhibition to the presence of multiple copies of LyP-1 on each nanocomplex, thereby improving avidity through multivalent binding. In contrast, LyP-1 did not inhibit functional siGFP delivery by 9R-LyP-1, suggesting this nanocomplex carrier failed to enter cells in a p32-specific manner. Taken together, our results illustrated that 6R-LyP1 and TP-LyP-1 nanocomplexes enabled efficient and p32-dependent delivery of siRNA *in vitro*.
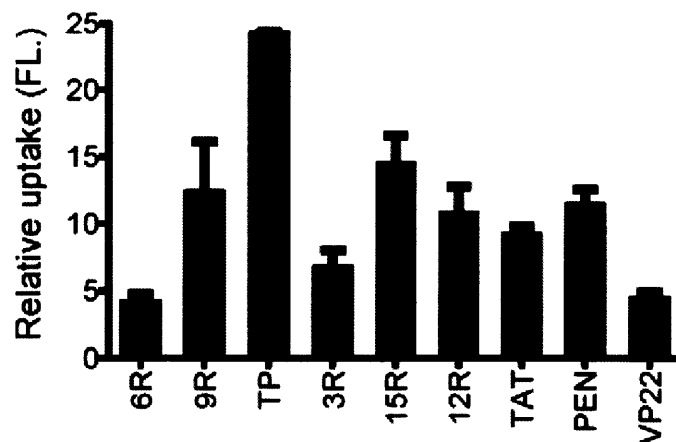
Figure 3.6. Cellular uptake of tandem peptides *in vitro*. HeLa cells were treated with 0-100 nM siRNA bound to TAMRA- labeled tandem peptides at a ratio of 1:20 (siRNA-to-peptide carrier) and cellular uptake of peptides is assessed by flow cytometry after 4 h incubation. *Inset,* Immunofluorescence microscopy analyses showed binding of LyP-1 targeted nanocomplexes(TP-LyP-1) but not controls (TP-ARAL) to MDA-MB-435 cells.
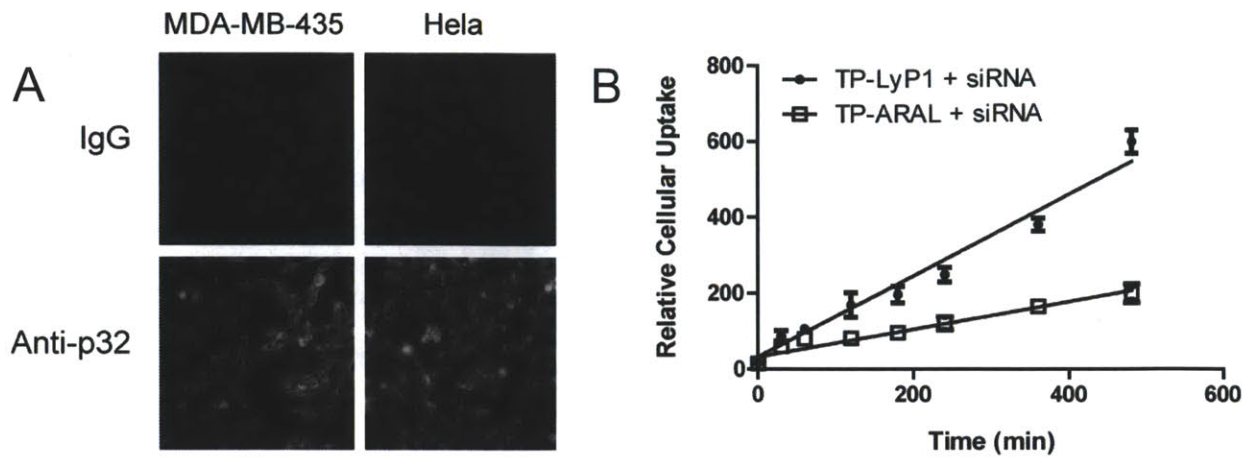
Figure 3.7. Cellular binding of LyP-1 targeted tandem peptides depends on p32 expression. (A) Immunofluorescence staining showed that MDA-MB-435 and HeLa cell lines both express p32 on the cell surface. Rabbit IgG or a polyclonal antibody against full-length p32 was applied to live cells and detected with an Alexa 488–labeled secondary antibody. **(B)** Flow cytometry analysis of cellular uptake of TP-LyP-1 versus TP-ARAL peptide labeled with a TAMRA fluorophore over time.
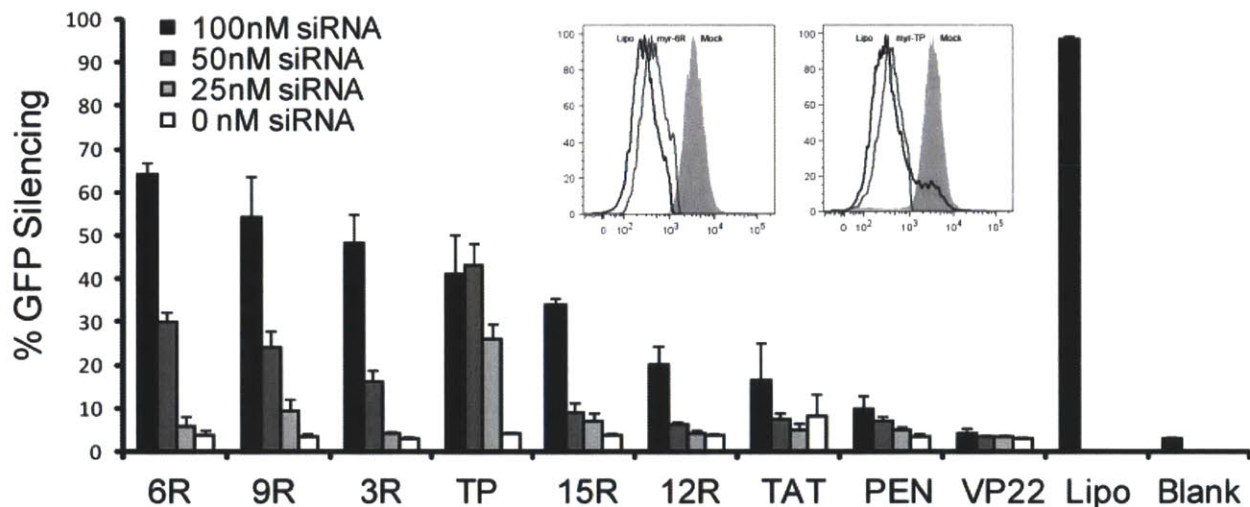
Figure 3.8. Gene silencing by tandem peptide-mediated delivery of siRNA. HeLa cells stably expressing destabilized GFP were transduced with nanocomplexes carrying siRNA against GFP. The amount of gene silencing as determined by the geometric mean of cells undergoing RNAi was determined by flow cytometry 48 h later. Lipofectamine was used as a positive control. Representative histograms for 6R- and TP-LyP-1 peptides (inset) and cumulative data from three independent experiments are shown.
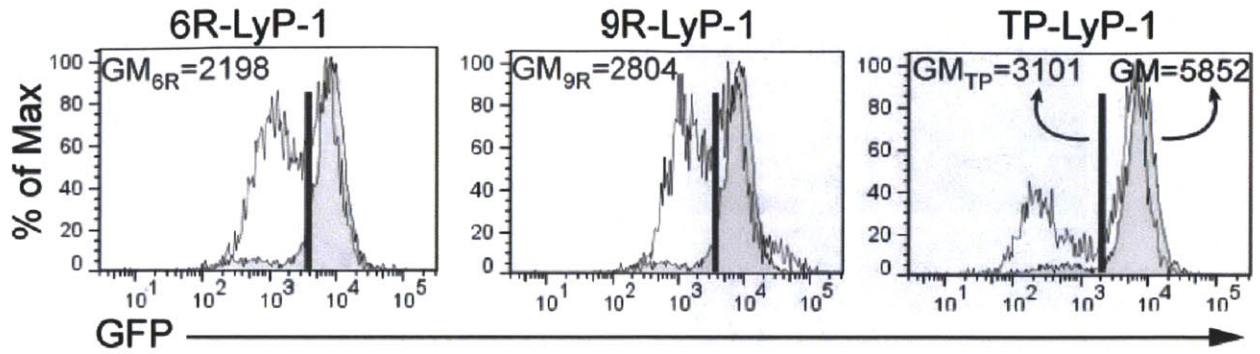
Figure 3.9. Gene silencing by tandem peptide-mediated siRNA delivery. Flow cytometry histograms of HeLa cells expressing GFP 24 h after transfection with 3 tandem peptides (6R, 9R, and TP) carrying GFP-siRNA (100 nM). Mock treated cells are shaded in gray. Geometric mean (GM) of the population is indicated with a vertical line. The geometric mean of the mock treated cells is shown in black.
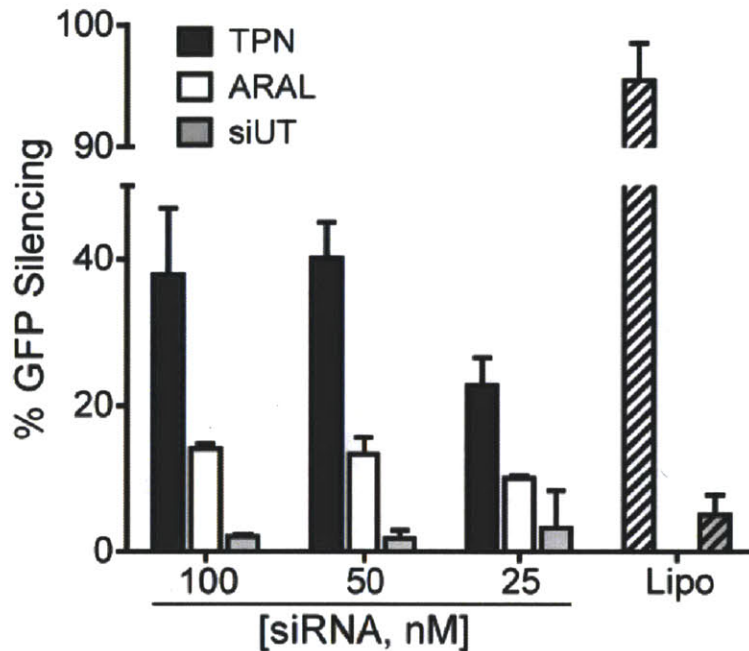
Figure 3.10. Receptor- and sequence-specificity of nanocomplex siRNA delivery. Normalized GFP knockdown by TP-LyP-1 nanocomplexes carrying siRNA against GFP (black bars), siRNA against an irrelevant sequence (siUT, dashed bars), or by TP-ARAL carrying GFP siRNA (gray bars). Mean values were normalized to percent of untreated control. Error bars indicate averages ± s.d.
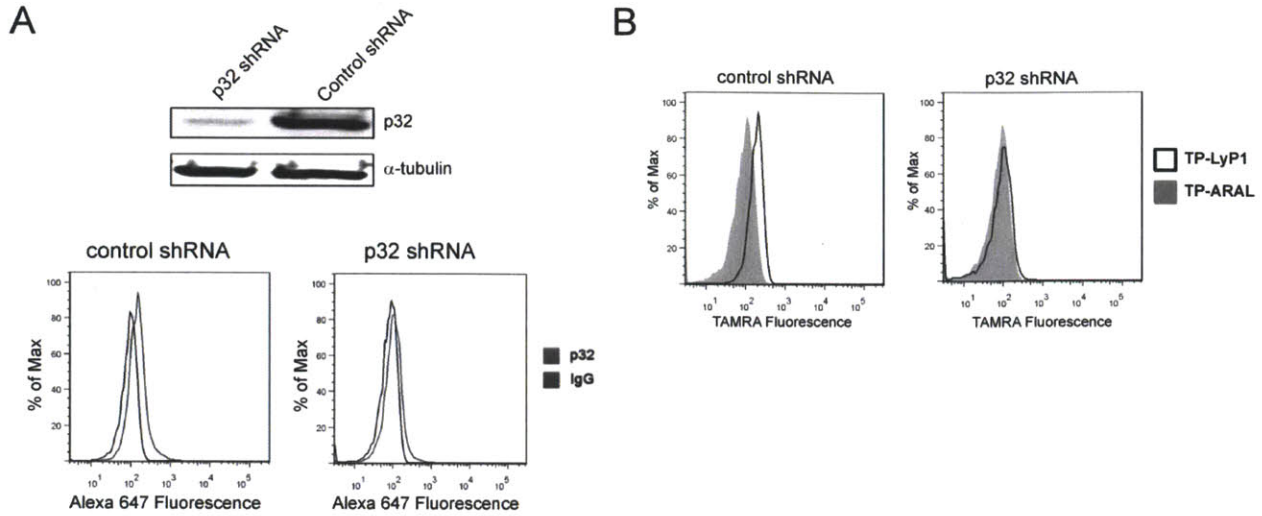
Figure 3.11. Nanocomplex binding is p32-specific. (A) Western blot on whole-cell lysates from MDA-MB-435 tumor cells stably expressing shRNA for p32 or a base mismatch control shRNA (top). Flow cytometry analysis of the same cell lines for surface levels of p32 using polyclonal anti–full-length/NH_2-terminal p32 or IgG isotype control (bottom). **(B)** TAMRA-labeled tandem peptides bearing the LyP-1 homing domain or a control domain (ARALPSQRSR, *ARAL*) were incubated over p32 shRNA cells. TP-LyP-1 binding was only observed in the control cells but not in p32 knockdown cells. TP-ARAL did not bind to either cell line.
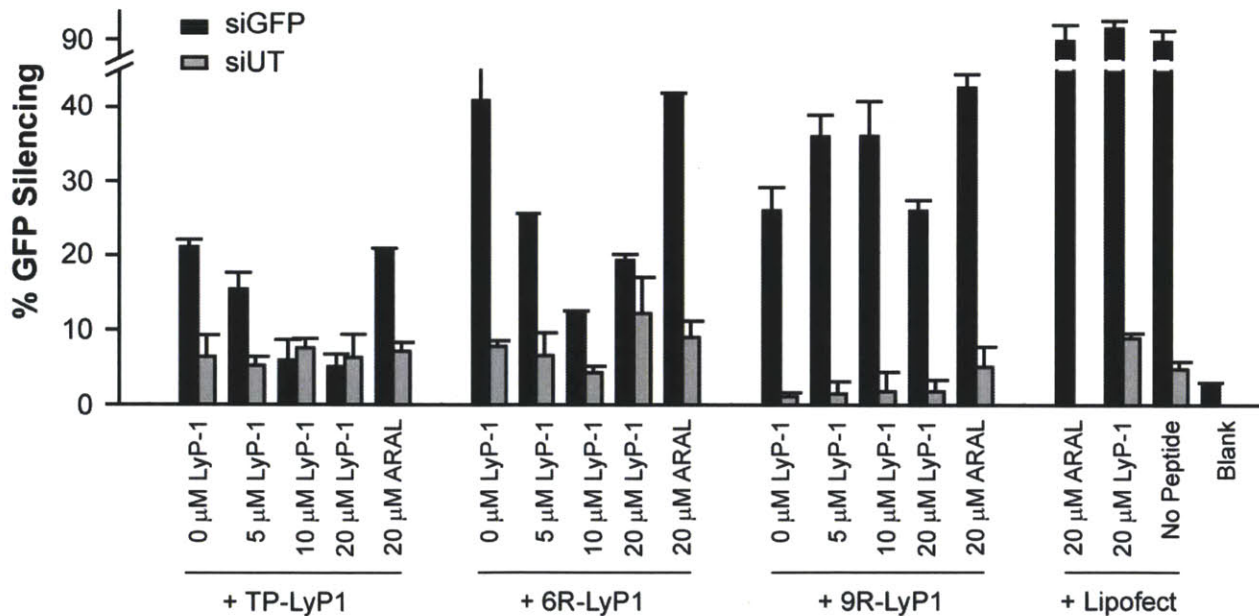
Figure 3.12. A subset of tandem peptides are p32-specific. GFP silencing was re-examined in HeLa cells treated with siRNA delivered using three different tandem peptide candidates: TP-LyP-1, 6R-LyP-1, and 9R-LyP-1, in the presence of free LyP-1 peptide (5 to 20 μM) or control peptide (ARAL, 20 μM). Transfection by lipofectamine was used as a positive control.

3.2.3 *In vivo* siRNA delivery

For in vivo applications, an ideal carrier should stably circulate in the blood, extend the half-life of siRNA in serum by protecting it from nuclease degradation, and yet readily dissociate from siRNA once in the cytosol of target cells to allow for RISC incorporation. We found that complexation by TP-LyP-1 extended the stability of siRNA in the presence of serum to > 12 h (**Figure 3.5**), and the size of nanocomplexes remained stable in serum (**Figure 3.13**). Furthermore, we observed unpacking of nanocomplexes upon exposure to endolysosomal pH via monitoring the intercalation of a nucleic acid-binding dye (TO-PRO-3) (**Figure 3.14**). Collectively, these findings suggest that TP-LyP-1 effectively condensed siRNA into stable nanocomplexes that have the potential for *in vivo* applications.

We next set out to investigate the *in vivo* homing behavior of nanocomplexes after systemic administration in mice. Near-infrared fluorochrome-labeled siRNA was complexed with TP-LyP-1, while siRNA complexed with untargeted peptides and naked siRNAs were used as negative controls. After administration into immunodeficient mice bearing subcutaneous MDA-MB-435 melanoma xenografts, a significant fraction of both naked siRNAs was rapidly removed via renal clearance as indicated by bladder accumulation of siRNA owing to their small size. By contrast, nanocomplexes were renally cleared more slowly and distributed to tumor tissues over time (**Figure 3.15**). After clearance from circulation (4 h), the distribution of nanocomplexes was examined via near-infrared imaging of the whole-animal and fluorescence imaging of explanted organs. We found an over three-fold increase in the tumor accumulation of LyP-1 targeted nanocomplexes compared to ARAL targeted control nanocomplexes (**Figure 3.16; Figure 3.17**).

Histologically, TP-LyP-1 targeted nanocomplexes carrying fluorescein-labeled siRNAs accumulated in the interstitium of harvested tumors. Vascular staining with CD31 showed that nanocomplexes extravasated from the vasculature. Tumor cell staining with anti-p32 showed that p32 positive cells were also efficient at taking up targeted nanocomplexes (**Figure 3.18**). This pattern of distribution was consistent with previously reported LyP-1 peptide, Lyp-1 phage and LyP-1 targeted nanoparticle homing [200, 224]. Similar results in tumor targeting were also obtained by injecting TPN intraperitoneally (**Figure 3.19**), suggesting the potential for multiple routes of administration.

We sought to apply this approach to silence genes of interest in ovarian cancer, a disease that is largely confined to the peritoneal cavity. Standard chemotherapy suffers from drawbacks such as acute toxicity and emergence of drug resistance [225]; therefore, novel gene-based approaches such as RNAi therapeutics may be beneficial in helping patients overcome the disease. To establish a murine model of ovarian carcinoma, we implanted T22H mouse ovarian tumor cells orthotopically in the peritoneal space of syngeneic nude mice. Total metastatic tumor burden was assessed via non-invasive whole-animal bioluminescent imaging of luciferase expression. Cohorts of mice with established tumors were treated intraperitoneally with luciferase-targeting siRNA bound to TP-LyP-1 (5 mg siRNA/kg). A significant reduction in the bioluminescence was observed 48 h after treatment; the BLI signal was gradually restored in mice over a 6-day period after a single TP-LyP-1/siRNA injection (**Figure 3.20**). By contrast, all other cohorts, including those receiving untargeted nanocomplexes carrying siRNA targeting luciferase, did not exhibit any significant luciferase knockdown (**Figure 3.21**).
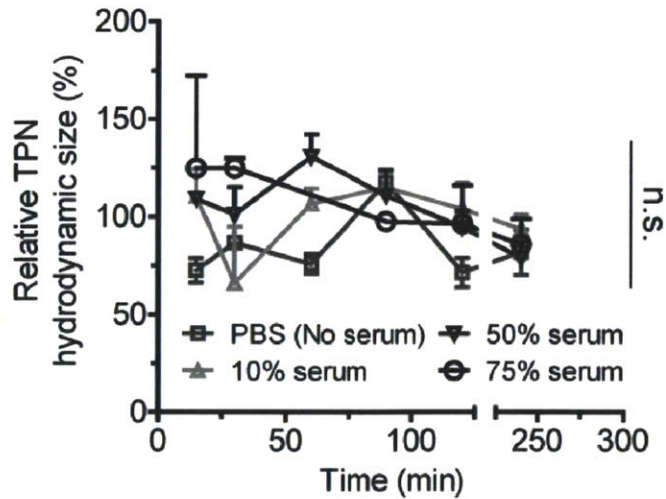
Figure 3.13. Nanocomplexation is stable in serum. Dynamic light scattering (DLS) measurements of TPN in various concentrations of mouse serum at 37°C over time. The hydrodynamic diameter of TPN measured in each serum concentration over time is normalized to the size of TPN in PBS at time 0. Error bars indicate s.d. from 6 independent measurements. n.s., not significant.
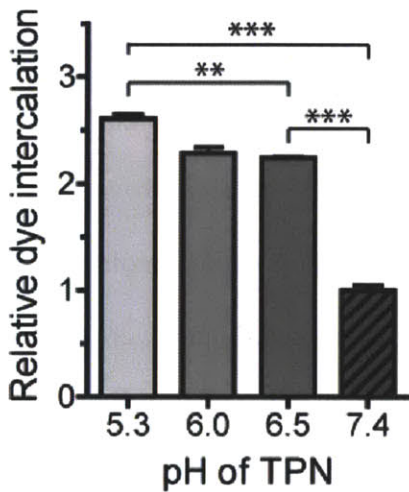
Figure 3.14. Intercalation of a nucleic acid-binding dye into siRNAs packaged in nanocomplexes. Binding of siRNA to TPN prevents intercalation of TO-PRO-3 into siRNA and results in decreased TO-PRO-3 fluorescence. Upon exposure to endolysosomal pH, siRNA is released from TPN and results in increased fluorescence. Error bars indicate s.d. from 4 independent experiments. $**p<0.01$; $***p<0.001$.
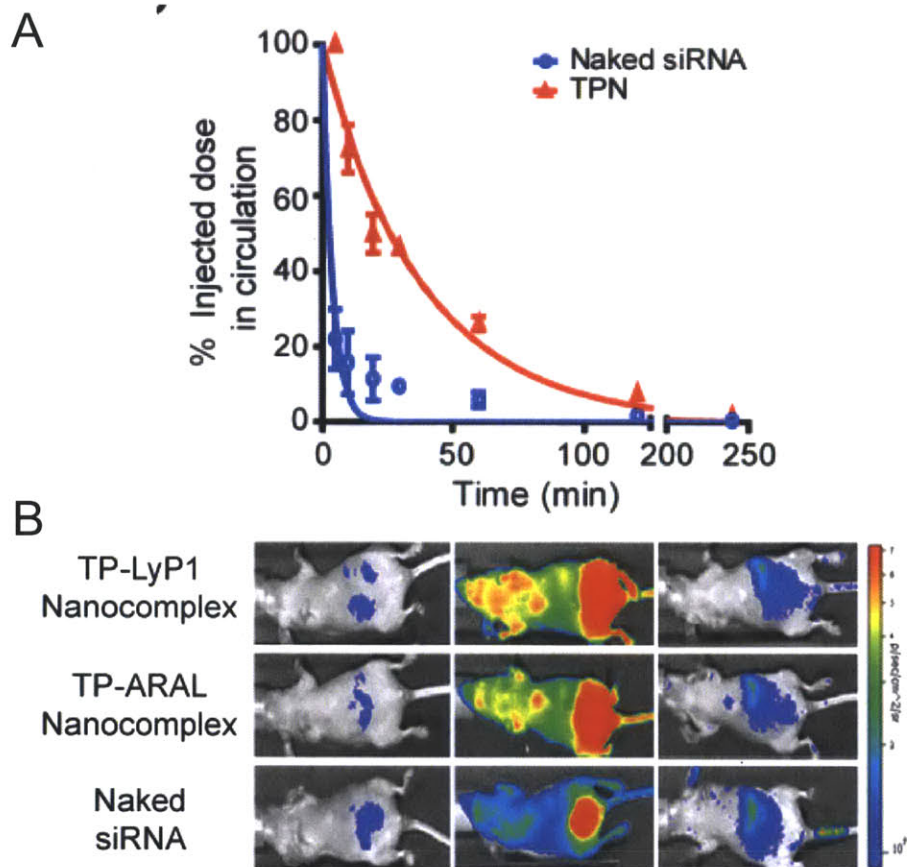
Figure 3.15. *In vivo* targeting of TP-LyP-1/siRNA nanocomplexes. (A) Peptide-bound siRNA has greater circulation time *in vivo* compared with naked siRNA upon intravenous administration into mice. Error bars indicate s.d. (n=3). **(B)** Whole-animal imaging of non-tumor bearing mice at multiple time points after systemic administration of siRNA payloads labeled with a near-infrared fluorophore (VivoTag-750) bound to either TP-LyP-1 or TP-ARAL, or naked siRNA without a carrier.
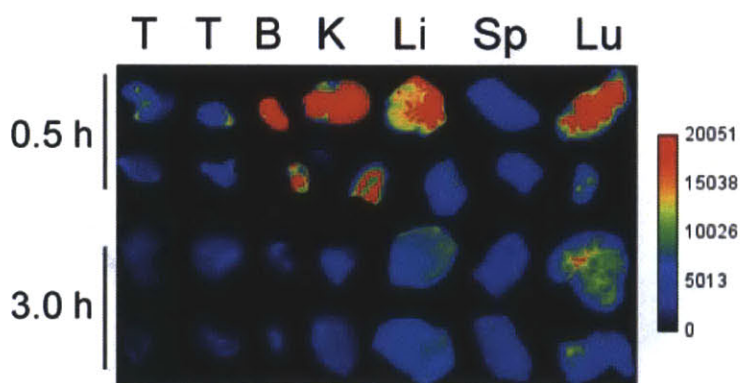
Figure 3.16. Biodistribution of systemically administered TP-LyP-1 nanocomplexes. At 30 min and 3 h post intravenous injection, organs and tumors were harvested from mice bearing OVCAR-8 flank xenografts and imaged. Two representative sets of tissues are shown in pseudocolor. T-tumor, B-bladder, K-kidney, Li-liver, Sp-spleen, Lu-lung.
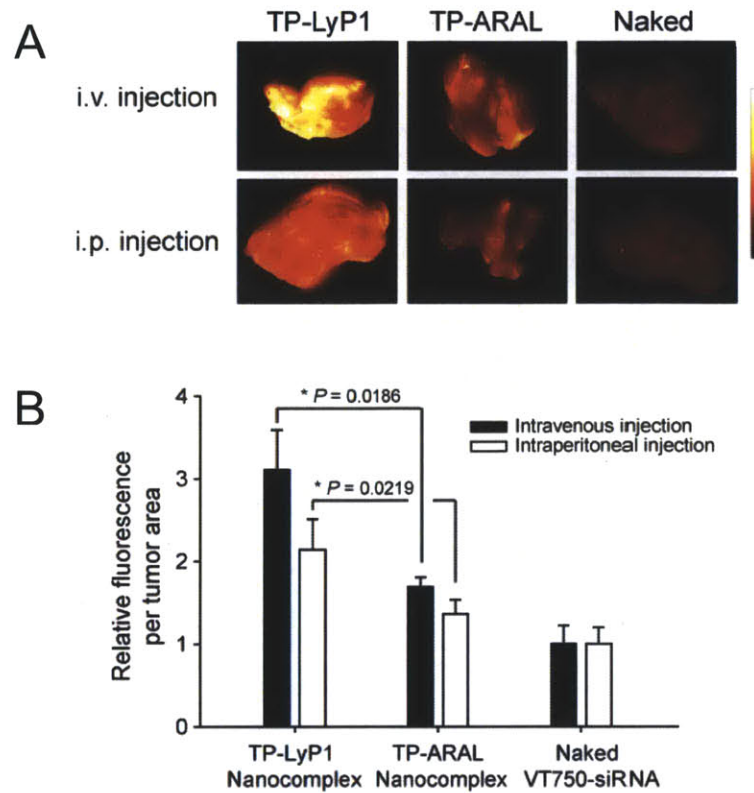
Figure 3.17. *In vivo* **tumor targeting by TPNs.** **(A)** Representative fluorescence images of tumor explants harvested after injection of TPN carrying siRNA, untargeted nanocomplexes, or naked siRNA (5 nmols per mouse) i.v. or i.p. Tumors were harvested after TPN were cleared. **(B)** Quantification of near-infrared fluorescence from tumor explants from A. Error bars indicate s.d. (n=3).
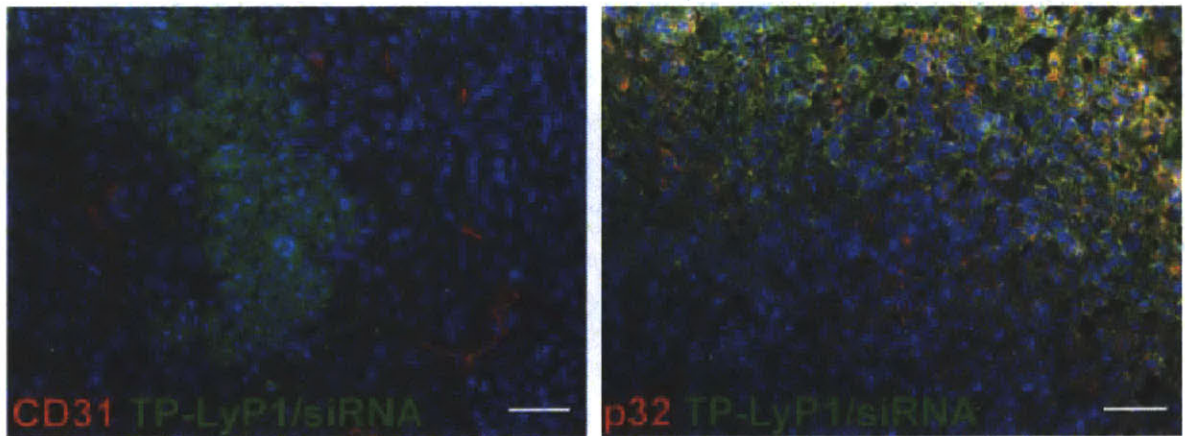
Figure 3.18. Intratumoral localization of TP-LyP-1 targeted nanocomplexes. Histological analysis of fluorescein-labeled siRNA distribution in MDA-MB-435 tumor sections (Green: TP-LyP1/siRNA nanocomplexes; Red: CD31 (*left*) and p32 (*right*); Blue: DAPI counterstain). Scale bar is 50 μm.
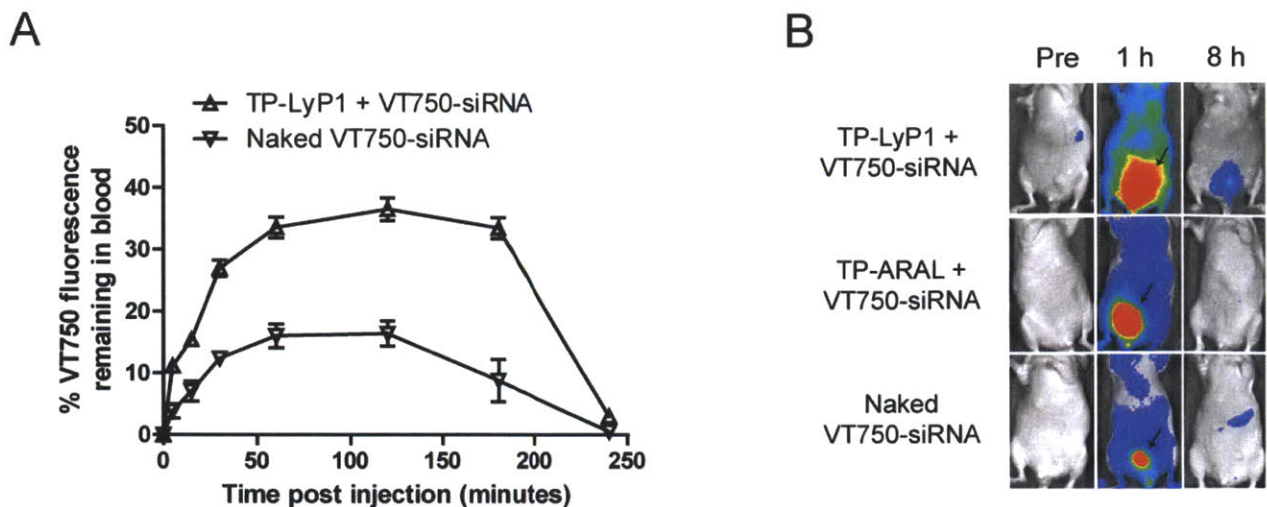
Figure 3.19. *In vivo* **homing of nanocomplexes after intraperitoneal administration. (A)** Circulation time of i.p. injected, fluorescently-labeled siRNA (5 nmols) either in its naked form or complexed to a TPN. Error bars indicate s.d. (n = 3). **(B)** Whole-animal fluorescence imaging at multiple time points after intraperitoneal injection in mice. Arrows indicate bladder accumulation.
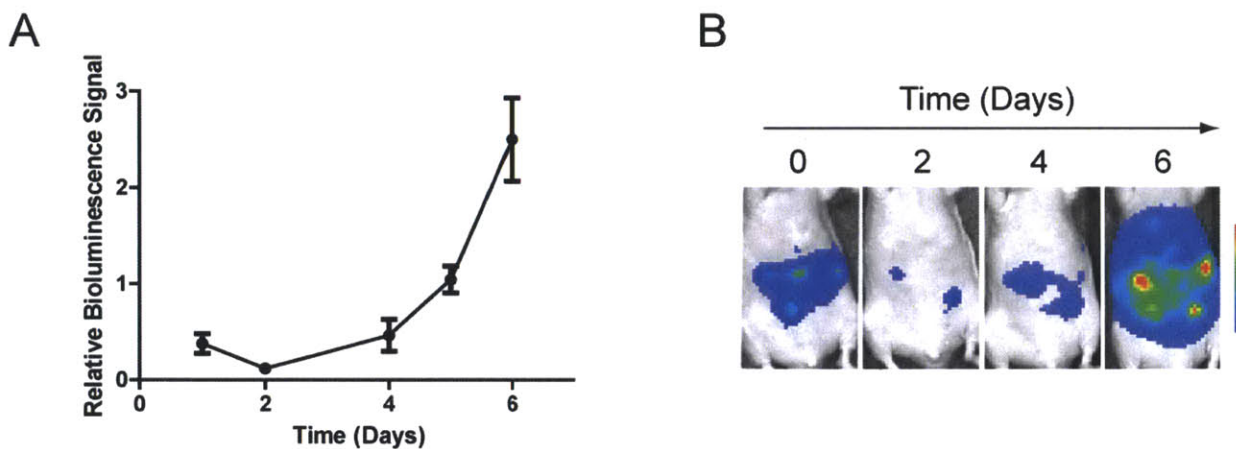
Figure 3.20. Duration of gene silencing by TPN. (A) Mice were injected intraperitoneally with tandem peptide/siRNA nanocomplexes, and the duration of gene silencing was determined by whole-animal bioluminescence imaging of luciferase expression on the indicated days. Error bars indicate s.d. (n=3); **(B)** Representative bioluminescence images from mice in (A).
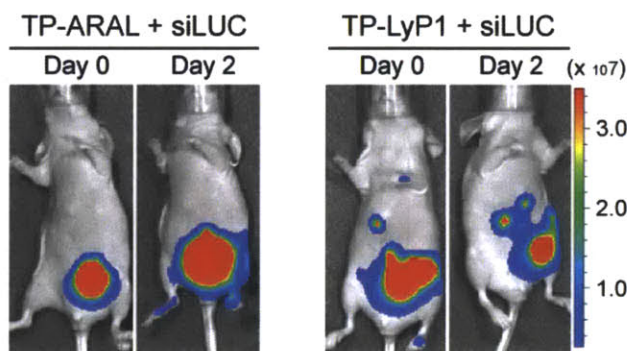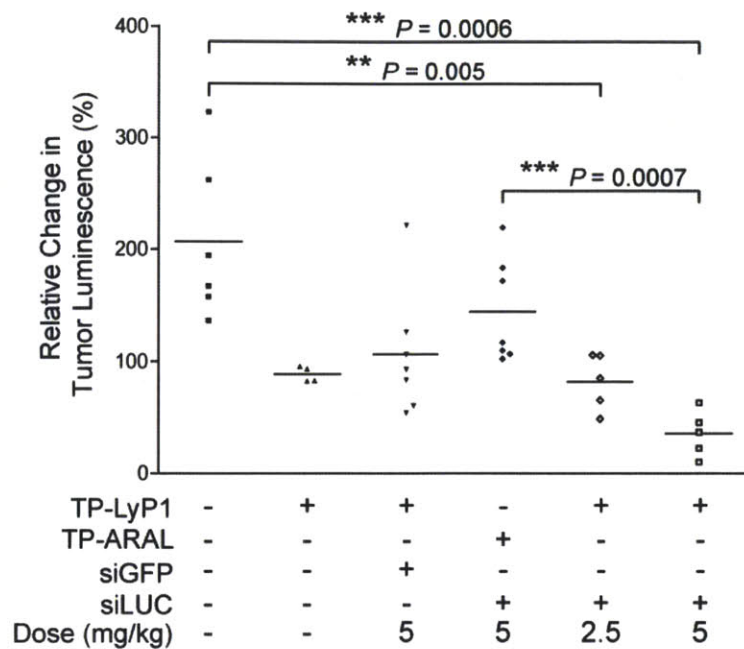
Figure 3.21. *In vivo* **siRNA delivery and gene knockdown by TPN.** *Top,* mice bearing luciferase expressing T22H tumors were injected i.p. with siRNA against luciferase bound to nanocomplexes. The amount of gene silencing was measured by bioluminescence imaging 48 h later. Statistical analyses were performed with ANOVA and Bonferroni post-test for pair-wise comparisons. Horizontal lines, mean values. (n = 4-6); **$p < 0.01$, ***$p < 0.001$. *Bottom,* representative bioluminescence images of luciferase activity of mice before and after treatment.

3.3 Conclusion

In this chapter, we described a novel nanotechnology-based system for tumor-targeted delivery of siRNA payloads *in vivo*. The delivery system consists of a multifunctional, tandem peptide that contains a tumor-penetrating motif (LyP-1) discovered *via* phage display, a nucleic-

acid binding motif, and a domain for transporting siRNA cargoes into the cytosol of tumor cells (Transportan, TP) that aberrantly express the mitochondrial protein p32. Potent and cell type-specific suppression of several reporter genes was achieved using this delivery approach both in established human cancer cell lines and in a syngeneic mouse model of ovarian carcinoma.

Our delivery platform may be modular in that both homing and cell penetrating domains can be varied independently from each other to identify the best performing peptide, and be easily adaptable to other homing domains and cancer models. By leveraging new discoveries in amplified vascular transportation and tissue penetration of constitutive and cryptic CendR ligands, this tandem peptide platform has the potential to enable broad access of parenchymal tumor cells to RNAi-based therapeutics that would otherwise be inaccessible via vascular targeting means. Such a capability may have broad utility for *in vivo* validation and clinical translation of novel oncogene targets in parenchymal cancer cells that are identified from large-scale genomic screens, which will be described in *Chapters 4-5*.

4 Targeted tumor-penetrating siRNA nanocomplexes for credentialing cancer targets

4.0 Abstract

The comprehensive characterization of a large number of cancer genomes will eventually lead to a compendium of genetic alterations in specific cancers. Unfortunately, the number and complexity of alterations identified by these efforts complicate endeavors to identify biologically relevant mutations critical for tumor maintenance, since many of these targets are not amenable to manipulation by small molecules or antibodies. Although RNAi provides a direct way to study putative cancer targets, specific delivery of therapeutics to the tumor parenchyma remains an intractable problem. We describe a platform for the discovery and initial validation of cancer targets, composed of a systematic effort to identify amplified and essential genes in human cancer cell lines and tumors partnered with a novel modular delivery technology. We developed tumor penetrating nanocomplexes (TPN) comprised of siRNA complexed to a tandem tumor-penetrating and membrane-translocating peptide, which enables the specific delivery of siRNA deep into the tumor parenchyma. We employed TPNs *in vivo* to evaluate *ID4*, a novel oncogene that induces tumorigenesis by disrupting both differentiation and proliferation through direct regulation of *CDKN1A* and *HOXA9* transcriptional programs. We show that treatment of tumor-bearing mice with *ID4*-specific TPNs suppresses growth of established tumors and significantly improves survival. These observations not only credential ID4 as an oncogene in a substantial fraction of high grade ovarian cancers, but also provide a framework for the identification, validation, and understanding of novel cancer targets.

(Adapted with permission from [213])

4.1 Introduction

Genome scale studies of cancer samples have begun to provide a global depiction of genetic alterations in human cancers [34], but the complexity and sheer volume of data that emerges from these efforts has made dissecting the underlying biology of cancer difficult, and little is known about the functions of most of the candidates that emerge. For example, in studies of 489 primary high-grade serous ovarian cancer genomes, 1825 genes were identified as targeted by recurrent amplification events [226]. Systematic approaches to study the function of genes in cancer cell lines, such as genome-scale, pooled short hairpin RNA screens, offer a means to assess the consequences of the genetic alterations found in such genome characterization efforts, and we recently used this approach to find genes that are both overexpressed in primary tumors and also essential for the proliferation of ovarian cancer cells [48]. However, this approach yielded a large number of candidate genes that required further functional validation *in vivo*; for example, we identified 54 overexpressed and essential genes in ovarian cancer and 16 genes in non-small cell lung cancer. Furthermore, many of these candidates represent targets that are not amenable to antibody-based therapeutics or traditional small molecule approaches. Thus, if one envisions a discovery pipeline that begins with cancer genomes and ends with novel therapeutics, there is clearly a bottleneck at the point of *in vivo* validation of novel targets.

RNA interference offers a potentially attractive means to silence gene expression of candidates *in vivo*, particularly for "undruggable" gene products [1-3]. However, systemic delivery of siRNA to tumors has been challenging due to their rapid clearance, susceptibility to serum nucleases, and endosomal entrapment, in addition to their inherent inadequate tumor

penetration [5, 7]. Achieving silencing in the epithelial cells in the tumor parenchyma is especially critical to study the genetic alterations of interest.

Tumor penetration is a problem for the delivery of any cargo, including siRNA, and is characterized by limited transport into the extravascular tumor tissue beyond the perivascular region [227]. This low penetration is thought to arise from the combination of dysfunctional blood vessels that are poorly perfused, and a high interstitial pressure, especially in solid tumors, in part due to dysfunctional lymphatics [85, 228]. The leakiness of tumor vessels partially counteracts the poor penetration (the enhanced permeability and retention [EPR] effect), but the size dependency and variability of this property can limit its usefulness [92-93, 117]. Desmoplastic stromal barriers can further impede transport of therapeutics through tumors [115].

Recently, a new class of tumor-penetrating peptides were described which home to tumors and leverage a consensus R/KXXR/K C-terminal peptide motif to stimulate transvascular transport and rapidly deliver therapeutic cargo deep into the tumor parenchyma [117-118, 218]. These peptides are tumor-specific, unlike canonical cell-penetrating peptides that do not display cell or tissue-type specificity [229-230]. The tumor-penetrating peptides were able to significantly improve the delivery and efficacy of small molecules, antibodies, and even nanoparticles [119]. Despite their promise, this class of peptides has not been successfully co-opted for siRNA delivery, in part due to the additional challenges of delivering oligonucleotides across cell membranes, out of endosomes, and into the cytosol in order to interact with RISC and achieve gene silencing.

Here we sought to apply the siRNA delivery system developed in *Chapter 3* that can penetrate into the tissue parenchyma, target p32-expressing tumor cells, and easily accommodate siRNA payloads to modulate gene targets of interest. We envision that such a technology would

enable a platform wherein novel targets can be identified using structural and functional genomics and subsequently rapidly credentialed *in vitro* and *in vivo*. Follow-up studies could then identify the mechanism of action underlying the observations and establish (and ultimately prioritize) novel oncogenes as therapeutic targets (**Figure 4.1**). To achieve this goal, we have combined a systematic effort to identify genes that are both essential and genetically altered in human cancer cell lines and tumors with the development and deployment of a novel tumor-specific and tissue-penetrating siRNA delivery platform.
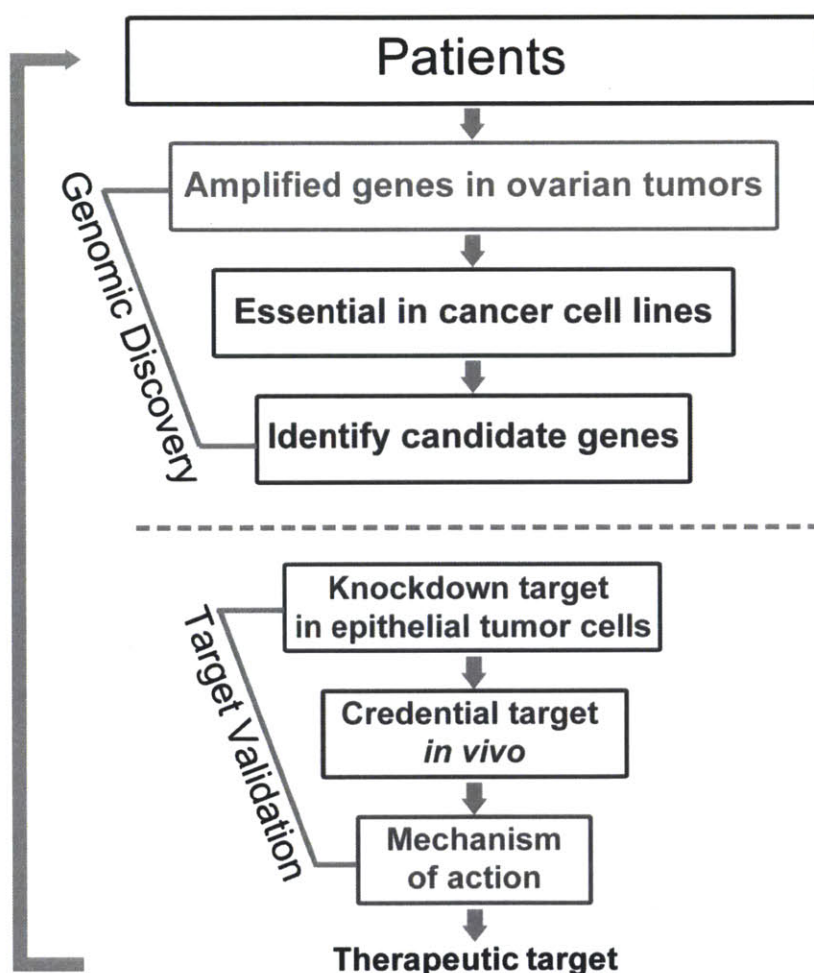
Figure 4.1. An integrated platform enables high-throughput genomic discovery and *in vivo* credentialing of cancer genes. Analyses of ovarian cancer genomes nominate genes that are amplified and essential. The application of TPN system for siRNA delivery overcomes the *in vivo* validation barrier (dotted line) by enabling rapid validation of candidate genes in animal models. Follow-up studies could identify the mechanism of transformation to establish novel therapeutic targets that can ultimately benefit patients.

4.2 Results

4.2.1 Identification of ID4 as an Essential Oncogene in Ovarian Cancer

To facilitate the identification of genes that are essential in specific cancer types, we initiated Project Achilles, a large scale effort involving genome-scale, pooled short hairpin RNA (shRNA) screens in human cancer cell lines [48]. In our initial analysis of 102 cell lines including 25 ovarian cancer cell lines, we identified lineage-specific essential genes, such as *PAX8* in ovarian cancer and *NKX2.1* in non-small cell lung cancer, as genes that were both overexpressed and required for proliferation in specific cell lineages [48].

Recent efforts to characterize the genomes of primary high grade serous ovarian cancer [226] have revealed a large number of recurrent regions of copy number gain [63] and loss [50], each containing a number of genes. To identify genes that are both recurrently amplified and essential in ovarian cancers that harbored increased copy number of these genes, we quantified the distribution of shRNA proliferation scores among all shRNAs for each amplified gene (**Figure 4.2**). We identified 206 cases in which shRNAs targeting the amplified gene were significantly depleted ($p<0.05$), including known ovarian cancer oncogenes *KRAS* [231-233], *AKT1* [226], *BCL2L1* [234] and *ERBB3* [235], and novel candidates including the *ID4* transcriptional regulatory protein and the *SKP2* E3-ubiquitin ligase [236].

We selected ID4, a helix-loop-helix (HLH) transcriptional regulator, for further study because recent genomic analyses indicate that it is frequently altered in ovarian cancer: the chromosomal region containing *ID4* (6p22) is amplified in 32% of high grade serous ovarian cancers [226] (**Figure 4.3**), and *ID4* is overexpressed in the majority of primary ovarian cancers but not expressed in normal ovary and fallopian tube and other tissues (**Figure 4.4**). In addition, by examining the transcript levels of *ID4* in a large panel of cancer cell lines, we found that ID4

was frequently overexpressed in the majority of ovarian cancer cell lines and cells derived from other cancer lineages, such as endometrial cancer, breast cancer and glioblastomas (**Figure 4.5**).

With the identification of ID4 as a candidate oncogene from amongst the many hits that resulted from the genome-wide studies of human samples, our next step was to establish preclinical models to credential the oncogenic potential of *ID4*, specifically by investigating the relationship between amplification, expression and essentiality of *ID4* in a panel of human cancer cell lines. First, we found that *in vitro* suppression of *ID4* by multiple shRNAs that did not alter the expression of the other ID family members (**Figure 4.6**) significantly inhibited the proliferation of 9 of 11 ovarian cancer cell lines and 2 glioblastoma cell lines tested (**Figure 4.8**). Cell lines that harbored increased copy number (**Figure 4.7**) and overexpression of *ID4* (**Figure 4.8**) died by apoptosis after *ID4* suppression (**Figure 4.9**). By contrast, 7 cell lines that express comparatively lower *ID4* levels were relatively insensitive to *ID4* suppression (**Figure 4.8**).

Since we found that ID4 was both recurrently amplified and essential for the survival of ovarian cancer cell lines that overexpress ID4, we tested whether *ID4* was an oncogene by investigating its ability to induce cell transformation. We previously showed that expression of oncogenic HRAS^{V12}or co-expression of known RAS effectors, such as *MEK* and *AKT1,* suffices to render immortalized human epithelial cells tumorigenic *in vivo* [36, 237-240]; therefore, to investigate the role of *ID4* in ovarian epithelial cells, we similarly created an ovarian surface epithelial cell line expressing the SV40 Large T and small t antigens, hTERT and MEK^{DD} (IOSE-M) (**Figure 4.10**), and used this cell line to identify genes that promote tumorigenicity. We found that expression of *ID4*at levels found in ovarian cancer cell lines dramatically increased the rate of tumor formation *in vivo*; however, addition of either a mutant ID4_DM

harboring mutations in the HLH domain, ID1, ID2, or ID3 each failed to confer significant

tumorigenicity (**Figure 4.11**).

Since recent work suggests that the majority of ovarian cancers may arise from the

fallopian tube (FT) epithelium rather than the ovarian surface epithelium [31, 241], we used

immortalized FT epithelial cells (FTSEC)[242] and assessed whether *ID4* expression also

induced cell transformation in these cells. As we found for ovarian epithelial cells, the expression

of ID4 induced anchorage independent growth in FT cells (**Figure 4.12**). These observations

show that *ID4* is amplified, essential and transforming in ovarian epithelial cells and thus show

that *ID4* is a novel ovarian cancer oncogene. Together, these observations identify *ID4* as a

transforming oncogene recurrently amplified in, broadly overexpressed in, and essential for the

survival of high grade serous ovarian cancers.

Determine if amplified gene
is essential in amplified lines

$p < 0.05$ shRNAs targeting
the amplified gene

Distribution of median
shRNA scores
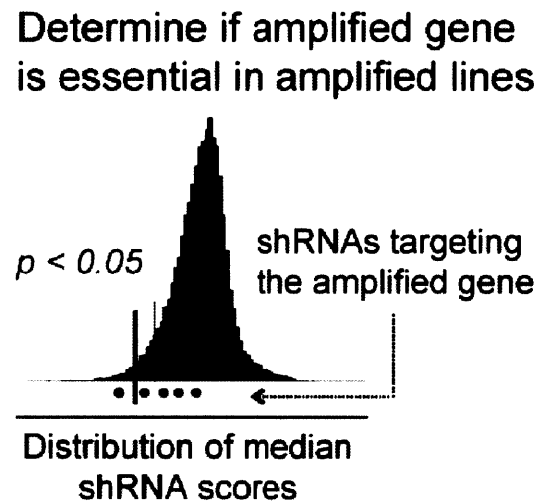
Figure 4.2. Schematic of shRNA analysis. Analysis of median shRNA depletion scores for each amplified gene. Copy number analysis using GISTIC of primary high-grade serous ovarian cancers identified 1825 recurrently amplified genes in 63 regions of genomic amplification. Schematic showing the distribution (blue bars) of median shRNA scores in cell lines that harbor copy number gain (log2 copy number ratio > 0.3) of a given gene. shRNAs targeting the amplified gene (dots) are considered significant (red) if p-value<0.05 (red line). Analysis is repeated for each of 1825 amplified genes in 63 recurrent regions of genomic amplification identified in primary serous ovarian cancer.
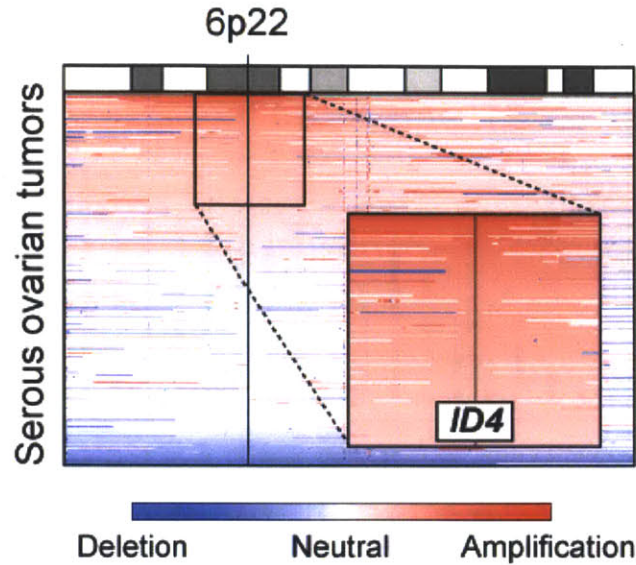
Figure 4.3. Amplification of ID4 in primary high-grade serous ovarian tumors. SNP array colorgram depicts genomic amplification of ID4 in subsets of primary ovarian tumors, sorted based on the degree of amplification of ID4. Regions of genomic amplification and deletion are denoted in red and blue, respectively.
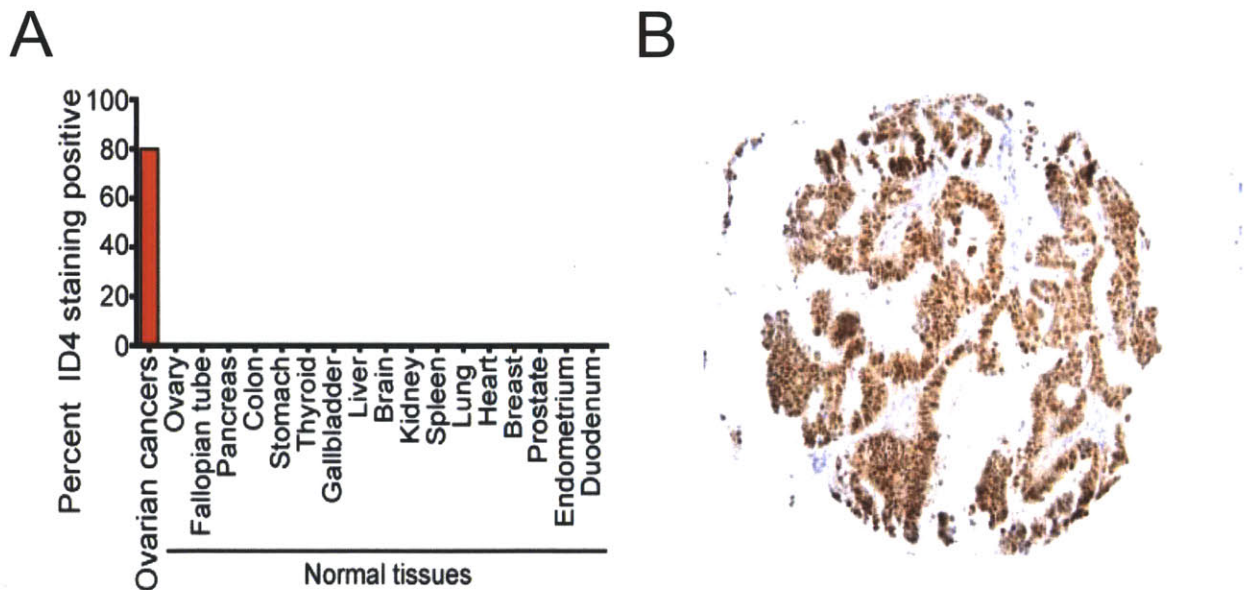
Figure 4.4. ID4 expression in primary ovarian cancers. (A) Immunohistochemical analysis of ID4 in primary ovarian cancers and normal tissues. Immunohistochemical staining of ID4 was performed on sections from tissue microarrays composed of primary ovarian cancers (n=131) and normal tissues (n=85). Percent of samples that were stained positive in ID4 is shown. **(B)** Representative micrograph of a primary ovarian cancer stained with an anti-ID4 antibody.
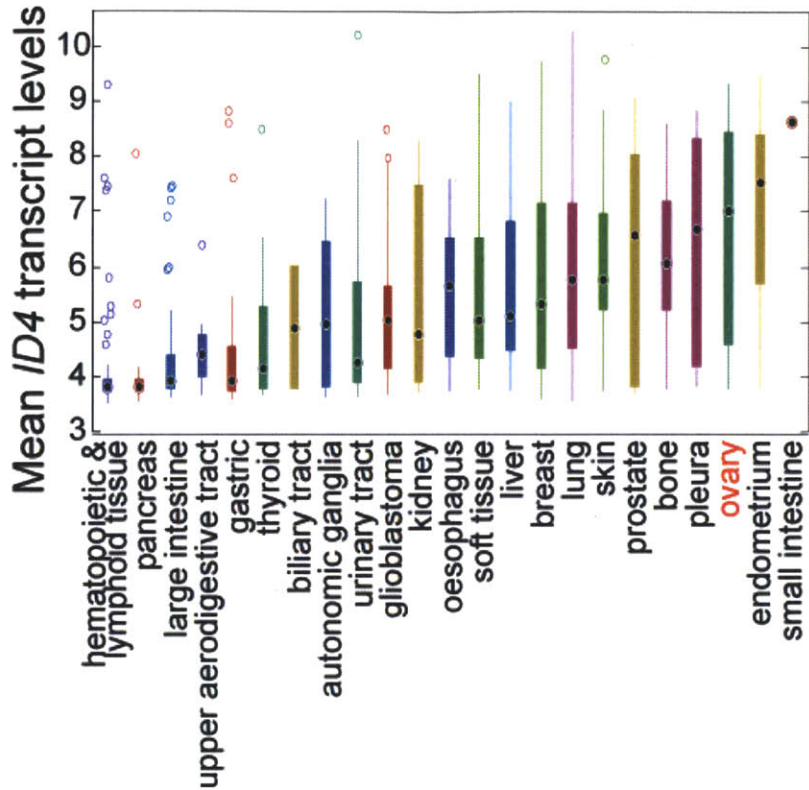
Figure 4.5. Boxplot showing ID4 expression in cancer cell lines derived from different lineages (http://www.broadinstitute.org/ccle). The black dot in each boxplot is the median expression value for each lineage, boxes represent the 25th to 75th percentile of the data and whiskers span the most extreme values of the group. Ovarian cancer cell lines are marked in red.

Figure 4.6. ID4 suppression by shRNAs did not affect other ID family members. Immunoblot of ID1, ID2, ID3 and ID4 in OVCAR-4 cells expressing a control shRNA targeting GFP or ID4-specific shRNAs.

OVCAR-4 5G:3R
OVCAR-8 4G:4R
Caov-3 4G:4R
OV-90 2G:2R
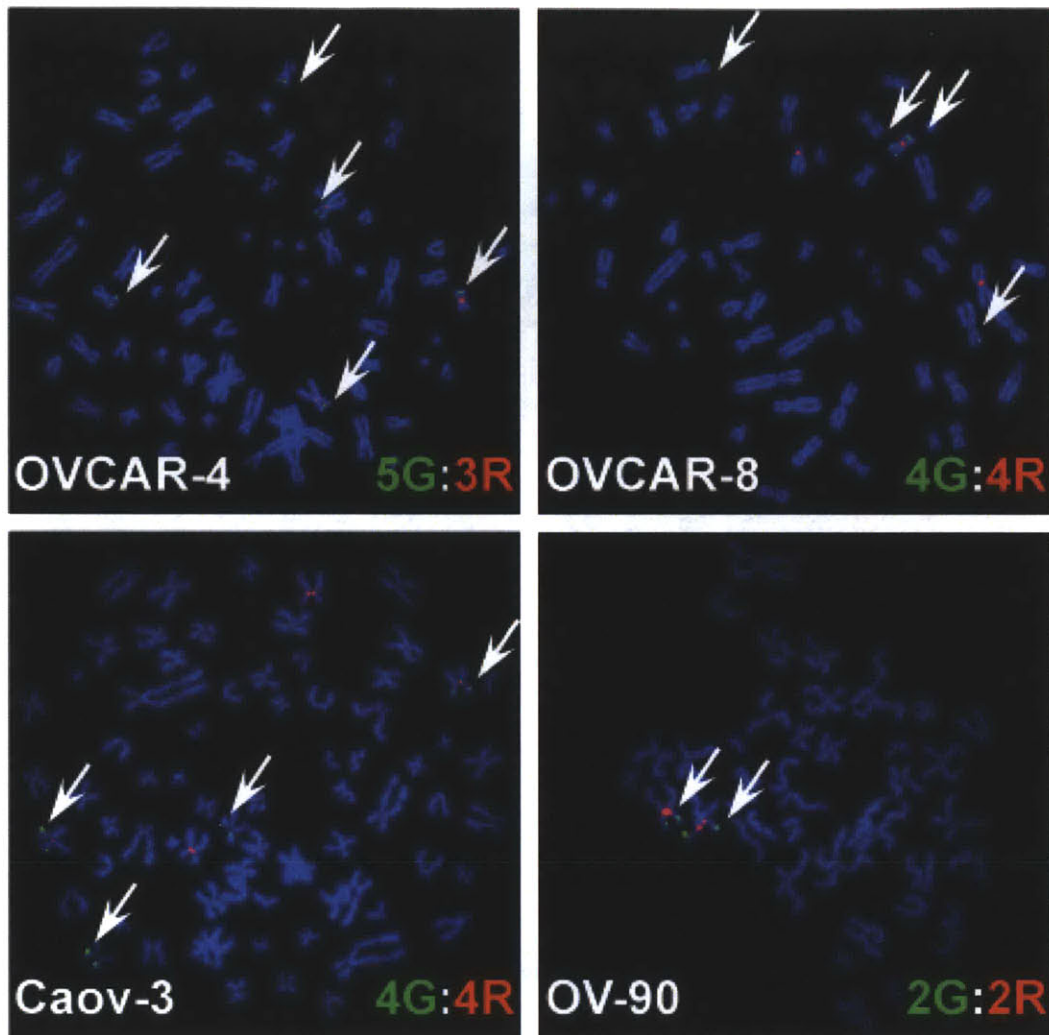
ID4-specific BAC probe
Chr.6 centromeric probe

Figure 4.7. FISH Analysis of ID4 in ovarian cancer cells. Four (4) ovarian cancer cell lines were analyzed for amplification of ID4 by FISH. OV-90 cells, which do not harbor 6p22 amplifications, was used as a negative control.
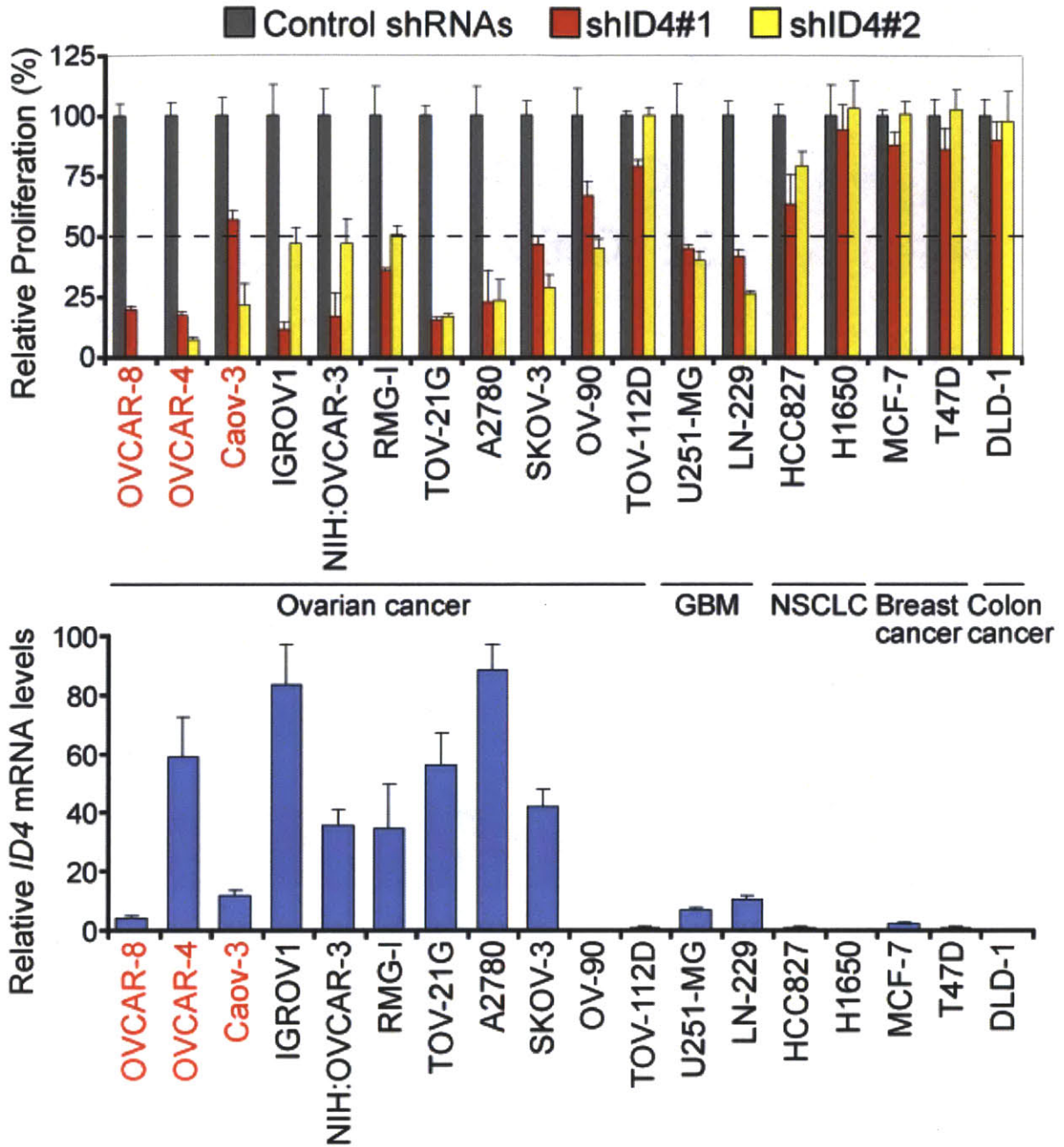
Figure 4.8. Effects of ID4 suppression in ovarian cancer cell lines. *Top*, Effects of ID4 suppression on proliferation of human cancer cell lines. Cells were infected with a control shRNA targeting GFP or 2 shRNAs targeting ID4 and the proliferation was measured 6 d after infection. Error bars indicate s.d. of 6 replicate measurements. *Bottom*, The relative ID4 mRNA levels; 6p22-amplified lines are marked in red. Error bars indicate s.d. of 6 replicate measurements.

100
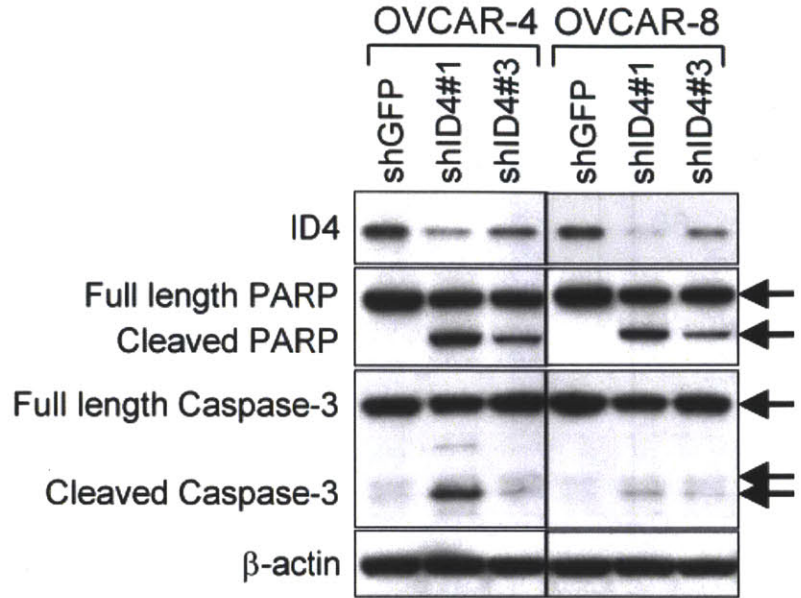
Figure 4.9. Induction of apoptosis by ID4 suppression in ovarian cancer cell lines. Immunoblot of PARP and caspase-3 after suppressing ID4 in 6p22-amplified cell lines. Arrows indicate the respective full length or cleaved PARP or Caspase-3.
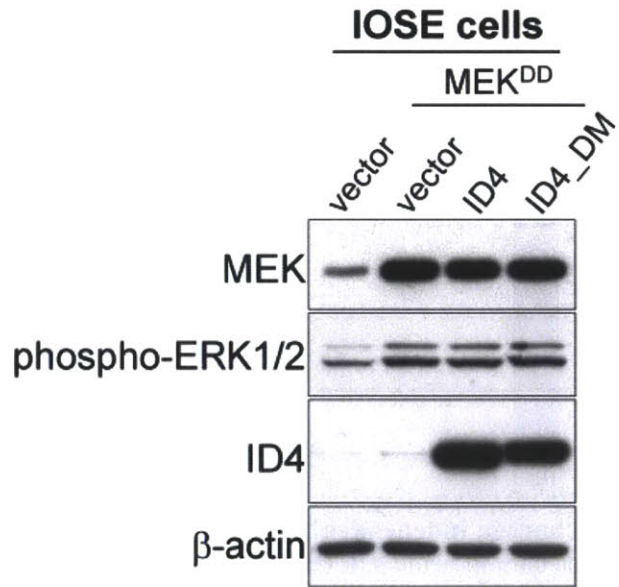
Figure 4.10. Establishment of ID4-overexpressing immortalized ovarian surface epithelial (IOSE) cells. Immunoblot of MEK, phospho-ERK1/2 and ID4 in immortalized ovarian surface epithelial cells expressing indicated constructs.
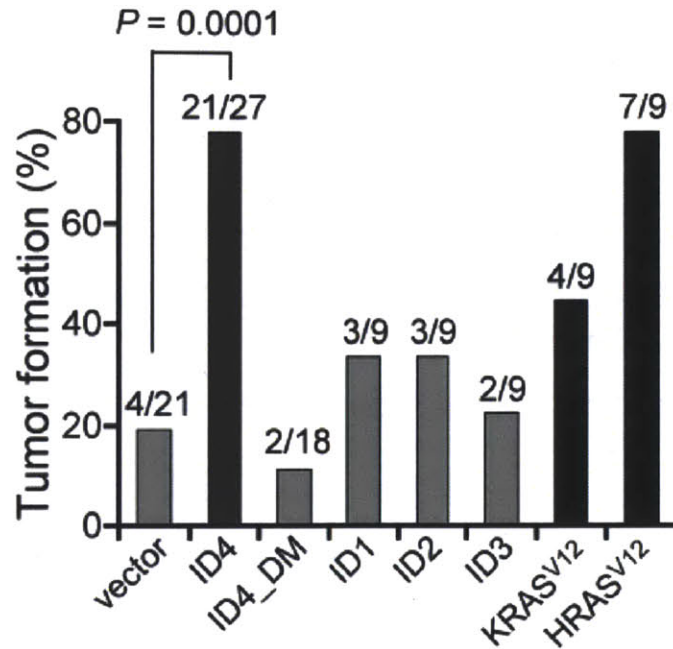
Figure 4.11. Potentiation of tumorigenicity in IOSEs overexpressing ID4 and other ID family members. IOSE-M cells expressing the indicated constructs were implanted subcutaneously into immunodeficient mice. The percent tumor formation is shown for each condition, and the number of tumors formed/number of injections is indicated above each bar. H-RAS^{V12} expressing IOSE cells were used as a positive control.
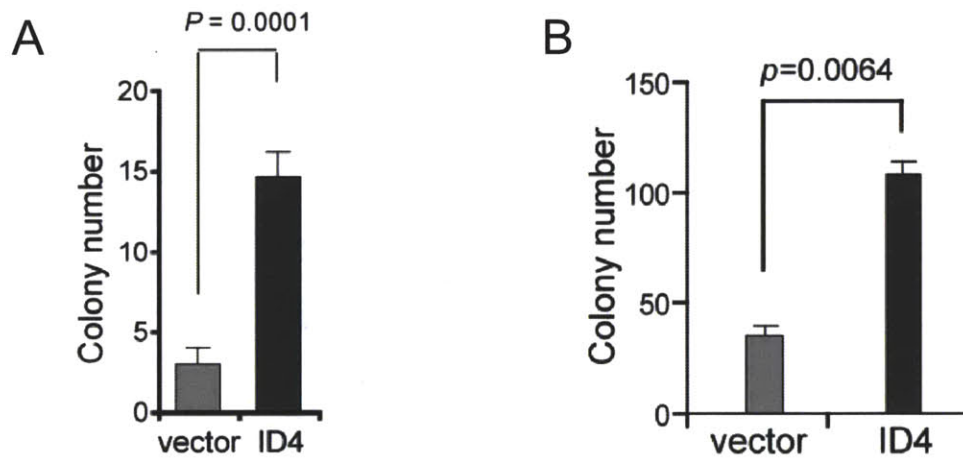
Figure 4.12. ID4 promotes anchorage independent growth. **(A)** ID4 promotes anchorage independent growth of FTSEC-M cells. Error bars indicate s.d. **(B)** Anchorage independent growth of IOSE-M cells expressing ID4 or control vector. Error bars indicate s.d.

4.2.2 TPNs for ovarian cancer-specific siRNA delivery

To rapidly assess whether *ID4* or any other candidate gene functions as a therapeutic

target for ovarian cancer, we required a modular siRNA delivery platform that will permit tumor-

penetrating access to specific cancer cells and manipulate the expression of any arbitrary gene in

those cells. Although we and others have previously used inducible shRNAs to evaluate potential

candidates, this approach is labor-intensive, time-consuming and requires extensive manipulation

of cell lines *in vitro*, which limits its utility to analyze more than a small number of candidates.

In addition, the ideal siRNA delivery vehicle should integrate unique functions of bulk tissue

penetration and cellular membrane translocation, thereby overcome the transport permeability

barrier by penetrating into the tumor tissue, and target receptors that are differentially expressed

on epithelial tumor cells. To accomplish this task, we utilized the delivery system developed in

Chapter 3 that conformed to these design principles, and generated tumor-penetrating

nanocomplexes (TPN) that consisted of siRNA bound to TP-LyP-1 tandem peptides.

To apply TPN to assess the effects of suppressing ID4 *in vivo*, we first selected cell lines

that were both ID4-sensitive and compatible with TPN-targeted delivery of siRNA. Both

OVCAR-4 and OVCAR-8 ovarian cancer cells showed elevated surface p32 expression (**Figure**

4.13) and required ID4 expression as assessed by *ID4*-specific shRNAs and TPN/si*ID4in vitro*

(**Figure 4.14**). Specifically, when ID4 was suppressed in these cell lines *in vitro* using TPNs, we

observed a decrease in cell viability (**Figure 4.14**) and an increased rate of apoptosis (**Figure**

4.15; Figure 4.16). We therefore selected the OVCAR-4 and OVCAR-8 ovarian cancer cell

lines for our preclinical *in vivo* evaluation of *ID4*.

Before testing the functionality of TPNs on delivery of *ID4*-siRNA to orthotopic ovarian tumors *in vivo*, we assessed whether TPNs enabled receptor-specific siRNA delivery to ovarian tumor parenchyma. After intravenous administration to mice bearing subcutaneous OVCAR-8 tumor xenografts, we found an over five-fold increase in the tumor fluorescence of LyP-1 targeted TPNs compared to ARAL targeted control TPNs (**Figure 4.17**).

Although bulk tumor accumulation provides a global measure of targeting, it does not provide spatial information on the extravascular and tumor interstitial availability of TPNs, which ultimately determines their efficacy. We thus performed histological characterization of TPN penetration in subcutaneous OVCAR-8 tumors at various time points and found that TPN exhibited an initial intravascular distribution and subsequently extravasated into the tumor interstitium (**Figure 4.18**). The fraction of TPNs that were sequestered beyond the intravascular space was significantly higher than that of untargeted controls (**Figure 4.19**). Furthermore, LyP-1 targeted TPNs accumulated in the tumor parenchyma to a similar degree as TPNs bearing a different tumor penetrating motif, iRGD (CRGDKGPDC) [117], whereas non-penetrating nanocomplexes (TP-RGD4C) [100] or a commercial cationic lipid siRNA delivery reagent (lipofectamine) failed to show a similar distribution (**Figure 4.20**). These observations demonstrate that TPNs exhibit the desired tumor homing and parenchymal penetration properties necessary for *in vivo* target validation.
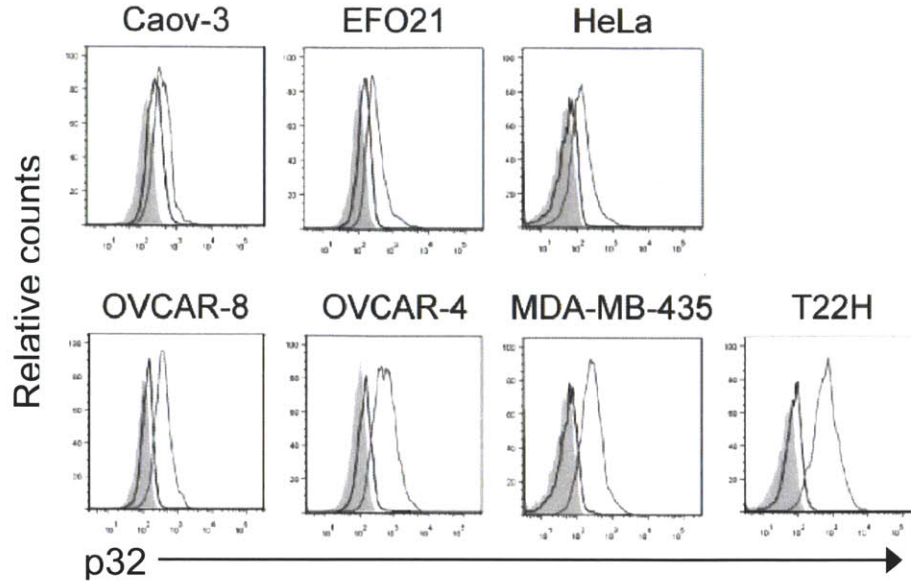
Figure 4.13. Surface expression of p32 in cancer cell lines. Six human cancer cell lines derived from ovarian cancer (CaOV3, EFO21, OVCAR-8 and OVCAR-4), cervical cancer (HeLa), melanoma (MDA-MB-435), and a mouse ovarian cancer cell line (T22H) were surveyed for surface expression of p32 by flow cytometry with a polyclonal rabbit antibody directed against the full-length p32 peptide. A rabbit IgG isotype control was used (black). Unstained cells are shaded in gray.
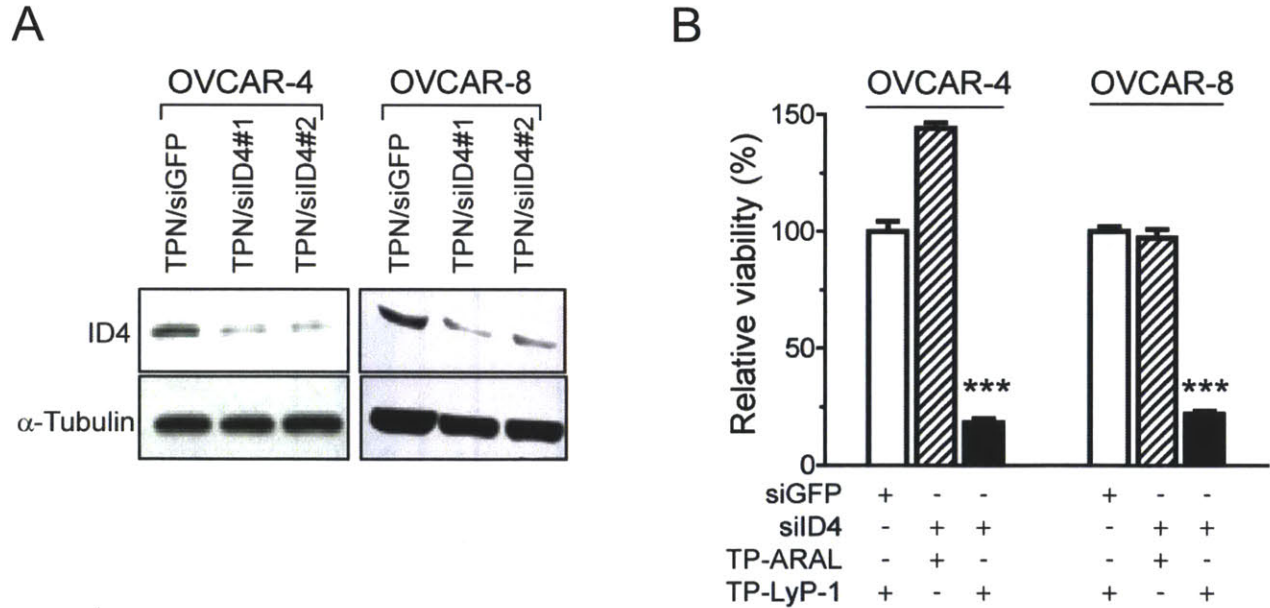
Figure 4.14. ID4 suppression by TPN-mediated siRNA delivery in vitro. (A) Immunoblot of ID4 in two 6p22-amplified ovarian cancer cell lines (OVCAR-4 and OVCAR-8) treated with TPNs containing two ID4-specific siRNAs or a control siRNA targeting GFP. α-Tubulin is used as a loading control. **(B)** Effects of ID4 suppression on cell proliferation. Proliferation of ovarian cancer cell lines treated with TPNs containing GFP-siRNA (white bars), untargeted TPN (TP-ARAL) carrying ID4-siRNA (hashed bars), and TPNs carrying ID4-siRNA (black bars). Error bars indicate s.d. from 4 independent experiments. ***$p<0.001$.
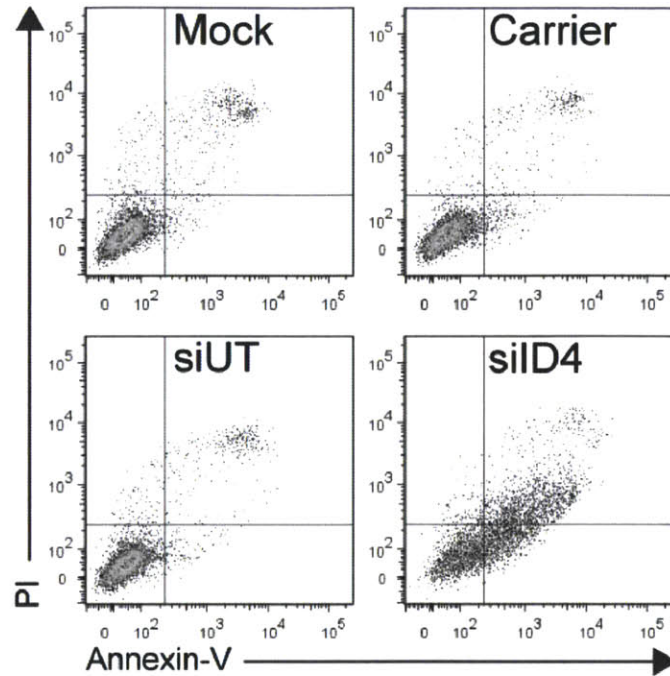
Figure 4.15. Effects of ID4 suppression on apoptosis. ID4 knockdown by TPNs carrying *ID4*-siRNA in OVCAR-8 ovarian cancer cells led to an increased proportion of the population that binds Annexin-V, relative to untreated cells (mock), cells treated with TP-LyP-1 (carrier) or with TPN carrying an irrelevant siRNA (siUT).
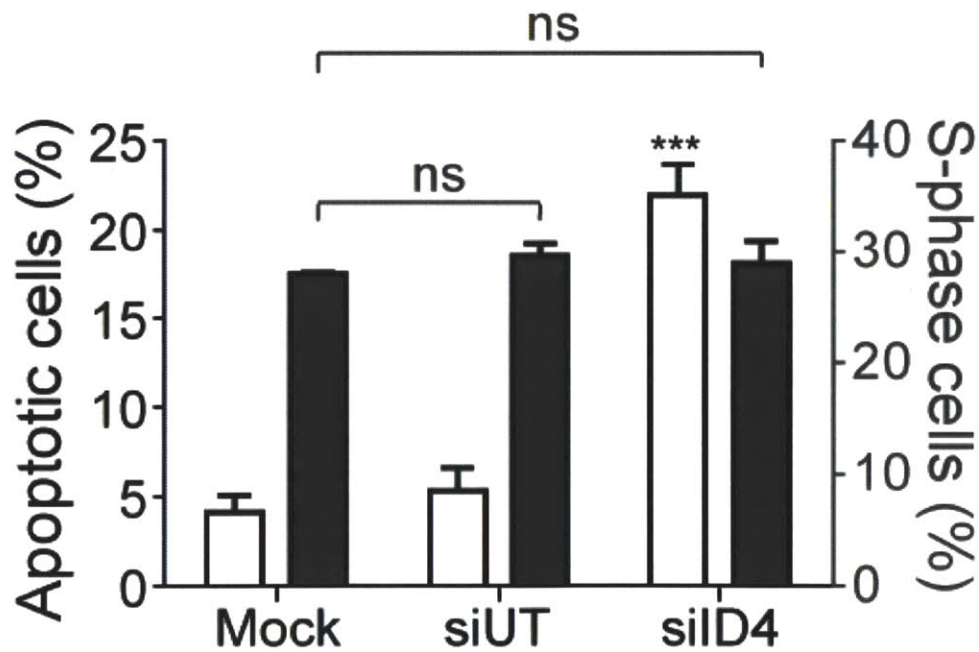
Figure 4.16. Summary of Annexin-V assays (white bars) and cells entering S-phase by the Click-iT-EDU assay (red bars). The percentages of apoptotic and S-phase cells were calculated. Three independent experiments were pooled and analyzed as a combined data set. Error bars indicate s.d. from 3 independent experiments. n.s., not significant; ***$p<0.001$.

106

A

B
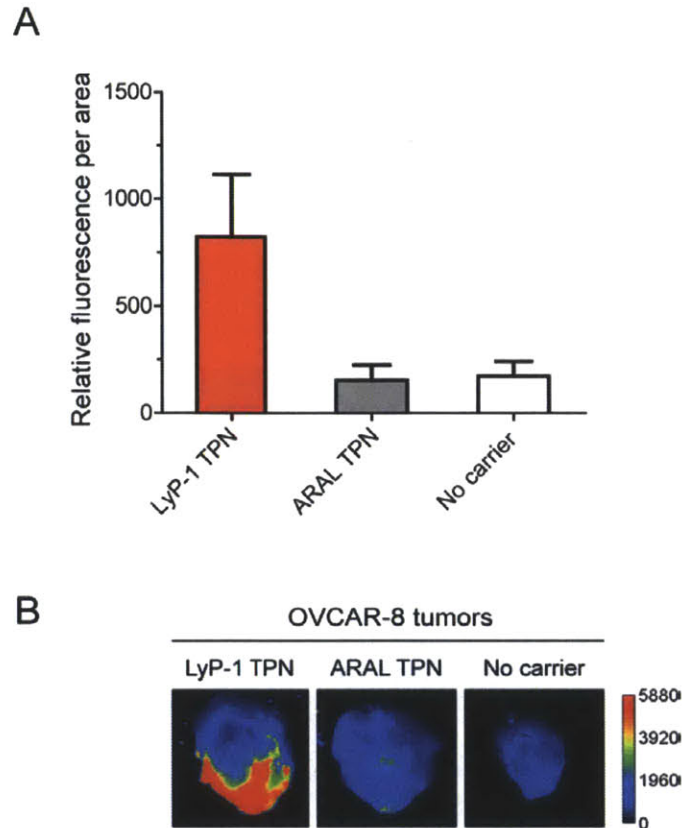
Figure 4.17. Ovarian tumor targeting by TPNs. (A) Quantification of siRNA fluorescence per area of subcutaneous OVCAR-8 ovarian tumor xenografts harvested 6 h after tail-vein injection of LyP-1 TPNs (red bar), untargeted nanocomplexes (ARAL TPNs, gray bar), or carrier-less siRNA (No carrier, white bar) labeled with a near infrared fluorophore (VivoTag-750). Error bars indicated s.d. (n=4). **(B)**Near-infrared fluorescence images of OVCAR-8 tumor xenografts.
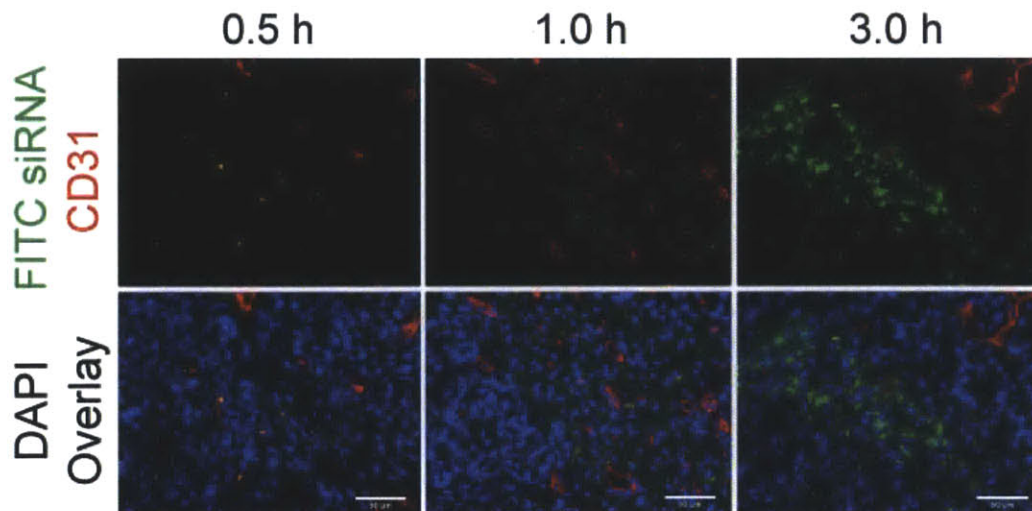
Figure 4.18. Time-course of tumor penenetration by TPN. Histological analysis of time-dependent homing of TPN carrying FITC-labeled siRNA (pseudocolored green) in relation to cells (DAPI, blue) and blood vessels (CD31, red) in mice bearing bilateral s.c. OVCAR-8 tumors. Scale bars, 50 μm.
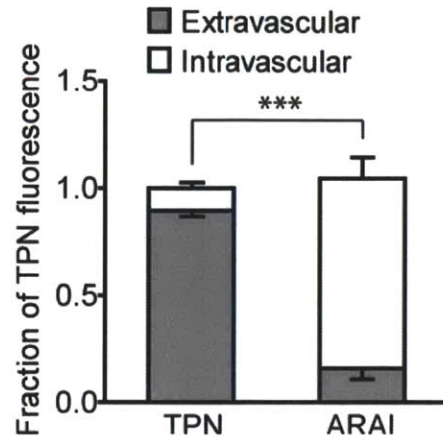
Figure 4.19. Quantification of the extravascular and intravascular fractions of TPNs. Data from representative sections of 6 independent tumors is shown. Error bars indicate s.d. ***$p<0.001$.

siRNA (FITC), CD31, DAPI
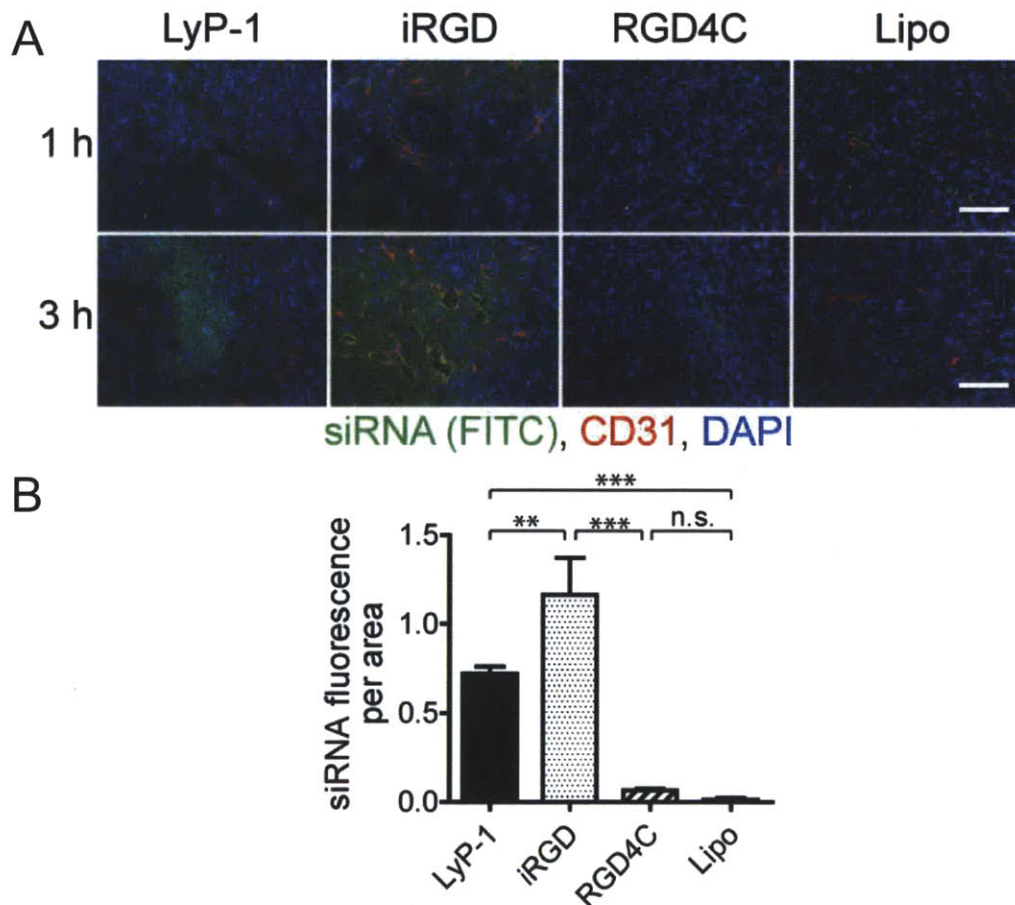
Figure 4.20. Quantification of tumor parenchymal penetration by TPN. (A) Comparison of bulk tumor parenchymal penetration of FITC-labeled siRNA in different TPN formulations: LyP-1 TPN (LyP-1), iRGD TPN (iRGD), a non-penetrating nanocomplex (RGD4C), and lipofectamine (Lipo) in OVCAR-8 tumors at 1 h or 3 h post i.v. injection (n = 6 per formulation). Scale bars, 50 μm. **(B)** Quantification of tumor fluorescence. Error bar indicates averages ± s.d. from 6 randomly selected views per condition. n.s., not significant; **$p<0.01$; ***$p<0.001$.

108

4.2.3 Loss of tumor maintenance after TPN-mediated suppression of ID4

Since suppression of *ID4* by TPN inhibited the proliferation of ovarian cancer cell lines that overexpress ID4 *in vitro* and TPN could deliver siRNA to the extravascular milieu of ovarian tumors *in vivo*, we next tested whether ID4 was essential for tumor maintenance through TPN-mediated delivery of *ID4*-siRNA in human ovarian cancer xenografts. Mice harboring existing subcutaneous OVCAR-4 tumors were injected i.v. or i.p. with TPN/si*ID4* nanocomplexes every 3 days. We observed that repeated, systemic administration of the nanocomplexes prevented additional growth of the tumors, and thus resulted in 80-90% reduction in tumor burden relative to control animals (**Figure 4.21; Figure 4.22**).

Correspondingly, TPN/si*ID4* treatments led to a significant suppression of *ID4 mRNA* in the residual tumors. We also found that TPN/si*ID4* nanocomplexes induced *CDKN1A* (p21$^{WAF1/CIP1}$) transcript levels (**Figure 4.23**), a known target of *ID4* [243-244]. Residual TPN/si*ID4* treated tumors exhibited significant apoptosis (**Figure 4.24**). In contrast, nanocomplexes carrying an unrelated siRNA (siUT) or tandem peptide alone (Carrier) had no effect. We also observed that tumor growth was static in si*ID4*-treated cohorts for an additional 30 d after the termination of TPN treatment (**Figure 4.22**). These observations demonstrated that TPN/si*ID4* nanocomplexes induce specific tumor delivery and target suppression when introduced systemically, and yield a functional impact on recipient cells.

We then tested whether TPNs could induce therapeutic activity in mice harboring disseminated ovarian tumors. We established orthotopic OVCAR-8 tumors, confirmed intra-abdominal dissemination three weeks post implantation, and then initiated intraperitoneal injection of TPN every 3 days. We found that the tumor burden in mice that received TPN/si*ID4* regressed, and the recipients survived beyond 60 d, even after the nanocomplex treatments

ceased (**Figure 4.25; Figure 4.26**). In contrast, control tumors continued to grow and recipient mice developed hemorrhagic ascites, which may have attenuated tumor bioluminescence resulting in an underestimation of tumor burden [245].

After 40 d, we found disseminated tumors in control cohorts but no visible tumor lesions in 4 out of 5 TPN/si*ID4* treated mice upon necroscopy, indicating tumor regression (**Figure 4.27; Figure 4.28**). Histological analysis of the single remnant tumor revealed significant reduction in ID4 levels and increased apoptosis in the tumor parenchyma (**Figure 4.29; Figure 4.30**). We noted that the level of p32 in the si*ID4* treated tumors was higher than that in the controls (**Figure 4.31**). Since the surface expression of p32 is known to increase under stress [217, 219], this finding is consistent with the potential that uptake of these TPNs may be enhanced upon repeated exposures to tumoricidal siRNA.

In some cases, apparent therapeutic effects of RNAi may be confounded by non-sequence specific innate immune responses mediated by toll-like receptors [70]. Therefore, we independently measured serum levels of IFN-α, TNF-α, and IL-6 in immunocompetent mice after TPN administration and failed to observe induction of these cytokines in treated animals compared to mice that received a known immunostimulatory siRNA [69] (**Figure 4.32**).

Moreover, we failed to observe deleterious effects on animal weight in any of the cohorts for both mouse models of ovarian cancer (**Figure 4.33**). Finally, histological examination of numerous vital organs from TPN/si*ID4* treated mice, including the bladder, kidneys, liver, spleen, heart, and ovaries, failed to reveal evidence of organ toxicity (**Figure 4.34**).
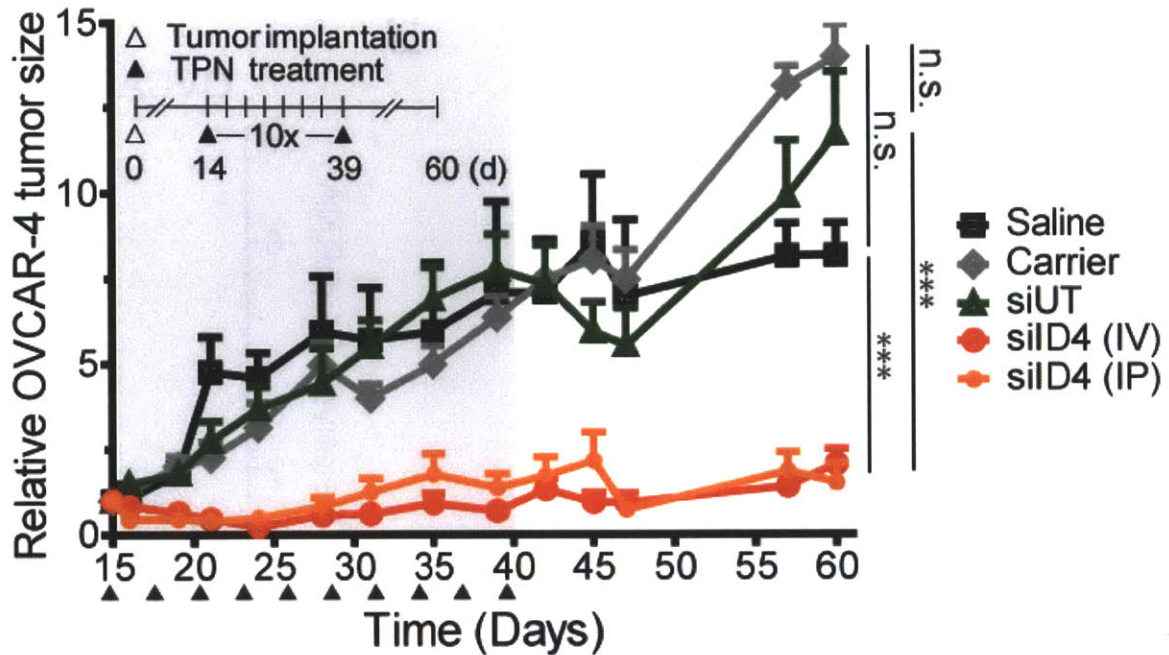
Figure 4.21. Efficacy of TPN-mediated delivery of *ID4*-siRNA in *in vivo*. OVCAR-4 cells were xenografted subcutaneously and allowed to form tumors of up to 5mm in diameter for 14 days before start of treatment with indicated formulations every 3 d for 25 d (at 1mg siRNA/kg/injection, arrowheads). Mice in the carrier group received TP-LyP-1 peptide without siRNA (at 6.5mg peptide/kg). *Inset,* the timeline of the experiment. Tumor size was measured by digital caliper and the volume was calculated based on the modified ellipsoidal formula volume = ½ (length x width^2) and normalized to that at the start of treatment (day 14). Treatment period is shaded in gray. n = 8-10 tumors per group. Error bars indicate s.d.; n.s., not significant; ***p<0.001.
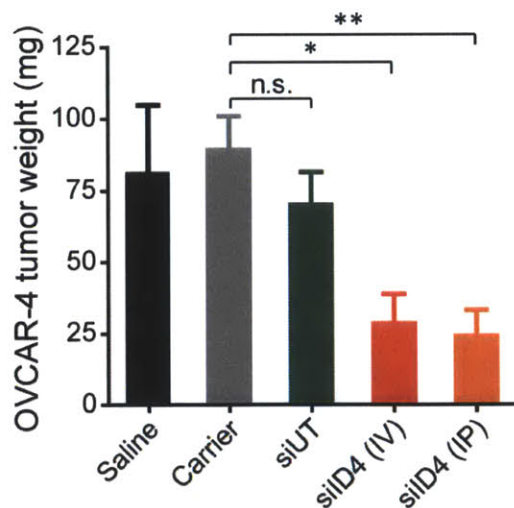
Figure 4.22. Theraepeutic effects of TPN/siID4 treatment in OVCAR-4 tumor-bearing mice. Weight of OVCAR-4 tumors at day 60. (n = 5-10 tumors per each cohort); *p<0.05; **p<0.01; n.s., not significant.

A OVCAR-4 tumors
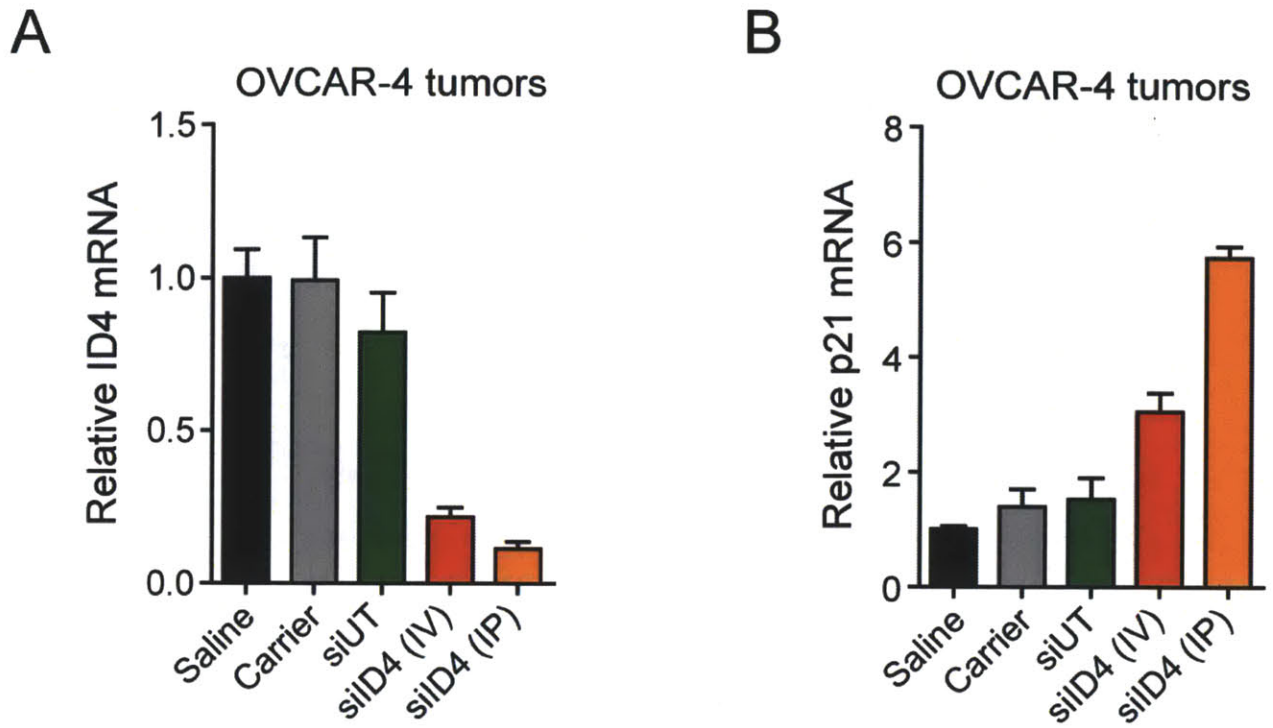
B OVCAR-4 tumors

Figure 4.23. Effects of TPN-mediated ID4 suppression in OVCAR-4 tumor xenografts. Relative ID4 and p21 mRNA levels from tumors harvested from all cohorts at day 60.
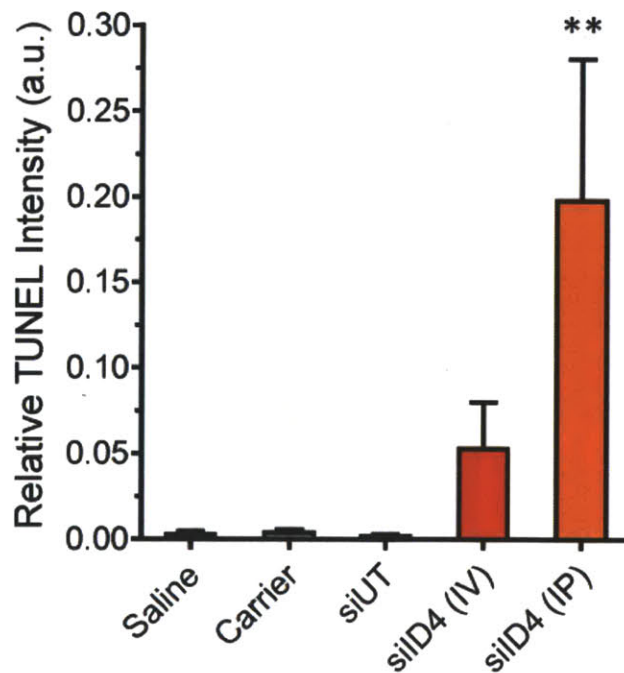
Figure 4.24. Induction of apoptosis by TPN/si*ID4*treatment. Quantification of TUNEL staining intensities from 6-10 randomly selected OVCAR-4 tumor sections after 30 d of TPN treatment.**$p<0.01$.
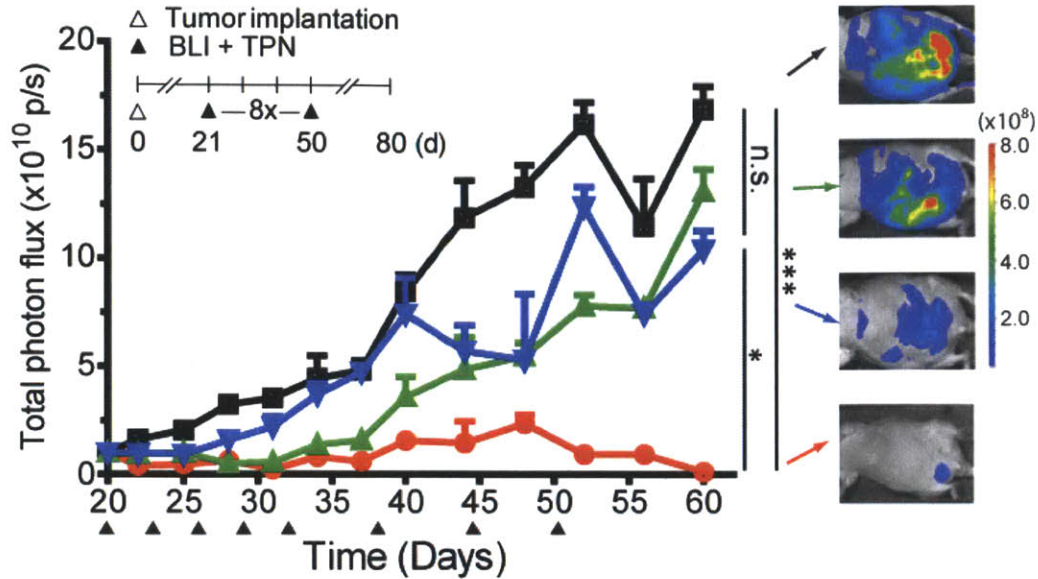
Figure 4.25. Therapeutic efficacy of TPNs in mice bearing disseminated tumors. *Left,* OVCAR-8 cells were xenografted intraperitoneally and allowed to form tumors over 20 d. On day 21, mice were randomly divided into 4 groups with matching tumor burdens and treated every 3 d for 14 d and then once weekly thereafter with: TPNs carrying *ID4*-specific siRNA (red circles); saline (black squares); TPN carrying GFP-siRNA (green triangles); and untargeted TP-ARAL nanocomplexes carrying *ID4*-specific siRNA (blue triangles), at 5mg siRNA/kg/injection (arrowheads). *Inset,* the timeline of the OVCAR-8 tumor therapy experiment. Total tumor burden was followed by bioluminescence imaging (BLI). n = 5 per group. Error bars indicate s.d.; n.s., not significant; *$p<0.05$; ***$p<0.001$. *Right,* Representative whole-animal bioluminescence images of mice in the groups treated in D confirmed disseminated intraperitoneal tumor burden. Images were taken on day 60.
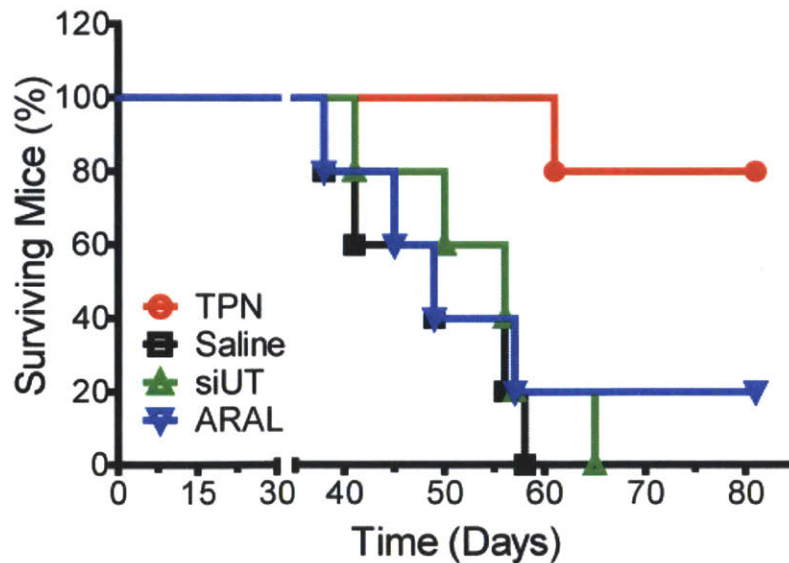
Figure 4.26. Kaplan-Meier plot of overall survival. Survival of animals bearing disseminated orthotopic OVCAR-8 xenograft tumors from cohorts shown in Figure 4.25 (n = 5 per group).
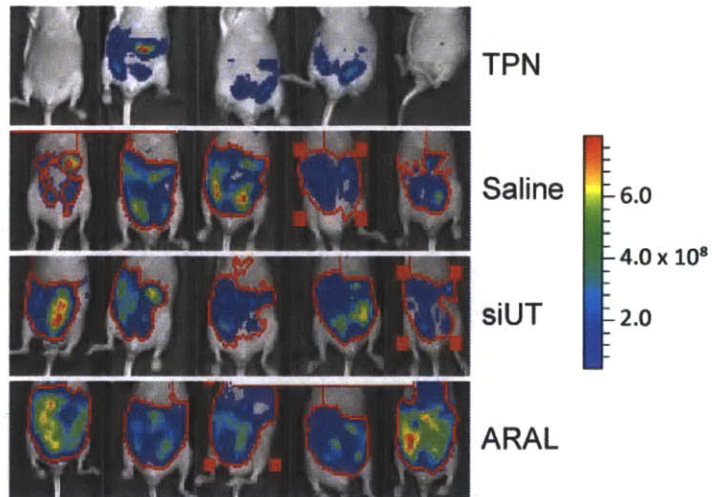
Figure 4.27. Bioluminescence imaging (BLI) of OVCAR-8 tumor burden. All cohorts of mice bearing orthotopic OVCAR-8 ovarian tumor xenografts were imaged serially. Images shown were obtained on day 40 of therapeutic trial.
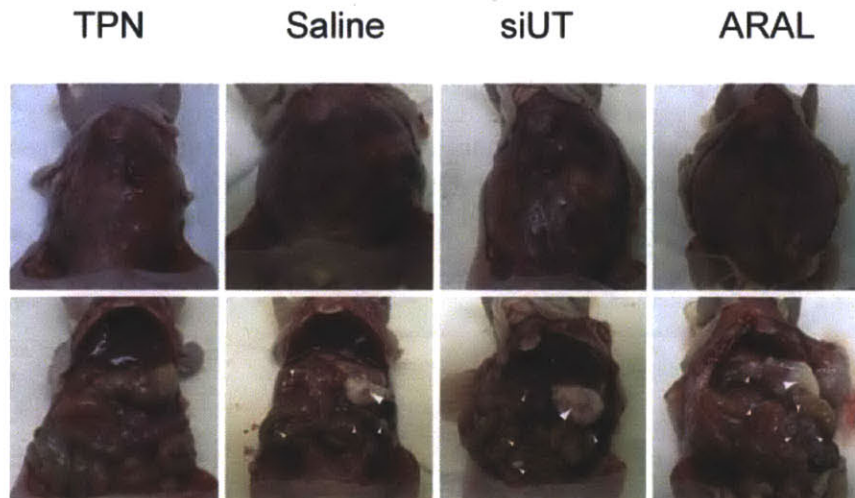
Figure 4.28. Photographs of representative OVCAR-8 tumor bearing mice from each cohort upon necropsy at day 60. Arrowheads indicate the presence of disseminated intraperitoneal ovarian tumor nodules. No visible tumors were seen in the TPN/siID4 treated mice.

OVCAR-8 orthotopic tumors
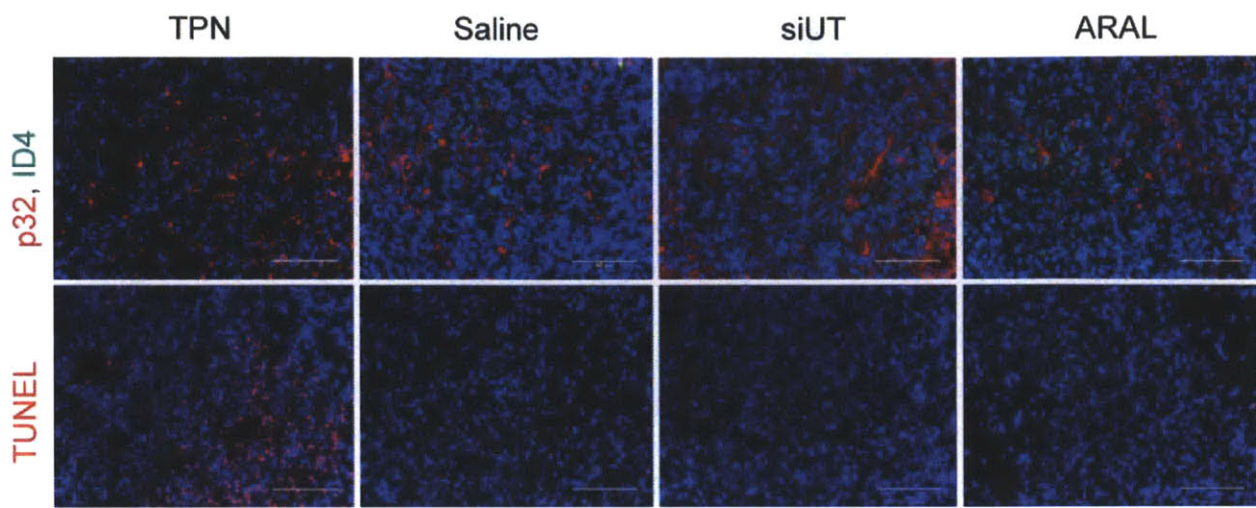
Figure 4.29. Effects of TPN-mediated si*ID4* delivery *in vivo*. Tumor sections harvested from all 4 cohorts on day 40 were stained for p32 (pseudocolored red) and ID4 (pseudocolored green) (top) and for induction of apoptotic cell death (bottom) by TUNEL (red). Scale bars, 50 μm.
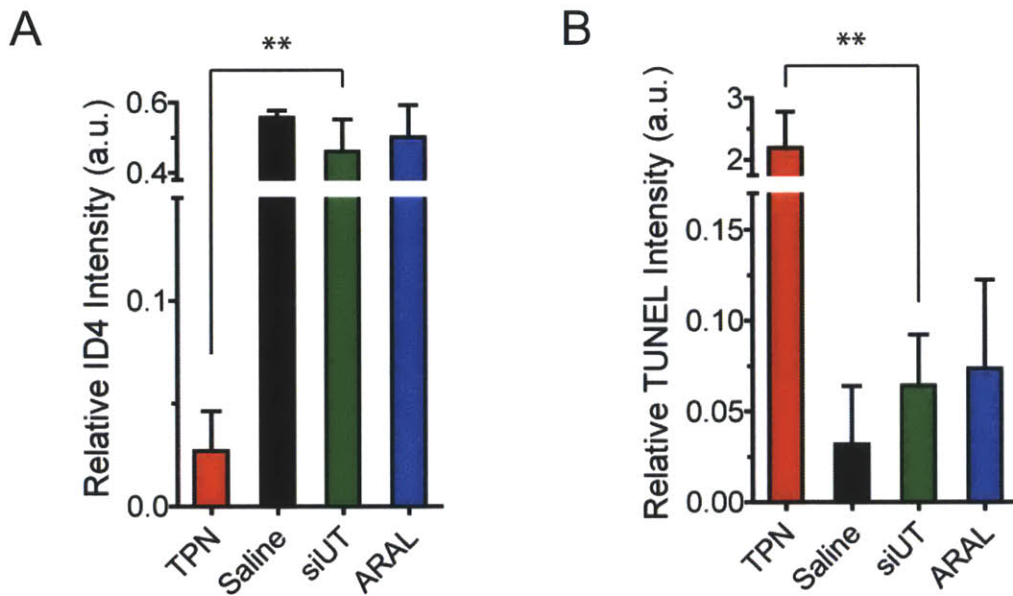
Figure 4.30. Downstream effects of ID4 suppression in OVCAR-8 tumors. Quantification of ID4 and TUNEL intensities from OVCAR-8 tumors after TPN treatment. Statistical analyses were performed using ANOVA; Error bars indicate s.d. **$p<0.01$.

115
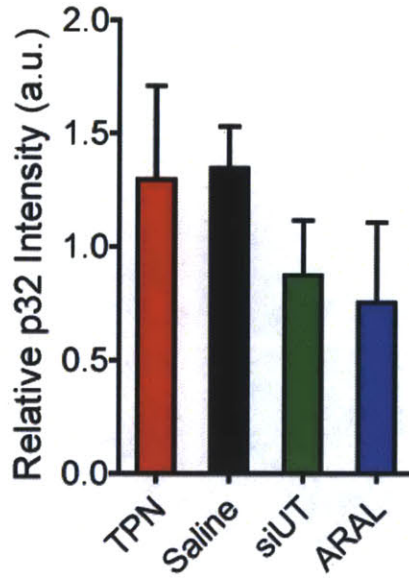
Figure 4.31. Quantification of p32 intensities from OVCAR-8 tumors after TPN treatment.
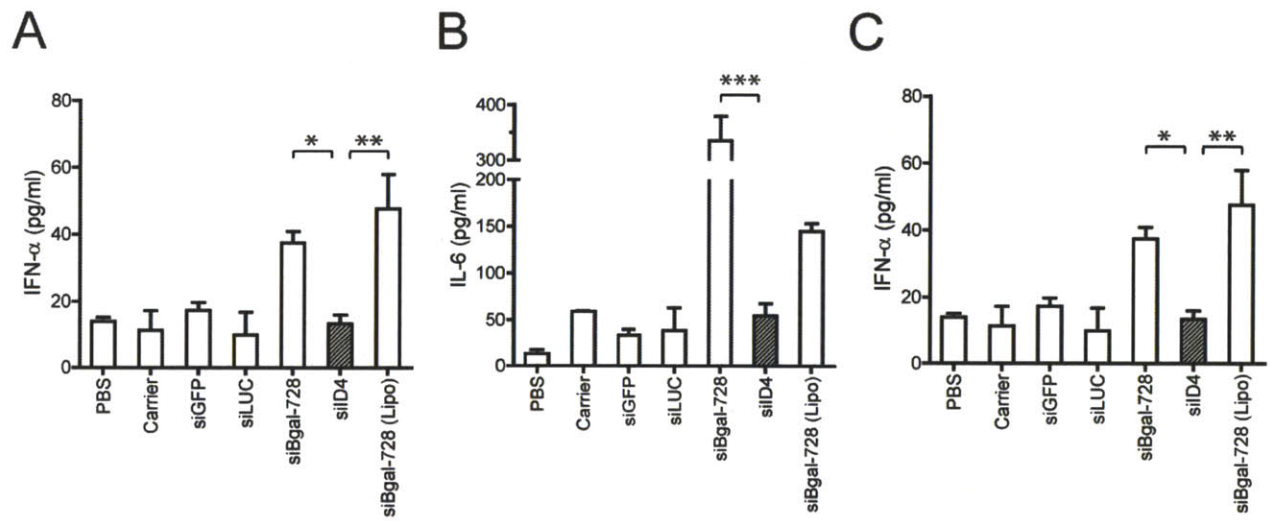
Figure 4.32. Lack of immunostimulation by TPN. Immunocompetent Balb/c mice were injected intraperitoneally with TPNs and 6 h later, serum samples were tested for levels of: **(A)** interferon-alpha (IFN-α), **(B)** IL-6, and **(C)** TNF-α, by ELISA. The immunostimulatory siRNA sequence, siβgal-728, was complexed to either lipofectamine or TP-LyP1 and these were used as positive controls for non-specific immunostimulation. n = 4-8 per group. Error bars indicate s.d. *$p<0.05$; **$p<0.01$; ***$p<0.001$.
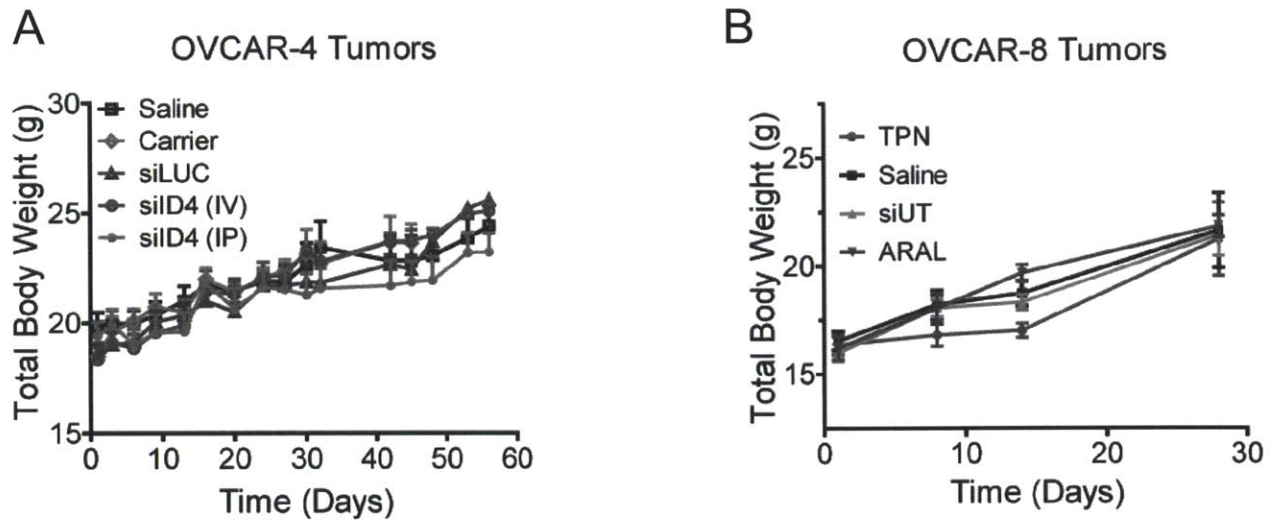
Figure 4.33. Effects on body weight from TPN treatment. (A) Total body weight of OVCAR-4 subcutaneous tumor xenograft-bearing mice over the course of TPN treatment. Error bars indicate s.d. **(B)** Total body weight of OVCAR-8 orthotopic tumor xenograft-bearing mice during TPN/siID4 treatment. Error bars indicate s.d.
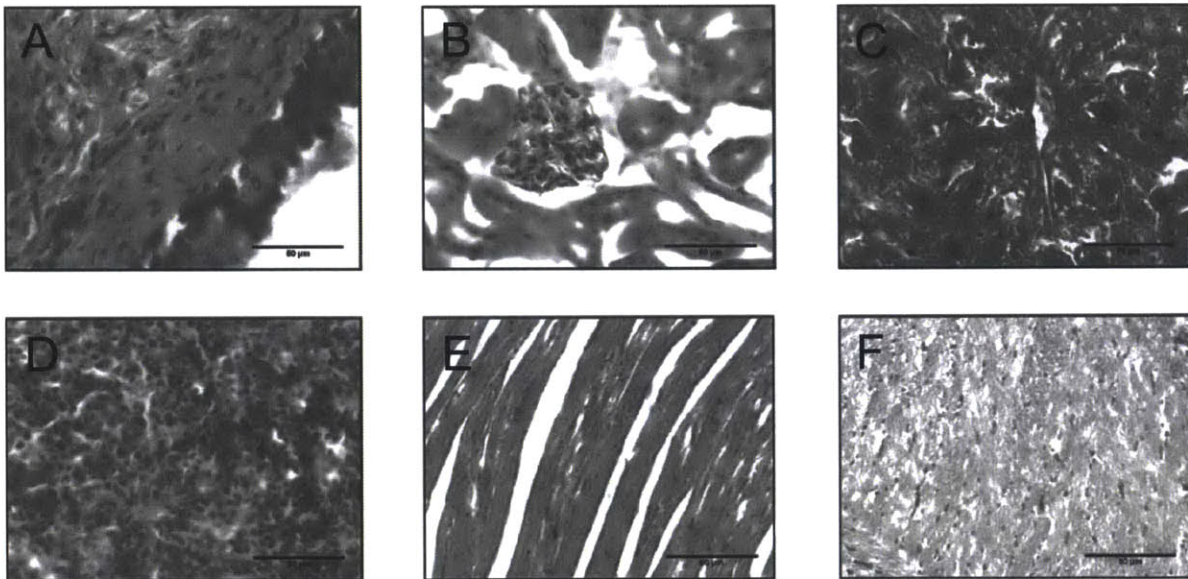
Figure 4.34. Absence of general toxicity after TPN treatment. Organs were harvested from OVCAR-8 tumor bearing mice after TPN treatment for 40 d (5 mg siRNA/kg) and stained with H&E: **(A)** bladder. **(B)** kidney. **(C)** liver. **(D)** spleen. **(E)** heart. **(F)** ovary. No relevant histological or morphological evidence of toxicity was observed in these organs. Scale bar is 50 μm.

4.2.4 ID4 induces transformation by regulating HOXA9 and CDKN1A

To explore the mechanism of action by which *ID4* induces transformation, we performed

gene expression profiling in immortalized ovarian surface epithelial (IOSE-M) cells that

overexpress *ID4* or a control vector. Among the top 5 gene sets, we found highly significant enrichment of 3 gene sets upregulated by expression of the oncogenic NUP98-HOXA9 fusion protein [246] (**Figure 4.35**).

We confirmed that expression of *ID4* in IOSE-M cells consistently increased expression of multiple *HOXA* genes, including *HOXA9*, *HOXA7* and *HOXA3* (**Figure 4.36**) while suppression of *ID4* led to significantly reduced levels of these same genes (**Figure 4.37**). To determine whether HOXA9 was required for *ID4*-induced cell transformation, we introduced previously validated *HOXA9*-specific shRNAs [247] or control shRNAs (targeting GFP) into *ID4*-overexpressing IOSE-M cells (**Figure 4.38**). We found that suppression of *HOXA9* only slightly reduced cell proliferation (**Figure 4.39**) but significantly inhibited *ID4*-induced anchorage independent growth and reduced the rate of tumor formation (**Figure 4.40**).

Finally, to confirm these observations in human ovarian cancers, we analyzed the expression profiles from primary ovarian tumors[226] and found that many genes within the HOXA9 expression signature were significantly downregulated in tumors that express low levels of *ID4* (**Figure 4.41**). We also found that tumors that harbor *ID4* amplifications showed significantly increased expression of the p21$^{WAF1/CIP1}$ target gene set (**Figure 4.42**). These observations demonstrate that expression or amplification of *ID4* induces the HOXA9 and CDKN1A transcriptional programs to disrupt the normal regulation of proliferation and differentiation.
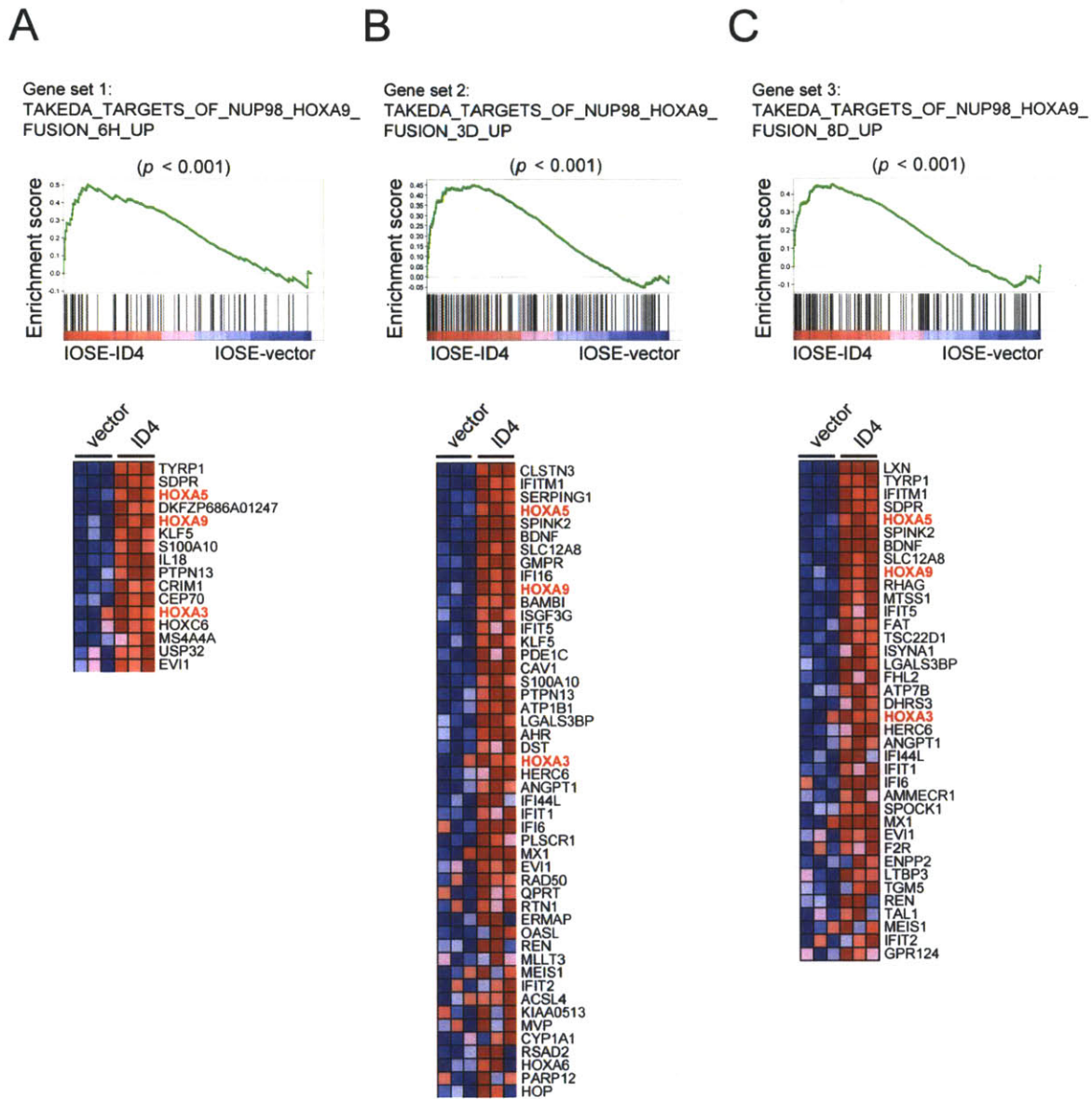
Figure 4.35. ID4 regulates HOXA9 activity. Gene expression profiling and GSEA were performed on IOSE-M cells expressing ID4 or a control vector. Top, Enrichment plots show the running enrichment score (*y*-axis) in green for the ranked list of genes (*x*-axis) based on their differential expression (signal to noise value) between cells expressing ID4 or a control vector. Black bars at the bottom of the figure indicate the location of genes in a gene set upregulated by expression of NUP98-HOXA9 fusion protein generated 6 h **(A)**, 3 d **(B)**, and 8 d **(C)** after induction within the ranked list. Significant upregulation of these genes (*p*=0.001) was observed in cells expressing ID4. Bottom, Heatmaps showing the expression levels induced by ID4 overexpression (triplicate measurements) of a subset of genes within each of the gene set. High and low expression levels are indicated by red and blue colors, respectively. Members of the homeobox family of transcription factors are marked in red.
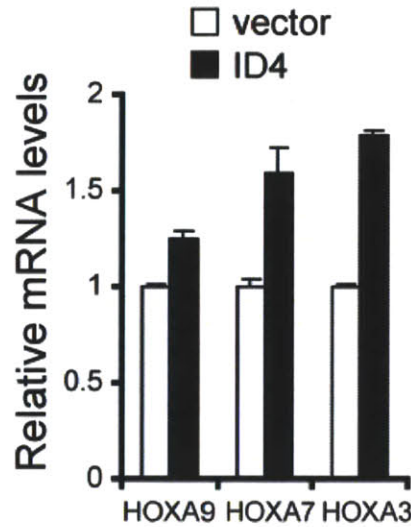
Figure 4.36. Overexpression of ID4 in IOSE-M cells increases mRNA levels of *HOXA9*, *HOXA7* and *HOXA3*. Quantitative PCR analysis of HOXA9, HOXA7 and HOXA3 in IOSE-M cells overexpressing ID4 or a control vector. Error bars indicate s.d. of 6 replicate measurements.

A
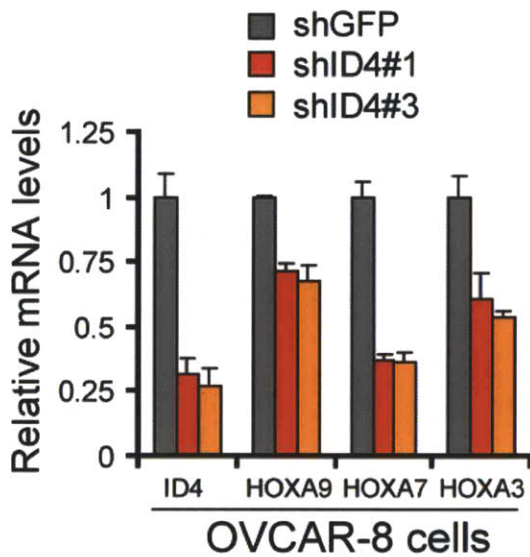
B
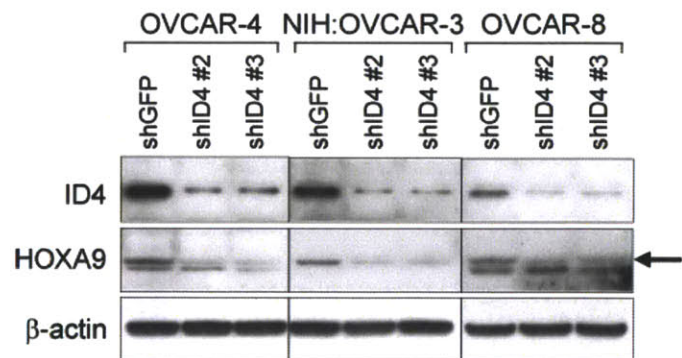
Figure 4.37. Suppression of ID4 reduces HOXA9, HOXA7 and HOXA3. (A) Quantitative PCR analysis of HOXA9, HOXA7 and HOXA3 in OVCAR-8 cells 3 days after infection with a control shRNA targeting GFP or two shRNAs targeting ID4. Error bars indicate s.d. of 6 replicate measurements. **(B)** Suppression of ID4 reduces expression of HOXA9 proteins. Immunoblot of ID4 or HOXA9 in OVCAR-4, NIH:OVCAR-3 and OVCAR-8 cells expressing a control shRNA targeting GFP or ID4-specific shRNAs. Arrow indicates the specific HOXA9 band. β-actin included as a loading control.
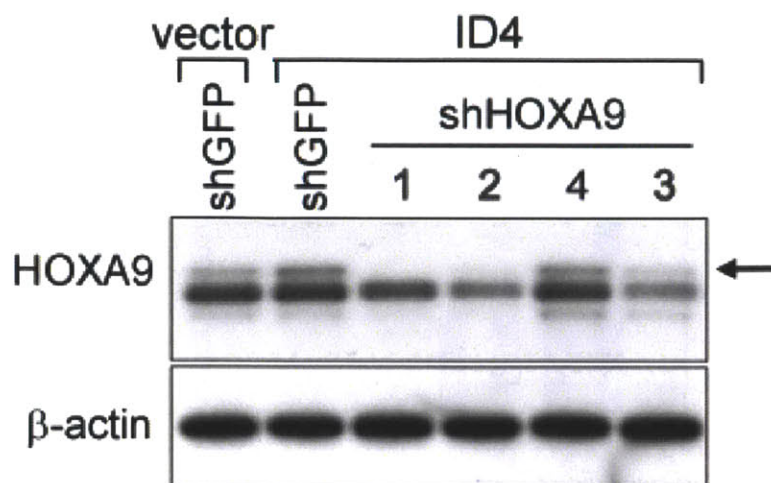
Figure 4.38. Suppression of HOXA9 protein levels. Immunoblot of HOXA9 in IOSE-M cells expressing indicated constructs.
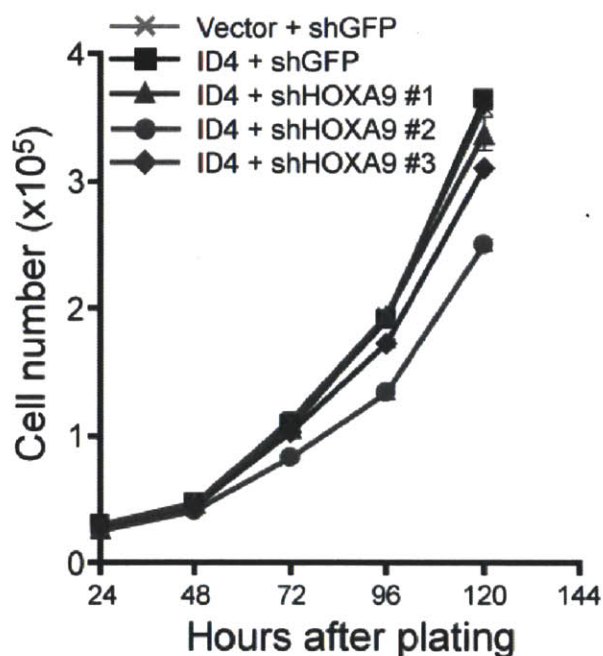
Figure 4.39. Effect of suppressing *HOXA9* on proliferation of IOSE-M cells. Cells expressing indicated constructs were plated in triplicate and counted daily. Suppression of *HOXA9* by the most effective *HOXA9*-specific shRNA (shHOXA9#2) resulted in 30% inhibition on cell proliferation 120 h after plating.
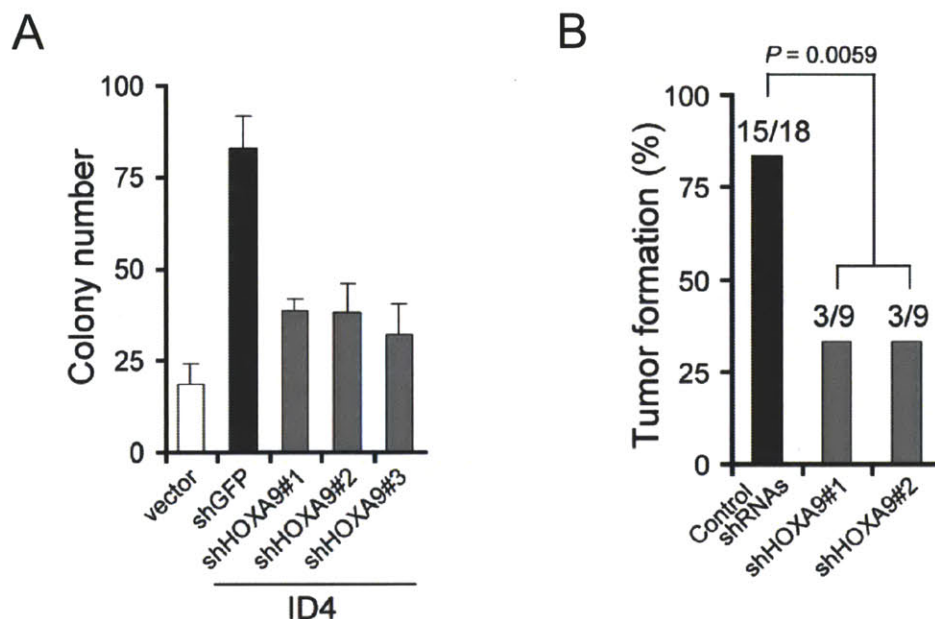
Figure 4.40. HOXA9 is necessary for ID4-mediated transformation. (A) HOXA9 is necessary for ID4-mediated transformation. Suppression of HOXA9 by previously described shRNAs (54) inhibited anchorage-independent growth of ID4-overexpressing IOSE-M cells. (B) Suppression of HOXA9 suppressed ID4-induced tumorigenicity in immunodeficient mice. ID4-overexpressing IOSE-M cells expressing indicated shRNAs were subcutaneously implanted into immunodeficient mice. Tumors were monitored for 5 months. Percent tumor formation based on number of injection sites is depicted.
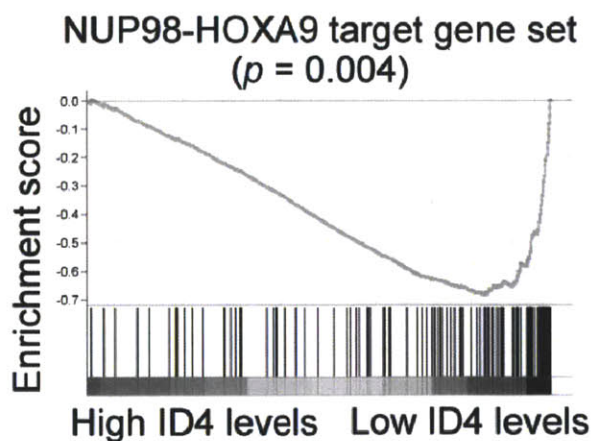
Figure 4.41. ID4 expression in ovarian tumors correlates with HOXA9 activity. Expression data from primary ovarian tumors were used to perform GSEA on 44 samples with low ID4 expression levels vs. 45 samples with high ID4 expression (thresholds were 1 s.d. below and above the mean expression of all the samples). Enrichment plots are as described in C. Black bars at the bottom of the figure indicate the location of genes in a NUP98-HOXA9 downregulated gene set (TAKEDA_TARGETS_OF_NUP8_HOXA9_FUSION_10D_DN). Significant enrichment of these genes ($p = 0.004$) was observed in tumors with low ID4 levels.

Primary ovarian cancer samples
p21 target gene set
($p = 0.016$)
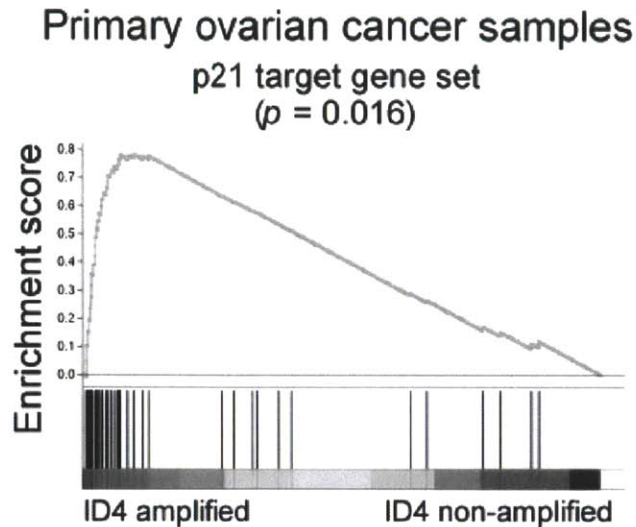
Figure 4.42. *ID4* amplification in ovarian tumors correlates with decreased p21 activity. Expression profiling of primary ovarian tumors with matched copy number data was used to perform GSEA on amplified *ID4* (log_2 copy number ratio >0.3) and non-amplified *ID4* samples (log_2 copy number ratio <0). All genes were ranked by their differential expression (signal to noise) between 81 non-amplified and 109 amplified *ID4* primary tumors. Black bars at the bottom of the figure indicate the location of genes in the p21[WAF1/CIP1] target gene set (P21_P53_ANY_DN); significant upregulation (p=0.016) of the gene set was observed in amplified tumors.

4.3 Discussion

4.3.1 Integrated platform to credential oncogenes *in vivo*

Current genome characterization efforts will eventually provide insight into the genetic alterations that occur in most cancers and identify statistically significant recurrent alterations that define new cancer targets. However, most epithelial cancers harbor hundreds of genetic alterations as a consequence of past or on-going genomic instability. For example, although recent work from TCGA have demonstrated that recurrent somatic alterations occur in a small number of genes in high-grade ovarian cancers, ovarian cancer genomes are instead characterized by multiple regions of copy number gain and loss involving at least 1825 genes.

123

This genomic chaos complicates efforts to identify biologically relevant mutations critical for tumor maintenance.

One approach to identifying genes involved in cancer initiation, tumor maintenance and/or metastasis is to analyze the function of genes recurrently altered in cancer genomes by the systematic manipulation of the candidate oncogenes. Here we have used the information derived from Project Achilles, a large scale effort to identify genes essential for proliferation and survival in human cancer cell lines through the application of genome scale loss of function screens, together with genome characterization data derived from the study of high grade ovarian cancers to identify potential ovarian cancer oncogenes. Using this approach, we identified several known oncogenes as well as ID4 and used the TPN system to efficiently demonstrate that ID4 is essential for tumor maintenance. These observations provide proof-of-principle evidence that the combination of functional genomics with TPN-mediated siRNA delivery constitute a highly flexible and scalable platform for the discovery and validation of cancer targets (**Figure 4.43**).

4.3.2 Identification of *ID4* as an ovarian cancer oncogene

Mutations, amplifications and translocations involving transcription factors play a key role in the pathogenesis of hematopoetic malignancies. Indeed, the paradigm of dysregulation of differentiation, usually through the disruption of a lineage-specific transcription factor, accompanied by a constitutive proliferative signal, such as those imparted by an activated kinase oncogene, has provided a foundation for the discovery of a number of oncogenes in leukemias[248]. Although the physiologic programs that regulate differentiation in most epithelial tissues remain incompletely understood, recent work has identified a number of transcription factors that are activated in the majority of specific types of cancers, including

MITF in melanoma [249], *NKX2.1* in lung adenocarcinomas [250], *SOX2* in squamous cell lung cancers [251] and *TMPRSS2-ERG* fusions in prostate cancer [252].

Using integrated genomic approaches derived from the interrogation of hundreds of primary ovarian tumors and cell lines, we identified *ID4* as an oncogene, amplified in 32% of high grade serous ovarian cancers. In addition, *ID4* is overexpressed in a large fraction of high grade serous ovarian cancers, and ovarian cancer cell lines that overexpress ID4 are highly dependent on ID4 for survival and tumorigenicity. Expression of ID4 at levels corresponding to those observed in patient derived samples in either immortalized ovarian epithelial or fallopian tube epithelial cells induces cell transformation. These observations credential ID4 as a bona fide ovarian cancer oncogene and suggest that ID4 is one of a growing class of lineage-restricted transcriptional factor oncogenes in human epithelial cancers.

Like other ID family proteins, ID4 binds to and regulates the activity of E protein transcription factors such as E2A and HEB. Indeed, we found that ID4 regulates cell proliferation in part through its effects on p21$^{WAF1/CIP1}$. In addition, when we generated an expression signature corresponding to ID4 in ovarian epithelial cells, we found that the transcriptional program induced by ID4 was similar to that induced by *HOXA9*. Although it is clear that *ID4* regulates the expression of many genes, we found that suppression of *HOXA9* abrogated the cell transformation induced by *ID4*. ID4 has been reported to regulate differentiation of neural progenitor cells, adipocyte cells and osteoblast cells [253-257]. As a result, the majority of *Id4*-deficient mice died either *in uteri* and postnatally due to rapid weight loss and only ~20% of mice survived to adulthood with significantly smaller brain size due to diminished fraction of neural progenitor cells [253-255, 257]. HOXA9 is known to regulate normal hematopoiesis by controlling differentiation, proliferation and self-renewal [258], and

overexpression of HOXA9 or HOXA9-NUP98 in hematopoietic precursors results in the expansion of hematopoietic stem cells and promotes the development of leukemias in a cooperative manner with MEIS1 or RAS signaling [259-260]. HOXA9 is also required for survival in the mixed lineage leukemia gene (MLL)-rearranged acute leukemias [247]. In addition, *HOXA* genes have been shown to play essential roles in specifying regional differentiation of mullerian duct into oviduct, uterus, cervix and vagina [261]. Therefore, our observations suggest that ID4 expression may contribute to transformation by affecting both $p21^{WAF1/CIP1}$ and HOXA9 transcriptional programs that affect differentiation and proliferation and contribute to the development of ovarian cancer.

Although prior work has shown that manipulation of the expression of ID1, ID2 or ID3 induces compensatory changes in the expression of the other ID family members, we found that expression of ID4 but not the other ID family members induced cell transformation in ovarian epithelial cells. Since amplifications involving other *ID* family members have not been observed in ovarian cancers, this observation suggests the ID4 has a unique role in the transformation of this tissue type. Collectively, these observations suggest that inappropriate overexpression of ID4, in part by regulating the transcriptional program of *HOXA9*, alters the physiologic differentiation program of the ovary.

4.3.3 Development of tumor penetrating nanoparticles

To credential a novel oncogene as a therapeutic target, both *in vitro* and *in vivo* perturbation of tumor cells harboring the gene product is required (**Figure 4.43**). Achieving this goal, particularly in an established, disseminated tumor, is facilitated by efficient, targeted delivery accompanied by significant tissue penetration. Here we show that a myristoylated tandem peptide (TP-LyP-1) with both a membrane-translocating domain and a tumor-penetrating

domain condenses siRNA into nanocomplexes that, upon systemic administration into ovarian tumor-bearing mice, penetrates the tumor parenchyma and silences a novel ovarian oncogene, *ID4*, in a receptor-specific manner. Treatment with TPN/si*ID4* over time led to a complete growth suppression of ovarian tumors and a significant survival improvement in mice.

The systematic delivery of siRNA to achieve suppression in animals continues to represent a major barrier to the development of nucleic acid-based therapeutics. Many different approaches have been explored extensively with a primary focus on developing strategies that will achieve silencing in patients [7]. To enable the genomic discovery pipeline outlined (**Figure 4.43**), we favored a strategy that was modular, tumor-specific, and tumor-penetrating. Importantly, the TPNs are biodegradable and did not elicit innate immune responses upon systemic delivery, enabling repeated administration for tumor regression studies. Moreover, the TPN system extravasates from the vasculature and moves through the tumor extracellular matrix to delivery siRNA to specific parenchymal cancer cells.

Other methods for siRNA delivery include covalent coupling of siRNA to carriers and therefore require specialized chemically-reactive siRNA and additional purification steps in the formulation process, rendering this approach less amenable to the modular 'mix and dose' paradigm motivated by the volume of emerging genomic targets [127, 132, 212]. Targeted siRNA delivery approaches have been reported for specialized populations of cells such as immune cells [134, 140, 165], neurons via viral mimicry [166], and hepatocytes by leveraging LDL trafficking and vitamin A uptake [126, 142]; however, these methods cannot easily be generalized across tissue types as would be necessary in the study of aberrant cancer genomes.

Elsewhere, siRNA has been targeted to tumors; however, not in a tumor-penetrating fashion [151, 262]. As described earlier, tumor penetration is a longstanding challenge in cancer

delivery. As an alternative to crossing the vascular wall to achieve tumor penetration, tumor endothelium has instead been targeted using RGD-targeted nanoparticles [262]; however, this approach does not enable silencing in parenchymal tumor cells, such as those identified with genetic alterations in TCGA [34, 226]. Passive targeting (e.g. EPR) of siRNA in neutral liposomes or transferrin-targeted cyclodextrin has also been described in mouse models and recently in humans, but tumor penetration remains a challenge [145, 159]. The importance of tumor penetration is not merely a theoretical constraint. In fact, studies with small molecules and antibody-based therapeutics indicate that reducing tumor transport barriers via permeability enhancement or inhibition of hedgehog signalling can have profound consequences on the penetration, accumulation, and ultimately efficacy [107, 115, 119, 263].

The modularity in our siRNA delivery platform enables the potential for leveraging other homing peptides selected from phage-displayed libraries, such as new discoveries in amplified vascular transportation of CendR ligands, thereby expanding the number and type of parenchymal tumor cells that can be accessed by TPNs. Herein, human ovarian cancer cells that overexpress ID4 were highly sensitive to TPN-mediated suppression of ID4, and tumor-penetrating delivery of *ID4*-siRNA produced powerful antitumor effects against orthotopically implanted ovarian tumors. Since ID4 cannot be inhibited by means of small-molecule inhibitors or monoclonal antibodies, this technology represents an important therapeutic paradigm for systemic targeting of undruggable proteins that are essential in tumor maintenance.

4.3.4 Wider Implications

Although focused on ID4, the specific delivery technology reported here can be generalized to other cancers. The surface expression of p32, the receptor targeted by our nanocomplex, was examined in 81 different human tumors from 11 different tumor types.

Approximately 60 of the 81 samples across 10 tumor types scored positive to p32 [217]. The technology is also readily adaptable to other siRNA cargo, as we reproduced prior work on another target, claudin-3 (CLDN-3), using this same experimental platform (data not shown). This study provides evidence that TPN can be used as a facile system to evaluate the consequences of manipulating putative oncogenes on tumor maintenance *in vivo*.

More generally, the integration of on-going cancer genome characterization efforts with similarly comprehensive functional studies will narrow the number of potential cancer targets but will still nominate a large number of genes that will require *in vivo* studies to validate their role in tumor initiation or maintenance. These TPNs when combined with genomic studies illustrate an efficient platform to functionally characterize the genes found to be altered in tumors and to identify and validate the subset of such genes critical to cancer initiation and maintenance. As such, these studies provide one path to bypassing a critical bottleneck in identifying and credentialing genes involved in cancer.

Although it is clear that further mechanistic studies, such as those presented here that identified HOXA9 as a target of ID4, will be necessary to understand the biology of new oncogenes, only a fraction of such candidates will be amenable to target by traditional small molecule chemistry or antibodies. Theoretically, RNAi provides a means to both assess and act on novel candidate oncogenes but targeted delivery of siRNA remains a challenging barrier. Although further work will be necessary to validate TPNs as a therapeutic delivery vehicle, these studies demonstrate that these TPNs exhibit both specificity and pharmacokinetic properties that may provide a platform for siRNA delivery in humans.
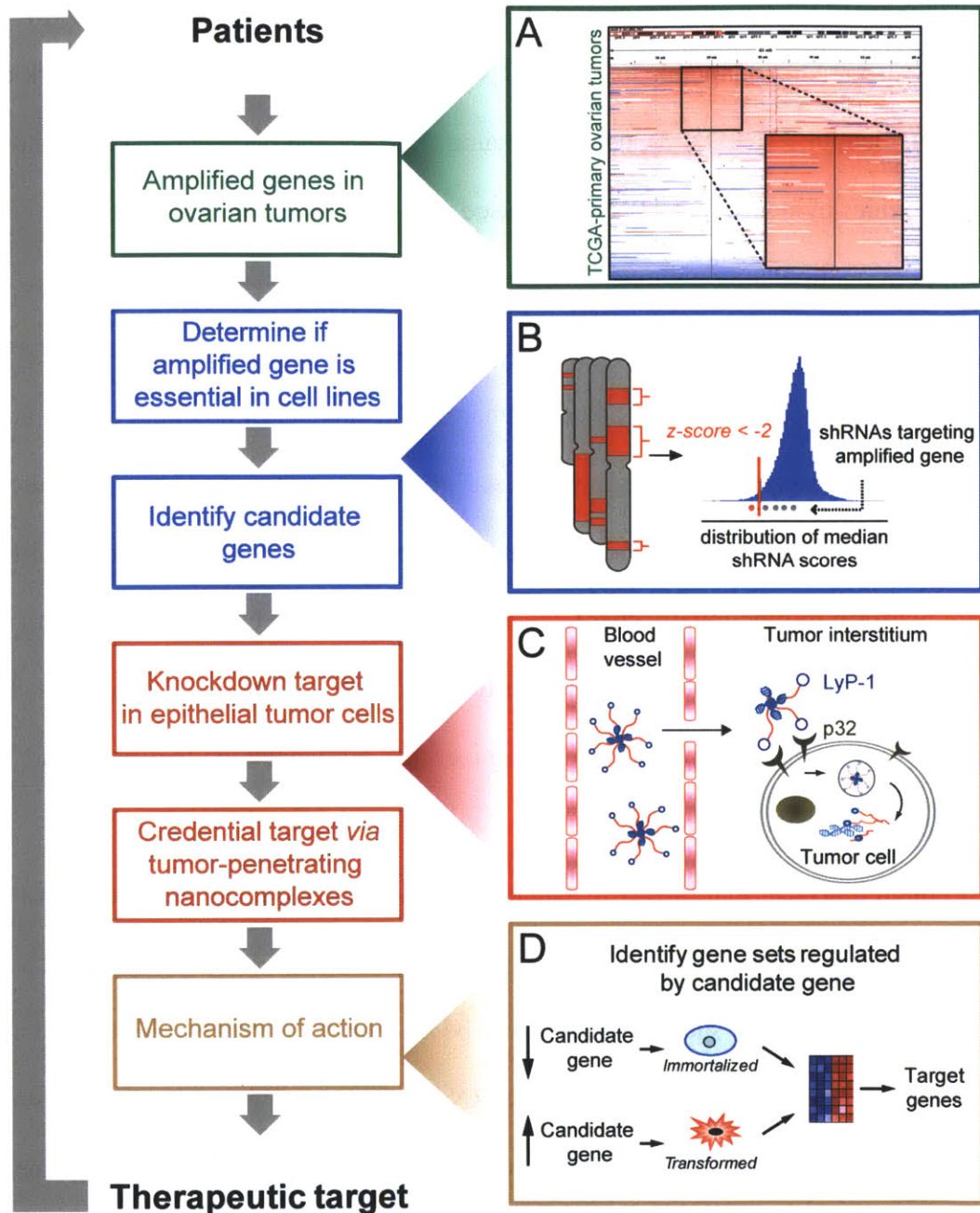
Figure 4.43. An integrated platform to credential oncogenes *in vivo*. (A) Structural genomic analyses of tumors from patients. **(B)** Schematic of ovarian-amplified gene analysis. Distribution (blue bars) of median shRNA scores are shown in cell lines that harbor copy number gain of a given gene. shRNAs targeting the amplified gene (dots) are considered significant (red) if z-score < -2. Analysis was repeated for each of 1825 amplified genes. **(C)** Development of a tumor-penetrating siRNA nanocomplex (TPN) to deliver siRNA to tumor cells in a receptor-specific manner and validates gene targets in mouse models. **(D)** Follow-up studies to identify the mechanism of transformation and establish novel therapeutic targets

130

4.4 Conclusion

In this work, we developed a targeted tumor-penetrating nanocomplex capable of precisely delivering siRNA deep into the tumor parenchyma, and have combined this technology with large scale methods to interrogate the function of genes in cancer genomes to credential *ID4* as an oncogene target in ovarian cancer by studying preclinical disease models. Nanocomplexes comprised of TP-LyP1 tandem peptides and *ID4* siRNA were able to potently impede the growth of aggressive, metastatic ovarian tumors. The role of tumor homing in this system stands in marked contrast to other *in vivo* siRNA delivery methods that lack tumor penetration domains [128-129, 159, 264], systems that require direct conjugation and custom synthesis [162, 212], and carriers where target cells cannot be molecularly specified [126, 151, 245]. Furthermore, by leveraging new discoveries for amplification of transvascular transport through a diversity of novel tumor-penetrating ligands, the tumor and membrane penetrating domains of this tandem peptide platform can be varied independently, enabling broad access of parenchymal tumor cells to RNA-based therapeutics. As large scale efforts to characterize all cancer genomes accelerate, this capability illustrate a path to identify genes found to be altered in tumors, validate those that are critical to cancer initiation and maintenance, and rapidly evaluate *in vivo* the subset of such genes amenable to RNAi therapies and clinical translation.

5 Cancer Vulnerabilities Unveiled by Genomic Loss

5.0 Abstract

Genome instability is a common feature of many cancers and leads to extensive somatic copy number alterations. As a result, most cancers exhibit loss of substantial fractions of their genomes, including regions containing known tumor suppressor genes and collateral loss of many other genes. Here we performed an integrated genomic analysis to identify novel cancer-specific vulnerabilities that result from copy number loss of genes irrespective of tumor suppressor activity. For 6,085 genes, we correlated partial copy number loss to the anti-proliferative effect of expressing shRNAs targeting that gene in 86 cancer cell lines. We identified 102 genes for which suppression of the gene specifically inhibited the proliferation of cells with partial copy loss of that gene. This class of CYCLOPS (Copy number alterations Yielding Cancer Liabilities Owing to Partial losS) genes is enriched for multiple components of the spliceosome and proteasome. One CYCLOPS gene, *PSMC2*, encodes an essential member of the 19S proteasome regulatory complex, which is normally not limiting for 19S complex assembly. The excess PSMC2 resides in a known complex that also contains PSMC1, PSMD2, and PSMD5, and serves as a buffer that enables cells to maintain a functional 26S proteasome after partial copy number loss or experimental suppression of PSMC2. Cells that harbor partial *PSMC2* copy number loss lack this reservoir and are exquisitely sensitive to further suppression of *PSMC2* both *in vitro* and *in vivo*. These observations define a new class of cancer specific liabilities predicted by partial copy number loss and provide a novel strategy to target the consequences of genome instability in cancer.

(Reprinted with permission from [265])

5.1 Introduction

Cancers arise as the result of the accumulation of somatic genetic alterations within a cell, including chromosome translocations, single base substitutions, and copy number alterations [266-267]. Although a subset of these alterations ("driver events") promote malignant transformation by activating oncogenes or inactivating tumor suppressor genes, most somatic genetic alterations are the consequence of increased genomic instability that occurs in cancer but do not contribute to tumor development ("passenger events"). The demonstration that cancers are often dependent on specific driver oncogenes has stimulated efforts to find and exploit these targets therapeutically. For example, cancers that harbor acquired translocations (such as *BCR-ABL* or *EML4-ALK*) [268-269] or mutations (such as *EGFR* or *BRAF*) [270-271] depend on the activity of these gene products for tumor maintenance. Therefore, the presence of such an alteration often predicts response to drugs that inhibit the function of these proteins.

An alternative strategy to target cancers is to target genes that are not oncogenes, but which cancers require to accommodate cancer-specific stress [272]. In comparison to normal cells, cancer cells exhibit a variety of stress, including DNA damage replication stress, proteotoxic stress, mitotic stress, metabolic stress, and oxidative stress. Therefore, cancers rely inordinately on pathways that abrogate such stress [273]. Even though proteins within stress support pathways may be essential in all cells, pharmacologic inhibition can still create a therapeutic window as a result of a cancer stress phenotype [273-274].

The proteasome, which recognizes and degrades proteins that possess a poly-ubiquitin post-translational modification, is one such target [275]. The 26S proteasome is responsible for basal protein turnover, degradation of excess and unfolded proteins, and regulation of concentrations of key regulatory proteins. The 26S proteasome is composed of a 20S catalytic

complex and a 19S regulatory complex. One function of the19S complex is to recognize poly-ubiquitin modified substrates and regulate access to the 20S catalytic sites. The 19S complex contains at least 19 proteins that are further divided into a base (9 proteins) and lid (10 proteins) [276]. Prior to assembly, the 9 components of the base are divided into three modules, each containing three components. Each module also contains a different chaperone protein that catalyzes the hierarchical assembly of the 19S base. The chaperone proteins and each of the nine 19S complex base components are essential to form a functional 19S complex and reconstitute the 26S proteasome [277]. Although proteasome function is essential in all cells, multiple myeloma (MM) cells produce and secrete excessive amounts of immunoglobulin and are especially dependent on effective protein turnover by the 26S proteasome. As a result, MM is exquisitely sensitive to the 20S proteasome inhibitor, bortezomib (Velcade), which is now used in the clinical treatment of MM [278].

Despite these advances, many non-kinase oncogenes (*RAS, MYC*) and tumor suppressors (*ARF, TP53*) are still difficult to target with existing drugs. To identify new vulnerabilities in cancer, an alternative approach is to target the effects of genomic alterations on non-cancer genes that are the consequence of either driver or passenger events. For example, driver events such as copy number losses of tumor suppressor genes often involve multiple neighboring genes that are not necessarily involved in oncogenesis; the relative loss of essential genes could in turn cause a deficiency in essential cellular processes, rendering cells highly vulnerable to further suppression of those genes. Targeting such genes have been postulated to render cancer cells highly vulnerable to further suppression or inhibition of those genes [279].

Here, we integrated both genome scale copy number and loss of function data on a panel of 86 cancer cell lines to determine if partial copy number loss of specific genes renders cells

highly dependent on the remaining copy. We identified a class of genes, enriched in proteasome and spliceosome components that render cells that harbor copy number loss highly dependent on the expression of the remaining copy.

5.2 Results

5.2.1 Identification of essential and haplosufficient genes

When we analyzed copy-number profiles from 3,131 cancers across several dozen histologic types, we found that 50% of cancers exhibit copy-number loss affecting at least 11% of the genome and many cancers exhibit much more extensive loss (**Figure 5.1A**). Much of this widespread genomic disruption is due to copy number alterations of whole chromosomes or chromosome arms (**Figure 5.1B**). As a consequence, most genes undergo copy-number loss in a substantial fraction of cancers. While some of these are likely "driver" genes whose loss contributes to malignant transformation, others are unlikely to contribute to cancer development. Copy number loss of non-driver genes often results from involvement in a passenger event; in other cases non-driver genes are recurrently lost because of their proximity to a frequently deleted tumor suppressor gene (**Figure 5.2**). We therefore hypothesized that for a subset of non-driver genes, hemizygous loss may be tolerated and frequent but complete loss would lead to cell death. In some of these cases, hemizygous loss might lead to sensitivity to further inhibition of the gene relative to cells that harbor two copies of these genes.

To identify genes whose loss correlated with a greater sensitivity to further gene suppression, we integrated gene dependencies and copy-number data from 86 cell lines. Specifically, we analyzed gene essentiality data from Project Achilles, a dataset derived from

screening 102 cell lines with a shRNA library composed of 55,000 shRNAs targeting 11,194 genes [48]. In parallel, we determined DNA copy-numbers for these same cells. For each gene, we classified each cell line as either copy-number loss or being copy-neutral, calculated the mean gene dependency score among cell lines in each group, and determined the difference in mean scores between the copy-loss and copy-neutral groups. Of the 102 candidate genes identified (FDR p-value < 0.25) (**Table 5.1**), also known as Copy-number alterations Yielding Cancer Liabilities Owing to Partial losS (*CYCLOPS*) genes, proteasome- and spliceosome-related pathways were particularly enriched. Both of these pathways involve macromolecular complexes that perform obligate cellular functions.

The highest ranked *CYCOPS* candidate was *PSMC2*, which encodes an ATPase AAA domain containing protein that is an essential component of the 19S proteasome regulatory complex. To study the effect of *PSMC2* loss on PSMC2 protein levels, we evaluated PSMC2 levels in IOSE cells and ten ovarian cancer cell lines, including five $PSMC2^{Neutral}$ and five $PSMC2^{Loss}$ lines. All five $PSMC2^{Loss}$ cell lines expressed lower levels of PSMC2 than others (**Figure 5.3A**). Since PSMC2 is essential for cell proliferation, we concluded that $PSMC2^{Neutral}$ cells either require more PSMC2, or produce more PSMC2 than is required. We therefore investigated whether $PSMC2^{Neutral}$ cells can tolerate greater suppression of PSMC2 expression.

We found that the anti-proliferative effect of suppressing *PSMC2* was highly specific to cells with copy number loss involving *PSMC2* ($PSMC2^{Loss}$), but not in cells that harbor both copies of *PSMC2* ($PSMC2^{neutral}$) (**Figure 5.4**). Specifically, in OVCAR-8 ($PSMC2^{Loss}$) and A2780 ($PSMC2^{Neutral}$) cells that express PSMC2-specific shRNA under the control of a doxycycline-regulated promoter (hereafter described as the *PSMC2* inducible shRNA system) (**Figure 5.3B**), the addition of doxycycline led to the suppression of PMSC2 in both OVCAR-8

and A2780 cells, but only affected the viability of OVCAR-8 cells (**Figure 5.4**). The magnitude

of the anti-proliferative effect is dependent on the amount of PSMC2 suppression: A2780 cells

proliferated until 60% of PSMCS2 was depleted while OVCAR8 cells exhibited cell death when

we achieved only 20% suppression of PSMC2 (**Figure 5.4**). Based on these observations, we

concluded that higher levels of PSMC2 in A2780 cells do not reflect an increased requirement

for PSMC2, but instead constitute a "reservoir" of PSMC2.

A

B
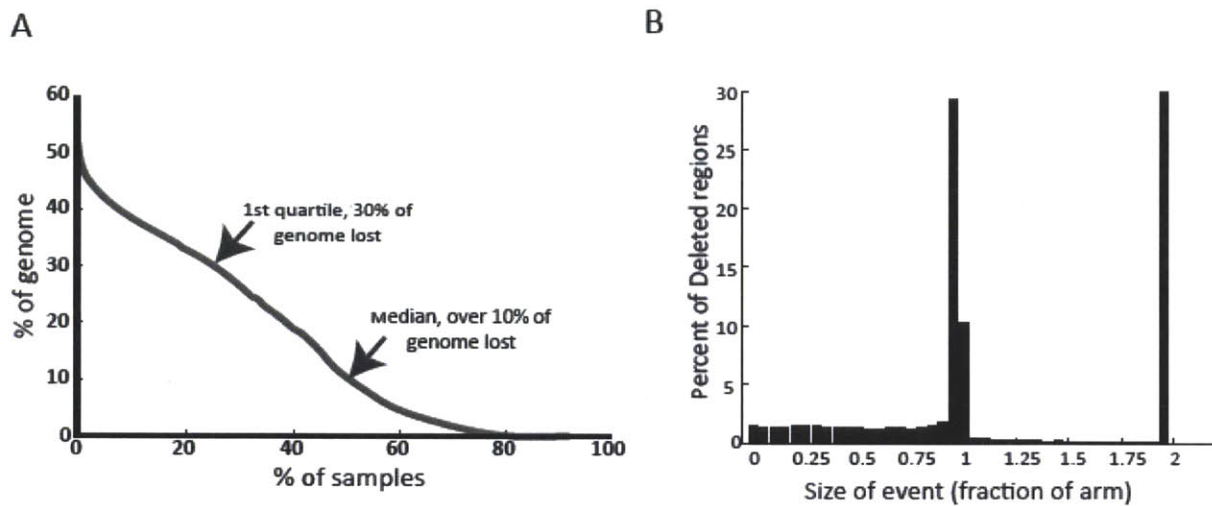
Figure 5.1. The identification of *CYCLOPS* genes amongst the genes that undergo copy number loss in cancer. **(A)** The percentage of the cancer genome that undergoes copy number loss. **(B)** The size of genomic deletions that result in copy number loss in cancer genomes. The length of individual deletions (as a fraction of the chromosome arm where they occur) was determined as previously described.
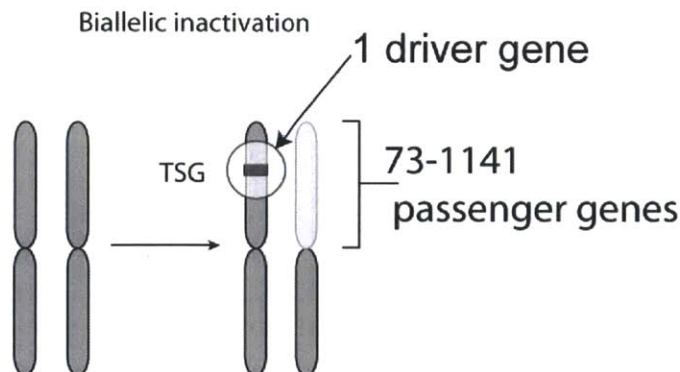
Figure 5.2. Schematic describing one mechanism by which tumor suppressor gene inactivation results in partial loss of non-driver genes. Tumor suppressors often require bi-allelic inactivation for tumor initiation or maintenance. Here, one allele is lost as a result of an alteration that affects a small genomic region that includes the tumor suppressor gene (in red). The second allele is lost as a result of chromosome arm loss, leading to complete tumor suppressor inactivation.

A

PSMC2^Neutral   PSMC2^Loss

IOSE, IGROV, A2780, RKN, TYKNU, COV434, OVISE, RMGI, SKOV3, OVCAR8, HEYA8

PSMC2

A-tubulin

B

shLacZ, shRNA2, shLacZ, shRNA2, shLacZ, shRNA2, shRNA3, shLacZ, shRNA2, shRNA3

Dox   − − + +   − − − + + +

PSMC2

βActin
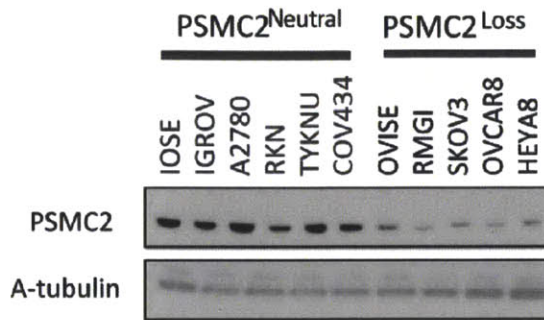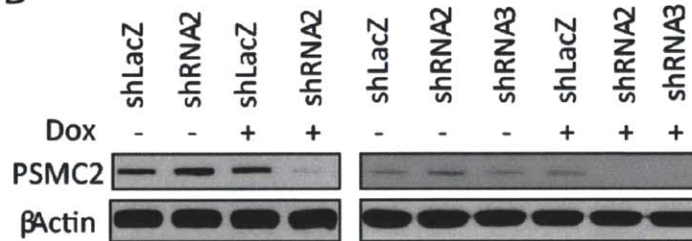
Figure 5.3. Expression of PSMC2 in ovarian cancer cell lines. (A) PSMC2 levels in ovarian cancer cell lines. Lysates collected from ten ovarian cancer lines and one immortalized ovarian surface epithelial cell line (IOSE) were analyzed by immunoblot. Cell lines with partial PSMC2 copy number loss are indicated. **(B)** PSMC2 levels in cells that express an inducible shRNA that targets PSMC2.

Correlation between PSMC2 mRNA and the proliferation of A2780 cells

Correlation between PSMC2 mRNA and the proliferation of OVCAR8 cells

■ PSMC2 mRNA
□ Proliferation
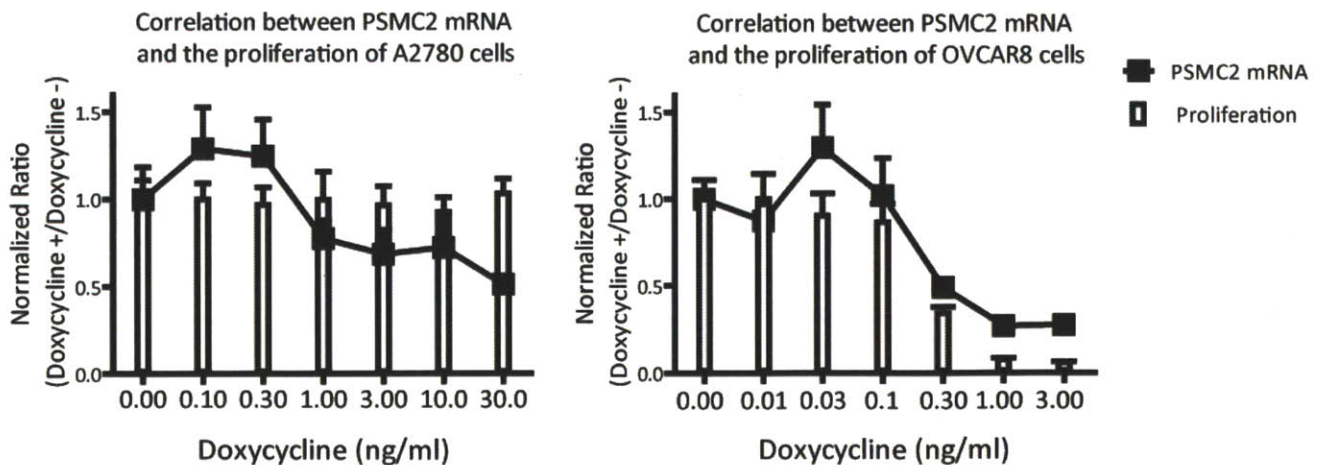
Figure 5.4. A non-linear relationship between PSMC2 levels and proliferation of ovarian cancer cells. A2780 (Left) and OVCAR-8 (Right) cells were cultured in varying concentrations of doxycycline. Cells were collected three days after to assess the levels of *PSMC2* mRNA by qPCR. In parallel, cell proliferation was determined and normalized to the untreated samples.

Table 5.1. A list of genes that exhibit "Copy-number alterations Yielding Cancer Liabilities Owing to Partial losS".

Rank	Gene	Mean Difference	P value (FDR)
1	PSMC2	-2.07	0.01
1	TXN	-1.12	0.01
1	RPS15	-1.12	0.01
1	PHF5A	-0.76	0.01
5	PABPN1	-0.87	0.01
6	SMU1	-1.09	0.01
7	POLR2A	-0.93	0.01
8	NUP54	-0.61	0.02
9	PAFAH1B1	-1.29	0.02
10	ATP6V0A1	-1.01	0.03
11	RBX1	-0.57	0.03
12	CKAP5	-1.37	0.03
13	USPL1	-0.86	0.03
14	PRSS23	-0.44	0.03
15	PCNA	-1.19	0.04
16	TXNRD2	-0.39	0.05
17	SF3A2	-0.62	0.05
18	EEF1A1	-1.01	0.06
19	SMC2	-0.89	0.06
20	GUCY1A2	-0.91	0.06
21	PSMD11	-1.15	0.06
22	FOXD4L4	-0.96	0.06
23	POLR2F	-0.76	0.08
24	OR52I2	-0.50	0.09
25	USP8	-0.63	0.11
26	PRPF8	-0.57	0.11
27	FBXO7	-0.25	0.13
28	CTDSPL	-0.56	0.15
29	ANAPC10	-0.38	0.15
30	LSM6	-0.99	0.15
31	COPS8	-0.94	0.15
32	RIOK1	-0.96	0.16
33	ALDH2	-0.49	0.16
34	PSMD13	-0.70	0.16
35	ZNF25	-0.52	0.16
36	CSF3R	-0.56	0.16
37	NUTF2	-0.84	0.16
38	EIF2B2	-0.68	0.16
39	BMP8A	-0.55	0.16
40	NUPL1	-0.62	0.17
41	EEF2	-0.63	0.18
42	SNRPD3	-0.91	0.19
43	CPT1B	-0.43	0.19
44	LSM7	-0.52	0.22
45	PRPSAP2	-0.37	0.23
46	MAD1L1	-0.59	0.25
47	PREP	-0.30	0.25

5.2.2 The reduction of PSMC2 levels inhibits tumor growth

To explore the therapeutic potential of *PSMC2* suppression *in vivo*, we tested the

consequences of suppressing PSMC2 in xenograft ovarian tumors. Specifically, we utilized a

nanoparticle-based delivery system developed in *Chapter 3* that can penetrate into the tumor

parenchyma and deliver siRNA payloads to select tumor cells expressing p32 [213]. We

generated tumor-penetrating nanocomplexes (TPN) consisting of *PSMC2*-specific siRNAs non-

covalently bound to TP-LyP-1 tandem peptides.

We first assessed the compatibility of cell lines with TPN-targeted delivery of siRNA by

surveying cells for surface expression of p32, the cognate receptor for the tumor-specific

domain, LyP-1. Both OVCAR8 (*PSMC2^{Loss}*) and A2780 (*PSMC2^{Neutral}*) cells, but not a normal

ovarian epithelial cell line (IOSE), exhibited elevated cell surface p32 expression as assessed by

flow cytometry (**Figure 5.5**). To ascertain whether p32 expression correlated with selective TPN

uptake, we quantified by flow cytometry TPN-mediated delivery of fluorescently-labeled siRNA

into the cytosol. We observed significant accumulation of siRNA in both OVCAR8 and A2780

cells, but not in IOSE. Further, TPN-mediated siRNA delivery is p32 receptor-specific; a

monoclonal antibody directed against p32 (mAb 60.11) abrogated TPN uptake (**Figure 5.6**),

whereas an isotype-matched control antibody had no effect. To confirm suppression of *PSMC2*

using TPN *in vitro*, we investigated the effects of *PSMC2*-specific siRNA on the proliferation of

PSMC2^{Loss} and *PSMC2^{Neutral}* cells. Treatment with TPN carrying siRNAs targeting non-

overlapping exons of *PSMC2* mRNA resulted in reduction of PSMC2 protein levels in both

OVCAR8 and A2780 cells. This reduction was associated with a corresponding decrease in

proliferation only in OVCAR8 cells (**Figure 5.7**).

To probe the therapeutic effects of PSMC2 inhibition *in vivo*, mice harboring orthotopic OVCAR8 (*PSMC2^{Loss}*) tumor xenografts expressing firefly luciferase were injected with TPN carrying *PSMC2*-siRNA (1 mg siRNA/kg/injection) intraperitoneally every 3 days for 14 days. Repeated administrations of *PSMC2*-siRNA, but not a scrambled control siRNA (si*Ctrl*), led to a significant reduction in PSMC2 levels in the tumor (**Figure 5.8**), resulting in over 75% suppression of the overall growth of OVCAR8 (*PSMC2^{Loss}*) tumors over time (**Figure 5.9A**). To confirm that the therapeutic effect were due to sequence-specific RNAi, we performed an *in vivo* therapeutic rescue experiment using orthotopic tumor xenografts from OVCAR8 cells expressing an *N*-terminal V5-tagged form of PSMC2. V5-PSMC2 expression in OVCAR8 cells rescued the expression of PSMC2 after *in vivo* treatment of nanocomplexes targeting the p32 receptor and carrying *PSMC2*-specific siRNA. In the setting of ectopic PSMC2 expression, TPN/si*PSMC2* injections every 3 days for 21 days (1 mg siRNA/kg/injection) failed to suppress tumor growth, confirming that the therapeutic benefits in the presence of TPN/si*PSMC2* was due to the reduction of PSMC2 levels in *PSMC2^{Loss}* tumor cells (**Figure 5.9B**).

To directly assess whether the sensitivity in PSMC2^{Loss} to TPN/si*PSMC2 in vivo* is the direct result of decreased PSMC2 expression, we measured their efficacy in isogenic xenografts generated from *PSMC2^{Neutral}* cells engineered to inducibly express *PSMC2*-shRNAs. Specifically, we established orthotopic A2780 (*PSMC2^{Neutral}*) tumors expressing *PSMC2*-specific shRNAs under the control of a doxycycline regulated promoter, confirmed tumor establishment by bioluminescence imaging, and initiated twice weekly treatments of TPN/si*PSMC2* for 2 weeks (1 mg siRNA/kg/injection). In contrast to OVCAR-8 tumors, PSMC2 suppression *in vivo* did not show efficacy in A2780 cells without doxycycline induction, consistent with the *in vitro*

finding that A2780 cell proliferation is insensitive to PSMC2 suppression, owing to the presence of a buffer from excess PSMC2 protein (**Figure 5.10**).

The induction of *PSMC2*-shRNAs by doxycycline in A2780 (*PSMC2^{Neutral}*) tumors did not significantly abolish tumor initiation or growth, consistent with the model that a reduced PSMC2 level is still sufficient for tumorigenesis. However, doxycycline does sensitize A2780 (*PSMC2^{Neutral}*) tumors to further PSMC2 reduction. The combination of doxycycline and TPN/si*PSMC2* reduced tumor growth and significantly improved overall survival (median survival = 33 d), with 3 out of 7 mice surviving after 42 days (**Figure 5.11**). In contrast, mice that received doxycycline but TPN carrying a control siRNA (TPN/siGFP) grew uninhibited, with all 6 animals of the cohort succumbed to tumors within 20 days (median survival = 16 d). Collectively, these findings validate the therapeutic efficacy of PSMC2 suppression *in vivo*, and support the theory that *PSMC2^{Loss}* cells are specifically sensitive to suppression of PSMC2 through decreased basal levels of *PSMC2* mRNA.
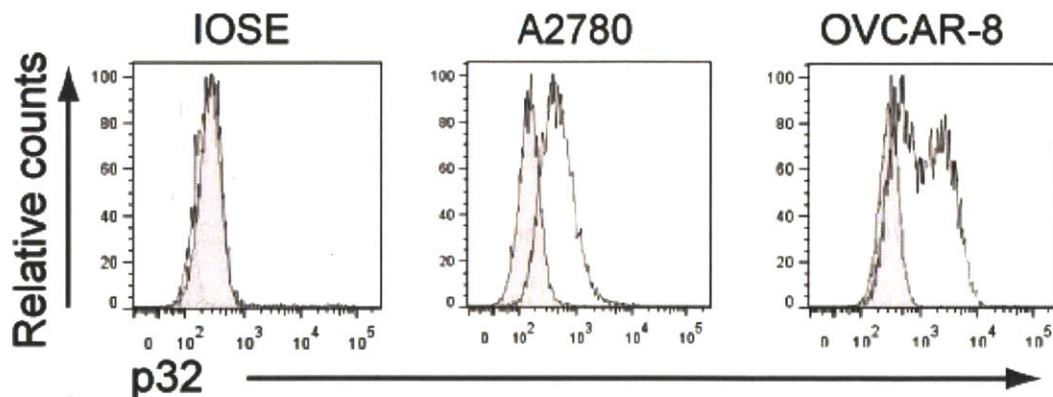
Figure 5.5. Surface expression of p32, the cognate receptor for TPN. Immortalized ovarian surface epithelial (IOSE) cells and two ovarian cancer cell lines (A2780 and OVCAR-8) were examined by flow cytometry for overexpression of p32 receptor on the surface. Isotype-matched control are shown in gray.
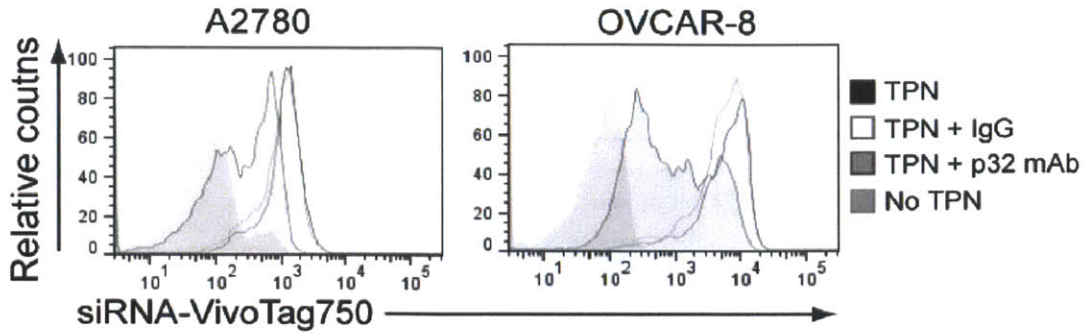
Figure 5.6. Uptake of TPN in A2780 and OVCAR-8 cells. Ovarian cancer cell lines are incubated with TPN carrying siRNA labeled with a near-infrared fluorophore (VivoTag750) and cellular uptake was assessed by flow cytometry. To probe the receptor-specificity of TPN uptake, a monoclonal antibody against p32 (p32 mAb) was added along with TPN (red). Control cells received an isotype-matched antibody (gray).
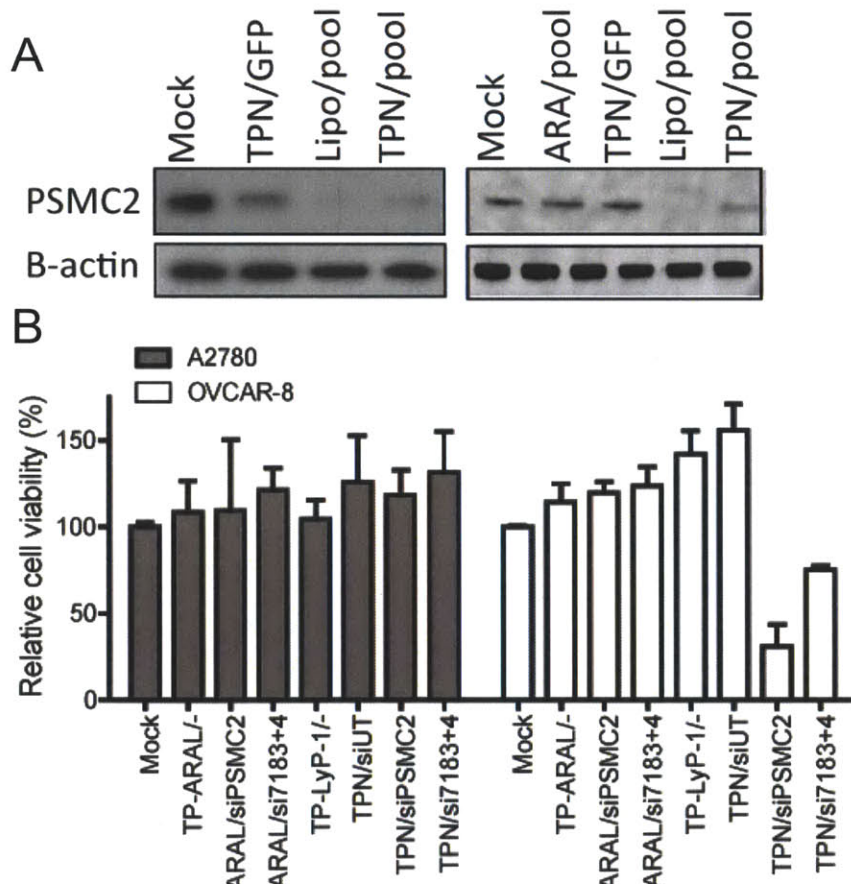
Figure 5.7. TPN suppression of PSMC2 in ovarian cancer cell lines impact their viability. (A) Immunoblots of PSMC2 levels after treatment with TPN carrying a pool of PSMC2-specific siRNAs. Control cells received TPN carrying a control siRNA (GFP), lipofectamine carrying PSMC2-siRNA, or untargeted control nanocomplexes (ARAL) carrying PSMC2-siRNA. **(B)** A2780 and OVCAR-8 cellular proliferation measured by total ATP content after treatment with indicated TPN formulations.
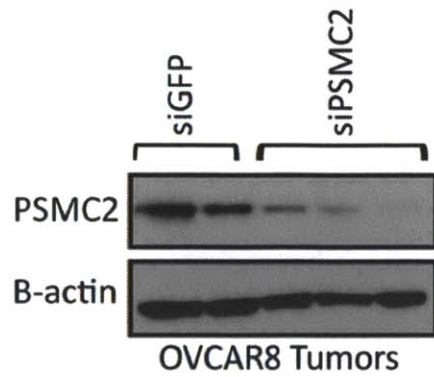
Figure 5.8. Immunoblotting of lysates from residual OVCAR-8 tumors. β-actin was used as the loading control.
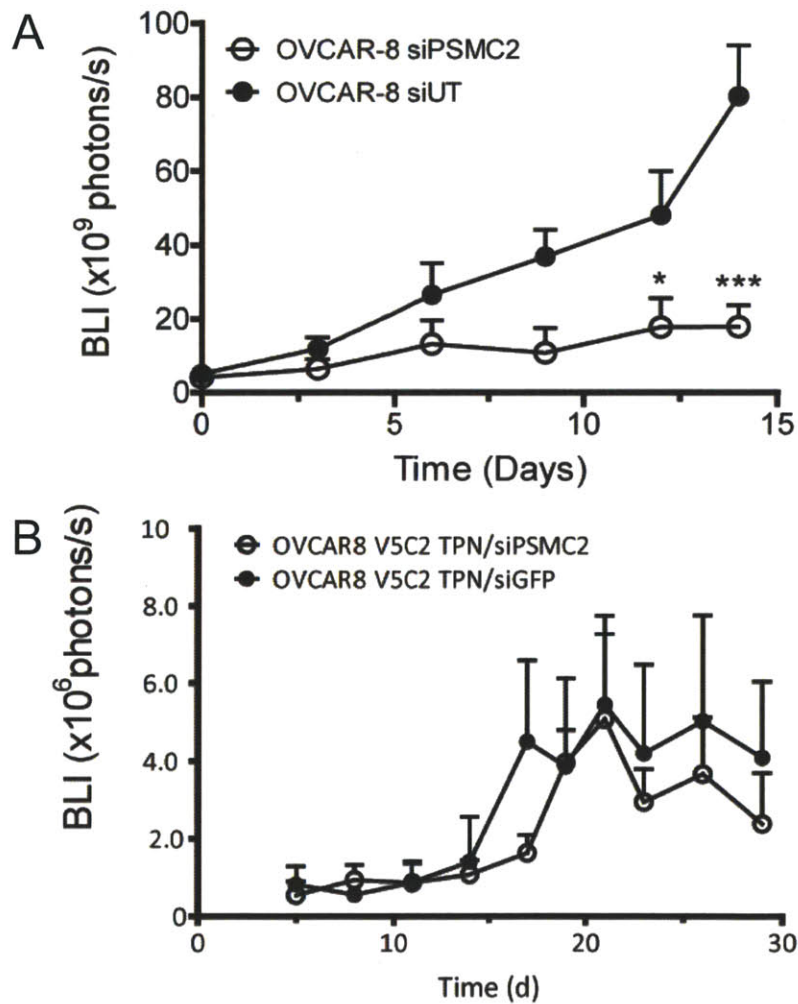
Figure 5.9. Therapeutic effects of PSMC2 suppression in mice bearing orthotopic OVCAR-8 xenograft tumors. (A) Tumor burden over time in mice treated with TPN/siPSMC2. $*p<0.05$, $***p<0.001$, by one-way ANOVA. **(B)** Tumor burden over time in mice bearing orthotopic tumors derived from OVCAR-8 cells expressing a V5-tagged PSMC2.
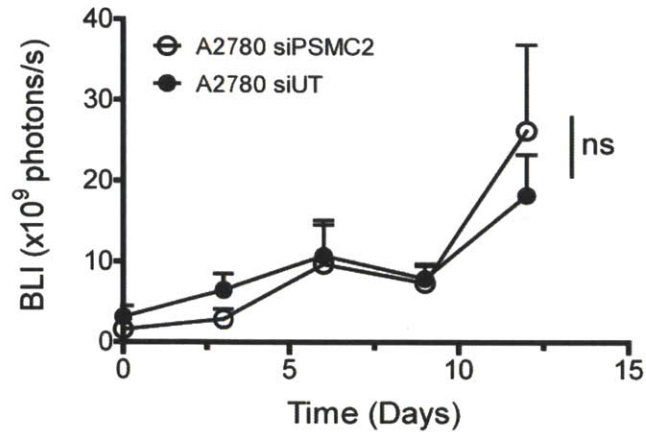
Figure 5.10. Therapeutic effects of PSMC2 suppression in mice bearing A2780 orthotopic ovarian tumor xenografts. Mice with existing tumors were treated with TPN carrying *PSMC2*-specific siRNA and tumor burden was monitored overtime via non-invasive whole-animal bioluminescence imaging.
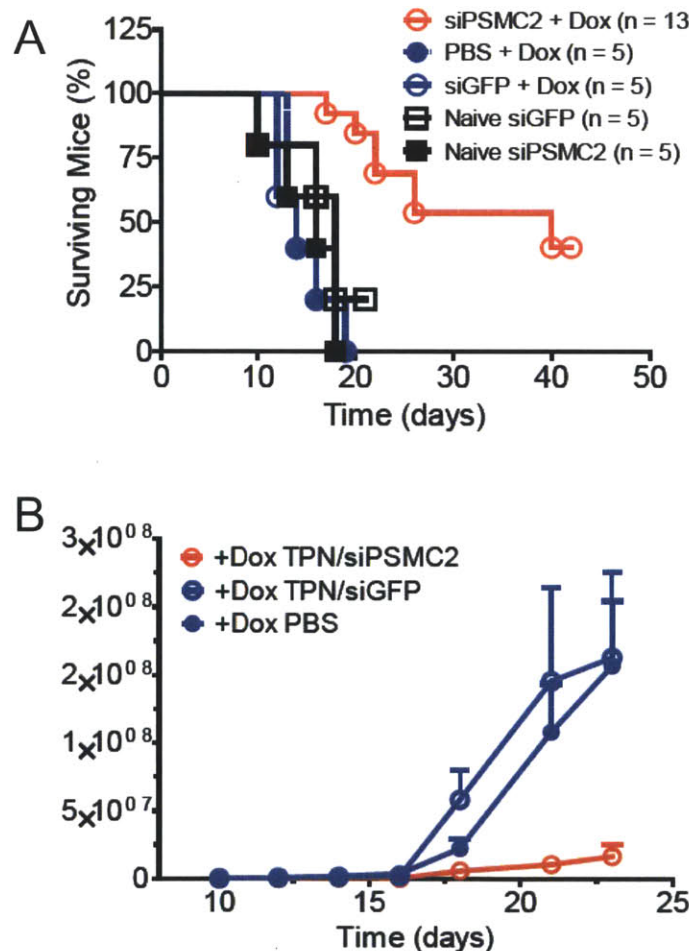
Figure 5.11. Therapeutic effects of PSMC2 suppression by TPN in the dox-inducible shRNA system. (A) Mice bearing A2780 orthotopic tumor xenografts were fed with doxycycline and treated with TPN carrying PSMC2-specific siRNA every 3 days for 20 days (n = 5). Control cohorts of received either TPN carrying GFP-specific siRNA (n = 5) or phosphate-buffered saline (PBS, n = 5). **(B)** Overall survival of mice that were fed with doxycycline and treated with TPN/siPSMC2 (sh7183 + Dox, n = 8), compared against mice that were only treated with TPN/siPSMC2 (sh7183 – Dox, n = 6).

145

5.3 Discussion

The resulted presented here suggest that hemizygous loss of *PSMC2* in particular, and *CYCLOPS* genes in general, represent a new class of cancer specific vulnerabilities. More importantly, direct inhibition of PSMC2 by RNAi suppressed the growth of ovarian tumors, suggesting that PSMC2 may be a potential therapeutic target for clinical translation.

Existing approaches to identify targeted therapeutics tend to focus on genes that drive cancer growth or diminish cancer's response to specific stresses. The suppression of *CYCLOPS* genes such as *PSMC2* does not fit into either of these categories. The partial loss of *CYCLOPS* genes, while frequently observed in cancer, is unlikely to directly promote oncogenesis. Ectopic expression of PSMC2 did not inhibit proliferation *in vitro* or tumor progression *in vivo*. Nevertheless, the copy number loss phenotype could be maintained in cancer due to mechanisms such as a "Founder" effect or inherent proximity to nearby tumor suppressors.

Targeting *CYCLOPS* genes represents an alternative approach to synthetic lethality, in which a genomic event can be identified as a non-driver vulnerability, even if no specific pathway has been negatively affected. For example, in breast and ovarian cancer cells with *BRCA1* or *BRCA2* loss, repair of damaged DNA by homologous recombination is impaired, thereby making them dependent exclusively on nucleotide-excision repair of DNA damage [280-281]. Inhibition of the DNA repair enzyme Poly (ADP-ribose) polymerase 1 (PARP1) by small molecules or siRNA [282] is effective against these BRCA-deficient cancers *via* synthetic lethality. If two events are synthetic lethal, one would expect not to find them in the same cancers. Indeed, our results show that loss of both alleles of *CYCLOPS* genes is rarely observed. Conversely, partial loss of *CYCLOPS* genes is frequently observed, indicating such partial loss is tolerated. This suggests a potential alternative path to identify *CYCLOPS* and similar

vulnerabilities in cancer cells: investigate cancer genomes for combinations of events that are significantly underrepresented, under the hypothesis that the low frequencies of these combinations reflect the effects of negative selection.

PSMC2 is an essential component of the 19S regulatory proteasome. Standard proteasome inhibitors such as bortezomib have shown significant clinical activity and low toxicity in several cancers, suggesting that a therapeutic window exists in targeting *CYCLOPS* genes that are also part of the proteasome complex. Furthermore, standard proteasome inhibitors do not fully take advantage of *CYCLOPS* -associated vulnerabilities, as *PSMC2* copy number loss does not dramatically affect the amount or activity of the 26S proteasome. In contrast, inhibition of *PSMC2* by small interfering RNAs exhausted a surplus of a requisite precursor and inhibited proteasome function *in vitro* and *in vivo*. Recently, siRNAs have also been recently utilized to discriminate and target closely related isoforms of an essential glycolytic enzyme to induce tumor regression [283]. Together, RNAi provides a tool to assess and act on candidates that not only include classic oncogenes, but also genes that result from unstable genomes that do not necessarily contribute to a malignant phenotype.

In this work, the tumor-penetrating delivery of siRNA targeting *PSMC2* resulted in a significant reduction of PSMC2 *in vivo* and inhibited the growth of tumors that harbored copy number loss of *PSMC2*. Importantly, a preclinical therapeutic trial with systemic administrations of TPN/si*PSMC2* over 20 days was associated with minimal toxicity in animals. The delivery system is highly modular; other tumor-penetrating ligands and siRNA cargo can be varied with ease. Therefore, as genomic efforts unveil more *CYCLOPS* genes in the future, this siRNA delivery system could be easily adapted to discover and validate additional cancer-specific vulnerabilities.

5.4 Materials and Methods

Pooled shRNA Library Screen. Genome-scale pooled shRNA screens [284] in 102 cancer cell lines were performed using a lentivirally delivered pool of 54,020 shRNAs targeting 11,194 genes. Each cell line was infected in quadruplicate and propagated for at least 16 population doublings[48]. The abundance of shRNAs relative to the initial DNA plasmids was measured by microarray hybridization and normalized using dCHIP and GenePattern modules before identifying essential genes (See Extended Experimental Procedures for details).

Analysis of shRNA screening data. Raw .CEL files from custom Affymetrix barcode arrays were processed with a modified version of dCHIP software [284]. The GenePattern module 'HPscores' was used to calculate the log fold change scores derived from replicate measurements of the shRNA abundance in each cell line at the conclusion of the screening relative to initial DNA reference pool. This score was adjusted to de-emphasize shRNAs that showed high variability among replicates of the DNA pool. This log fold change score was divided by the s.d. of the DNA pool after it had been mean centered at 1 and floored at 1 to de-emphasize shRNAs that showed high variability among replicates of the DNA pool, which likely arises from technical artifacts including shRNA under-representation in the initial DNA pool or sub-optimal array probe performance. The Gene Pattern module 'NormLines' was then used to normalize the adjusted log fold change scores among cell lines by scaling and centering these scores with Peak median absolute deviation (PMAD) normalization, a variation of ZMAD. PMAD normalization consisted of, first, centering the shRNA scores per cell line at 0 by subtracting the value of each shRNA from the modeled peak value of the distribution of each cell line. The shRNA scores for each cell line were then rescaled so that each line had similar data ranges by dividing the centered data for each shRNA by the median absolute deviation (MAD).

To identify genes that were both amplified in ovarian tumors and essential in amplified cell lines, each gene identified as amplified in primary ovarian tumors [82] were tested one by one across the entire panel of 102 cell lines screened. For those genes that have 5 or more lines with an amplification of the gene, the median shRNA score for each shRNA in the pool was calculated and used to convert shRNA scores to z-scores. Amplified genes that had mapped shRNAs with a z-score<-2.0 were identified. All data files can be accessed at the Integrative Genomics portal (http://www.broadinstitute.org/IGP/home). *Please utilize Login: reviewer, Password: achilles to browse data.*

Analysis of TCGA Data
All primary high grade serous ovarian cancer data were downloaded from the TCGA portal (http://tcga-data.nci.nih.gov/tcga). TCGA has characterized copy number alterations in 489 primary high grade serous ovarian tumors using Illumina 1MDUO arrays. 63 recurrent regions of amplification were identified using GISTIC 2.0. The boundaries of these regions were set with at least 95% confidence to include the target gene(s), resulting in the identification of 1270 amplified genes. The frequency of amplification for *ID4*, *KRAS*, *ERBB3* and *SKP2* genes was determined by using a threshold of $\log_2$ copy number ratio > 0.3 within a subset of tumors in TCGA project (345 tumors). Screenshots of the same tumor data were taken using the Integrative Genome Browser (IGV; http://www.broadinstitute.org/igv).

Cell culture and generation of stable cell lines. All human cancer cell lines are cultured as described [48]. Immortalized human ovarian surface epithelial cells (IOSE)[238] were maintained in 1:1 Medium 199:DMEM supplemented with 10% fetal bovine serum (FBS, Sigma). HeLa, MDA-MB-435, and T22H cells were cultured in Dulbecco's modification of Eagle's medium (Invitrogen) with 10% bovine serum (Invitrogen). OVCAR-8 cell line stably expressing firefly luciferase was generously provided by Dr. Joyce Liu. Retroviruses were generated by transfection of 293T packaging cells with pBabe/pWzl and pCL-Ampho plasmids [36].Lentiviruses were produced by transfection of 293T packaging cells with a three-plasmid system [284]. To generate stable cell lines, cells were seeded into 10-cm dishes for 24 h

before infection with either 5 ml of retroviruses or 0.3 ml of lentivirusesfor 3 h in the presence of 4 μg/ml polybrene. After the incubation, medium was replaced with fresh medium for another 24 h before selection in media containing 2 μg/ml of puromycin for 2 d, 10 μg/ml of blasticidin for 4 d or 800 μg/ml of neomycin for 5 d.

Plasmids. Human ID1, ID2, ID3 (obtained from the CCSB human ORFeome collection,Dana-Farber Cancer Institute) and ID4 (obtained from Origene) were cloned into pLenti6.3-blast (*Bam*HI and *Bsr*GI sites).The ID4^{S73P,L94P}(or ID4_DM) mutant was generated using the Quikchange Site-Directed Mutagenesis kit (Stratagene). The pLenti6.2-LacZ was used as a control vector. Human HOXA9 was provided by Anna Schinzel at Dana-Farber Cancer Institute and cloned into pWzl-blast (*Bam*HI and *Eco*RI). The human HRAS^{V12} and KRAS^{V12} in pBabe-puro vectors have been described[285]. The human MEK^{D218,D222} (or MEK^{DD}) fragment was removed from pBabe-puro-MEK^{DD} plasmid[36]with *Bam*HI and *Sal*I and inserted into pBabe-neomycin.Lentiviral pLKO.1-puro-shRNA constructs were obtained from The RNAi Consortium. The shRNA constructs used are as follows: control shRNA targeting *GFP* (TRCN0000072181), *ID4*-specific shRNAs (shID4#1: TRCN0000017323, shID4#2: TRCN0000017325 and shID4#3: TRCN0000071444) and *HOXA9*-specific shRNAs (shHOXA9#1: TRCN0000012509, shHOXA9#2: TRCN0000012510, shHOXA9#3: TRCC0019251728, shHOXA9#4: TRCC0019251729).

Peptides and siRNAs. The tandem peptide library was synthesized via standard FMOC solid-phase peptide synthesis and purified by high-performance liquid chromatography at the MIT Biopolymers Core, Tufts University Core Facility or CPC Scientific, Inc. The tandem peptides were then cyclicized by bubbling air into 3 μM aqueous peptide solutions for 24 h, followed by lyophilisation and storage at -80 °C for later use. All siRNAs were obtained from Dharmacon, Inc. The sequences of siRNAs (5'-3') are as follows: si*GFP* (GGCUACGUCCAGGAGCGCA),

si*LUC*(CUUACGCUGAGUACUUCGA),   si*Bgal-728*   (CUACACAAAUCAGCGAUUU), si*ID4_568*(GAUAUGAACGACUGCUAUA),   si*ID4_621*(CAACAAGAAAGUCAGCAAA), si*ID4_564*(GUGCGAUAUGAACGACUGCUA), and si*ID4_1195*(CCGACUUUAGAAGCCUACUUU).

Fluorescent labelling of siRNA. siRNAs bearing 3'-amine on the sense strand was reacted in PBS with twenty-fold molar excess of Vivotag S-750 amine-reactive dye (Visen Medical, Inc.) for 1 h at 37°C. The reaction mixture was then precipitated overnight at−20°C in 0.5 M NaCl and 40% ethanol. Precipitated siRNA was pelleted through centrifugation at 8000xg for 20 minutes at 4°C, washed once with 70% ethanol, and centrifuged again before being air-dried. This labelling process was repeated to yield approximately 3.5 fluorophores per siRNA duplex.

Gene expression profiling. OVCAR-8 cells (2×10^5) were infected with lentiviruses expressing a control shRNA targeting *GFP* (shGFP) or two *ID4*-specific shRNAs (TRCN0000017323 and TRCN0000071443)for 24 h. Cells were then cultured in fresh medium containing puromycin for 48 h to select transduced cells (the pLKO.1 vector also encodes the puromycin resistance gene). Total RNA was extracted by Trizol reagent (Invitrogen) followed by RNeasy column purification (Qiagen). For overexpression experiments, immortalize ovarian serous epithelial cells expressing activated MEK(IOSE-M) cells were subjected to a 3 h infection with lentiviruses expressing control vector or ID4. Cells were then cultured in medium containing blasticidin (blasticidin resistance gene encoded in the pLenti6.3-blast vector) for 4 d togenerate polyclonal populations of stable lines and passaged twice before set-up for total RNA extraction. Cells (4×10^5) expressing the indicated constructs were plated onto 10-cm dishes for 48 h and total RNA was extracted as described above. Gene expression profiling was then performed on Affymetrix HG-U133A_2 GeneChips by the Microarray Core at the Dana-Farber Cancer Institute. Probes were aligned to a transcript database consisting of RefSeq (36.1) and complete coding sequences from GenBank (v.161). Gene-centric expression values were generated for every gene with at least 5 probes.

Data for each experiment was normalized and summarized using robust multichip average (RMA), then logged and row normalized.

Gene Set Enrichment Analysis (GSEA) [286]. Processed expression data from either the ID4 shRNA or ID4 overexpression experiments was analyzed using GSEA v2.06(http://www.broadinstitute.org/gsea/). For the shRNA experiments, we compared expression profiles derived from OVCAR-8 cellsinfected with a control shRNA targeting *GFP* (shGFP) and OVCAR-8 cells infected with *ID4*-specific shRNAs. For overexpression experiments, IOSE-M cells expressing a control vector were compared to cells overexpressing ID4. GSEA was run using the default settings, except for the following; permutations were based on the gene sets, not on phenotype and data was not collapsed to gene symbols (this was done prior to GSEA). We additionally identified gene sets enriched in particular populations of ovarian tumor samples. GSEA comparing 109 samples with amplified *ID4* (log_2 copy number ratio > 0.3) vs. 81 non-amplified *ID4* samples (log_2 copy number ratio < 0) was performed using expression data from primary ovarian samples with matched copy number from TCGA. GSEA was also performed with the same dataset, using 44 samples with low ID4 expression levels vs. 45 samples with high ID4 expression (thresholds were 1 standard deviation below and above the mean ID4 expression of all the samples).

Fluorescence *in situ* hybridization (FISH). BAC RP11-72I11 clone containing *ID4* (Invitrogen) was labeled with Digoxigenin (Roche) using BioPrime labeling mix (Invitrogen). A reference probe specific for the centromeric region of Chromosome 6 (CEP6 SpectrumOrange Probe, #06J36-016) was purchased from Abbott Molecular. Labeled DNA was precipitated at -80°C for 2 h with 1 µl of glycogen (20 µg/µl), pelleted by centrifugation at 18,000 ×g for 15 min at 4°C, air-dried for 10 min, and resuspended in 50 µl of hybridization buffer (50% deionized formamide, 10% dextran sulfate, 2× SSC).

Slides containing metaphase chromosomes were pretreated with 1:25 Digest-All III (Invitrogen) at 37°C for 6 min before fixation in 10% buffered formalin for 1 min at room temperature. Slides were dehydrated for 2 min each in 70%, 85%, 95% and 100% ethanol at room temperature. Probes were prepared by mixing 2 µl of each labeled probe, 1 µl Cot-1 DNA (1 mg/ml; Invitrogen), and 11 µl of hybridization buffer. Probes were applied to air-dried slides; coverslips were applied and sealed with rubber cement. These preparations were denatured at 72°C for 5 min. Hybridization was performed for 18 h at 37°C in a dark humid chamber. Coverslips were gently removed and slides were washed in 0.5× SSC at 72°C for 5 min, rinsed at room temperature in 1× PBS containing 0.025% Tween-20. Slides were blocked with CAS-Block containing 10% normal goat serum (Invitrogen) and then incubated with FITC-anti-Digoxigenin (Roche). Slides were washed in 1× PBS containing 0.025% Tween-20 and counterstained with DAPI (Invitrogen). Images were captured by using Zeiss Axio Observer Z1 microscope (Zeiss) and AxioVision digital imaging software (Zeiss).

Gel-shift and stability assays. For the gel-shift assay, siRNA was mixed with tandem peptide at specified molar ratios in phosphate buffered saline (PBS) for 10 – 15 min at room temperature. The mixture was analyzed by non-denaturing gel electrophoresis using a 15% acrylamide gel for siRNA, stained with SYBR-Gold, and visualized under UV light. For the siRNA stability assay, siRNA (100 pmol) was mixed with TP-LyP1 or 6R-LyP1 (2 nmol) in PBS for 10 – 15 min at room temperature. Naked siRNA or peptide-complexed siRNA was then added to 100% murine serum (10:1 v/v) and incubated at 37 °C up to 24 h, after which the RNA is extracted and precipitated according to established protocols, separated on a 15% TBE gel, stained with SYBR-Gold, and visualized under UV light.

Peptide uptake and gene silencing. For the initial screen, HeLa cells expressing GFP were cultured in 96-well plates to ~40-60% confluence. siRNA (0-100 nM) was incubated with 20-fold molar excess of tetramethylrhodamine-labeled tandem peptides in PBS for 10-15 min at room temperature, incubated over cells for 4 h at 37 °C, after which the medium was replaced. Transfection with Lipofectamine RNAiMAX was used as a positive control. The cells were cultured for an additional 24-48 h before being examined

by flow cytometry on a BD LSRII instrument. % Knockdown based on the geometric mean of GFP fluorescence of the entire population was normalized to GFP signal of mock treated cells. For competition experiments with free LyP1 peptide, cells were pre-incubated with unlabeled LyP1 or ARAL control peptide at specified concentrations from 5 to 20 μMfor 1 h at 37 °C before nanocomplex treatment.

For *ID4* silencing, siRNAs targeting different exons of the *ID4* mRNA (100 pmol) were mixed with TP-LyP1 at a molar ratio of 1:20 in PBS. The mixture was added to OVCAR-8 or OVCAR-4 cell cultures (plated at 0.2 x 10^6 cells in 6-well plates 48 h prior) for 4-6 h at 37 °C and was then replaced with fresh serum-containing media. Cell lysates were collected 48 h later for immunoblotting.

Cell proliferation assay. A total of 800-2000 Cells were seeded into each well of 96-well plates 24 h prior to infection. Six replicate infections were performed for control shRNAs and each gene-specific shRNA in the presence of 4 μg/ml polybrene for 24 h followed by selection with2 μg/ml of puromycin. The ATP content was measured at 6 d post-infection by using CellTiter-Glo luminescent cell viability assay (Promega). To measure the toxicity of nanocomplexes *in vitro*, HeLa cells grown in 96-well plates at 40-60% confluency were incubated in triplicate with nanocomplex formulations for 24 h. Viability was measured using CellTiter-Glo luminescent viability assay (Promega). To measure the cytotoxicity of ID4 suppression, OVCAR-8 and OVCAR-4 cells grown in 6-well plates at 40-60% confluence were transfected twice on two consecutive days with nanocomplexes containing siRNA against ID4 (100 pmol) or containing siRNA against GFP. Twenty-four (24) h after the second transfection, cells were trypsinized and plated in 96-well plates in quadruplicate. The plateswere analyzed 24 h later using Celltiter-Glo assays (Promega) according to manufacturer's instructions.

Anchorage-independent growth assay. Growth in soft agar was determined by plating 1×10^4 cells in triplicate in 5 ml of medium containing 0.35% Noble agar (BD Biosciences) which was placed on top of 4 ml of solidified 0.7% agar [285]. Colonies greater than 100 μm in diameter were counted 4 weeks after plating. Data represent mean ± s.d. from three independent experiments.

Flow Cytometry. Fluorescence-activated cell sorting (FACS) analysis of cell-surface p32 was done on live cells. Approximately 2.5 x 10^5 cells were stained with a polyclonal anti-full-length/NH2-terminal p32 or rabbit IgG isotype control (1 μg per 1 x 10^6 cells) and Alexa-647 goat anti-rabbit secondary antibody, each for 45 min at 4 °C, analyzed by gating for propidium iodide-negative (live) cells. For analysis of apoptosis, cells were resuspended in 1x Annexin-V binding Buffer (BD Biosciences, San Jose, CA). Cells were incubated with Annexin V – FITC and propidium iodide for 15 minutes in the dark according to the manufacturer's recommendation. % of cells in S-phase was determined using the Click-iT EdU cell proliferation assay (Invitrogen) according to manufacturer's instructions.

Immunoblotting. Cell lysates were prepared by scraping cells in lysis buffer [50 mM Tris HCl (pH 8), 150 mM NaCl, 1% Nonidet P40, 0.5% sodium deoxycholate and 0.1% SDS] containing complete protease inhibitors (Roche) and phosphatase inhibitors (10 mM Sodium Floride and 5 mM Sodium Orthovanadate). Protein concentration was measured by using BCA Protein Assay kit (Pierce). An equal amount of protein (30 μg) was separated by NuPAGE Novex Bis-Tris 4-12% gradient gels (Invitrogen) and then transferred onto a polyvinylidene difluoride membrane (Amersham). The membrane was then incubated with primary antibody for 1 h at room temperature. Antibodies againstID1 (sc-488), ID2 (sc-489), ID3 (sc-490), ID4 (sc-13047), K-RAS (sc-30) and H-RAS (sc-29) were purchased from Santa Cruz Biotechnology. Antibodies specific for Caspase-3 (#9665), MEK (#9122), PARP (#9532) and phospho-ERK1/2 (#9101) were from Cell Signaling Technology. Antibody specific for HOXA9 (#07-178) was from Millipore. Antibody specific for α-tubulin (#13-8000)was from Invitrogen. After incubation with the appropriate horseradishperoxidase-linked secondary antibodies (Bio-Rad), signals werevisualized by enhanced chemiluminescence plus Western blottingdetection reagents (Amersham). Expression of β-actin wasalso assessed as an internal loading control by using a specific antibody (sc-8432-HRP,Santa Cruz). Immunoblots of cell lysates after TPN treatment were incubated with IRDye 680 goat anti-mouse IgG or

IRDye 800 goat anti-rabbit IgG (Li-COR) and scanned using the Odyssey infrared imaging system (Li-COR). Intensities ofbands were quantified by LabWorks image analysis software (UVP) or ImageJ (http://rsbweb.nih.gov/ij/).

Real-time quantitative Reverse-Transcription PCR. Total RNA was extracted with Trizol reagent (Invitrogen). 4 μg of total RNA for each sample was used to synthesize the first-strand cDNA by using Oligo(dT)$_{20}$/random hexamer primer cocktails and SuperScript III reverse transcriptase (Invitrogen). Quantitative PCR reactions were performed using SYBR green PCR Master Mix (Applied Biosystems). The primer sequences used are as follows: *ID4* (forward: 5'-CCGAGCCAGGAGCACTAGAG-3'; reverse: 5'-CTTGGAATGACGAATGAAAACG-3'), *HOXA3* (forward:5'-TGCTTTGTGTTTTGTCGAGACTC-3'; reverse: 5'-CAACCCTACCCCTGCCAAC-3'), *HOXA7* (forward: 5'-TATGTGAACGCGCTTTTTAGCA-3'; reverse: 5'-TTGTATAAGCCCGGAACGGTC-3'), *HOXA9* (forward: 5'-GAGTGGAGCGCGCATGAAG-3'; reverse: 5'-GGTGACTGTCCCACGCTTGAC-3') and *GAPDH* (forward: 5'-CCTGTTCGACAGTCAGCCG-3'; reverse: 5'-CGACCAAATCCGTTGACTCC-3').Triplicate reactions for the gene of interest and the endogenous control, (*GAPDH*) were performed separately on the same cDNA samples by using the ABI 7900HT real time PCR instrument (Applied Biosystems).The mean cycle threshold (Ct) was used for the ΔΔCt analysis method (ABI User Bulletin #2).

Tumorigenicity assay. Female Balb/c and NCR/nude mice (Charles River Laboratories) were obtained at 4-6 weeks of age. All animal experiments were approved by the MIT Committee on Animal Care under approved protocols. Tumor xenograft experiments were performed as described[238]. IOSE cell lines expressing indicated constructs were trypsinized and collected in media supplemented with 10% FBS. Cells (8×10^6) were resuspended in 400 μl of 1× PBS and mixed with 400 μl of BD Matrigel™-Basement Membrane Matrix, LDEV-free (BD Biosciences) prior to injection. 200 μl of the cell mixture (containing 2×10^6 cells) was injected subcutaneously into 8-week-old female BALB/c nude mice. Tumor injection sites were monitored for 5 months for tumor formation. Mice were euthanized when tumors reached 1.5 cm in diameter. For HOXA9 experiments, ID4-overexpressing IOSE-M cells were infected with lentiviruses expressing control shRNAs or two previously described *HOXA9*-specific shRNAs[247](shHOXA9#1: TRCN0000012509 and shHOXA9#2: TRCN0000012510). Cells were then cultured in fresh medium for 24 h before selection in 2 μg/ml of puromycin for another 2 d. Infected cells were then passaged once before injection into immunodeficient mice as described above.

Systemic administration and *in vivo* characterization of TPNs. Female NCR/nude mice were injected subcutaneously on the bilateral flanks with 2×10^6 MDA-MB-435 melanoma or 2×10^6 OVCAR-8 ovarian cancer cells mixed with Matrigel and allowed tumors to form over two weeks. For circulation experiments, 5 nmols of near-infrared fluorophore (Vivotag-750) labeled siRNA was complexed to tandem peptides (at a molar ratio of 1:20 siRNA to peptide) in 5% glucose and injected either intravenously or intraperitoneally into mice bearing bilateral subcutaneous MDA-MB-435 tumors. The mice were imaged at specified times using the IVIS 200 imaging system (Caliper Life Sciences). Blood was periodically drawn retroorbitally and near-infrared fluorescence from circulating siRNAs was measured using the Odyssey imaging system (Li-COR Biosciences). The organs were harvested 6 h after injection and were also imaged using IVIS. Tumor explants were examined at higher resolution (84 μm) using the Odyssey imager with an excitation wavelength of 785 nm. To study time-dependent homing and tumor penetration in OVCAR-8 tumors, TPNs carrying FITC labeled-siRNA were administered intravenously to tumor bearing mice (5 nmols siRNA/injection). Tumors and tissues were collected 6 h later for subsequent analyses by immunofluorescence or quantification of total injected dose.

To determine the % injected dose accumulated in the tissue, organs and tumors harvested from mice were pulverized under liquid nitrogen and homogenized in 10 mM Tris buffer with 1% SDS. The homogenate was heated at 95°C for 10 minutes and centrifuged at 14,000xg. Fluorescence of the lysate

was measured using the Odyssey imager. To generate a standard curve for each organ, organs and tumors from uninjected animals were processed and known amounts of fluorescent siRNAs were spiked into the lysates. The lysates were imaged under the same settings, and the integrated fluorescence intensities versus siRNA concentrations were fitted with a 3-parameter exponential equation ($f=y0+a*(1-exp(-b*x))$; SigmaPlot).

To test knockdown of luciferase expression *in vivo*, mice bearing orthotopic luciferase-expressing T22H tumors were injected i.p. with nanocomplexes (2.5 and 5 mg/kg). Control groups received saline, peptide alone, nanocomplexes containing siRNA against GFP, or untargeted nanocomplexes containing si*LUC* (all 5 mg/kg). Whole-animal imaging of luciferase activity was performed 48 h later. To measure the duration of luciferase silencing, bioluminescence imaging was performed at specified time points.

Animal model of metastatic ovarian cancer. For the OVCAR-4 tumor model, 3×10^6OVCAR-4 cells mixed with Matrigel were implanted in the subcutaneous space on the bilateral flanks of 4- to 6-week-old NCr/nude mice (Charles River Laboratories). Once tumors were established, animals were divided into cohorts of five mice each and were treated with saline, or TP-LyP-1 carrier only without siRNA (6.5mg peptide/kg body weight, Carrier), TPNs carrying GFP-specific siRNA (siUT), or TPNs containing *ID4*-specific siRNA injected either intravenously (si*ID4*(IV)) or intraperitoneally (si*ID4*(IP)) all at 1mg siRNA/kg body weight/injection, every 3 days for 25 days. For the OVCAR-8 tumor model, OVCAR-8 cells stably expressing firefly luciferase were injected intraperitoneally into 4- to 6-week-old NCr/nude mice (Charles River Laboratories) at 10^6 cells per mouse. Three weeks after injection, tumor establishment was confirmed by an increase in total bioluminescence signal. The animals were then randomly divided into cohorts of five mice each. The first cohort received nanocomplexes containing TP-LyP1 and siRNA against *ID4* (si*ID4*_568 and si*ID4*_621, 5 mg siRNA/kg body weight). The other control cohorts received saline, TP-LyP1/GFP-siRNA (siUT, 5 mg/kg), or TP-ARAL/*ID4*-siRNA (ARAL/siID4, 5 mg/kg). For all treatments, siRNA was mixed with peptide at a molar ratio of 1:20 (siRNA to peptide) in 500 µL of PBS with 5% glucose, and injected intraperitoneally. Treatments were repeated twice weekly for 14 days, after which the dose was reduced to once weekly for 3 more weeks. On day 60, tumors/organs were harvested for immunohistochemical analyses. Whole-animal optical imaging was performed every 3 days. Mice were anesthetized using isofluorane, injected with 150 mg/kg D-luciferin (Promega), and imaged 10-15 min after injection once the signal peaked.

Immunostaining and analysis. For histological analysis, harvested tumors were fixed in 4% paraformaldehyde at 4°C overnight, soaked in 30% sucrose (w/v) for 24 h, then snap frozen. Rat anti-mouse CD31 (1:50, BD PharMingen) and a polyclonal anti-full length p32 antibody were used for immunohistochemical staining. Rat or rabbit IgGs were used as isotype controls. Sections were washed and detected with AlexaFluor-488 goat anti-rat or anti-rabbit IgG (1:1000; Invitrogen). The slides were counterstained with DAPI and mounted on glass slides for microscopic analysis. At least three images from representative microscopic fields were analyzed for each tumor sample using the ImageJ software.

Immunogenicity studies in mice. Balb/c immunocompetent mice were injected intraperitoneally with TP-LyP1 complexed to siRNAs against ID4, GFP, firefly luciferase, and siβgal-728 (5mg siRNA/kg body weight). siBgal-728 encapsulated in Lipofectamine RNAiMAX was used as a positive control. Serum samples obtained 6 h after injection were processed for measurements of IFN-α, TNF-α, and IL-6 by ELISA (PBL Biomedical Laboratories and BD Biosciences) in accordance with the manufacturer's instructions.

Statistical Analysis. Statistical analyses were performed using built-in statistical functions in GraphPad Prism (GraphPad Software). Tumor burden between different cohorts and averaged fluorescence intensities from immunofluorescence staining, and Western blots were analyzed using one-way ANOVA and appropriate post-hoc tests.

6 Characterization of receptor-specific cell-penetrating peptides for siRNA delivery

6.0 Abstract

Tumor-targeted delivery of siRNA remains to be a major barrier in fully realizing the therapeutic potential of RNA interference. While cell-penetrating peptides (CPP) are promising as carriers of siRNA, they are universal internalizers that lack cell-type specificity. In *Chapter 3*, we have developed tandem tumor-targeting and cell-penetrating peptides that condense siRNA into stable nanocomplexes for cell type-specific siRNA delivery. In *Chapters 4 &5*, we utilized tumor-penetrating nanocomplexes as a platform to validate cancer targets identified from large-scale genomic efforts. Here, we present follow-up physiochemical and biological analyses of nanocomplexes uptake, endosomal escape, carrier unpacking, and ultimately delivery of siRNA to the cytosol in a receptor-specific fashion. To better understand the structure-activity relationships that govern receptor-specific siRNA delivery, we employ computational regression analysis and identify a set of key convergent structural properties, namely the valence of the targeting ligand and the charge of the peptide, that help transform ubiquitously internalizing cell-penetrating peptides into cell type-specific siRNA delivery systems.

(Reprinted with permission from [287])

6.1 Introduction

RNA interference (RNAi) offers an attractive means to silence gene expression with extraordinary specificity, particularly for the subset of "undruggable" gene targets [1]. This capability is particularly appealing for diseases with complex genotypic alterations such as

cancer. However, siRNA molecules are large (~14 kDa), highly anionic, hydrophilic, and susceptible to degradation by nucleases. Upon systemic administration, naked siRNAs cannot penetrate into tumor tissue, target extravascular cancer cells, and cross cellular membranes to act in the cytosol. Therefore, to bring RNA-based therapeutics into the clinic, one must improve the pharmacokinetic properties of siRNA and overcome several delivery barriers [5, 7].

Approaches to target the delivery of siRNA to tumor cells include lipophilic conjugations such as cholesterol [131], attachment to targeting moieties such as antibodies or aptamers [127-128], or encapsulation in polymer-based or liposomal carriers targeting tumor-specific markers [126]. Nonetheless, to date, none of the approaches enable active penetration into the tumor parenchyma to achieve gene silencing in epithelial tumor cells where genetic alterations reside. Elsewhere, cell penetrating peptides (CPP, also known as protein transduction domains) such as TAT and poly-Arginine have been shown to bring DNA- and RNA-based payloads into the cytosol [230]. While CPPs are a class of promising siRNA carriers that rapidly penetrates the cell membrane, they lack receptor specificity; they bind to and are internalized by cells *via* heparan sulfates and other glycosaminoglycans in nearly all cell types *in vitro* and *in vivo* [288-289]. Thus, an ideal siRNA delivery system should possess two complementary characteristics: it should efficiently penetrate tissues and cross cellular membranes, but it should also be cell type-specific by targeting only tumor cells while sparing normal cells. Efforts to enhance the specificity of CPPs include attachment to homing peptides or restriction of cargo activity to specific cells [290-292]. However, the development of receptor-specific CPPs has been highly empirical: peptides were tested one at a time without systematic optimization of functional properties. Consequently, tumor-specific delivery of siRNA by CPPs is not routinely achieved.

Recently, a new class of cell-internalizing and tumor-penetrating peptides has been described which leverage a consensus C-terminal (R/K)XX(R/K) motif (the CendR rule) to activate transvascular transport, cell internalization, and parenchyma penetration [117, 119]. Two peptides that both contain tumor-homing and cryptic CendR motifs, iRGD (CRGDKGPDC) and LyP-1 (CGNKRTRGC), have been shown to significantly improve the delivery of small molecules, antibodies, and nanoparticles to tumors [218]. Leveraging this discovery, we have previously developed tandem peptide sequences bearing a constant tumor-penetrating domain (LyP-1) and variable cell-penetrating/siRNA-binding domains to chaperone siRNA cargo deep into the parenchyma of ovarian tumors *in vivo* and suppress a novel ovarian oncogene [213]. However, the intracellular trafficking mechanism by which siRNAs are delivered to tumor cells expressing specific receptors remain incompletely understood. Furthermore, the structure-activity relationships that favored cell internalization and maximized gene silencing, while maintained receptor-specificity and cell type-specific penetration and have yet to be determined.

Here, we present an analysis of tandem peptides developed in *Chapters 3* to better understand the properties that govern receptor-specific siRNA delivery. We characterized a library of nanocomplexes formed by siRNAs non-covalently bound to tumor-specific peptides bearing structurally distinct cell-penetrating domains. A subset of nanocomplexes achieved functional delivery of siRNA in a cell type-specific manner. To gain quantitative mechanistic insights, we studied the intracellular trafficking mechanisms of peptide-siRNA nanocomplexes by measuring cellular siRNA uptake, escape from endosomal entrapment, and dissociation of siRNA from the carrier. To understand the relationship between peptide material properties and receptor-specific siRNA delivery, we fused data from physiochemical characterizations with regression modeling to derive structure-activity relationships. Two structural properties, the

valence of the tumor-specific ligand on the nanocomplex and peptide charge, are key

considerations when designing a siRNA delivery system that is both membrane-penetrating and

receptor-specific. Specifically, we found that myr-TP-LyP-1 met the desired material properties,

condensed siRNA into nanocomplexes that are multivalent, and delivered siRNA to human

cancer cell lines in a receptor-specific fashion.

6.2 Results and Discussion

6.2.1 Characterization and in vitro cellular uptake of tandem peptides

To develop tumor-specific and cell-penetrating peptides for siRNA delivery, we set the

following design criteria: the delivery system should non-covalently condense siRNA in a single

step, remain stable in physiologic conditions, multivalently display homing peptides for tumor-

targeting, and readily dissociate once inside the cytosol to enable siRNA incorporation into the

RNA-induced silencing complex (RISC). Towards this goal, we synthesized a library of 9

tandem peptide carriers composed of distinct cell penetrating domains at the NH_2-terminus and a

tumor-specific CendR peptide, LyP-1, at the C-terminus (**Figure 6.1;Table 6.1**). LyP-1 homes to

tumor cells and tumor lymphatics *via* binding to its receptor p32, a mitochondrial protein that is

aberrantly expressed on the surface of tumor cells and tumor-associated macrophages [101, 217].

We generated N-terminally myristoylated versions of each of the 9 tandem peptides, since

myristoylation has been shown to enhance hydrophobic interactions and peptide affinity to lipid

bilayers such as the cell membrane [221]. The selection of cell-penetrating domains included

representatives of polycationic sequences including oligoarginines, the HIV TAT protein [293],

and the HSV-1 tegument protein VP22 [294]; as well as amphipathic CPPs such as penetratin [295] and transportan [161].

We found that tandem peptides readily condensed siRNA into tumor-penetrating nanocomplexes (TPNs) in a one-step procedure, without the need for exogenous stabilizing lipids. To determine the amount of peptide needed to fully encapsulate free siRNAs into stable nanocomplexes, we mixed siRNA with each tandem peptide at increasing molar ratios in the presence of a dye (TO-PRO-3) that fluoresces when intercalated into double-stranded nucleic acids. Upon particle formation, we observed a decrease in dye fluorescence likely due to steric exclusion of dye binding to siRNA by peptides in the nanocomplex (**Figure 6.2**). Near-maximal (> 95%) encapsulation of siRNA occurred consistently at molar ratios between 1.6:1 and 20:1 (peptide-to-siRNA) for all peptides in the library. Since the positively-charged CPP domain binds the negatively charged backbone of the siRNA, this variation in encapsulation ratio can lead to differences in the valence of the LyP-1 ligand of the nanocomplex, which in turn can affect the affinity of binding to the p32 receptor on the cell surface.

Using TEM and dynamic light scattering (DLS), we observed that the majority of TPNs have hydrodynamic diameters ranging from 50 to 100 nm in water and from 200 to 400 nm in PBS, with a narrow size distribution (polydispersity index < 0.2) (**Figure 6.3; Figure 6.5**). The zeta potential of TPNs ranges from +20 to +40 mV (**Table 6.1**). No significant changes in TPN size was observed when placed in mouse serum at 37°C (**Figure 6.4**). Moreover, TPNs remained intact for at least 24 h in phosphate-buffered saline (pH 7.1) at 37°C as indicated by minimal change in TO-PRO-3 fluorescence (**Figure 6.5**). To ensure that TO-PRO-3 fluorescence indeed corresponded to the presence of intact nanocomplexes, we disrupted TPNs with a detergent and observed restoration of dye fluorescence (**Figure 6.5**). These results collectively suggest that

158

tandem peptides can non-covalently condense siRNA into stable nanocomplexes at defined

molar ratios.
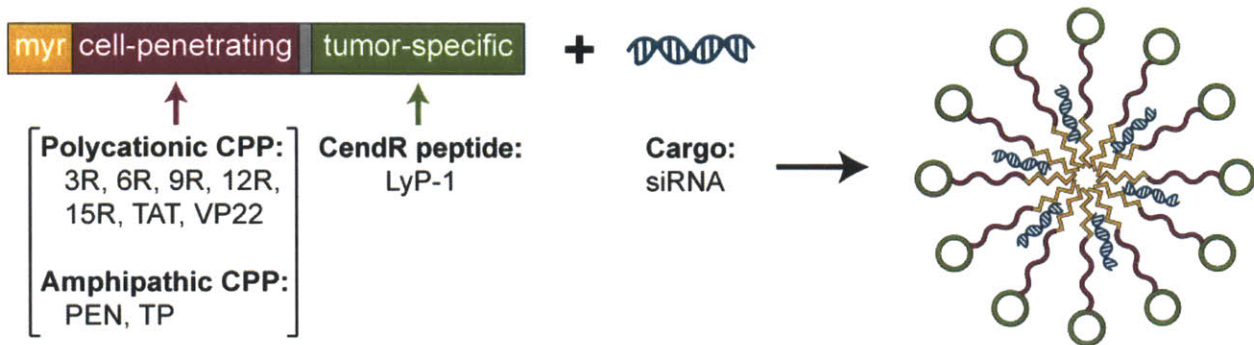
Figure 6.1. Schematic representation of the tumor penetrating nanocomplex (TPN). siRNA (blue) is non-covalently bound to tandem peptides composed of a cyclic tumor-specific domain (LyP-1, green) and various cell-penetrating peptide domains (purple) separated by a 4-glycine spacer (gray). A subset of the tandem peptides tested were N-myristoylated (myr, orange). Cell-penetrating peptide domains tested include representatives from both polycationic and amphipathic CPPs.
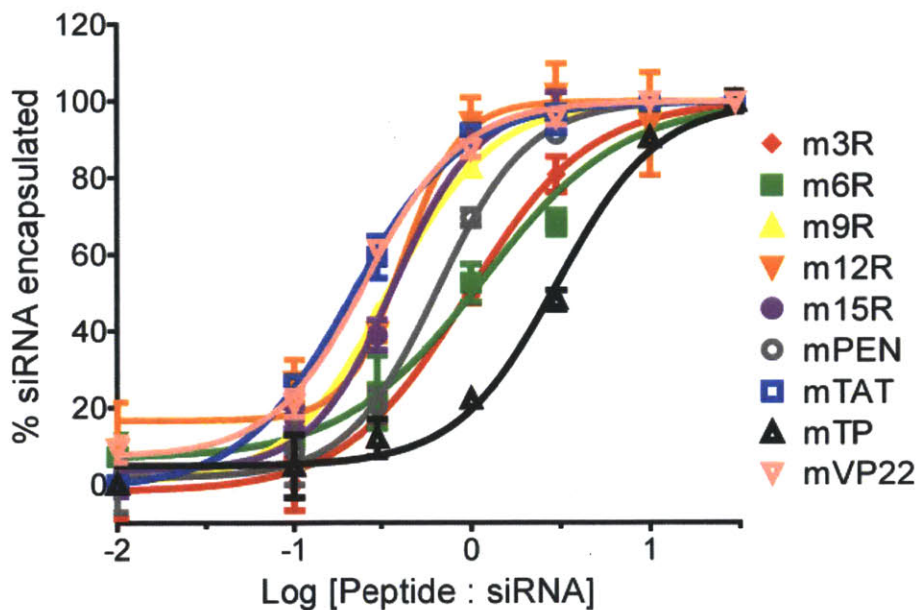
Figure 6.2. Encapsulation of siRNA by tandem peptides. Tandem peptides were mixed with siRNA at varying molar ratios, and the amount of siRNA encapsulated in nanocomplexes was determined by measuring the fluorescence of a nucleic-acid intercalating dye (TO-PRO-3) normalized to dye fluorescence with siRNA alone.

159
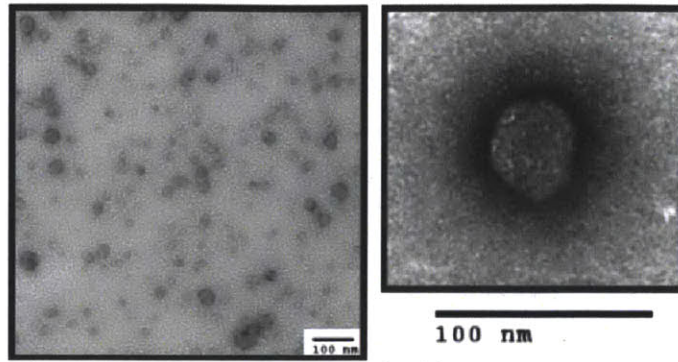
Figure 6.3. Representative TEM of a tandem peptide/siRNA nanocomplex formed in water and negatively stained with uranyl acetate; scale bar = 100 nm.
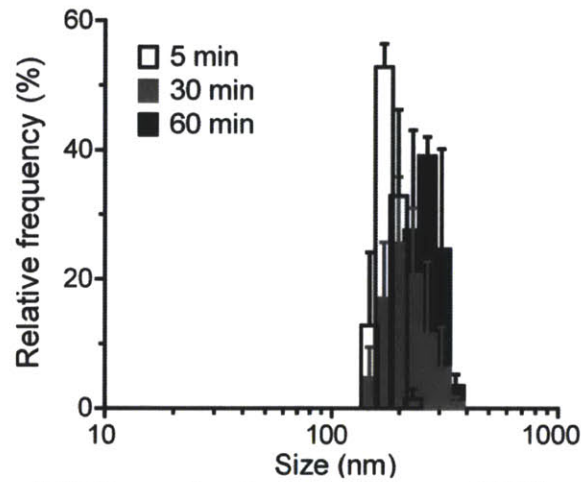
Figure 6.4. Size histograms of TPN over time in mouse serum at 37°C.
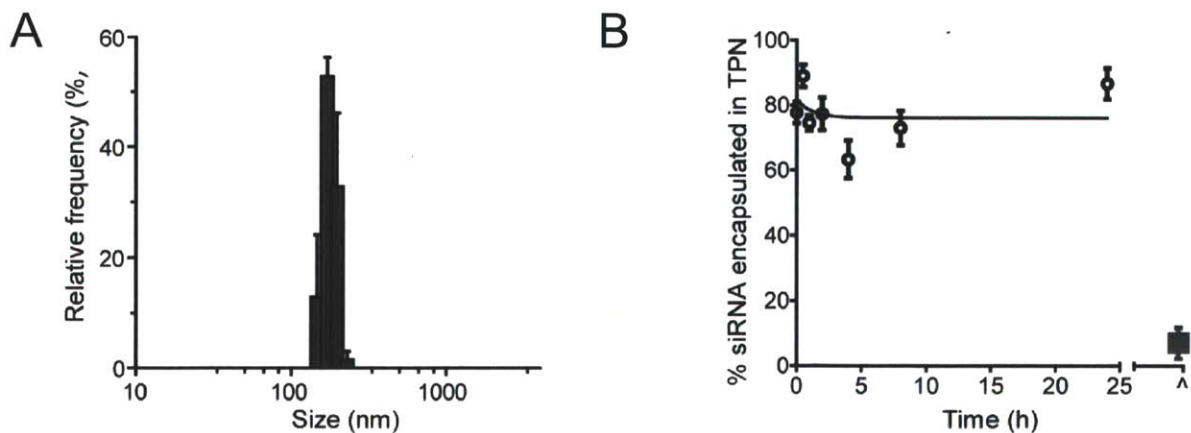
Figure 6.5. Characterization and stability of TPNs. (A) Hydrodynamic size histograms of TPN from dynamic light scattering measurements. **(B)** Stability of TPNs in saline at 37 °C, as measured by intercalation of TO-PRO-3 dye. The final data point (red, marked with ^) represents disruption with 0.1% Triton-X 100 detergent. Error bars indicate s.d. from three independent experiments.

160

Table 6.1. Structural properties of nanocomplexes. (A) The myr- prefix denotes NH2-terminal myristoylation. (dR)n = oligoarginine where n is the number of d-Arginine residues; PEN = penetratin; TAT = HIV TAT (48-60); TP = transportan; VP22 = HSV-1 VP22 protein. **(B)** Mean hydrodynamic size based on dynamic light scattering measurements. Errors indicate s.d. from at least 3 separate measurements. **(C)** Zeta-potential of nanocomplexes. Errors indicate s.d. from at least 3 independent measurements. ND, not determined.

Name	Sequence[A]	Diameter (nm)[b]	ζ-Potential (mV)[c]
3R	(dR)$_3$GGGGK(TAMRA)CGNKRTRGC	517.0 ± 33.9	7.8 ± 5.6
6R	(dR)$_6$GGGGK(TAMRA)CGNKRTRGC	364.3 ± 42.0	11.6 ± 8.6
9R	(dR)$_9$GGGGK(TAMRA)CGNKRTRGC	291.7 ± 21.2	ND
12R	(dR)$_{12}$GGGGK(TAMRA)CGNKRTRGC	175.5 ± 42.3	ND
15R	(dR)$_{15}$GGGGK(TAMRA)CGNKRTRGC	211.4 ± 18.9	ND
PEN	RQIKIWFQNRRMKWKKGGGGK(TAMRA)CGNKRTRGC	259.0 ± 36.1	ND
TAT	GRKKRRQRRRGYKGGGGK(TAMRA)CGNKRTRGC	175.3 ± 5.5	ND
TP	GWTLNSAGYLLGKINLKALAALAKKILGGGGK(TAMRA)CGNKRTRGC	310.5 ± 61.2	ND
VP22	DAATATRGRSAASRPTERPRAPARSASRPRRPVDGGGGK(TAMRA)CGNKRTRGC	253.5 ± 6.5	ND
m3R	myr-(dR)$_3$GGGGK(TAMRA)CGNKRTRGC	209.0 ± 40.5	21.8 ± 5.0
m6R	myr-(dR)$_6$GGGGK(TAMRA)CGNKRTRGC	151.0 ± 11.1	27.3 ± 4.0
m9R	myr-(dR)$_9$GGGGK(TAMRA)CGNKRTRGC	207.8 ± 19.6	36.6 ± 7.1
m12R	myr-(dR)$_{12}$GGGGK(TAMRA)CGNKRTRGC	191.2 ± 17.9	27.6 ± 15.0
m15R	myr-(dR)$_{15}$GGGGK(TAMRA)CGNKRTRGC	377.2 ± 49.4	36.0 ± 7.5
mPEN	myr-RQIKIWFQNRRMKWKKGGGGK(TAMRA)CGNKRTRGC	337.6 ± 54.9	29.0 ± 5.1
mTAT	myr-GRKKRRQRRRGYKGGGGK(TAMRA)CGNKRTRGC	194.6 ± 43.6	35.8 ± 8.0
mTP	myr-GWTLNSAGYLLGKINLKALAALAKKILGGGGK(TAMRA)CGNKRTRGC	343.6 ± 32.3	31.9 ± 3.7
mVP22	myr-DAATATRGRSAASRPTERPRAPARSASRPRRPVDGGGGK(TAMRA)CGNKRTRGC	233.0 ± 58.8	30.8 ± 4.8

6.2.2 Cellular uptake of TPNs

To effectively deliver siRNA, the carrier should exhibit high cellular uptake with minimal cytotoxicity. We examined a panel of established, human cancer cell lines and identified three (HeLa, MDA-MB-435, and OVCAR-8) that overexpress p32, the cognate receptor for the tumor-specific domain, LyP-1, on the cell surface. Viability of HeLa cells was not affected after TPN treatment for the majority of tandem peptides with the exception of 12R and 15R, whose excess cationic charges may have contributed to disruption of membrane integrity and reduction in cell viability (**Figure 6.6**).

To gain insight into the siRNA delivery capabilities of TPNs, we first assessed by flow cytometry the effect of NH_2-terminal myristoylation of the carrier on the cellular uptake of siRNA. In OVCAR-8 human ovarian cancer cells, the myristoylated species of the tandem peptides were significantly more efficacious in delivering fluorescently-labeled siRNA relative to their non-myristoylated counterparts (**Figure 6.7**). This may be due to enhanced particle stability due to hydrophobic interactions between myristoyl moieties, or enhanced interactions between myristoylated peptides and membrane lipids. To confirm that siRNA delivery was indeed correlated with uptake of the carrier, we repeated the experiments with tandem peptides singly labeled with tetramethylrhodamine (TAMRA) and compared intracellular peptide fluorescence with siRNA fluorescence for each peptide (**Figure 6.8**). In general, the relative cellular uptake of the carrier correlated linearly with that of the siRNA cargo. Short oligo-arginine CPPs such as 3R and 6R showed poor siRNA delivery in comparison to longer poly-arginines such as 12R and 15R, likely due to the lower number of cationic charges available to bind the negatively-charged siRNA backbone and provide sufficient charge shielding for membrane translocation. Similar patterns in cellular uptake were observed in MDA-MB-435 and

HeLa cells (not shown). Collectively, these results indicate that a subset of tandem peptides can effectively carry siRNA payloads into cell linesthat express p32 on the surface; additionally, *N*-terminal myristoylation of the peptide carrier can further enhance siRNA delivery into the cell.

Next, we assessed whether siRNA delivery by nanocomplexes is cell type-specific. To confirm p32 receptor-specificity, we examined by flow cytometry siRNA uptake in the presence of a monoclonal antibody (mAb 60.11) directed against the NH2-terminus of p32 polypeptide. In OVCAR-8 cells, uptake of nanocomplexes bearing CPP domains such as TAT, 9R, 12R, and 15R was unaltered in the presence of the antibody. In contrast, the p32 antibody reduced siRNA delivery by TP, 3R, 6R, and PEN nanocomplexes in a dose-dependent manner by up to 80% (**Figure 6.9**). Compared to cationic CPPs such as 12R and 15R that formed nanocomplexes at a peptide-to-siRNA molar ratio of nearly 1:1, TP-, 3R-, and 6R-LyP-1 nanocomplexes were formed at a ratio of at least 9:1. This difference in encapsulation likely resulted in nanocomplexes with a varying apparent valence of the LyP-1 ligand. Since multivalent receptor-ligand interactions enhance specificity through avidity effects [170, 203], the higher p32-affinity (lower IC_{50} of mAb) observed for the subset of nanocomplexes (TP, 3R, 6R) is attributable to multivalency effects.
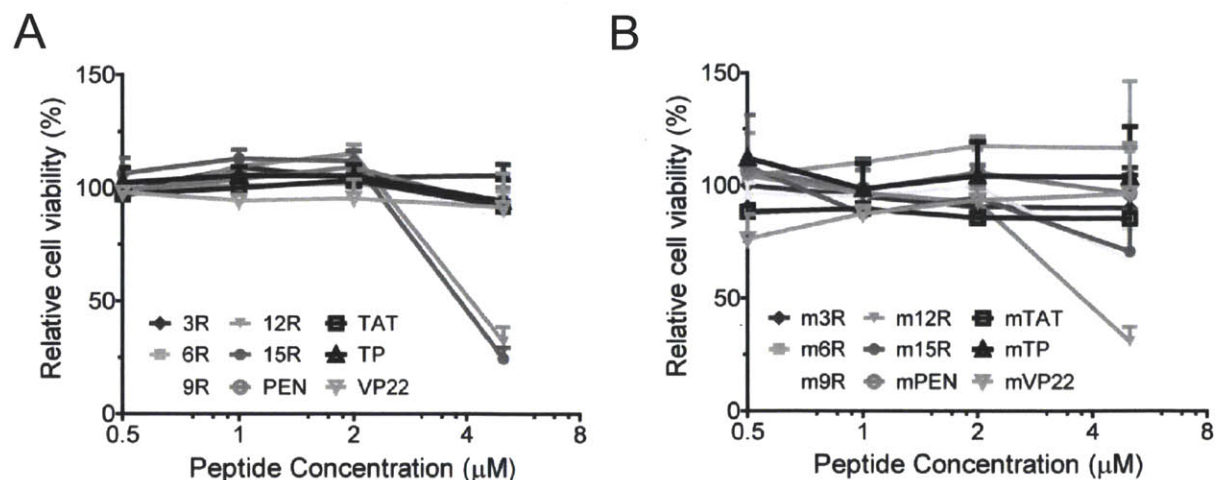
Figure 6.6. Cytotoxicity of TPNs. **(A)** Viability of HeLa cells after 4 h treatment with myristoylated tandem peptides at varying concentrations as determined by the MTT assay. Total viability was normalized to cells mock treated with media. **(B)** Viability of HeLa cells after 4 h treatment with unmyristoylated tandem peptide carriers. Error bars indicate s.d. from at least 4 independent measurements.
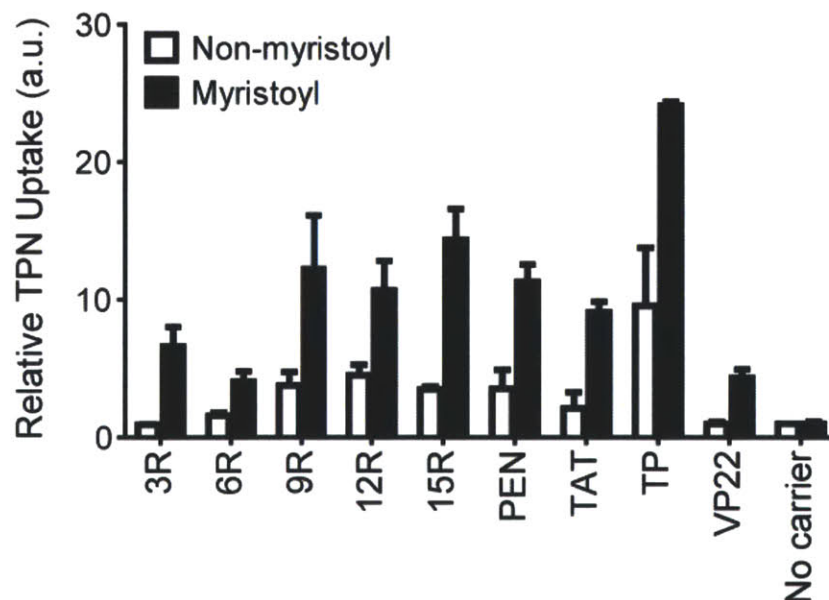
Figure 6.7. Cellular uptake of TPNs. OVCAR-8 ovarian cancer cells were incubated with TPNs carrying siRNA labeled with a near infrared fluorophore (VivoTag-S750). Cellular uptake is assessed by flow cytometry for both non-myristoylated and myristoylated tandem peptides. Error bars indicate s.d.from 4-6 independent experiments.
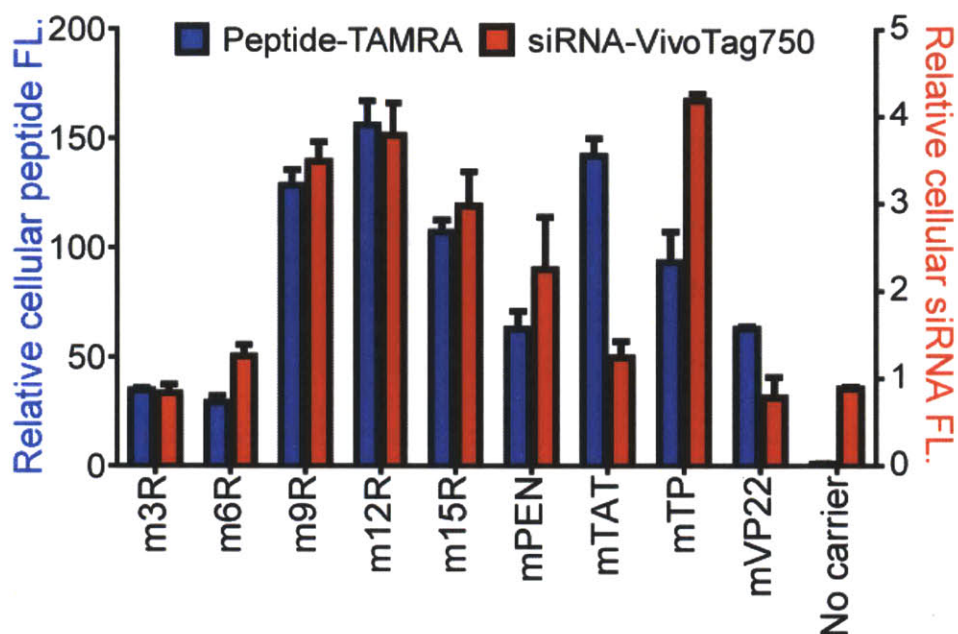
Figure 6.8. Cellular uptake of TPNs composed of TAMRA-labeled peptides (blue) and VivoTag-S750-labeled siRNA (red) in OVCAR-8 cells. Error bars indicate s.d.from 4-6 independent experiments.
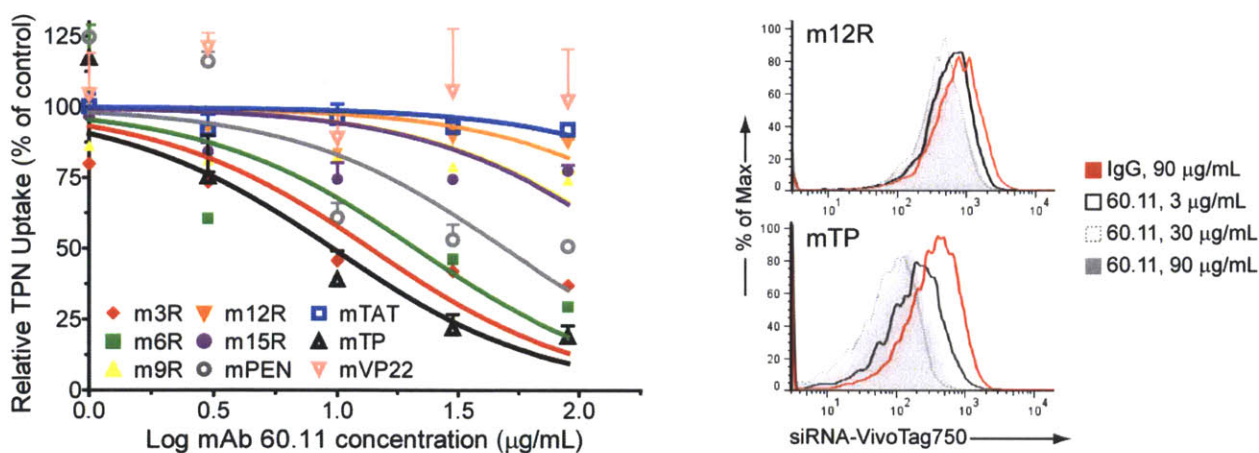
Figure 6.9. p32-specificity of TPN uptake. *Left,*TPN uptake by OVCAR-8 cells in the presence of increasing concentrations of a p32-specific monoclonal antibody (mAb 60.11) directed against the NH_2-terminus of p32 polypeptide. Uptake of nanocomplexes was normalized to that without antibody inhibition. Error bars indicate s.d. from 6 independent experiments. *Right,* Representative histograms from flow cytometry for cellular uptake of myr-12R-LyP-1 (top, m12R) and myr-TP-LyP-1 (bottom, mTP), in the presence of indicated concentrations of mAb 60.11 (black and gray) or a IgG control (red).

165

6.2.3 Gene silencing with TPNs

We next set out to determine *in vitro* gene silencing activity of siRNAs delivered by TPNs. HeLa cells stably expressing a destabilized green fluorescence protein reporter (dGFP) was used as a model system for direct quantification of the RNAi response. Cells were treated with siRNA against GFP bound to either tandem peptides or lipofectamine and analyzed by flow cytometry for GFP knockdown. Consistent with previous findings that myristoylation improves cellular uptake, myrisoylated carriers were more efficient in delivering siRNA and suppressing GFP expression than non-myristoylated ones (**Figure 6.10; Figure 6.11**). Six (6) of 9 tandem peptide carriers were able to silence GFP expression by over 50%, as determined by comparing the geometric means of the entire cell population. The amount of GFP suppression was correlated with the dose of siRNA (**Figure 6.12A**), was detectable starting at 24 h, and was maintained through at least 48 h after transfection (**Figure 6.12B**).

For tumor-specific siRNA delivery, an ideal system should target the delivery of siRNA to tumor cells while sparing non-tumor or essential cells, thereby achieving gene knockdown in a cell type-specific manner. To quantitatively assess the ability of nanocomplexes to deliver siRNA in a receptor-specific fashion, we measured the "fitness" of each candidate nanocomplex as the normalized sum of gene silencing efficiency and p32-receptor specificity (normalized $1/IC_{50}$ of mAb 60.11) (**Figure 6.13**). In particular, VP22 has low fitness because cellular uptake was non cell-type specific and gene knockdown was also poor. By contrast, nanocomplexes bearing polycationic CPP domains (12R and 15R) readily penetrated cellular membranes and carried siRNA into the cytosol; however, they do so in a non-cell type-specific manner as the presence of excess cationic charges likely abrogated receptor-specificity, resulting in low fitness. In comparison, cellular uptake by amphipathic CPPs such as PEN and TP is blocked by a p32-

specific antibody, suggesting that the receptor-specificity of the LyP-1 domain is retained; nevertheless, TP nanocomplexes are much efficient than PEN in suppressing gene expression. Indeed, the nanocomplex formed with myr-TP-LyP-1 has the highest fitness value of all carriers, owing to both potency in knockdown (> 50% suppression of GFP) and p32 receptor specificity (lowest IC_{50} of mAb 60.11).

A

B
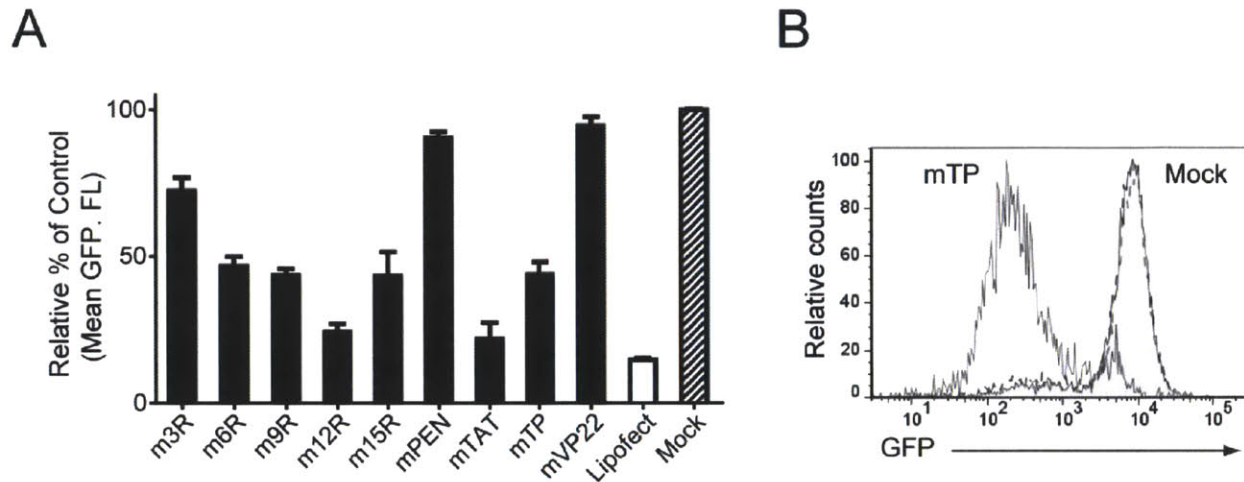
Figure 6.10. TPN-mediated receptor-specific gene silencing *in vitro*. (A) HeLa cells stably expressing destabilized GFP were transfected with TPNs carrying siRNA against GFP. The amount of GFP knockdown was determined by flow cytometry24 h later. Lipofectamine was used as a positive control. Error bars represent s.d. from cumulative data of three independent experiments. **(B)** Representative histograms for myr-TP-LyP1 nanocomplexes carrying *GFP*-specific siRNA. Mock treated cells are shaded in gray.
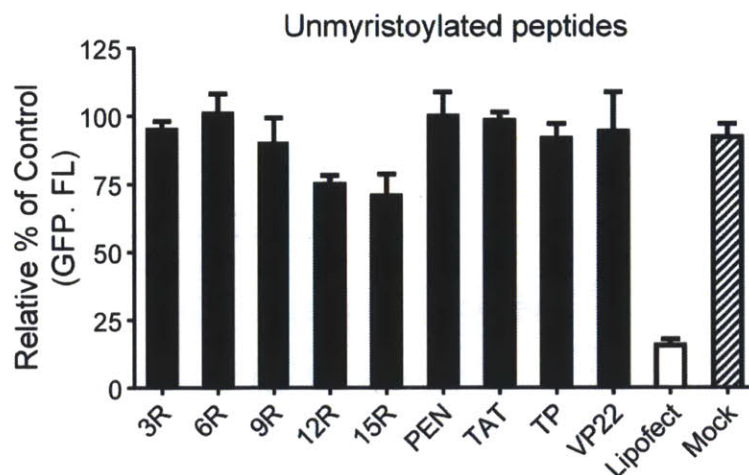
Figure 6.11. Gene silencing by unmyristoylated TPNs. (A) HeLa cells expressing destabilized GFP were transfected with non-myristoylated tandem peptides complexed to siRNA against GFP and analyzed by flow cytometry 24 h later. Lipofectamine was used as a positive control. Error bars indicate s.d. from 3 separate experiments.
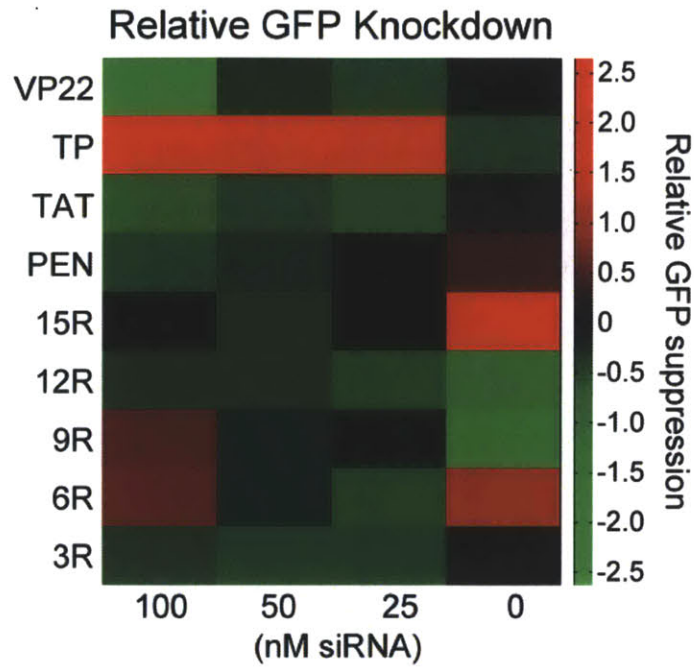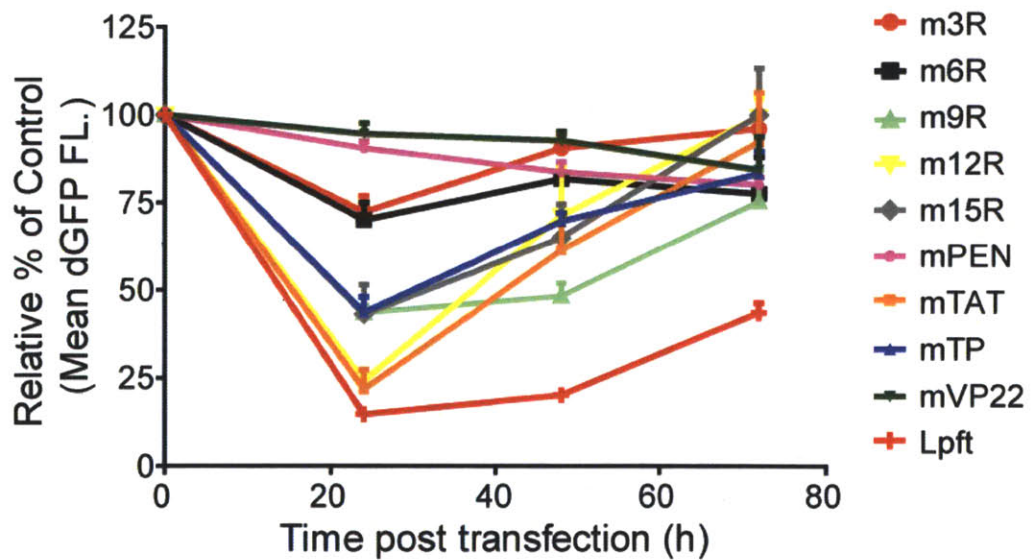
Figure 6.12. Gene suppression by TPN-mediated siRNA delivery. (A) GFP suppression by myristoylated TPNs carrying different concentrations of siRNA (100 nM, 50 nM, or 25 nM). For each siRNA concentration, the percent GFP knockdown for a particular TPN was shown after normalizing by the mean GFP knockdown of all TPN candidates at that siRNA concentration. The heat map is pseudocolored to indicate high efficiency in GFP knockdown (red) and low efficiency in knockdown (green). **(B)** Kinetics of GFP suppression by TPN candidates as determined by flow cytometry measurements at the indicated time points (24 h, 48 h, and 72 h) post transfection.
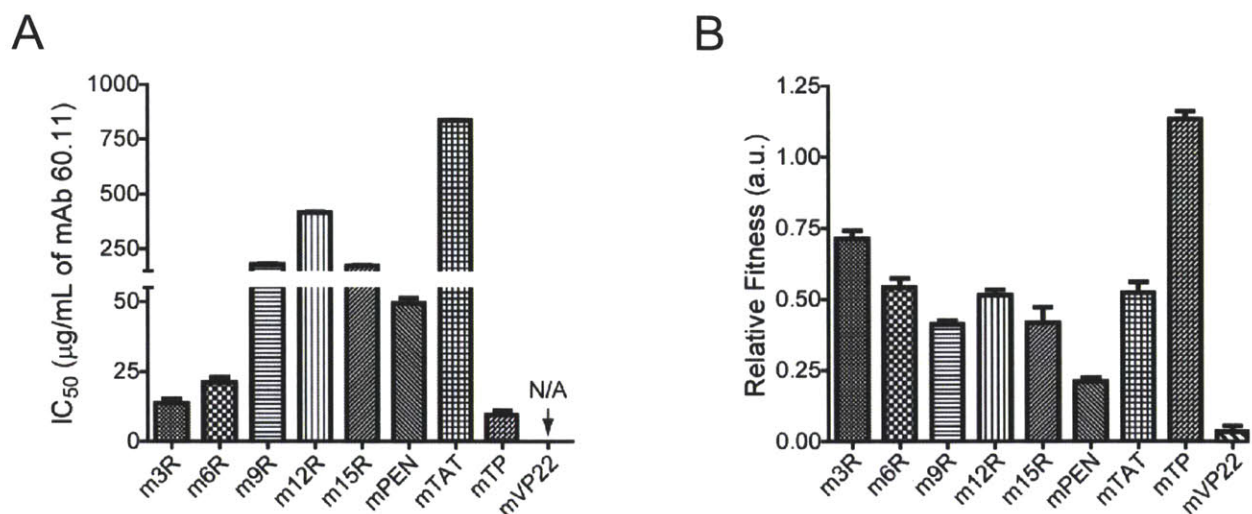
Figure 6.13. Fitness of nanocomplex candidates. (A) TPN receptor-specificity quantified as the concentration of p32-specific monoclonal antibody to inhibit TPN uptake by 50% (IC_{50}). Increasing concentrations of mAb 60.11 was added to cells for 1 h without TPN and subsequently in the presence of TPN for 4 h. Percent inhibition of TPN uptake was determined by flow cytometry. IC_{50} values were derived by fitting a standard normalized dose-response curve for inhibitory binding effects. **(B)** The fitness of each tandem peptide, as determined by the sum of knockdown efficiency and p32-specificity.

6.2.4 Intracellular trafficking of TPNs

Our results thus far have demonstrated that the tandem presentation of a tumor-homing ligand with various CPP domains can lead to varying degrees of fitness. To better understand the properties that favored the conversion of a ubiquitously internalizing CPP into a receptor-specific siRNA delivery system, we next investigated the intracellular trafficking mechanisms by which nanocomplexes carry siRNA into the cytosol.

We applied myr-TP-LyP-1 nanocomplexes carrying siRNAs labeled with a near-infrared fluorophore to HeLa cells and visualized intracellular trafficking via microscopy. Fluorescent siRNAs were present in punctate vesicular structures consistent with sequestration in endosomes (**Figure 6.14**). To directly confirm the intracellular localization of siRNAs, TPNs were applied to HeLa cells either expressing a marker of early endosomes (Rab5a) or pre-labeled with a pH-sensitive marker of endolysosomes (Lysotracker) (**Figure 6.14**). Fluorescently labeled siRNAs

showed co-localization with both markers, suggesting that nanocomplexes carried siRNA payloads into the cell via endocytosis and were initially sequestered in endosomes.

We next sought to directly evaluate the ability of nanocomplexes to disrupt the endosomal membrane of HeLa cells and trigger the cytosolic release of cargo by co-delivery with Calcein, a membrane-impermeable fluorophore [296]. In the presence of Calcein alone or with LyP-1 peptide without the CPP domain, a vesicular distribution indicative of little or no endosomal escape was observed. By contrast, diffuse Calcein staining in up to 30% of cells suggestive of endosomal escape was seen with 12R, 15R, and TP tandem peptides. Endosomal escape was carrier dose-dependent (**Figure 6.15**; **Figure 6.16**) and was partially dependent on the proton sponge effect [297], as the escape efficiency correlated linearly with the number of arginines. In addition, N-myristoylated peptides were generally more efficient in enabling Calcein entry into the cytosol than their non-myristoylated counterparts, consistent with enhanced interactions between myristic acid and membrane lipids on the endosome that likely generate transient pores to allow leakage of molecules [222]. Similar results in endosomal escape were observed in OVCAR-8 cells (**Figure 6.17**).

To identify the trafficking pathways by which nanocomplexes undertake after endocytosis, we examined the uptake of myr-TP-LyP-1 nanocomplexes in the presence of small molecule inhibitors that each blocks a component of the endocytosis pathway [152]. Uptake of TPN was significantly decreased when treated with amiloride, an inhibitor of macropinocytosis; and with PDMP, an inhibitor of lipid-raft mediated endocytosis; but not with inhibitors of actin polymerization, clathrin-mediated endocytosis, or caveolae-mediated endocytosis. Deoxyglucose, an inhibitor of ATP biosynthesis, also inhibited GFP knockdown (**Figure 6.18**).

In order to achieve gene knockdown, the carrier must ultimately dissociate from the siRNA cargo after escaping from the endosome to allow the incorporation of siRNA into the RISC machinery. To ascertain whether TPNs de-complex and release siRNA subsequent to escaping from the endosome, we measured the relative amount of siRNA that dissociated from the carrier upon exposure to endolysosomal pH (pH 4-6) via monitoring the intercalation of TO-PRO-3 dye (**Figure 6.19**). We observed that long poly-Arginine peptides such as 12R and 15R did not readily release siRNA at low pH, likely due to the large number of positively-charged Arginines that retarded the unpacking of siRNA. In comparison, amphipathic CPP species that are less cationic, such as PEN and TP, readily unpacked and dissociated from siRNA at acidic pH. Taken together, these observations support a siRNA delivery mechanism that consisted of receptor-mediated endocytosis mediated by macropinocytosis and lipid-rafts, followed by escape from endosomal entrapment, and release of siRNA at acidic pH.
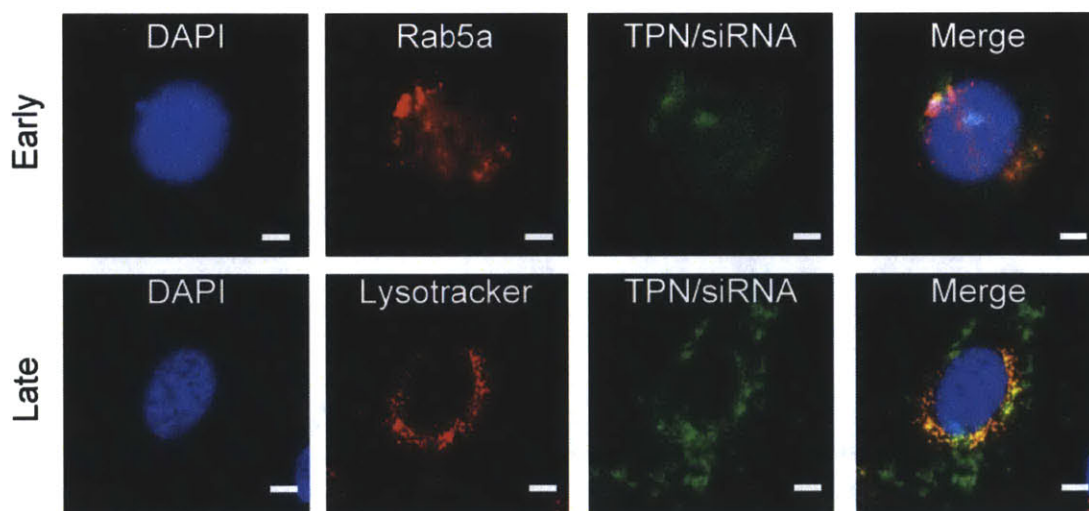
Figure 6.14. Intracellular trafficking mechanisms of TPNs.*Top,* Fluorescence microscopy images of human ovarian cancer cell line (OVCAR-8) transfected with Rab5a (CellLight™ Early Endosomes-GFP) 24 h prior (Early), and subsequently incubated with TPN carrying near infrared fluorophore-labeled siRNAs for 1 h. Images were pseudocolored for visualization: blue = DAPI; red = Rab5a; green = TPN/VivoTag-S750-siRNA. Co-localization of TPN with the early endosomal marker is shown in yellow. Scale bar, 10μm. *Bottom,* Fluorescence microscopy images of HeLa cells after 4 h treatment with 100 nM FITC-siRNA encapsulated in myr-TP-LyP-1 nanocomplexes, in the presence of 50 nM Lysotracker® dye to label late endosomes and endolysosomes (Late). Images are pseudocolored for visualization of co-localization: blue = DAPI; red = Lysotracker; green = FITC-siRNA. Scale bar, 10 μm.
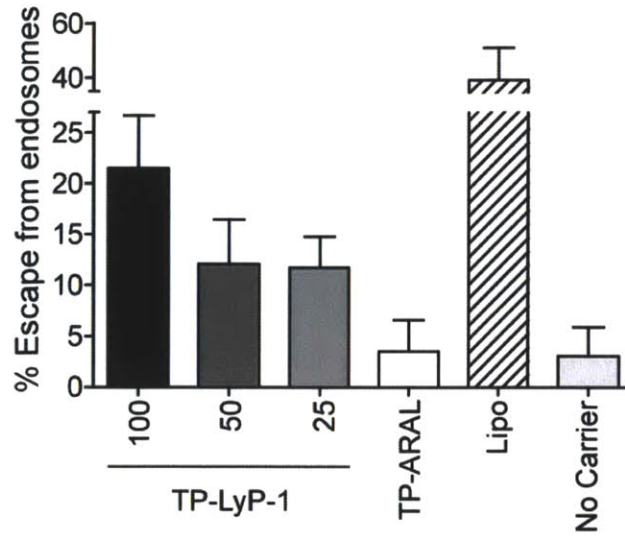
Figure 6.15. TPNs trigger endosomal escape. TPNs formed with myr-TP-LyP-1 peptides and siRNA trigger endosomal escape of siRNA in a carrier dose-dependent fashion (Black and shaded gray bars). TP-ARAL (white bar) did not trigger any significant escape beyond the negative control (no carrier, light gray). As a positive control, lipofectamine-mediated delivery resulted in ~40% cells showing endosomal escape of Calcein (hashed bar). Error bars indicate s.d. from 6 separate experiments.
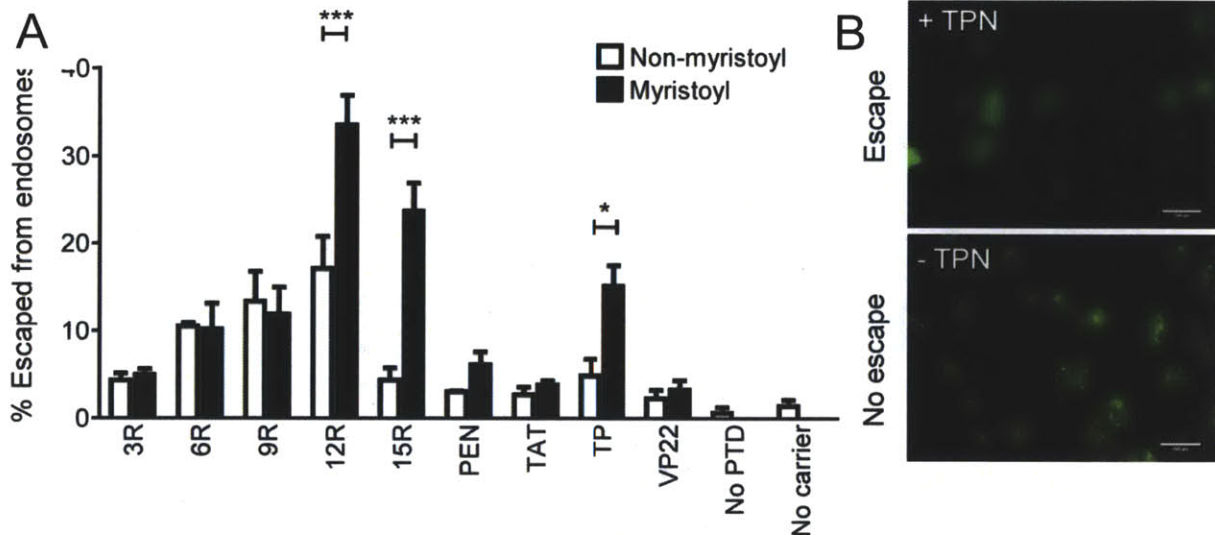
Figure 6.16. Tandem peptide carriers enable the delivery of Calcein, a membrane impermeant dye, into the cytosol of HeLa cells. (A) The mean percentage of cells displaying a uniform, cytosolic distribution of Calcein per each field of view was determined (n = 500-800 cells counted for each carrier). Error bars indicate s.d. from 3 independent experiments. *$p < 0.05$; ***$p < 0.001$. **(B)** Representative fluorescence microscopy images of HeLa cells treated with TPN + Calcein (top) or Calcein alone (bottom) (Green = Calcein).
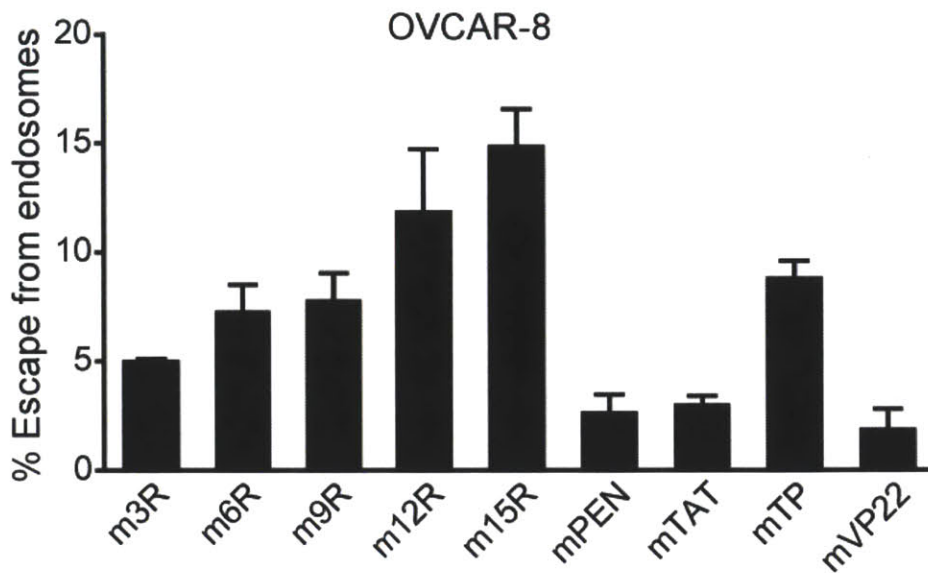
Figure 6.17. TPNs trigger endosomal escape of co-delivered cargo in OVCAR-8 cells. Myristoylated tandem peptide carriers enable the delivery of Calcein into the cytosol of OVCAR-8 cells. Error bars indicate s.d. from three separate experiments.
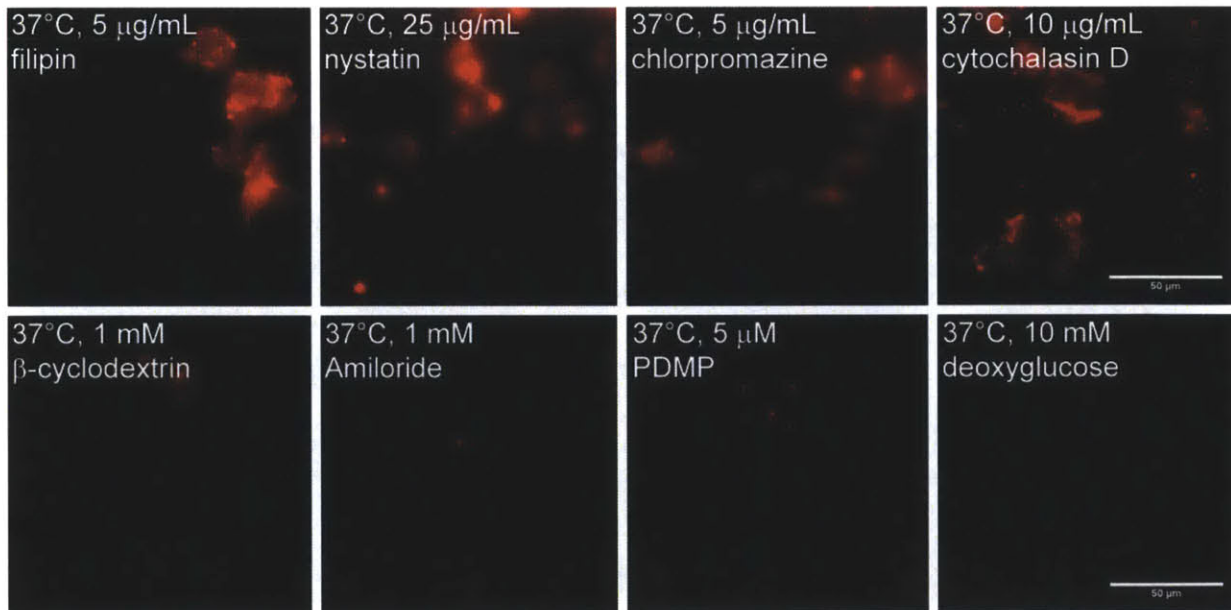
Figure 6.18. Intracellular trafficking of TPNs. Cellular uptake of myr-TP-LyP-1 nanocomplexes carrying FITC-labeled siRNA in the presence of small molecule inhibitors at the indicated concentrations. Scale bar, 50 μm.
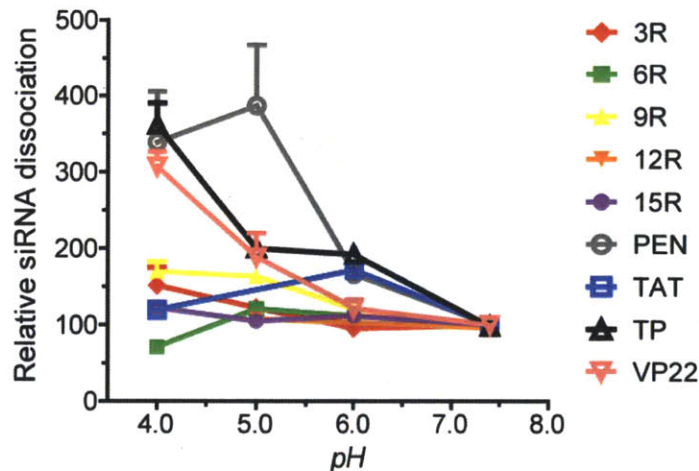
Figure 6.19. Quantification of the relative amount of siRNA dissociated from the nanocomplex carriers at endolysosomal pH (pH = 4-6).

6.2.5 Understanding structure-activity relationships

Nevertheless, the different fitness of nanocomplex candidates could only be partially

explained by differences in cellular uptake, endosomal escape, and rate of nanocomplex

dissociation. For example, the low fitness of PEN and VP22 peptides can be attributed to low

cellular uptake and endosomal escape activity, which resulted in poor siRNA. In contrast, 12R,

15R, and TP showed high cellular uptake and endosomal escape activity; however, they differ

significantly in fitness owing to differences in receptor-specificity. Therefore, other features of

TP nanocomplexes lacking in 12R or 15R dictate the efficiency and specificity of siRNA

transfection. As the optimized TPN formulation likely resides within a much broader and more

complex structural and functional space, a systematic screening of carrier structural parameters is

needed to identify and understand key properties that could impact fitness.

To this end, we took a quantitative computational approach to systematically identify carrier

properties that favored cell-type specific gene knockdown. We hypothesized that the relationship

between carrier properties and fitness is likely to be linear; therefore, a linear regression

approach that could establish a list of relative weights of significant model parameters was used

[298]. Specifically, we chose a regression model to generate relationships between carrier fitness – the efficiency of cell type-specific gene knockdown taken at two different siRNA concentrations (100nM and 50nM) and at two time points (24h and 48h) – and carrier structural properties, including diameter, zeta potential, valence of LyP-1, peptide charge at physiologic pH, percent of Lysine's or Arginine's and charge density (**Table 6.2**). To generate the data for the model, we screened every combination of structural parameters to select ones that were linearly independent and individually significant (T-test with $p<0.05$). Measurements for each parameter were centered and scaled to ensure that the value of the associated regression coefficient is a direct measure of parameter importance. The parameter subset that resulted in a model that best matched the measured fitness for each individual nanocomplex was selected for further analysis ($R^2=0.74$, $p<0.001$) (**Figure 6.20**).

Two structural properties, namely the valence of the targeting ligand and the peptide charge, were found to be significant variables for explaining differences in nanocomplex fitness (**Figure 6.21**). Namely, alterations in the valence of the targeting ligand or in peptide charge could exert the largest influence on cell type-specific knockdown by that nanocomplex. The regression coefficient for peptide charge was the most negative, suggesting that lowering peptide charge could enhance nanocomplex fitness. Consistent with our previous observations that multivalency favored high receptor-specificity; the regression coefficient for valence was the most positive, suggesting that increasing LyP-1 valence could also improve fitness.

To further validate the importance of LyP-1 valence and peptide charge in influencing cell type-specific gene knockdown, we separated all nanocomplex candidates into two groups based on their measured fitness values. Accordingly, nanocomplexes with high fitness (best fitness group) exhibited significantly higher peptide valence and lower peptide charge than those

with low fitness ($p<9.7e^{-5}$ and $p<0.01$ by F statistic, respectively), trends that were consistent

with regression coefficients determined from the model (**Figure 6.22**). Similar analysis for other

selected parameters (concentration, diameter, zeta error and charge density) did not yield

statistically significant differences (data not shown). In aggregate, quantitative regression

analysis enabled us to identify and validate two carrier structural properties – the valence of the

targeting ligand and the peptide charge – that explained differences in nanocomplex fitness.
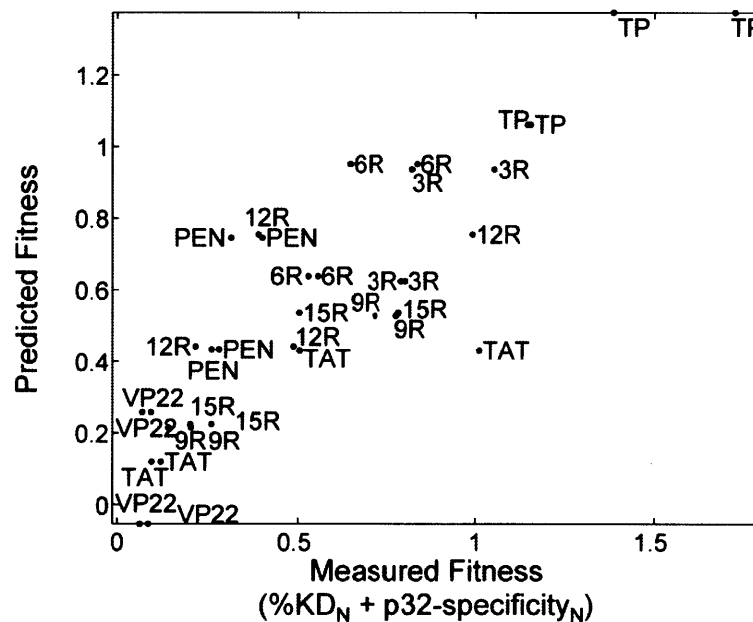
Figure 6.20. Computational modeling to identify carrier structural properties that influence fitness. Least square regression model used to predict carrier fitness versus measured fitness. The model is able to fit the data with $R^2=0.74$. Each data point represents the normalized fitness of a particular nanocomplex candidate at a specific siRNA concentration and time point post transfection.
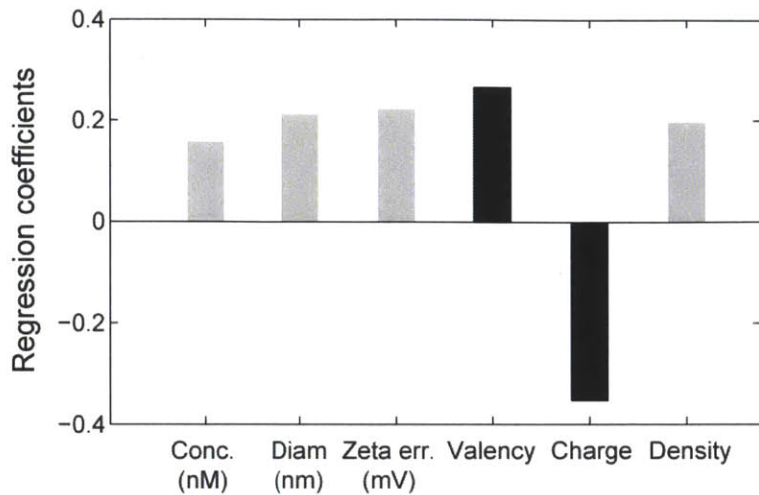
Figure 6.21. Regression coefficients of the structural properties determined to be significant in predicting fitness. The nanocomplex valence of the targeting ligand and the peptide charge (black) havethe highest impact on nanocomplex fitness.
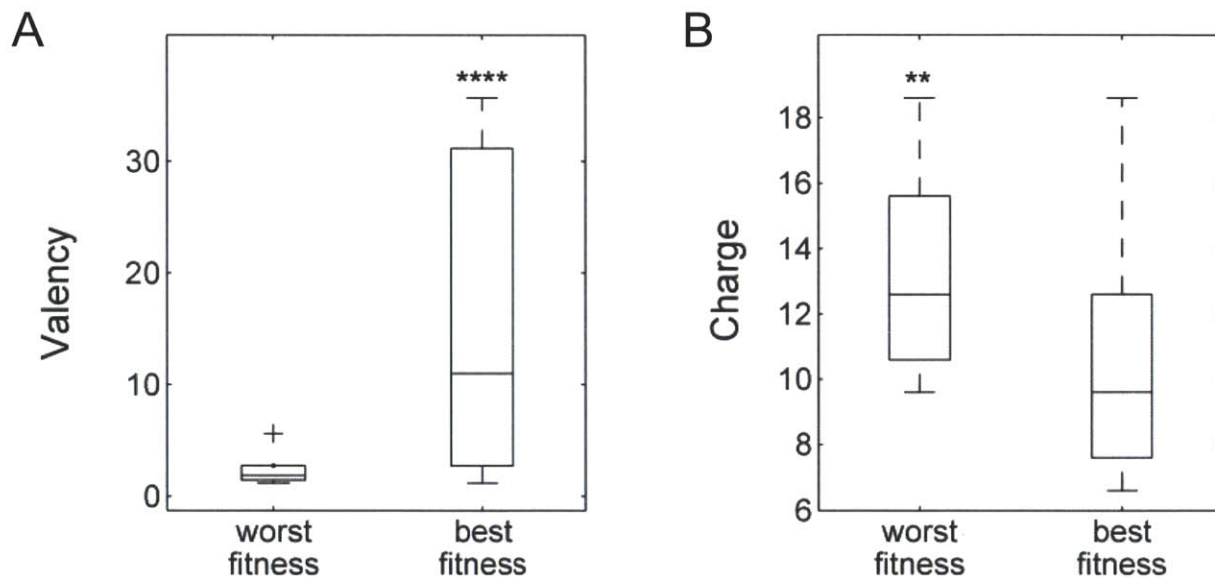
Figure 6.22. Nanocomplex populations were separated into two groups based on individual fitness (best fitness and worst fitness). The average LyP-1 valence of the nanocomplex (left) and peptide charge (right) are calculated for each group and compared. Consistent with regression results, significant separations between the groups confirmed the positive impact of valence and the negative impact of peptide charge on fitness. $**p < 0.01$; $****p < 0.0001$.

Table 6.2. Parameters used in the computational analysis. For linear regression analysis of fitness, the input parameters included: concentration of TPNs, time of transfection, hydrodynamic size, zeta potential, valence of the tumor-specific ligand, charge of the peptide at neutral pH, percent of amino acids that is either Lysine or Arginine, and the overall charge normalized by number of amino acids.

177

Conc (nM)	Time (h)	Diameter (nm)	Diam. err. (nm)	Zeta (mV)	Zeta err. (mV)	LyP-1 valence	Peptide charge	% K and/or R	Charge density
100	24	209	40.5	21.8	5	11.03	6.6	41.18	0.39
100	24	151	11.1	27.3	4	31.16	9.6	50	0.48
100	24	207.8	19.6	36.6	7.1	2.732	12.6	56.52	0.55
100	24	191.2	17.9	27.6	15	1.186	15.6	61.54	0.6
100	24	377.2	49.4	36	7.5	1.912	18.6	65.52	0.64
100	24	337.6	54.9	29	5.1	5.604	10.6	36.67	0.35
100	24	194.6	43.6	35.8	8	1.843	12.6	48.15	0.47
100	24	343.6	32.3	31.9	3.7	35.68	7.6	19.51	0.19
100	24	233	58.8	30.8	4.8	1.457	9.6	27.08	0.2
100	48	209	40.5	21.8	5	11.03	6.6	41.18	0.39
100	48	151	11.1	27.3	4	31.16	9.6	50	0.48
100	48	207.8	19.6	36.6	7.1	2.732	12.6	56.52	0.55
100	48	191.2	17.9	27.6	15	1.186	15.6	61.54	0.6
100	48	377.2	49.4	36	7.5	1.912	18.6	65.52	0.64
100	48	337.6	54.9	29	5.1	5.604	10.6	36.67	0.35
100	48	194.6	43.6	35.8	8	1.843	12.6	48.15	0.47
100	48	343.6	32.3	31.9	3.7	35.68	7.6	19.51	0.19
100	48	233	58.8	30.8	4.8	1.457	9.6	27.08	0.2
50	24	209	40.5	21.8	5	11.03	6.6	41.18	0.39
50	24	151	11.1	27.3	4	31.16	9.6	50	0.48
50	24	207.8	19.6	36.6	7.1	2.732	12.6	56.52	0.55
50	24	191.2	17.9	27.6	15	1.186	15.6	61.54	0.6
50	24	377.2	49.4	36	7.5	1.912	18.6	65.52	0.64
50	24	337.6	54.9	29	5.1	5.604	10.6	36.67	0.35
50	24	194.6	43.6	35.8	8	1.843	12.6	48.15	0.47
50	24	343.6	32.3	31.9	3.7	35.68	7.6	19.51	0.19
50	24	233	58.8	30.8	4.8	1.457	9.6	27.08	0.2
50	48	209	40.5	21.8	5	11.03	6.6	41.18	0.39
50	48	151	11.1	27.3	4	31.16	9.6	50	0.48
50	48	207.8	19.6	36.6	7.1	2.732	12.6	56.52	0.55
50	48	191.2	17.9	27.6	15	1.186	15.6	61.54	0.6
50	48	377.2	49.4	36	7.5	1.912	18.6	65.52	0.64
50	48	337.6	54.9	29	5.1	5.604	10.6	36.67	0.35
50	48	194.6	43.6	35.8	8	1.843	12.6	48.15	0.47
50	48	343.6	32.3	31.9	3.7	35.68	7.6	19.51	0.19
50	48	233	58.8	30.8	4.8	1.457	9.6	27.08	0.2

6.2.6 Quantifying the multivalency effect

Guided by the computational results, we further quantified the receptor-specificity and multivalency effects of myr-TP-LyP-1 nanocomplexes. In four (4) human cancer cell lines with varying p32 expression, we found that the uptake of TP nanocomplexes was enhanced relative to TPNs bearing a scrambled peptide (TP-ARAL), while remained linearly correlated with surface p32 levels across different cell lines (**Figure 6.23**).

In contrast to monovalent LyP-1 peptides, TP-LyP-1 nanocomplexes have higher affinity to cell surface p32, as demonstrated by the lower measured EC_{50} (concentration to produce 50% of maximal cellular binding) in two p32-expressing cell lines (**Figure 6.24**). The apparent dissociation constant (K_D) of TPNs was found to be 10-20 fold higher than that of free LyP-1 peptide ($K_{D,TPN}$ = 215 nM; $K_{D,LyP-1}$ = 5.6 μM), consistent with multivalent nanoparticle systems reported elsewhere [203]. TPN cellular uptake was saturated at higher concentrations, which further supports that TPN was taken up in a receptor-mediated manner (**Figure 6.25**).

To better understand how the number of LyP-1 peptides displayed on the nanocomplex influenced cellular binding, we synthesized TPNs with a mixture of TP-LyP-1 and TP-ARAL peptides. Mixed TPNs exhibited saturated uptake at a peptide-to-siRNA ratio of at least 10:1 (**Figure 6.26**). As the density of LyP-1 ligands exceeds the amount of p32 available for binding, additional LyP-1 peptides will likely not engage in receptor-mediated endocytosis and uptake will likely be saturated. Taken together, these results confirmed that p32 expression dictated siRNA delivery by multivalent nanocomplexes formed with myr-TP-LyP-1 tandem peptides.
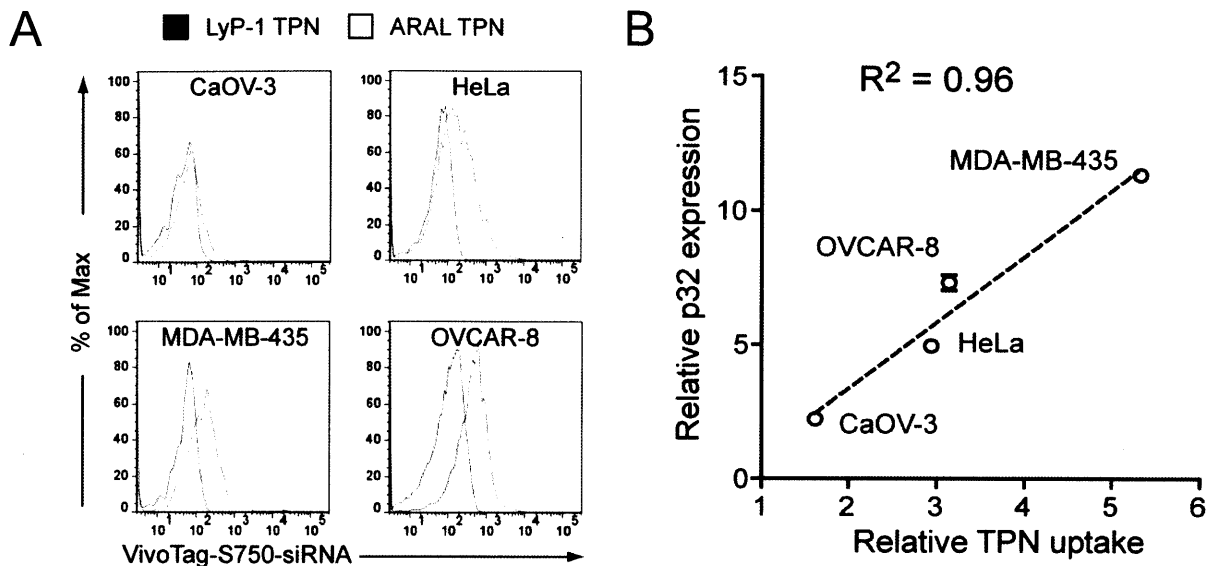
Figure 6.23. The myr-TP-LyP-1 nanocomplex delivers siRNA in a p32-specific manner and is multivalent. (A) Flow cytometry analysis showing cellular uptake of TP-LyP-1/siRNA-VivoTag-S750 nanocomplexes (LyP-1 TPN, black) in cancer cell lines. Uptake of scrambled TPNs consisted of TP-ARAL/siRNA-VivoTag-S750 (ARAL TPN, gray) was used as a negative control.**(B)** The relationship between surface p32 levels and the cellular uptake of TPNs carrying siRNA-VivoTag750 in four (4) human cancer cell lines that express varying amounts of p32, including cervical (HeLa), melanoma (MDA-MB-435) and ovarian (OVCAR-8 and Caov-3) cancer cells. Uptake was quantified using flow cytometry and normalized to that of a scrambled peptide control, TP-ARAL.
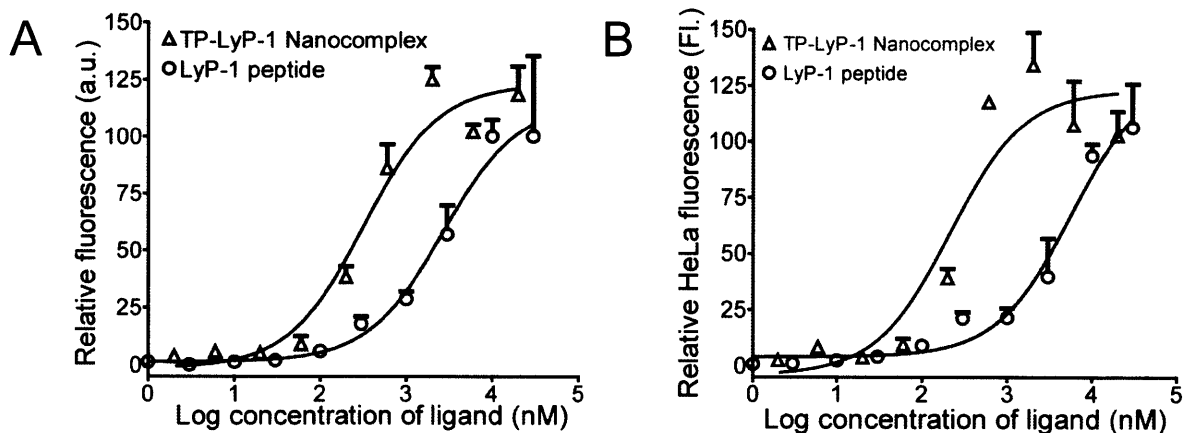
Figure 6.24. Quantification of the multivalency effect of TPNs. (A) Uptake of LyP-1 TPNs versus monovalent LyP-1 peptide in MDA-MB-435 cells.**(B)** Uptake of varying concentrations of LyP-1 TPNs (red) or monovalent LyP-1 peptides (blue) in HeLa cells. Error bars indicate s.d. from three independent experiments.

180
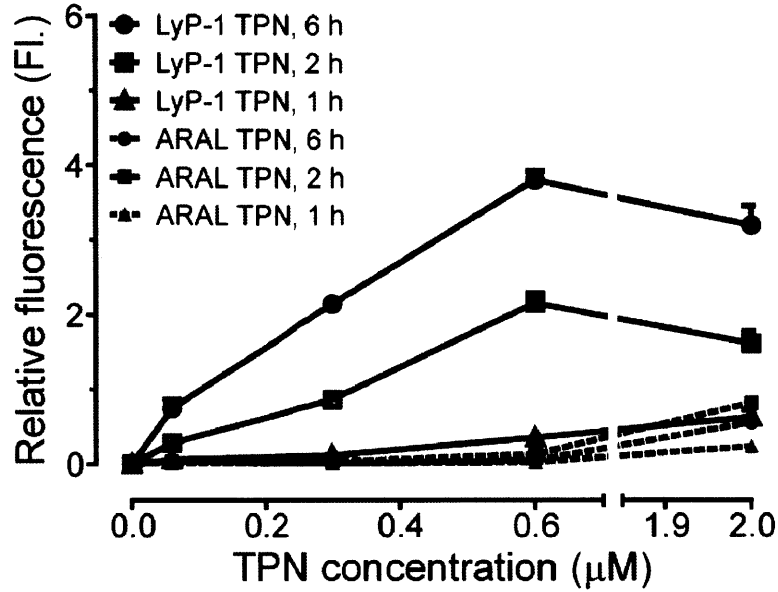
Figure 6.25. Uptake of nanocomplexes in HeLa cells over time. LyP-1 TPNs or ARAL TPNs are incubated over cells at various concentrations for the indicated times and cellular TPN fluorescence was determined by flow cytometry. Error bars represent s.d. from 3 separate experiments.
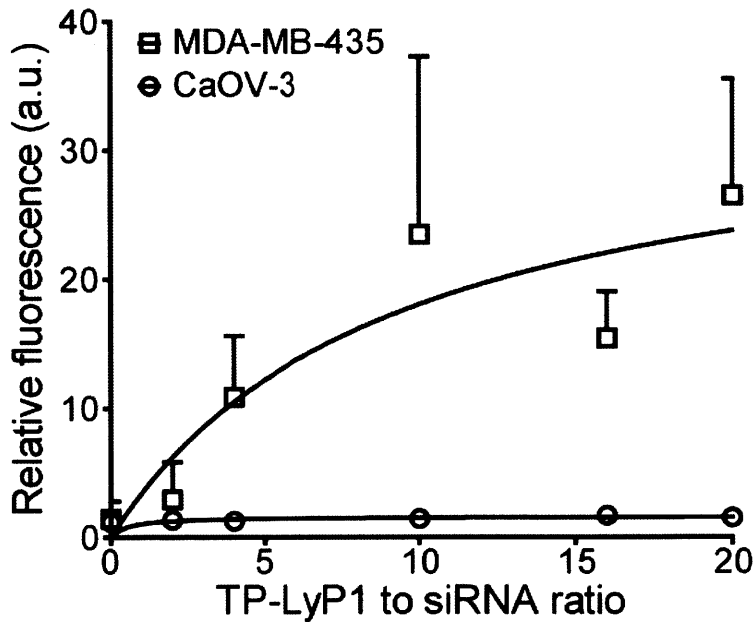
Figure 6.26. Uptake of TPNs bearing a mixture of TP-LyP-1 peptides and TP-ARAL peptides in MDA-MB-435 and Caov-3 cells measured by flow cytometry.

6.3 Conclusion

To design vehicles for cell type-specific siRNA delivery, there are several barriers the delivery system must negotiate before achieving gene knockdown. These include receptor-mediated cellular binding, internalization by endocytosis, escape from endosomal sequestration into the cytosol, and ultimately, dissociation of siRNA from the carrier for RISC incorporation. Each step can influence the fate of the intracellular cargo, which in turn affects the receptor-specificity and efficiency of gene knockdown. Here, we have taken a systematic, quantitative approach to designing and understanding peptides for cell type-specific siRNA delivery. To this end, we synthesized a library of tandem peptides bearing a tumor-specific domain and distinct cell-penetrating domains, and formed nanocomplexes with siRNA through non-covalent interactions. A subset of nanocomplexes delivered siRNA to human cancer cell lines that express the cognate p32 receptor on the surface. We further evaluated the mechanism by which nanocomplexes delivered siRNA to the cytosol by characterizing cellular uptake, endosomal escape, and siRNA dissociation.

Comparative analysis of 18 tandem peptides revealed that variations in structural properties had a significant impact on receptor-specificity and gene silencing efficiency. Powered by linear regression modeling, we identified the valence of the targeting ligand on the nanocomplex and the overall peptide charge as key structural properties that favored cell-type specific gene silencing. The analysis led to the identification of the myristoylated tandem peptide, myr-TP-LyP-1, which condensed siRNA into multivalent nanocomplexes and effectively delivered siRNA in a cell-type specific manner. This advancement suggests that a systematic approach to the design of cell-penetrating peptides is essential for optimizing tumor-specific delivery of siRNA therapeutics for therapeutic applications.

6.4 Materials and Methods

DLS and Zeta Potential. Peptide-siRNA nanocomplexes were prepared by mixing siRNA in nuclease-free H_2O ($20\mu M$) with each tandem peptide carrier ($400\mu M$) at a molar ratio of 1:20 (siRNA:peptide) in 1/5 of final volume in PBS for 10-15 min at room temperature. The hydrodynamic radii and zeta potential of nanocomplexes were determined using the zeta-potential and dynamic light scattering (DLS) instrument (Zetasizer-Nano, Malvern, Inc.).

Nanocomplex library gene silencing and uptake. To measure the cellular uptake of the TP-LyP1/siRNA nanocomplex, OVCAR-4, OVCAR-8, CaOV-3, and MDA-MB-435 cells were plated 48 h prior in 96-well plates and allowed to reach at least 70% in confluency. Nanocomplexes were added at 100nM siRNA/2 uM peptide for 2 h at 37 °C in serum-free DMEM. Cells were then washed with PBS/heparin, trypsinized, and analyzed by flow cytometry (LSR II). For TP-LyP1 nanocomplex blocking experiments with anti-p32 antibody, OVCAR-8 cellswere pre-incubated with anti-p32 polyclonal antibodyat specified concentrations for 1 h at 37 °C before nanocomplex treatment.

Endosomal Escape. HeLa and OVCAR-8 cells were plated 48 h prior in 96-well plates and allowed to reach at least 70% in confluency. Calcein (0.25mM) dye was added with or without various nanocomplex formulations (100nM siRNA, 2uM of carrier) in complete medium (DMEM with 10% bovine serum) for 1 h at 37 °C. The cells were then washed three times with PBS and visualized live with a fluorescence microscope using the FITC filter. The number of cells with efficient endosomal escape as indicated by a diffuse cytoplasmic FITC fluorescence was counted from at least 8 randomly selected fields of view and normalized to the total number of cells (n = 500-800 cells per carrier in each experiment).

Inhibition of endocytosis and imaging. HeLa cells grown in 96-well plates at ~70% confluence were incubated with small molecule inhibitors for 1 h at 37 °C, followed by incubation with nanocomplexescontaining both labeled peptide (2 μM) and GFP siRNA (100 nM) for an additional hour at 37 °C. The cells were washed three times with cold PBS and were subsequently trypsinized for flow cytometry analysis. To visualize the intracellular trafficking of nanocomplexes along with endosomal markers, Lysotracker Red DND-99 (Invitrogen) or CellLight Early Endosomes-RFP (Invitrogen) was prior to the addition of nanocomplexes according to manufacturer's instructions.

7 Receptor down-regulation improves the microdistribution of tumor-targeted theranostics

7.0 Abstract

Nanotechnology is an emerging field that has tremendous potential for developing new diagnostics and therapeutics for cancer. However, delivery of tumor-targeted nanoparticles into tumors is challenging due to the presence of so-called "binding site barrier"; spatial heterogeneities in receptor expression can lead to a non-uniform intratumoral distribution of nanoparticles. Here, we present a strategy to improve the tumor microdistribution and penetration of targeted nanoprobes through the systematic down-regulation of their cognate receptors in the tumor. We utilized tumor-penetrating nanocomplexes (TPN) developed in *Chapters 3 through 5* that target p32, a receptor overexpressed on the surface of cancer cells, and deliver siRNA payloads directed against *p32* to suppress its surface expression. We find that TPN suppressed p32 expression in multiple human cancer cell lines *in vitro*. In mice bearing tumor xenografts that express p32, down-regulation of p32 in perivascular tumor cells led to mitigation of the binding barrier, improved tumor penetration of successively administered TPN, and upregulation of glycolytic metabolism in tumors that is exploitable by PET imaging. Thus, strategies to modulate receptor expression should enhance the tumor microdistribution of targeted nanoparticles for diagnostic and therapeutic applications.

7.1 Introduction

Nanometer-sized carriers are an attractive platform for cancer drug delivery due to their ability to stabilize and protect drugs from degradation, prolong drug *in vivo* half-life by decreasing renal clearance, and enhance tumor accumulation *via* targeting. Since tumor blood vessels are malformed and leaky, long-circulating nanoparticles decorated with polyethylene glycol (PEG) can selectively extravasate from pores within the fenestrated endothelium. While some nanoparticle therapeutics such as Doxil and Myocet exploit this enhanced permeability and retention (EPR) effect for passive tumor targeting, EPR is not a constant feature of the tumor endothelium [300]. Moreover, additional barriers such as the highly pressurized tumor interstitial matrix must be negotiated before nanoparticles can reach the tumor cells [79, 89].

Elsewhere, nanocarriers have been decorated with homing ligands that specifically bind to markers that distinguish cancer cells from normal counterparts. High-throughput screening technologies using libraries of aptamers and bacteriophage-displayed peptides have enabled the identification of a wealth of ligands with extraordinary tumor specificity [118, 172, 200, 211]. For example, peptides containing the Arg-Gly-Asp (RGD) motif have been shown to enhance tumor drug delivery by binding to $\alpha v\beta 3$ and $\alpha v\beta 5$ integrins that are overexpressed in tumor endothelium [301]. Nonetheless, recent studies suggested that active targeting does not increase overall tumor accumulation, as the rate limiting step in tumor targeting is typically during extravasation through vascular pores [129, 302-303]. Furthermore, uniform tumor delivery is hampered by heterogeneities in tumor blood supply and hindered diffusion [304]. Therefore, strategies are still needed to improve the tumor penetration and distribution of nano-therapeutics.

In *Chapters 3 through 5*, we have described system of tumor-penetrating nanocomplexes (TPN) that could overcome these tumor transport barriers by chaperoning nucleic acid

185

therapeutics such as siRNA deep into the parenchyma of disseminated ovarian tumors in mice [213]. The homing peptide domain, LyP-1 (CGNKRTRGC), is tumor-specific and binds p32, a mitochondrial protein aberrantly expressed on the surface of cancer cells. While this approach is promising, histological examination of tumors repeatedly dosed with TPN revealed a heterogeneous TPN distribution that is mostly concentrated around the vasculature, likely owing to the presence of the so-called "binding site barrier" for nanoparticles directed by tumor-targeting probes. Namely, if the targeted probe cannot initially saturate the receptor binding capacity and the receptors can regenerate before the next dose of nanoparticles is introduced, successive TPN will bind to unoccupied receptors near the vasculature and will not diffuse further into the tumor. Indeed, experimental and theoretical analyses on antibody targeting have shown that low affinity antibodies or antibodies targeting antigens with low expression levels show improved penetration and distribution, due to their ability to dissociate from the receptor after binding and subsequently penetrate further into the tissue [305-307]. While antibody engineering approaches have enabled the precise tuning of antigen affinity for enhanced penetration [308], similar methods to optimize nanoparticle penetration has yet to be achieved.

In this work, we hypothesize that down-regulation of receptor expression in a temporal- and spatial-specific manner can improve the tumor microdistribution of targeted nanoprobes. Specifically, we investigated whether reducing the perivascular interactions between TPN and p32, its cognate receptor, can improve the *in vivo* tumor uptake and penetration of successively administered TPNs (**Figure 7.1**). First, TPN delivery of *p32*-specific siRNA was evaluated in cancer cell lines. Next, the effects of *in vivo* p32 receptor knockdown on tumor uptake, penetration and microdistribution of TPN are studied mice bearing tumor xenografts. Finally, the utility of p32 suppression for functional tumor imaging *via* PET/CT is also explored.
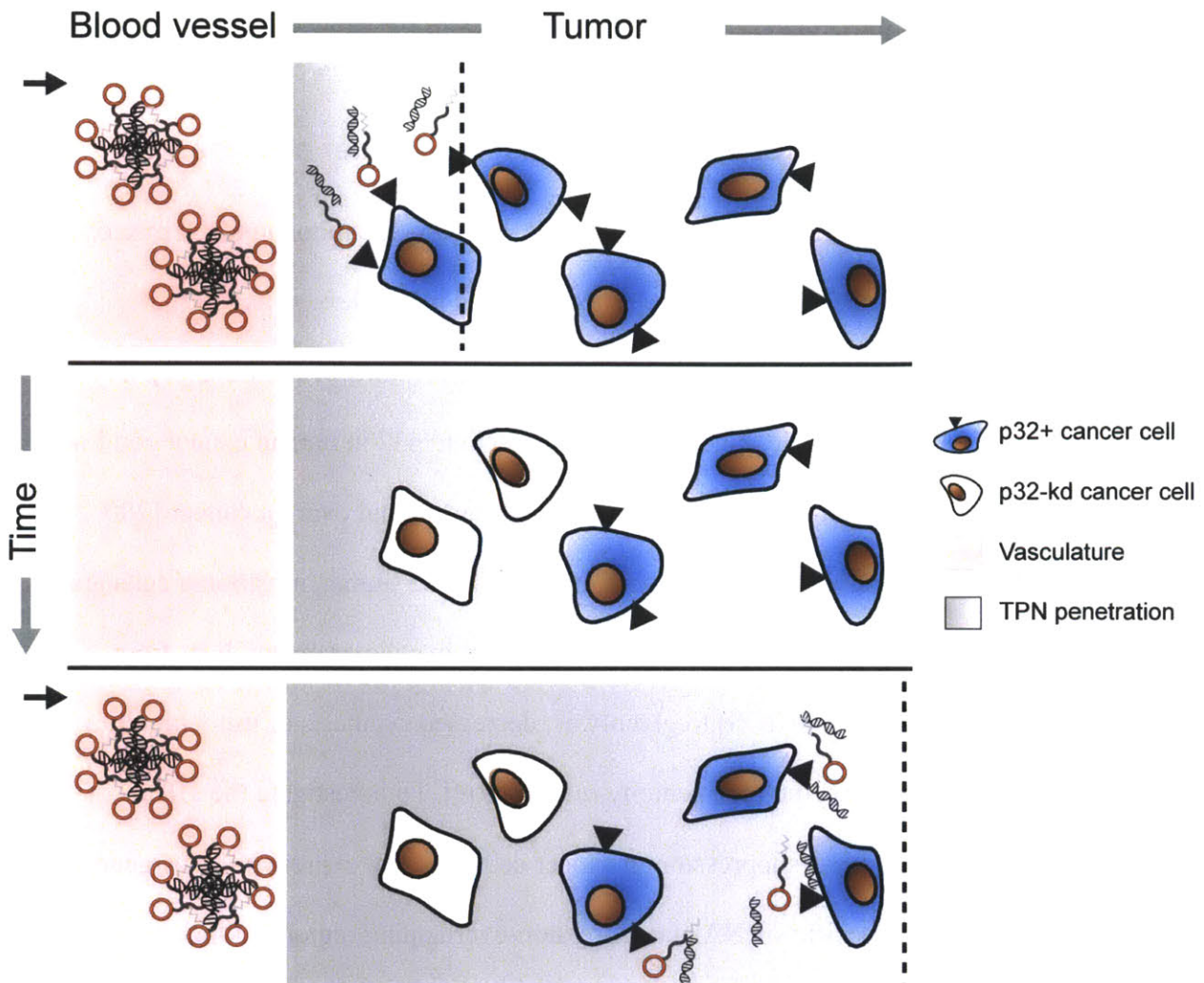
Figure 7.1. Schematic demonstrating the improvement in TPN microdistribution via modulation of receptor expression in the tumor microenvironment. A time-dependent analysis showing TPN penetration into the tumor parenchyma subsequent to extravasation from blood vessels. *Top,* TPN intratumoral diffusion is limited by the binding barrier located in regions immediately adjacent to the vasculature. *Middle,* TPN deliver y of siRNA can suppress receptor expression in tumor cells located near the vasculature. *Bottom,* Successive TPN administrations can now diffuse further into the tumor and bypass the binding barrier, which are ultimately taken up by receptors located on the surface of tumor cells further away from vasculature.

7.2 Results

7.2.1 Down-regulation of p32 in p32-expressing cancer cell lines

p32 (p33/HABP1/gC1qR), a protein primarily located in the mitochondrial matrix, is located on the cell surface of tumor cells and is expressed at higher levels than in their nonmalignant counterparts [217, 309]. The homing domain of tumor-penetrating siRNA nanocomplexes, LyP-1, is a cyclic nonapeptide shown to bind p32 in human cancer cell lines from several tumor types, including melanoma, cervical cancer, and ovarian cancer [200, 217]. Previously, stable p32 knockdown by shRNA in MDA-MB-435 human melanoma cells and MDA-MB-321 human breast cancer cells resulted in a shift in cellular metabolism from oxidative phosphorylation (OXPHOS) to glycolysis, decreased synthesis of mitochondrial OXPHOS proteins, and reduced tumorigenicity *in vivo* [309]. To investigate the effects of transient, siRNA-mediated p32 suppression in cancer cell lines that express p32, we generated TPN carrying three *p32*-specific siRNAs targeting non-overlapping regions of the exon. In OVCAR-8 human ovarian cancer cells, delivery of *p32*-specific siRNA (si*P32* #2) reduced *p32* mRNA by over 90% compared to a control siRNA, with a corresponding reduction in p32 protein (**Figure 7.2**). Gene knockdown is dependent on LyP-1-mediated cellular uptake, as untargeted control nanocomplex (UCN) bearing a scrambled homing peptide (ARAL, ARALPSQRSR) did not suppress p32 (**Figure 7.3**). To determine whether p32 knockdown is generalizable across cell lines derived from distinct tumor types, we further evaluated the efficacy of TPN-mediated siRNA delivery in cells from ovarian (OVCAR-4), cervical (HeLa), and skin cancers (MDA-MB-435). All showed reduction of *p32* mRNA and protein levels 48 h after TPN/si*P32* treatment but not with TPN/si*GFP* (**Figure 7.4**).

The affinity of the LyP-1/p32 interaction dictates the cellular uptake of TPN *in vitro* and tumor retention *in vivo*. According to the binding barrier model of antibodies [308, 310], the local concentration of free antibodies that is dissociated from the receptor determines the amount available to diffuse into the tumor. The importance of antibody availability was further underscored in studies that showed antigen expression can profoundly affect antibody penetration [311-312]. Therefore, we postulated that reducing p32 expression on the cell surface can effectively decrease the binding sink for TPN, thereby allowing further extravasation and creating a more uniform intratumoral distribution. In two ovarian cancer cell lines (OVCAR-4 and OVCAR-8) and a cervical cancer cell line (HeLa), TPN delivery of *p32*-siRNA reduced cell surface p32 levels by over 50% as determined by flow cytometry, compared to cells treated with a scrambled, GFP-targeted siRNA (**Figure 7.5**). Taken together, TPN can transiently suppresses p32 expression in a receptor- and siRNA sequence-specific manner in multiple cell lines.
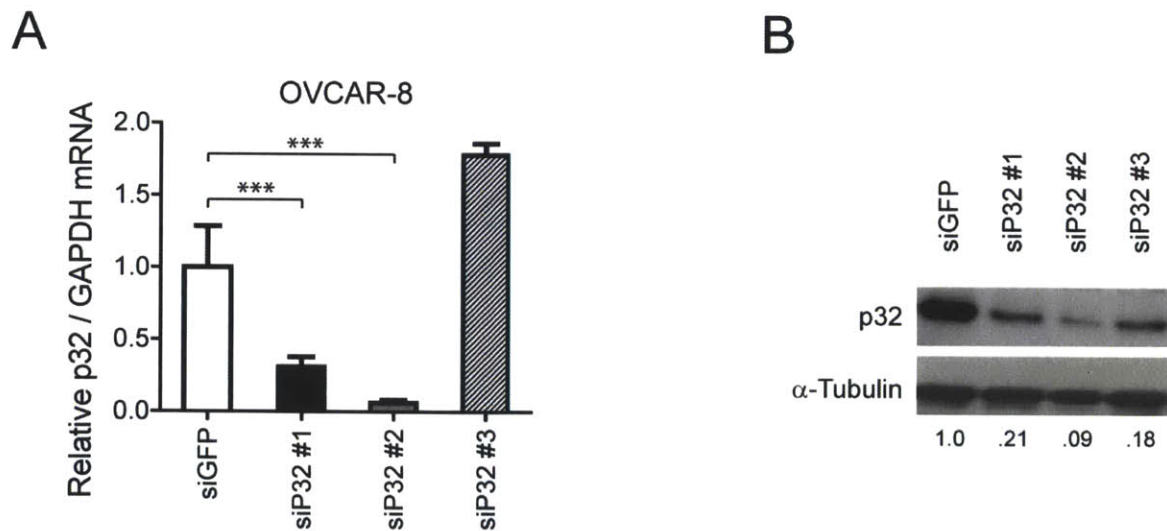
Figure 7.2. Suppression of p32 in vitro. (A) qPCR of p32 mRNA extracted from OVCAR-8 human ovarian cancer cells 48 h after treatment with TPN carrying three (3) distinct p32-specific siRNAs targeting non-overlapping regions of the p32 exon. TPN carrying a scrambled siRNA targeting GFP (siGFP) was used as a negative control. All p32 mRNA levels were normalized to an internal loading control (GAPDH). Data are averages ± s.d. ***$p<0.001$ by one-way ANOVA. **(B)** Immunoblotting of lysates from OVCAR-8 cells treated as in (A). a-Tubulin was used as the loading control. Quantification of band intensities are listed below the blot.
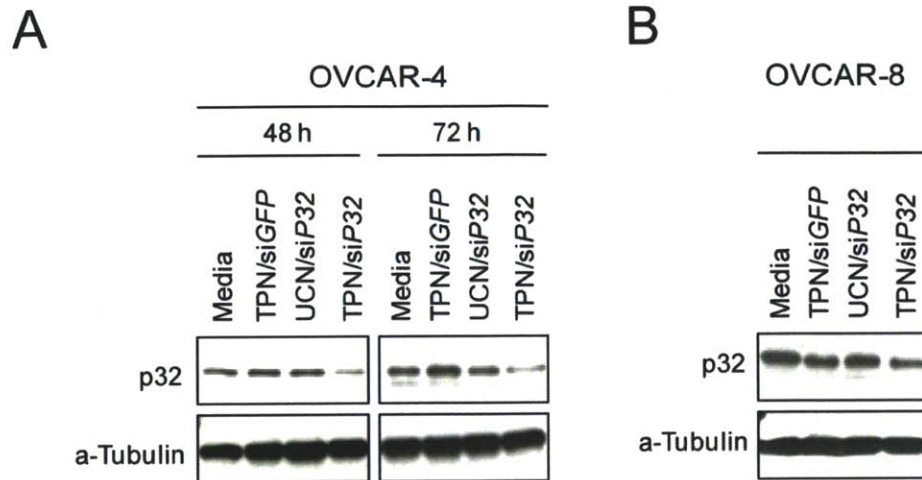
Figure 7.3. TPN-mediated suppression of p32 *in vitro*. (A) OVCAR-4 human ovarian carcinoma cells were treated with indicated TPN formulations carrying *p32*-siRNA or GFP-siRNA. Untargeted control nanocomplex (UCN) consists of TP-ARAL non-covalently bound to siRNA. At 48 h and 72 h post transfection, lysates were harvested and subjected to immunoblotting. a-Tubulin was used as a loading control. **(B)** Immunoblot of OVCAR-8 cells treated with either TPN carrying siP32 or UCN carrying siP32. A scrambled siRNA targeting GFP was used as a negative control.
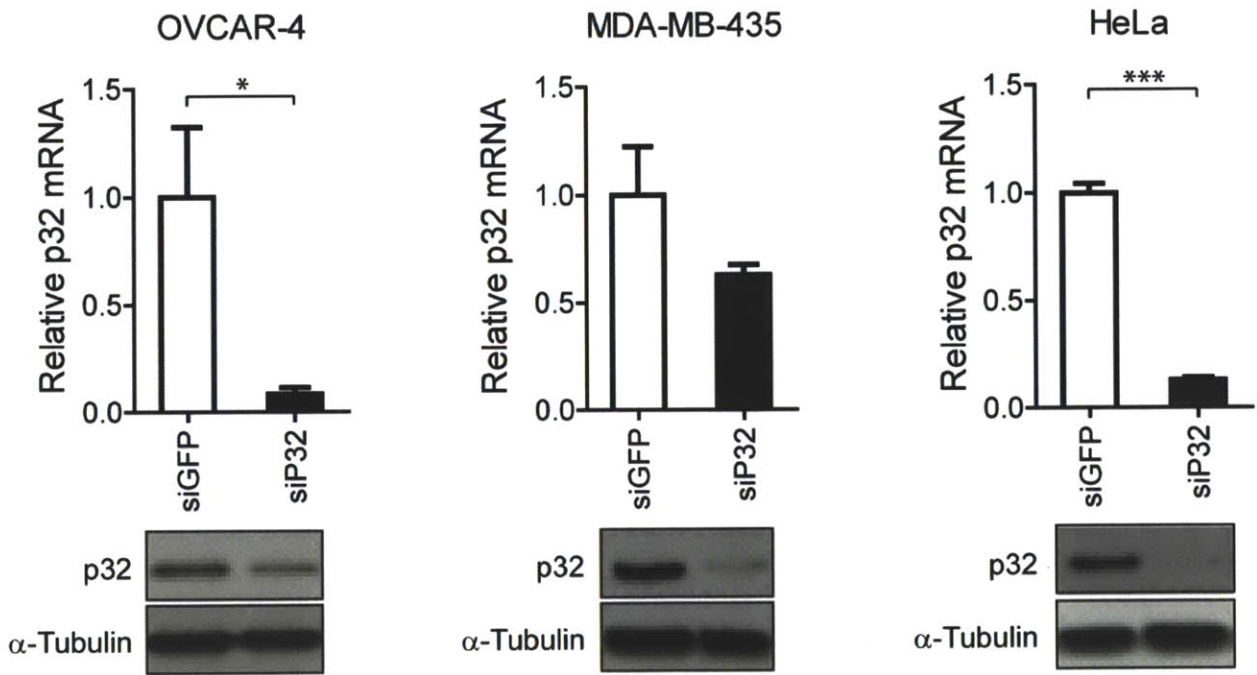
Figure 7.4. p32 suppression in human cancer cell lines. Human cancer cell lines derived from ovarian cancer (OVCAR-4), melanoma (MDA-MB-435) and cervical cancer (HeLa) were treated with TPN-bound *p32*-siRNA (siP32) or GFP-siRNA (siGFP), and p32 mRNA and protein levels were analyzed 48 h later by qPCR and immunoblotting, respectively. Data are averages ± s.d. (n = 3 independent experiments). *p<0.05; ***p<0.001 by unpaired Student's *t*-test.
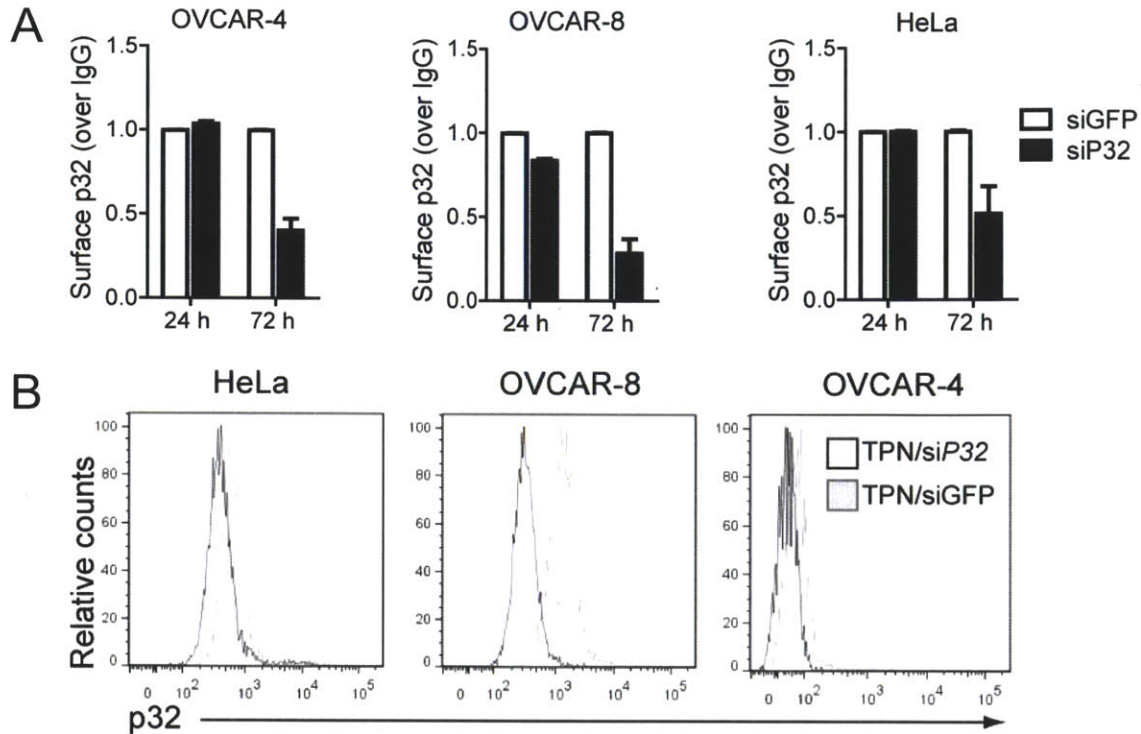
Figure 7.5. Suppression of cell surface p32 by TPN. (A) Summary of cell surface p32 levels 24 h and 72 h after treatment with p32-specific siRNA using TPN. A scrambled siRNA targeting GFP (siGFP) was used as a negative control. **(B)** Representative flow cytometry histograms from each cell line.

7.2.2 Metabolic consequences of p32 suppression

In MDA-MB-435 melanoma cells that harbored stable p32 knockdown, it was observed that they exhibited altered metabolism including elevated glycolysis and decreased oxidative phosphorylation[309]. A shift towards utilizing glycolytic pathways for ATP generation is associated with anaerobic conditions, higher glucose uptake and consumption, and increased lactic acid production, as glycolysis is less efficient than oxidative phosphorylation in ATP production. To ascertain whether transient, TPN-mediated, p32 knockdown can preferentially bias cells towards a more glycolytic phenotype, we measured the rate of glucose consumption and lactate production, two features that correlate with glycolysis, in cells treated with TPN/si*P32*. Suppression of *p32* did not significantly affect cell viability (> 80% viable cells), even in doses up to an order of magnitude higher than that required to knockdown p32 by over

90% (**Figure 7.7A; Figure 7.8A; Figure 7.9A**). Glucose consumption was consistently elevated in OVCAR-8 and HeLa cells from 24 h up to 72 h after TPN/si*P32* treatment (**Figure 7.9B and Figure 7.7B**) but was not altered in OVCAR-4 cells (**Figure 7.8B**), suggesting that factors other than p32 suppression can co-regulate glucose uptake. Furthermore, cells that consumed more glucose also exhibited higher production of lactic acid, a by-product of anaerobic glycolysis (**Figure 7.6; Figure 7.7C; Figure 7.8C; Figure 7.9C**).
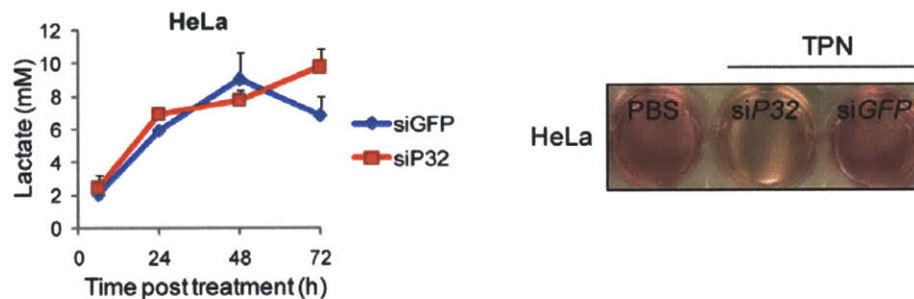
Figure 7.6. Effects of p32 suppression on lactate production *in vitro*. *Left*, Measurements of lactate concentration in the media of HeLa cells over time after TPN treatment with p32-siRNA. *Right*, Color of media from HeLa cells after TPN treatment.
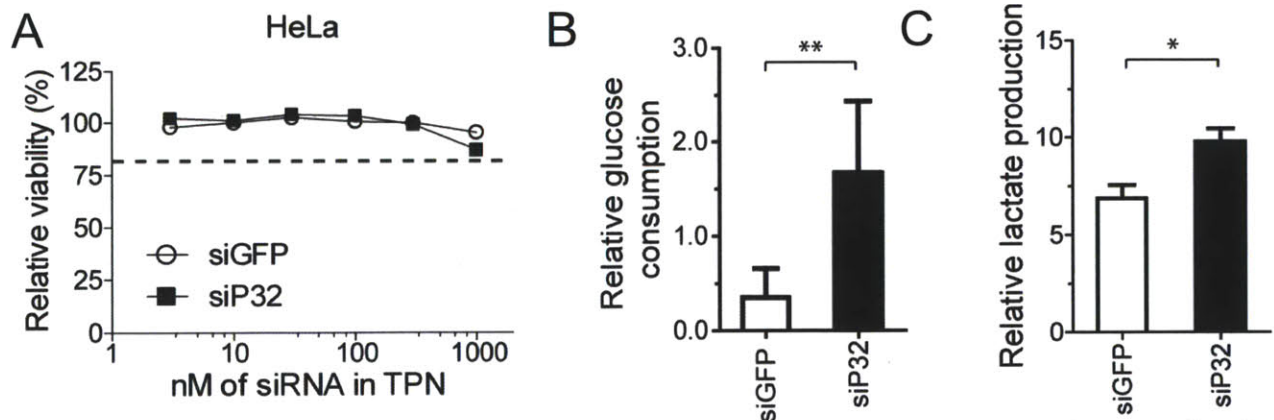
Figure 7.7. *In vitro* phenotype of p32-suppressed HeLa cells. (A) Cellular viability of HeLa cells after TPN delivery of *p32*-specific siRNA or a control siRNA (siGFP). The dotted line indicate >80% viability. **(B)** Glucose consumption rates of HeLa cells treated with TPN/siP32 compared to TPN/siGFP. **$p<0.01$, unpaired Student's *t*-test.Data are averages ± s.d. (n = 3 independent experiments). **(C)** Lactate production rates of HeLa cells treated with TPN/siP32. *$p<0.05$, unpaired Student's *t*-test. Data are averages ± s.d. (n = 3 independent experiments).
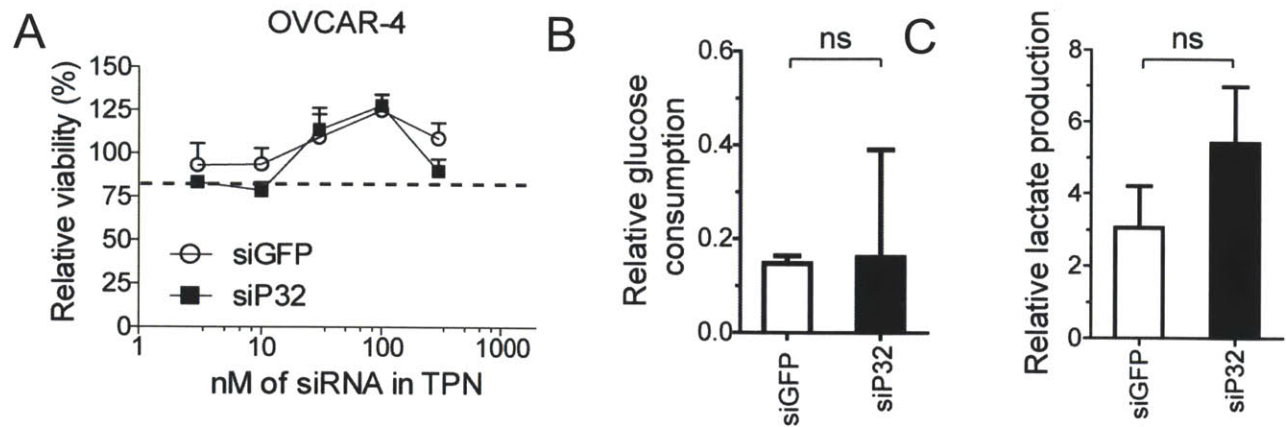
Figure 7.8. *In vitro* **phenotype of p32-suppressed OVCAR-4 ovarian cancer cells. (A)** Cellular viability of OVCAR-4 cells after TPN delivery of *p32*-specific siRNA or a control siRNA (siGFP). The dotted line indicate >80% viability. **(B)** Glucose consumption rates of OVCAR-8 cells treated with TPN/siP32 compared to TPN/siGFP. n.s, not significant, unpaired Student's *t*-test.Data are averages ± s.d. (n = 3 independent experiments). **(C)** Lactate production rates of OVCAR-8 cells treated with TPN/siP32. n.s, not significant, unpaired Student's *t*-test.Data are averages ± s.d. (n = 3 independent experiments).
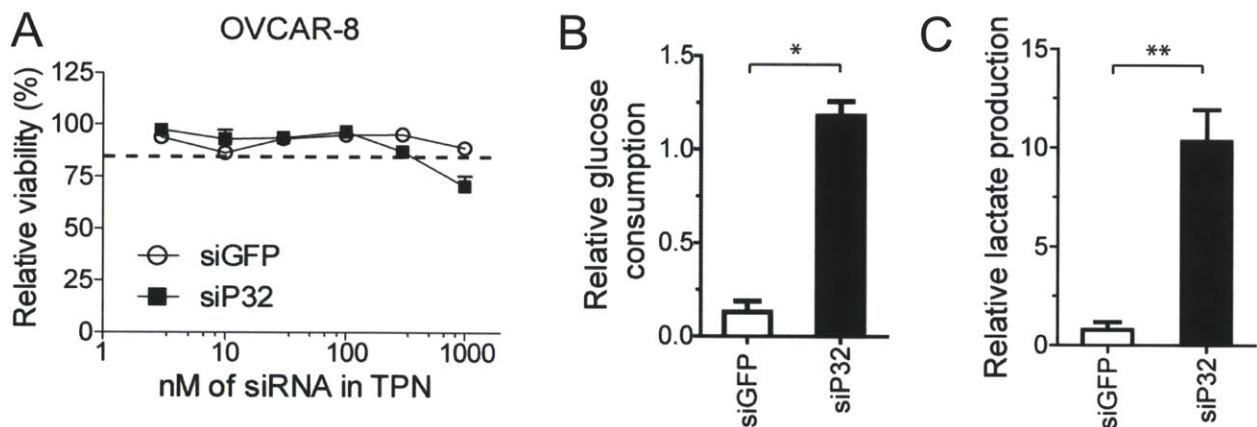
Figure 7.9. *In vitro* **phenotype of p32-suppressed cells. (A)** Cellular viability of OVCAR-8 cells after TPN delivery of *p32*-specific siRNA or a control siRNA (siGFP). The dotted line indicate >80% viability. **(B)** Glucose consumption rates of OVCAR-8 cells treated with TPN/siP32 compared to TPN/siGFP. *p<0.05, unpaired Student's *t*-test.Data are averages ± s.d. (n = 3 independent experiments). **(C)** Lactate production rates of OVCAR-8 cells treated with TPN/siP32. **p<0.01, unpaired Student's *t*-test. Data are averages ± s.d. (n = 3 independent experiments).

7.2.3 Suppression of p32 receptor expression *in vivo*

Having established that TPN can target p32-expressing cancer cell lines and deliver

siRNA to suppress p32 levels *in vitro*, we next investigated whether TPN can a) suppress p32

receptor expression *in vivo*, and if so, b) a reduction in p32 in perivascular tumor cells can improve the uptake and spatial distribution of successive TPN. We generated SCID mice bearing bilateral subcutaneous OVCAR-8 human ovarian carcinoma xenografts, and injected *via* the tail vein on two consecutive days (with TPN carrying either *GFP-* or *p32*-specific siRNA (1 mg of siRNA/kg/injection), respectively. Two days after the second injection, TPN encapsulated with siRNA labeled with a near-infrared fluorophore (VivoTag750-siRNA) were administered i.v. into both cohorts (1.5 nmols/injection), and tumors were harvested after TPNs were cleared (6 h) for histological assessment of p32 knockdown and nanoparticle accumulation **(Figure 7.10A)**.

Immunofluorescence studies revealed over 80 % reduction in p32 expression in tumors that received TPN/si*P32* **(Figure 7.10B, C)**. To gain more insight into the spatial distribution of p32 expression, whole-tumor sections were dual stained with p32 and an endothelial cell surface marker and examined for their co-localization. We found that p32 expression was reduced by over 85% in areas of the tumor where blood supply was abundant but remained high near avascular areas, indicating that the efficacy of TPN delivery was limited to perivascular zones where tumor cells highly express p32 **(Figure 7.11)**. Together, the data suggest that intravenously administered TPNs achieved functional delivery of p32-specific siRNA; however, knockdown of p32 was heterogeneous and was restricted to perivascular tumor cells.

To determine whether the modulation of p32 expression in the tumor microenvironment can influence the tumor uptake of successive TPNs, we quantified the amount of fluorescently-labeled TPNs that is present in the tumor xenografts by measuring bulk tumor fluorescence 6 h after TPN injection **(Figure 7.12A)**. Prior studies showed that intravenously administered TPNs were cleared from circulation after 4 h [213]. Tumors that were pre-treated with *p32*-specific siRNA showed slightly enhanced accumulation of TPNs compared to control tumors that

received a scrambled siRNA (si*GFP*). However, the difference was not statistically significant (**Figure 7.12B**), consistent with previous studies that suggest extravasation from blood vessels is the rate-limiting step in tumor targeting [313].

Although bulk uptake measurements revealed varying levels of nanoparticle accumulation due to alterations in the distribution of p32, it does not provide information on nanoparticle localization within the tumor. To gain a better understanding of the heterogeneity of TPN targeting on a microscopic scale, we adopted a method to unbiasedly quantify the distribution of extravasated antibodies in tumor sections [314]. Briefly, histological sections containing CD31-positive areas were isolated to generate a map of the vasculature. This mask was combined with tumor sections devoid of necrotic areas to create a Euclidean distance map between blood vessels and cell that took up TPNs. Finally, an intensity profile as a function of distance from the nearest vessel was created (**Figure 7.13**). To enable facile comparison between cohorts, the distance at which 50% of TPN/VivoTag-750-siRNA fluorescence remains ($d_{1/2}$_TPN) was measured and averaged for each cohort.

In tumors that received *GFP*-siRNA followed by successive administration of TPN carrying fluorescent siRNA, delivery of TPN was primarily localized to perivascular regions (**Figure 7.14**). The limited extravasation into the tumor parenchyma suggests the presence of a TPN binding sink created by p32-expressing tumor cells near the vasculature. In contrast, TPN penetration was significantly enhanced in tumors where p32-expression is suppressed from pre-treatments with *p32*-specific siRNA. Fluorescence intensity was high in the vasculature, perivascular cancer cells, as well as cells distant from blood vessels. Quantitative analysis of tumor cross-sections revealed that the average diffusion distance of TPN from the tumor blood vessels was improved by nearly five-fold, from 17 μm (range: 3.75 μm – 41 μm) to 83 μm

(range: 4 μm – 188 μm). Alternatively, the reduction of the p32 binding barrier enhanced TPN penetration from 1-2 cell layers to 4-6 cell layers away from vasculature (**Figure 7.15**).

Consistent with evidence from literature that suggests antigen abundance can negatively affect antibody penetration into tumors, these data collectively suggest that the TPN binding barrier can be overcome by reducing p32 receptor expression. Stochastic models based on microenvironmental parameters and measured nanoparticle properties (**Table 7.1**) are currently under development to reproduce experimental outcomes and establish guidelines to further improve TPN tumor penetration.
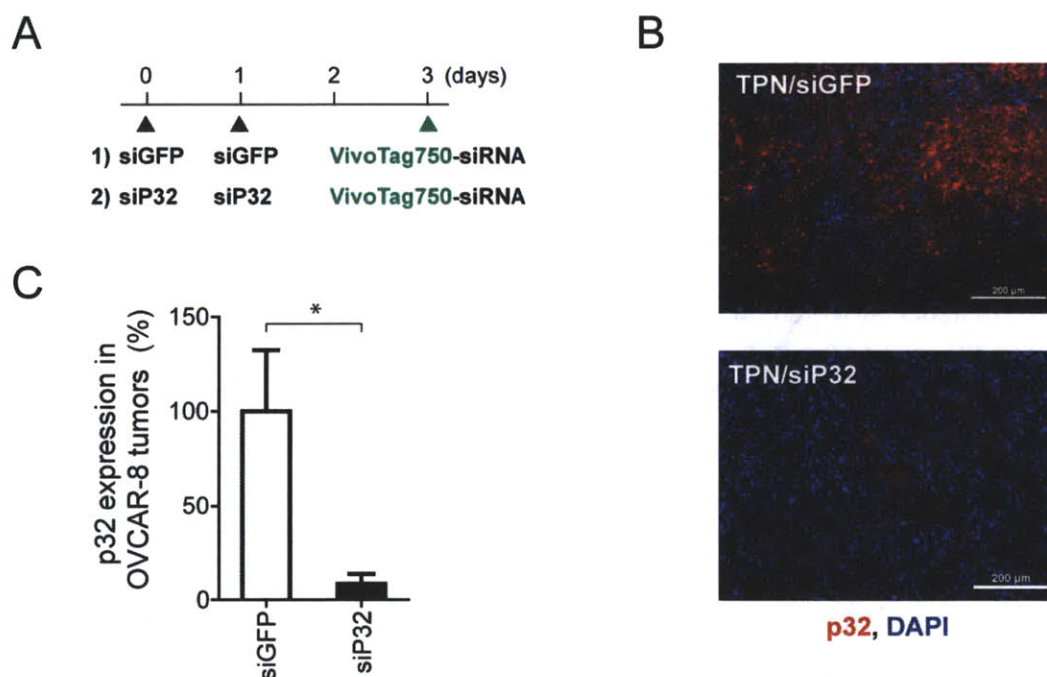
Figure 7.10. p32 knockdown by TPN. (A) Schematic of the experiment. Mice bearing s.c. OVCAR-8 human ovarian carcinoma xenografts were injected i.v. on day 0 and day 1 with TPN carrying either siGFP or si*P32*. Two days later, both cohorts of mice were injected i.v. with TPN carrying a fluorescently-labeled siRNA (VivoTag750). Tumors were harvest 6 h after injection. **(B)** Immunofluorescence staining of p32 (pseudocolored in red). **(C)** Quantification of p32 immunofluorescence intensities from tumor cross sections from (B). Data represent averages ± s.d. (n = 8-10 randomly selected tumor sections from each cohort). *$p < 0.05$, unpaired Student's *t*-test.

TPN/siGFP TPN/siP32

VivoTag750-siRNA, CD31, DAPI
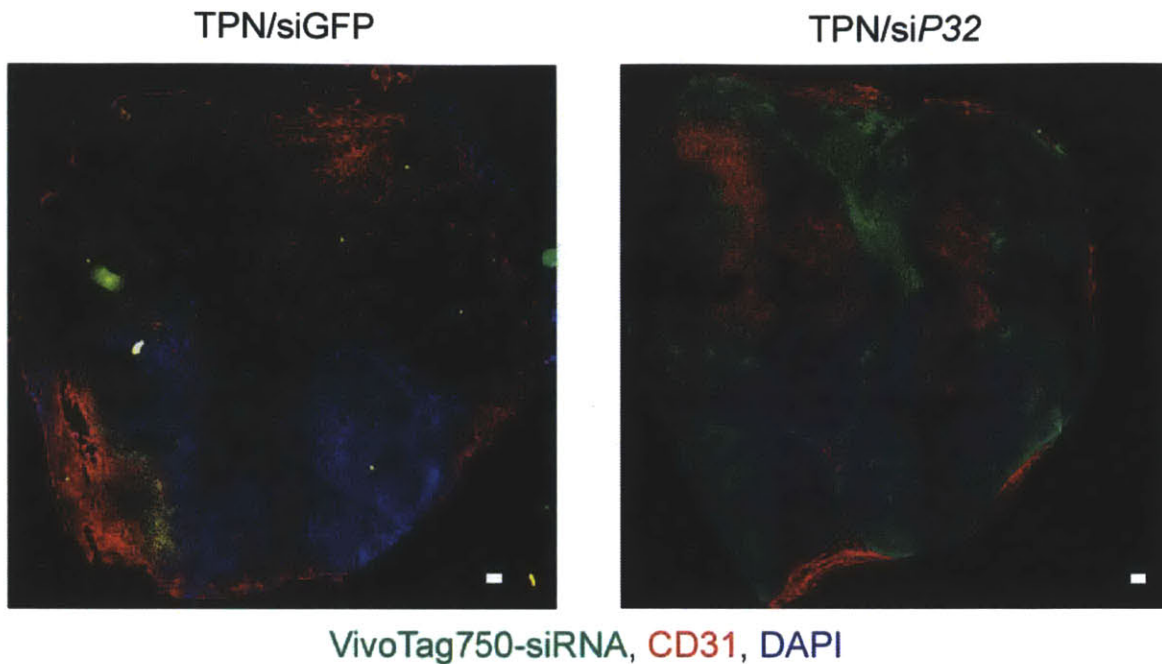
Figure 7.11. Whole-tumor immunofluorescence images from tumor xenografts harvested from mice treated with either TPN/siP32 or TPN/siGFP. Sections are stained with antibodies against CD31 (pseducolored red) and overlaid with fluorescence from the near-infrared channel to indicate localization of TPN carrying VivoTag750-siRNA. Scale bar, 500 µm.
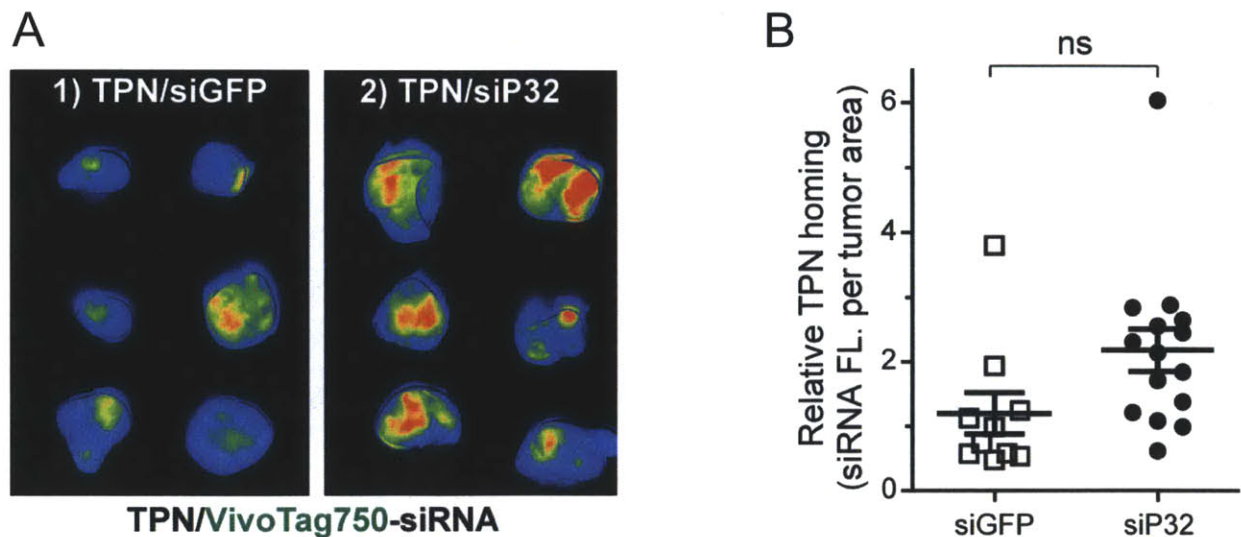
Figure 7.12. Tumor uptake of TPN after suppression of p32. (A) Near-infrared fluorescence imaging of TPN uptake in explanted tumors after suppression of p32 by TPN/siP32. **(B)** Quantification of VivoTag-750-siRNA fluorescenc intensity from (A). n.s., not significant, unpaired Student's *t*-test.
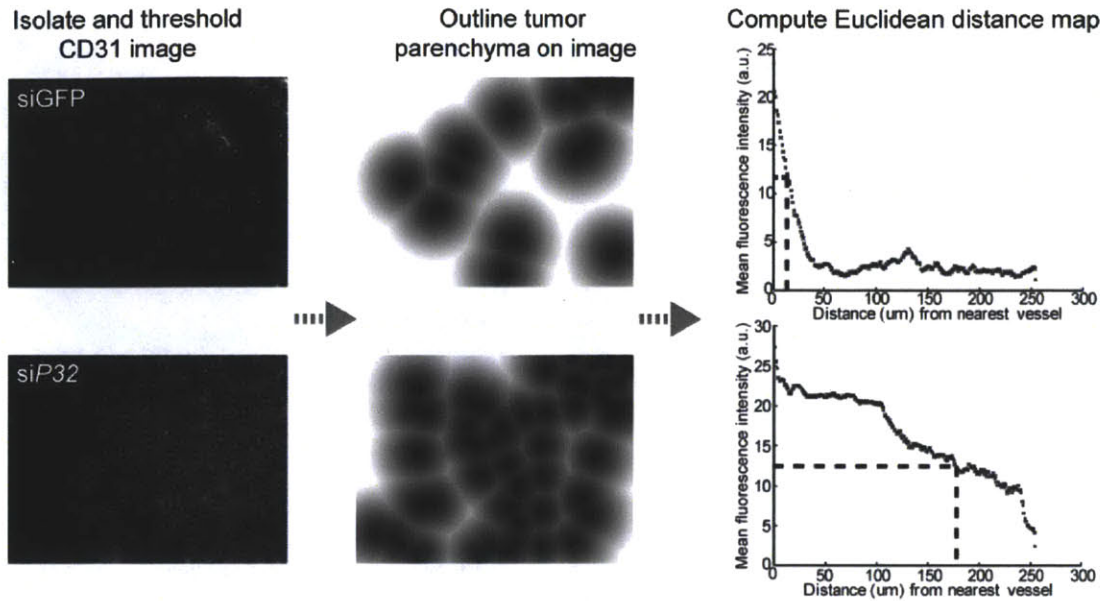
Figure 7.13. Schematic of quantitative image analysis of tumor penetration. Fluorescent images containing signal from CD31 are thresholded to generate a map of vasculature. Tumor sections are outlined manually to delineate regions of the tumor parenchyma for analysis. The vasculature map is applied to tumor sections to generate a Euclidean distance map of siRNA fluorescence as a function of distance from the nearest vascular structure. Finally, the distance at which siRNA fluorescence is at 50% of maximum is determined and averaged for animals within each cohort.

CD31, VivoTag750-siRNA, DAPI
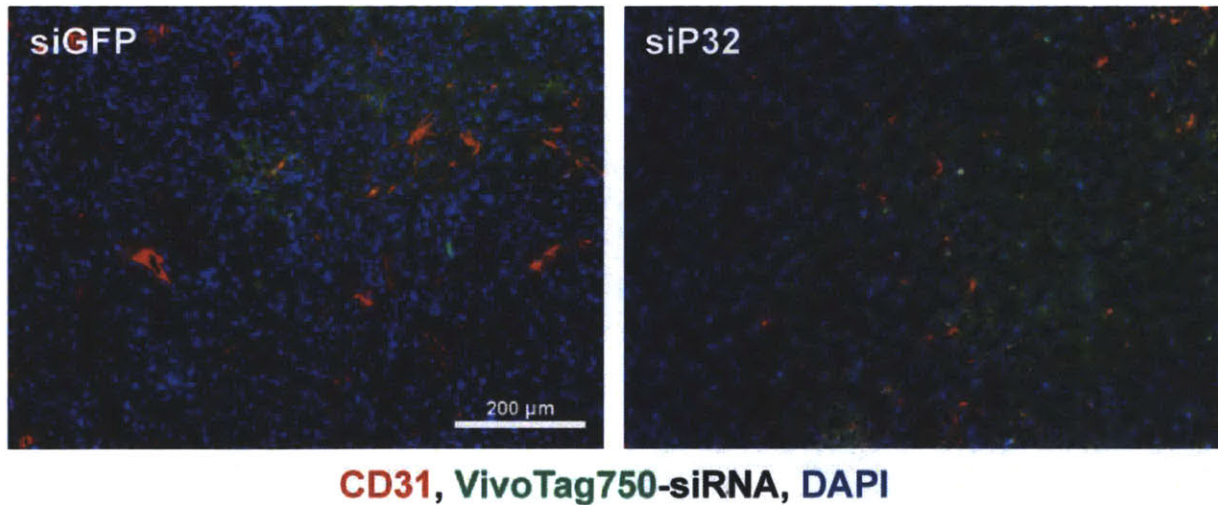
Figure 7.14. Immunofluorescence images of tumor penetration by TPN. Mice bearing s.c. OVCAR-8 tumor xenografts were treated with TPN/siP32 to suppress intratumoral p32 expression prior to administration of TPN carrying a fluorescently-labeled siRNA. TPN/siGFP pre-treatments were used as negative controls. Tumor sections were stained with anti-CD31 antibody to delineate blood vessels (pseudocolored red) and visualize co-localization with fluorescent siRNA payloads (pseudoclored green). Scale bar, 200um.

198
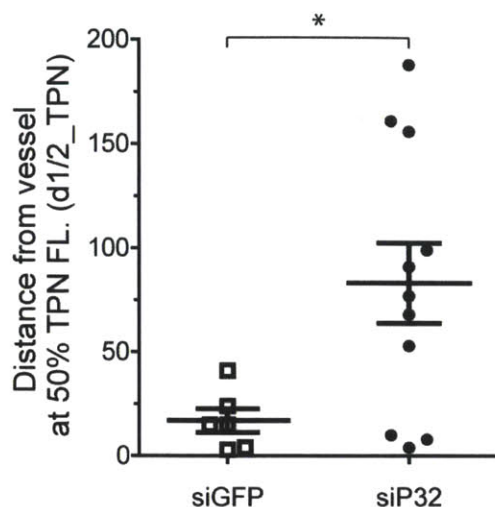
Figure 7.15. Quantification of tumor penetration distance. Immunofluorescence images of tumor cross-sections were analyzed using the algorithm outlined previously. The distance at which 50% of VivoTag-750 siRNA fluorescence remained was calculated for each image, and averaged for animals within the cohort. For each animal, 4-7 randomly selected images were analyzed. Data represent averages ± s.d. (n = 5 animals per cohort). *p<0.05, unpaired Student's *t*-test.

Table 7.1. Parameters used for stochastic modeling of TPN penetration

PARAMETER	DEFINITION	VALUE	(RANGE)	REF
V_t	Size of tumor (OV4, mm^3)	48	26-120	Measured
V_B	Plasma volume in ~20 g mouse	2 ml		*Assumed*
D	Diffusivity of TPN (Rh = 100nm)	2.97×10^{-9} cm^2/s		*Jain, 2001*
P	Vascular permeability	1.8×10^{-8} cm/s		*Jain, 1994&1995*
R_{cap}	Capillary radius	8 µm		*Wittrup 2011*
R_h	Diameter of TPN (nm, in H2O)	100		Measured
L_{tumor}	Slice of tumor section	10 um		Known
V_{sect}	Volume of tumor section (mm^3)	1.32E-01		Calculated
M_{tumor}	Average weight of tumor (mg)	27	24-30	Measured
N_{TPN}	Number of TPNs in tumor slice	2.02E+09		Calculated
K_{d_TPN}	TPN/p32 apparent affinity	282 nM	214 - 321	Measured
K_{d_LyP-1}	LyP-1/p32 apparent affinity	4.17 uM	2.7 - 5.64	Measured
$[p32]_{tot}$	Total # p32 per cell	70,000		Estimated
%KD$_{tumor}$	% Knockdown of p32 *in vivo*	91.5		Measured
%KD$_{cell}$	% Knockdown of p32 *in vitro*	65	60-70	Measured
k_{on}	On rate (Koff / Kd, M^{-1}s^{-1})	47.93		Calculated
k_{off}	Off rate (s^{-1})	1.35E-05		Measured
ID/g	Percent of injected dose per gram	4.51	4.35-4.66	Measured
ID$_{tot}$	Total dose (nmols)	1		Known

7.2.4 Utilization of p32 suppression for tumor imaging

Improvements in the tumor microdistribution of theranostic nanoparticles have been shown to provide better tumor imaging contrast and significantly enhance therapeutic efficacy in a variety of cancer types and mouse models [115-116, 315-316]. Therefore, we wondered whether the high glycolytic phenotype after transient p32 suppression by RNAi can be utilized for molecular imaging. Specifically, we postulated that cancer cells whose p32 expression is suppressed have enhanced uptake of glucose and its analog, 2-deoxyglucose (2-DG), the basis for functional imaging techniques such as positron-emission tomography (PET). To quantify glucose uptake in cells, we measured the cellular uptake of a fluorescent glucose analog using flow cytometry. In all three cancer cell lines treated with TPNs carrying *p32*-specific siRNA, we observed a consistent increase in the uptake of 2-[N-(7-nitrobenz-2-oxa-1,3-diaxol-4-yl)amino]-2-deoxyglucose (2-NBDG) (**Figure 7.16**). To visualize glucose utilization *in vivo*, we probed the uptake of a near-infrared fluorescent 2-deoxyglucose reporter molecule (IRDye 800CW 2-DG) in mice bearing s.c. OVCAR-8 human ovarian carcinoma xenografts, 48 h after treatments with either TPN/*p32*-specific siRNA or a scrambled control siRNA (**Figure 7.17**). Whole-animal optical imaging showed a significant increase in tumor uptake of 2-DG probe in si*P32*-treated mice (**Figure 7.17**). After the probe was cleared from circulation, *ex-vivo* analysis of explanted tumors showed over 100% improvement in probe fluorescence after p32 suppression relative to tumors that received a control siRNA (**Figure 7.18**).

While we observed an increase in the uptake of fluorescent 2-DG conjugates in si*P32*-treated tumors, this may not accurately represent true hypermetabolic activity [317]. Recent studies have suggested that the bulkiness of the fluorescent dye (700-1000 Da) compared to glucose (180 Da) could significantly alter the pharmacodynamics of the probe and promote its

non-specific retention in the tumor interstitial space, which could ultimately contribute to the enhanced tumor accumulation [318]. Indeed, immunofluorescence analysis of tumor sections revealed that the near-infrared probe was localized to both vascular structures (CD31+) as well as within the tumor interstitium, phenomena that can be associated with enhanced permeability and retention (EPR) in addition to tumor cell glucose uptake (**Figure 7.19**).

In light of these findings, we performed ^{18}F-FDG-PET imaging with computational tomography (PET/CT) to measure tumor metabolic changes after p32 suppression *in vivo*. Mice bearing bilateral s.c. OVCAR-8 tumors were pre-injected with two doses of TPN/si*P32* on two consecutive days (1 mg siRNA/kg/injection) and were subjected to PET/CT imaging 48 h after the second TPN injection. Tumors treated with *p32*-siRNA showed over 50% enhancement in uptake of ^{18}F-FDG compared to controls that received *GFP*-siRNA, as quantified by the total fraction of injected dose that is present in the tumor (**Figure 7.20**). Furthermore, we observed substantial ^{18}F-FDG uptake in the periphery of TPN/si*GFP*-treated xenografted tumors, owing to the presence of avascular, necrotic tumor areas. In contrast, TPN/si*P32*-treated tumors exhibited FDG delivery to both the periphery as well as areas near the tumor core (**Figure 7.20; Figure 7.21**), likely owing to a more uniform distribution of glycolytically-active tumor cells within the tumor parenchyma resulted from p32 suppression by RNAi. We did not observe a similar enhancement in ^{18}F-FDG uptake in mice bearing OVCAR-4 ovarian tumor xenografts (**Figure 7.21**), consistent with *in vitro* observations that p32 suppression in OVCAR-4 cells did not significantly shift their metabolism towards glycolysis (**Figure 7.8**). These observations in aggregate indicate that suppression of p32 in tumors could enhance the uptake of glucose and its analog, 2-deoxyglucose, thereby providing better contrast for tumor imaging by ^{18}F-FDG-PET.
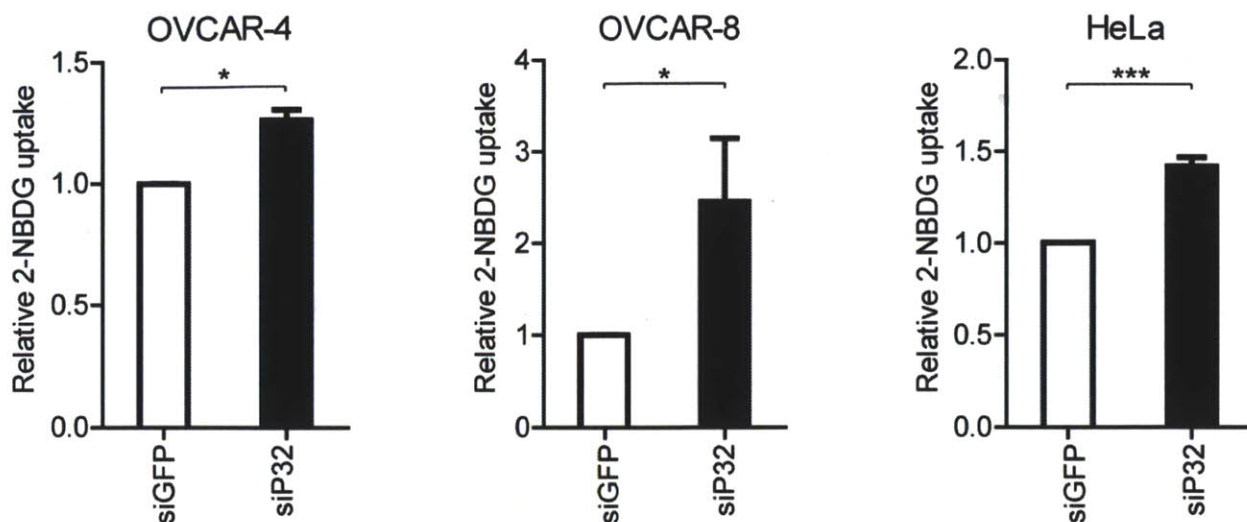
Figure 7.16. Uptake of fluorescent glucose analog in human cancer cell lines after p32 suppression. In OVCAR-4, OVCAR-8, and HeLa cells pre-treated with either TPN/siGFP or TPN/siP32, cellular uptake of 2-[N-(7-nitrobenz-2-oxa-1,3-diaxol-4-yl)amino]-2-deoxyglucose (2-NBDG) was examined 24 h later. Data represents averages ± s.d. (n = 3 independent measurements). *p<0.05; ***p<0.001, unpaired Student's *t*-test.
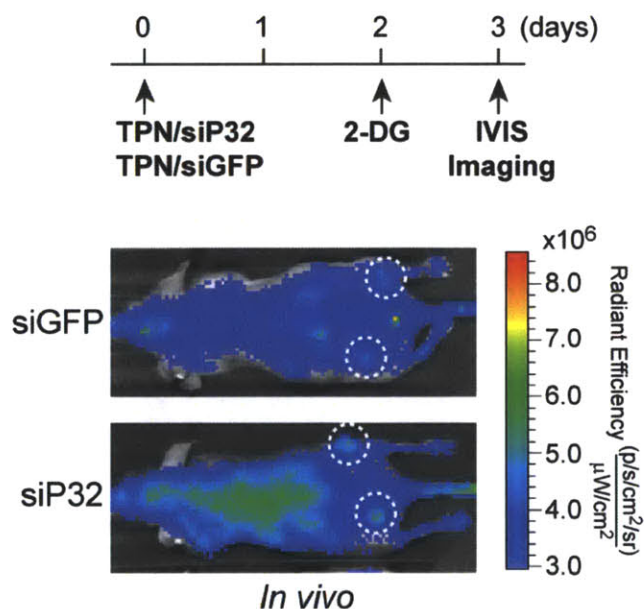
In vivo

Figure 7.17. Tumor uptake of fluorescent 2-deoxyglucose *in vivo*. Mice bearing s.c. OVCAR-8 human ovarian carcinoma xenografts were administered with TPN/siP32 two days prior to injection of a near-infrared fluorescent glucose analog. Bio-distribution and tumor uptake of 2-DG was determined via non-invasive whole animal imaging 24 h later.

202
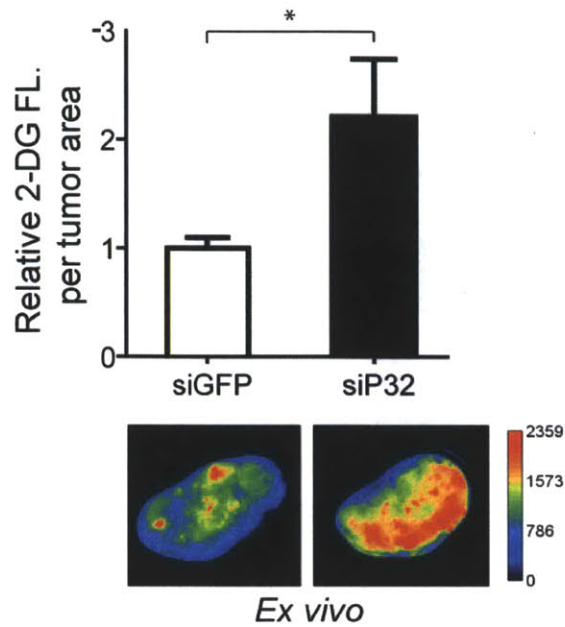
Figure 7.18. Quantification of 2-DG fluorescence in tumor explants. Top, data represents averages ± s.d. (n = 3 animals per group). *$p<0.05$ unpaired student's t-test.Bottom, representative fluorescent images of whole-tumor explants.
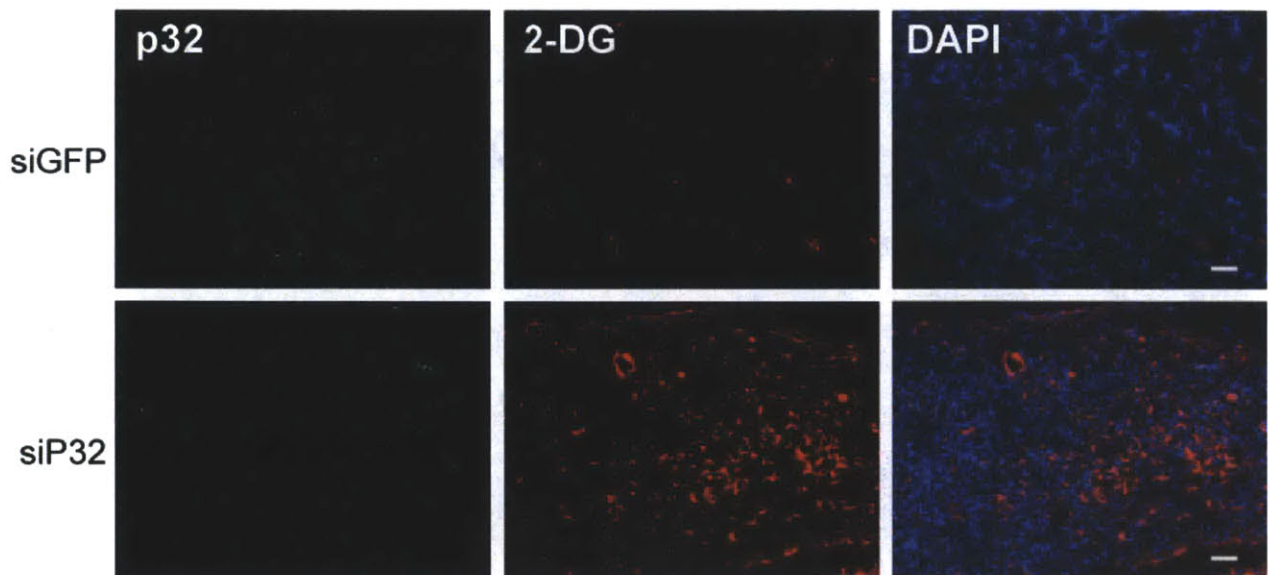
Figure 7.19. Immunofluorescence imaging of tumor sections. Tumors cross-sections were stained with anti-p32 (green). NIR 2-DG probe was pseudocolored red. Cell nuclei were counterstained with DAPI (blue). Scale bar, 50 μm.
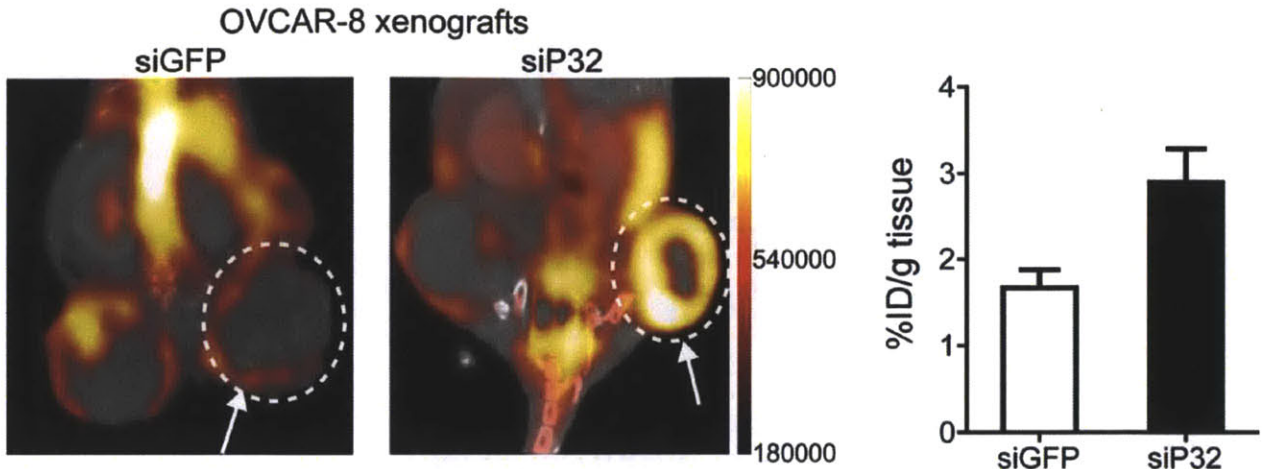
Figure 7.20. ^{18}**F-FDG-PET/CT imaging of OVCAR-8 tumor xenografts.** Tumor-bearing mice underwent FDG-PET and tumors were delineated by the dotted line and arrows. Quantification of ^{18}F-FDG uptake as the amount of injected dose localized to the tumor tissue (%ID/g tissue) are shown on the right. Data represent mean ± s.d. (n = 4 tumors).
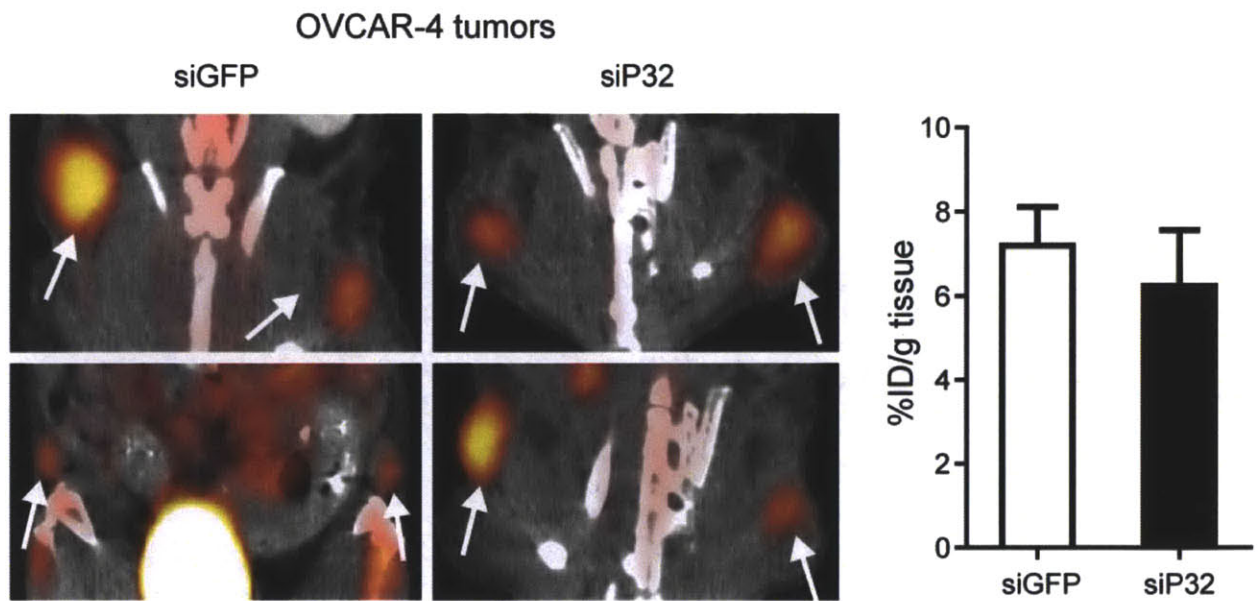
Figure 7.21. ^{18}**F-FDG-PET/CT imaging of OVCAR-4 tumor xenografts.**Quantification of FDG tumor uptake is shown on the right.

7.3 Conclusions

In this work, we have demonstrated that spatial- and temporal-control of receptor expression in the tumor parenchyma can affect the intratumoral microdistribution and penetration of receptor-targeted nanoparticles. Experimental studies using p32-targeted tumor-

penetrating nanocomplexes show that the binding site barrier for tumor penetration can be overcome through knockdown of p32. Specifically, down-regulation of p32 within the tumor reduces the heterogeneity of successive TPN uptake and improves siRNA delivery to deeper regions of the tumor parenchyma, potentially in avascular or hypoxic areas that are previously inaccessible to nanotherapeutics. Finally, the utility of this strategy in improving nanoparticle delivery is explored in tumor imaging by ^{18}F-FDG-PET/CT.

The TPN system described in this work is highly modular; other tumor-homing domains identified from high-throughput screens and siRNA cargoes directed against their receptors can be independently varied with ease. Efforts utilizing stochastic models for nanoparticle extravasation are underway to generate a framework and guidelines for overcoming the binding barrier and improving tumor penetration. By adapting the system to other tumor types and disease processes, this strategy can serve as a powerful and generalizable tool for overcoming the binding barriers of tumor transport, enhancing the delivery of theranostic agents to tumors, and facilitating the development of better diagnostic and therapeutic regimens.

7.4 Materials and Methods

Tumor penetrating nanocomplex (TPN) preparation. TPNs were prepared as described previously [213]. The sequences of siRNAs (5'-3') are as follows: siGFP (GGCUACGUCCAGGAGCGCA), siP32 #1 (CCCAAUUUCGUGGUUGAAGUUAUAA), siP32#2 (GAAGGCCCUUGUGUUGGAC), siP32#3 (CAGACAGAUGCUGAAAGCC).

Real-time quantitative Reverse-Transcription PCR. Total RNA was extracted using the RNeasy kit according to manufacturer's instructions (Qiagen). 1 µg of total RNA was used to synthesize cDNA by using random hexamer primer cocktails and reverse transcriptase (Invitrogen). Quantitative PCR reactions were performed using SYBR green PCR Master Mix (Applied Biosystems). The primers used are as follows: *GAPDH* (forward: 5'-CCTGTTCGACAGTCAGCCG-3'; reverse: 5'-CGACCAAATCCGTTGACTCC-3') and P32 (forward: 5'-AAAGTTGCCGGGGAAAAA-3'; reverse: 5'-TCCTCCTCACCATCAAATGTT-3'). Triplicate reactions for the gene of interest and the endogenous control, (*GAPDH*) were performed separately on the same cDNA samples. The mean cycle threshold (Ct) was used for the $\Delta\Delta C_t$ analysis method (ABI User Bulletin #2).

Flow Cytometry. Fluorescence-activated cell sorting (FACS) analysis of cell-surface p32 was performed on live cells. Approximately 5×10^5 cells were stained with a polyclonal anti-full-length/NH2-terminal p32 or rabbit IgG isotype control (1 μg per 1×10^6 cells) and Alexa-647 goat anti-rabbit secondary antibody, each for 40 min on ice, analyzed by gating for propidium iodide-negative (live) cells. Uptake of 2-NBDG was measured according to manufacturer's instructions (Invitrogen).

Measurements of glucose consumption and lactate production. HeLa, OVCAR-4, and OVCAR-8 cells were seeded in 6-well plates at a density of 0.1×10^6 cells per well. Two days after plating, cells were treated with TPN according to established protocols. The media from each well was collected at indicated time points and frozen at -80 °C. The concentrations of glucose and lactate were determined using glucose and lactate assay kits (BioVision). To determine glucose consumption rates, the concentration at each time point was normalized to that at time zero. For each experimental condition, media from at least 4 independent experiments was measured and averaged.

Systemic administration of TPNs into mice. Female nude NCR mice (Charles River Laboratories) were obtained at 4-6 weeks of age. All animal experiments were approved by the MIT Committee on Animal Care under approved protocols. For *in vivo* delivery of siRNA, TPNs were prepared as described previously [213] with siRNAs targeting either *P32* or GFP in 5% glucose and injected intravenously into mice bearing bilateral s.c. OVCAR-8 ovarian carcinoma xenografts. For tumor uptake, TPNs carrying near-infrared fluorophore labeled siRNA (1.5 nmols) was prepared in 5% glucose and injected *via* the tail vein. The mice were imaged using the IVIS 200 imaging system (Caliper Life Sciences). Tumor explants were examined at 84 μm resolution using the Odyssey imager using an excitation wavelength of 785 nm.

Deoxyglucose imaging in mice. A deoxyglucose probe labeled with a near-infrared fluorophore (IRDye 800CW 2-DG, LI-COR) was injected into tumor bearing mice via the tail vein at a dose of 10 nmols of probe per injection. One day after probe administration, mice were imaged using the IVIS system (Caliper Life Sciences) with a 745-nm excitation and 820nm emission filter. Total fluorescence normalized by tumor area was measured using LivingImage (Caliper Life Sciences) for each tumor.

^{18}F-FDG MicroPET/CT Imaging. Mice were imaged using ^{18}F-FDG-PET on an Inveon small animal PET/CT scanner (Siemens). PET/CT data was acquired using standard protocol as described elsewhere. After imaging, animals were euthanized and tumors were excised to determine the total injected dose per gram of tissue (%IDGT) within the tumor.

Immunostaining and co-localization analysis. Tumors were fixed in 4% paraformaldehyde at 4°C overnight and snap frozen in liquid Nitrogen. Rat anti-mouse CD31 (1:50, BD PharMingen) and/or a polyclonal anti-full length p32 antibody were used for immunofluorescence staining. Sections were washed and detected with AlexaFluor-488 goat anti-rat or anti-rabbit IgG (1:1000; Invitrogen). The slides were counterstained with DAPI and mounted on glass slides for microscopic analysis. For co-localization analysis of CD31 and p32, the number of non-zero pixels in the p32 channel that co-localized with non-zero pixels in the CD31 channel was normalized by total p32 intensity for each image. The analysis was repeated for a total of 4-6 images for each condition.

Measurement of tumor penetration on immunofluorescence sections. A method similar to the one described to measure antibody penetration was adapted [314] to quantify tumor penetration of TPN.

Statistical analysis. Statistical analyses were performed using built-in statistical functions in GraphPad Prism (GraphPad Software).Averaged fluorescence intensities from immunofluorescence staining, results from glucose/lactate assays, qPCR, and intratumoral fluorescence intensities were analyzed using Student's *t*-test.

8 Delivery of siRNA to primary ovarian cancer cell samples

8.0 Abstract

p32 (gC1qR/p33/HABP1), is a mitochondrial protein aberrantly expressed on the surface of ovarian cancer cell lines and the cognate receptor for targeted, tumor-penetrating nanocomplexes (TPN). Analysis of primary ovarian cancer cell samples freshly isolated from patients with advanced stage ovarian cancer revealed that p32 is also expressed on the surface in a subset of primary cancer cells. *In vitro*, TPN-mediated delivery of siRNA directed against *ID4*, an ovarian cancer-specific oncogene amplified in over 32% of high-grade serous ovarian carcinomas, resulted in significant suppression of ID4 expression in primary ovarian cancer cells. Additionally, p32 was found to be highly overexpressed in 49% of specimens in a tissue microarray of late-stage epithelial ovarian carcinomas. Taken together, these data suggest that p32 is a generalizable target for TPN targeting and RNAi therapy in patients with ovarian cancer.

8.1 Introduction

Ovarian cancer is one of the leading causes of cancer deaths in women, with over 15,000 deaths from over 21,000 cases in the U.S. in 2011 [8]. This high mortality rate is due to a lack of tools to detect early-stage disease with high sensitivity, as well as a paucity of effective drugs to control disease progression and metastasis. Despite recent progress in the understanding of the biology underlying ovarian cancer, our chemotherapeutic arsenal has remained practically unchanged. Platinum- and taxane-based drugs such as cisplatin and paclitaxel still remain as the standard of care for patients with advanced HGSOC in conjunction with cytoreductive surgery.

These genotoxic agents act *via* exploiting non-specific features that distinguish quiescent cells from rapidly proliferating cells; they do not target genomic vulnerabilities or genes that drive ovarian carcinogenesis. Consequently, standard chemotherapy is associated with significant dose-limiting toxicities due to side effects in organs such as the gastrointestinal tract, skin, bone marrow, and the central and peripheral nervous system. Furthermore, despite high initial response rates, over 70% of patients with advanced disease (Stage III or IV) re-present with progressively chemoresistant cancers, owing to the accumulation of numerous genetic mutations and activation of redundant survival pathways [18]. Therefore, there is a desperate need to develop more effective, less toxic, and "personalized" therapeutic strategies for ovarian cancer.

Recent progress in sequencing has provided unprecedented insight into the genetic basis of cancer initiation and progression by enumerating all genomic alterations in numerous cancer types including glioblastomas (GBM) and ovarian carcinomas [29, 34]. Efforts led by The Cancer Genome Atlas (TCGA) have identified 1825 genes located in over 63 regions of the genome that are targeted by recurrent amplification events and 55 regions that harbored recurrent focal deletions [29]. In parallel, genome-wide loss-of-function screens based on RNA interference have led to the identification of genes whose perturbations have direct consequences on cancer cell survival [48]. Together, the systematic integration of structural and functional genomics has enabled the distillation of genes that are not only mutated in cancer, but also represent putative cancer drivers. Nevertheless, a significant fraction of these genes represent "undruggable" targets that are not amenable to targeting by existing small molecule- or antibody-based therapies [1]. Furthermore, the number of genes nominated by these integrated efforts is too large for *in vivo* validation, as existing approaches based on genetically engineered mouse models or shRNAs are limited to analyzing only a small number of candidates.

In *Chapters 3 through 6*, we developed a solution to overcome this bottleneck of *in vivo* target validation which utilizes tumor-penetrating nanocomplexes (TPN), consisted of tandem tumor-penetrating and membrane-translocating peptides that chaperone siRNA payloads deep into the tumor parenchyma [213]. p32 (p33/HABP1/gC1qR) is a mitochondrial protein that is overexpressed and aberrantly localized to the surface of tumor cells [233, 304]. In *Chapter 4*, we showed that delivery of siRNA against *ID4*, a novel ovarian-specific oncogene amplified in 32% of HGSOCs, suppressed the growth of ovarian tumor xenografts in mice [213]. In *Chapters 5 &* *7*, we showed that the modularity of the TPN system enabled the tumor-specific delivery of siRNA against other genes for pre-clinical therapeutic or diagnostic intervention in animals.

While the TPN system holds promise in discovering genes that contribute to cancer progression and are amenable to RNAi inhibition in mouse models; clinical translation of this approach to patients requires further evaluation of efficacy and safety in primary human tumor specimens. In this work, we probe the utility of TPN-mediated delivery of siRNA therapeutics in human patient tumors. First, we evaluated primary ovarian cancer cells for p32-expression. In two human patient cell samples that selectively took up TPN in a p32-specific manner, delivery of siRNA targeting the ovarian oncogene *ID4* resulted in significant suppression of gene expression *in vitro*. Finally, the generalizability of TPN targeting in human patient tumors was evaluated *via* examining p32 expression in ovarian tissue microarrays (TMA).

8.2 Results

To investigate whether primary human patient ovarian cancer cells are amenable to TPN targeting and siRNA delivery, we began by examining the cell surface expression of p32, the cognate receptor for LyP-1 targeted TPN. Fresh primary tumor cells were obtained from malignant ascites fluids of patients with advanced ovarian carcinoma, purified, and subsequently

expanded as orthotopic xenografts in nude mice. The resulting primary ovarian cancer cell strains are further isolated from mouse cells and non-parenchymal cell types *in vitro*. Of the four (4) primary patient cell strains (DF09, DF14, DF37, DF59) examined by flow cytometry, three showed high surface expression of p32 at levels that are comparable to an established human ovarian cancer cell line, OVCAR-8 (**Figure 8.1**). To confirm that p32 expression mediates TPN uptake, primary cell samples were incubated with TPN bearing varying amounts of LyP-1 on the surface. In two of the p32-expressing samples (DF09 and DF14), uptake was saturated at increasing valence of LyP-1, consistent with the hypothesis that cellular binding of TPN is receptor-specific as all available p32 are engaged in LyP-1 binding (**Figure 8.2**).

To directly probe the interaction between p32 and TPN, we repeated the uptake assay in the presence of a p32-blocking antibody. A dose-dependent inhibition of TPN uptake was observed in samples incubated with the p32 antibody, whereas an isotype-matched control had no effect (**Figure 8.3**). Collectively, the data suggests that a subset of human patient ovarian tumor cells express p32 on the surface and can be targeted by TPN for therapeutic intervention.

We previously established that inhibitor of DNA binding 4 (*ID4*), a novel oncogene amplified in 32% of high-grade serous ovarian carcinomas, is a potential therapeutic target. In mouse models of ovarian carcinoma, TPN mediated suppression of ID4 resulted significant inhibition or elimination of the tumor burden [213]. Here, we expanded our evaluation of primary human patient tumors by examining their ID4 status by immunoblotting. Of the 20 different ovarian tumor cell strains analyzed, seven (7) overexpressed ID4, four of which at levels comparable to an established ovarian cancer cell line (**Figure 8.4**). The DF14 cell strain was chosen for further analysis because it overexpressed ID4 and can be targeted by TPN.

To ascertain whether ID4 can be depleted in primary patient cancer cells for therapeutic purposes, we investigated the effects of TPN-mediated delivery of *ID4*-specific siRNA in DF14 cells. Cells treated with TPN carrying siRNAs against *ID4* showed significantly decreased ID4 levels on immunoblotting; the amount of ID4 depletion by TPN is dependent on the dose of siRNA, is similar to that achieved by a commercial lipid reagent, and is similar to RNAi-mediated suppression in an established ovarian cancer cell line (**Figure 8.5**). Furthermore, TPN delivery of si*ID4* is specific to the LyP-1 domain, as untargeted control nanocomplex (UCN) bearing a scrambled domain was unable to achieve gene silencing (**Figure 8.5**).

Thus far, the utility of p32 overexpression in mediating tumor-specific delivery of siRNA therapeutics has been examined in established human cancer cell lines, orthotopic xenografts, and primary cell samples from patients. However, translational application of TPN requires further substantiation in larger-sized cohorts. Previous studies showed high p32 expression was observed in tissues from breast, endometrioid, melanoma, and colorectal tumors [217]. However, the expression of p32 in ovarian tumors has not been extensively examined. To facilitate this, we employed a tissue microarray (TMA) consisted of formalin-fixed, paraffin-embedded samples derived from biopsies from patients with primary high-grade, late-stage serous ovarian carcinomas and/or associated lymph node metastases. Since p32 is a mitochondrial protein that is also aberrantly expressed on the surface of tumor cells, standard immunohistochemical staining could fail to distinguish surface-localized p32 from mitochondrial p32. Therefore, we first quantitatively correlated total p32 levels from immunoblotting with surface p32 measured by flow cytometry in cell lines from ovarian cancer and melanoma. We observed a highly linear correlation between surface and total p32 levels; this is consistent with previous investigations showing that ~2% of total p32 was present on the cell surface of Vero cells [319] (**Figure 8.6**).

Results from p32 immunohistochemical staining of TMA showed that of 131 primary high-grade ovarian epithelial carcinomas, less than 4% (5/131) was p32-negative (score 0), 47% (62/131) of which showed low expression (score 1+), and 49% (64/131) was p32-positive (score 2+ and 3+) (**Figure 8.7**). The degree of p32 staining did not correlate with clinical-pathological outcomes such as overall survival or progression-free survival (data not shown). However, we observed a statistically significant cross-correlation with ID4 staining intensity in the dichotomized analysis ($P = 0.0363$, Fisher's exact test) (**Figure 8.8; Table 8.1**).
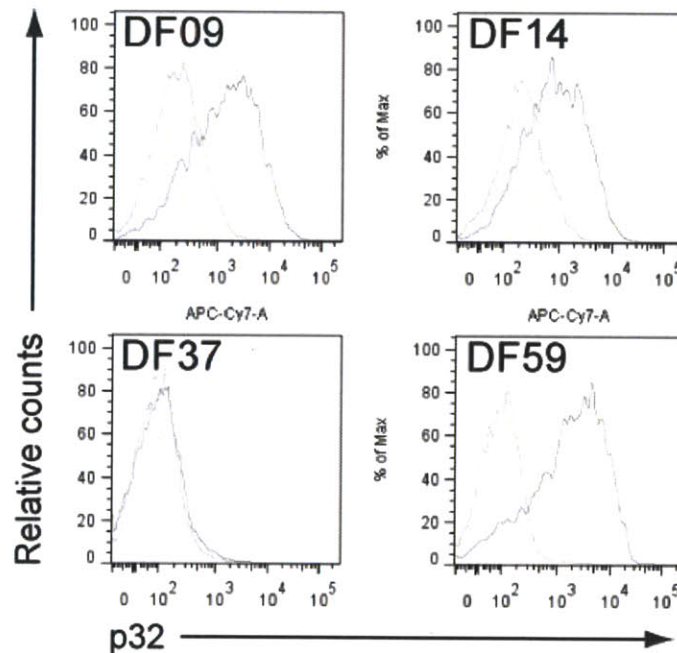
Figure 8.1. Expression of p32 on the surface of primary human patient ovarian cancer cell samples as determined by flow cytometry. The amount of p32 on the surface of four (4) primary cell strains (DF09, DF14, DF37, and DF59) was determined using a rabbit polyclonal antibody directed against the p32 peptide. Cells stained with an isotype-matched control are shown in grey.
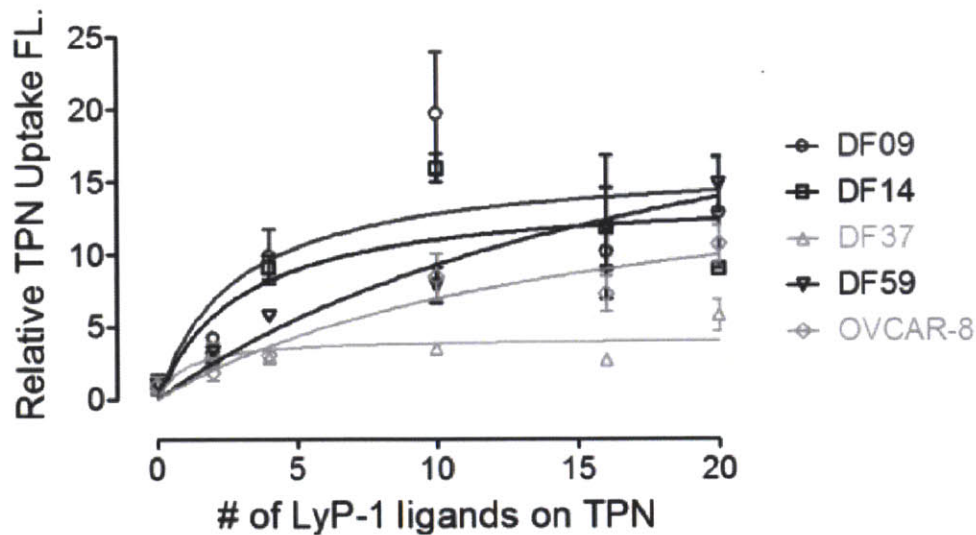
Figure 8.2. Uptake of TPN bearing different LyP-1 ligands on the surface by primary ovarian cancer cell samples. The cellular uptake of TPN bearing varying valence of the LyP-1 targeting peptide was determined by flow cytometry in four primary ovarian cancer cell samples as well as an established human ovarian cancer cell line (OVCAR-8). The siRNA payloads are labeled with an near-infrared fluorophore to enable monitoring of TPN uptake by flow cytometry. An exponential binding curve was fitted and overlaid. Each data point represents average ± s.d. from 6 independent experiments.
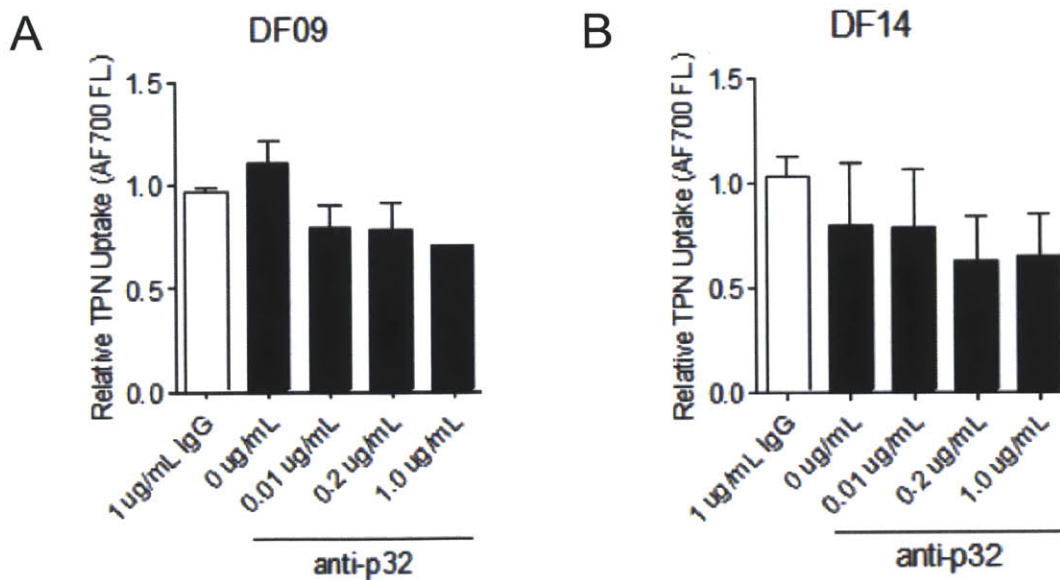
Figure 8.3. Effects of p32-antibody on TPN uptake. (A) Uptake of TPN carrying a near-infrared fluorophore-labeled siRNA by DF09 primary ovarian cancer cell samples measured by flow cytometry, in the presence of increasing concentrations of a p32-specific blocking antibody (anti-p32) or isotype-matched control (IgG). Error bars represent averages ± s.d. **(B)** Uptake of TPN in DF14 primary ovarian cancer cell samples.
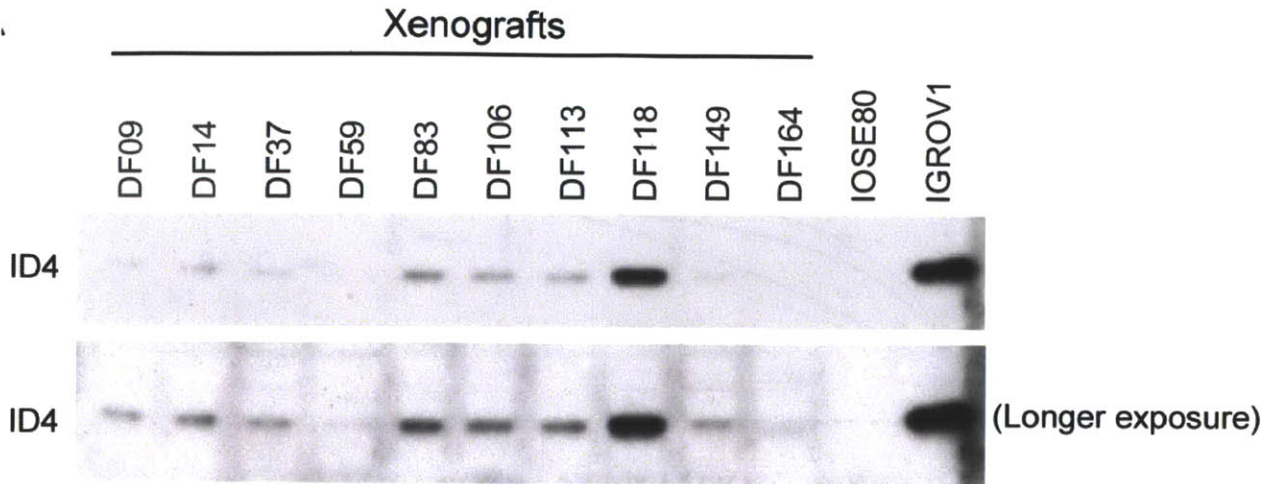
Figure 8.4. ID4 is expressed in a subset of primary human ovarian cancer cell samples. Freshly isolated patient primary ovarian cancer cells (denoted by DF##) were harvested and immunoblotted for ID4 expression. Lysates from immortalized ovarian surface epithelial cells (IOSE80) was used as a negative control. An established human ovarian cancer cell line (IGROV1) was used as a positive control. A longer exposure of the immunoblot was shown for better visualization of ID4 expression.
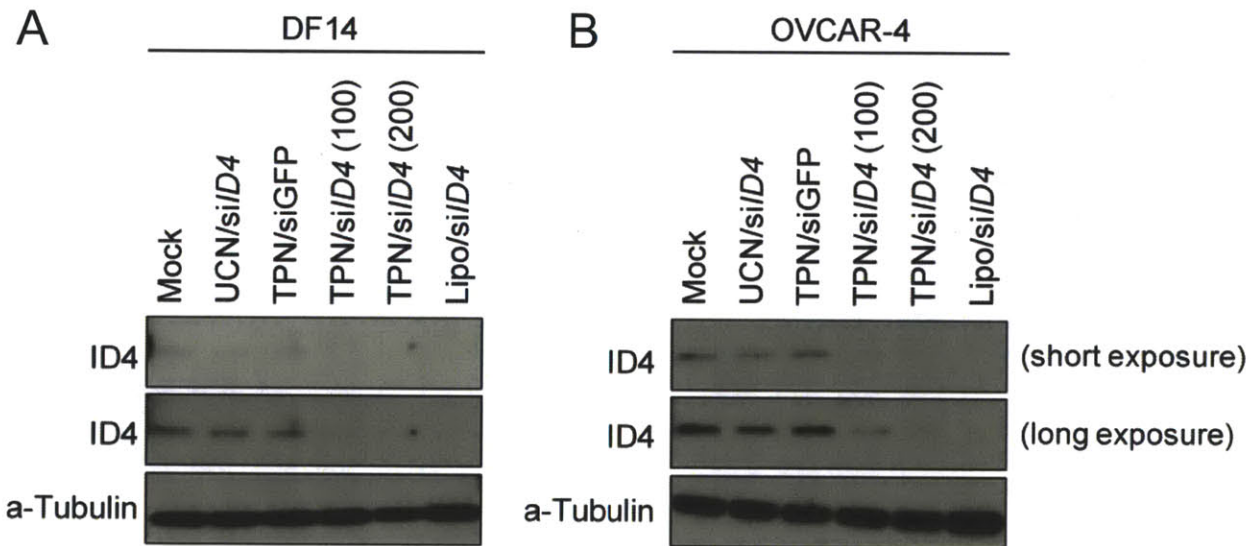
Figure 8.5. Suppression of ID4 by TPN-mediated siRNA delivery in primary patient-derived ovarian cancer cell samples and an established human ovarian cancer cell line. (A) Immunoblotting of ID4 from DF14 primary ovarian cancer cells that were treated on two consecutive days with TPN carrying ID4-specific siRNA (100pmol or 200pmol per treatment). Cells were harvested 48 h after the second transfection and lysed for immunoblotting. Control cells received either media (Mock) or untargeted control nanocomplex (UCN) carrying ID4-specific siRNA. Lipofectamine/siID4 was used as a positive control. A-tubulin was used as the loading control. **(B)** Immunoblotting of OVCAR-4 human ovarian cancer cell line subjected to similar TPN treatments as DF14.
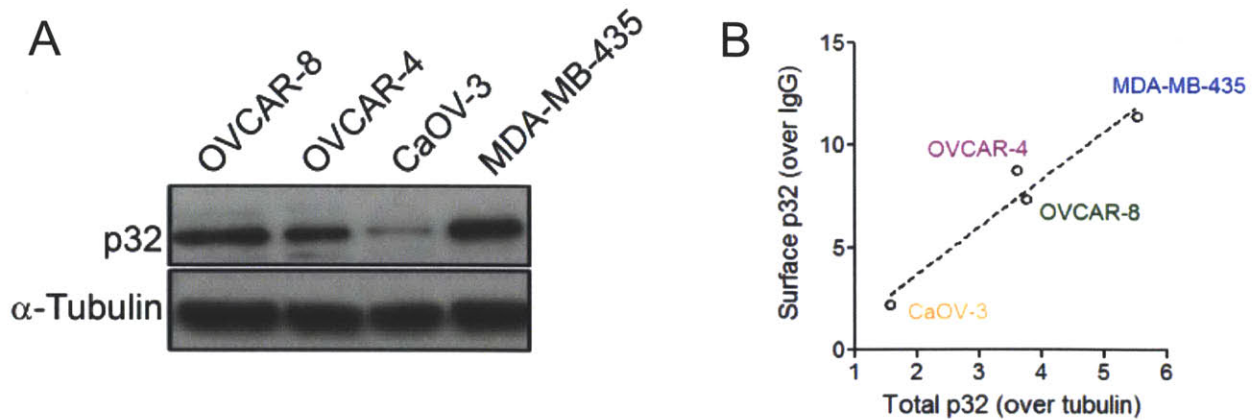
Figure 8.6. Correlation between total and surface p32 levels in cancer cell lines. *Top,* Immunoblotting of total p32 in lysates from four established human cancer cell lines from ovarian cancer (OVCAR-8, OVCAR-4, CaOV-3) and melanoma (MDA-MB-435). α-Tubulin was used as a loading control. *Bottom,* Correlation between surface p32 levels relative to an isotype-matched control as determined by flow cytometry with total p32 levels measured by immunoblotting. A linear correlation (R^2=0.97) was overlaid.
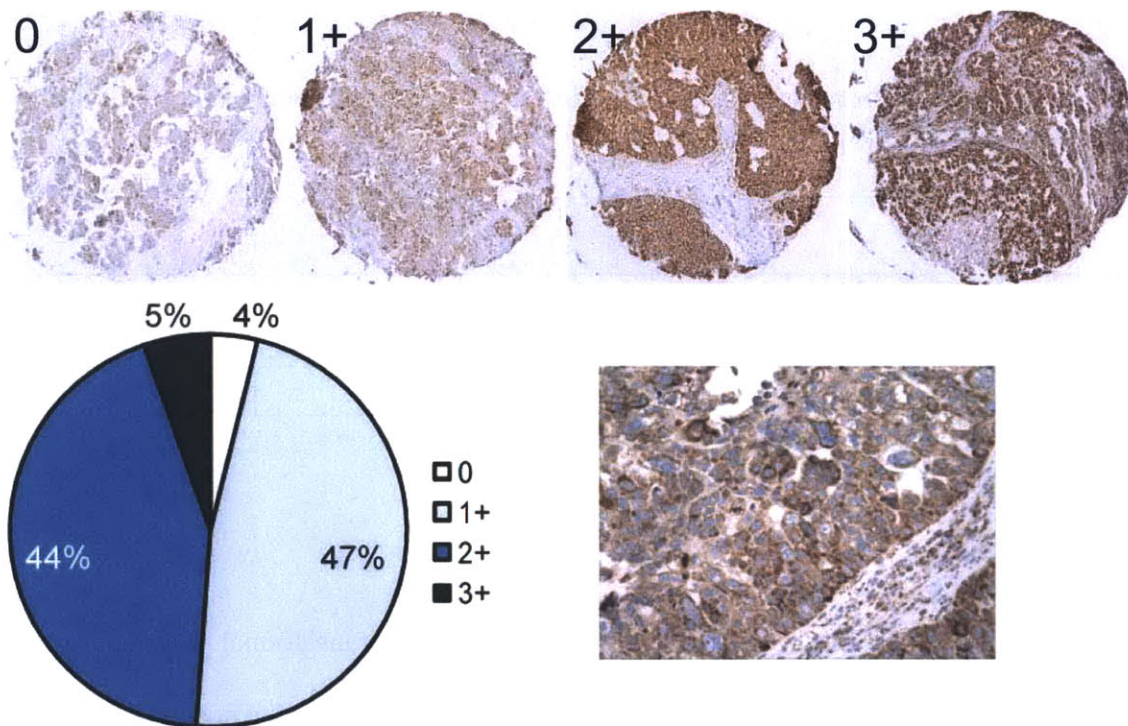
Figure 8.7. p32 expression in tissue microarrays analysis of ovarian cancer. In a TMA of 131 high-grade serous ovarian carcinomas, 49% of samples was p32-positive (Score 2+ and 3+), 47% of samples showed moderate p32 expression (Score 1+), while 4% was p32-negative (Score 0). *Top,* Representative micrographs of tissues with p32 immunohistochemical staining are shown. *Bottom left,* Distribution of p32 scores. *Bottom right,* An enlarged image for better visualization of p32 localization.

215

ID4 staining scores
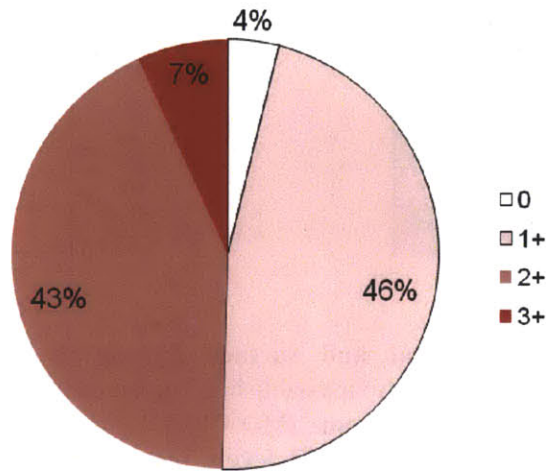
Figure 8.8. Distribution of ID4 immunostaining intensities. The TMA used for p32 scoring was also stained with ID4-antibody and staining intensities were quantified and graded using a similar scale. The intensities of ID4 and p32 for each tumor section was correlated and analyzed.

Table 8.1. Correlation between p32 and ID4 intensity in a tissue microarray of high-grade ovarian carcinoma.

		p32 Intensity		
		Low	*High*	*Total*
ID4 Intensity	*Low*	40	26	66
	High	27	38	65
	Total	64	67	131

8.3 Discussion

The primary aim of this study is to evaluate the clinical translational potential of the TPN platform for delivering siRNA therapeutics. To date, evaluations on the efficacy of TPN-mediated RNAi inhibition of gene expression are performed in either established human cancer cell lines or orthotopic xenograft mouse models. While these systems represent important models in which efficacy and safety studies must be carried out, they also suffer from several drawbacks that distinguish them from true models of cancer initiation and progression in patients. For

216

example, artifacts can be introduced during the process of adherence to tissue-culture plastic, as changes in the microenvironment may favor the activation of certain survival pathways. As a result, the phenotype of serially-passaged, adherent cancer cell lines may be drastically different from uncultured, primary patient-derived cell samples. Furthermore, xenograft mouse models have found to be poor at predicting cancer drug response, owing to their inability to recapitulate certain aspects of tumor progression, including the roles of mesenchymal cells, effects of the immune system, and contributions from tumor vasculature [320-322]. Therefore, the comprehensive evaluation of TPN in human patient tumor samples that are free of contaminations from tissue-culture is critical for eventual clinical translation.

Of the four primary patient ovarian cancer cell samples examined, three showed elevated p32 expression and are amenable to TPN targeting. In one particular cell sample (DF14), p32-specific TPN delivery and suppression of ID4, an ovarian-specific oncogene, was achieved. Follow-up studies are underway to evaluate the phenotypic consequences of ID4-depletion by siRNA *in vitro* and in xenografts *in vivo*. Results from these experiments could highlight a pathway towards clinical translation and efficacy studies in patients.

The expression of p32 was examined in a large cohort of high-grade ovarian tumor samples in a tissue microarray. Over half of the samples showed high p32 expression (Score 2+ and 3+), consistent with previous findings that suggest p32 is a general surface marker in a variety of tumor subtypes. Previous evidence also suggests that there is a correlation between aberrant p32 localization with mitochondrial dysfunction and maintenance of OXPHOS in established cancer cell lines. However, the exact functional role of p32 in ovarian cancer is still being investigated. While preliminary studies did not point to a statistical link between p32

overexpression and the clinical outcome of patients with HGSOC, a comprehensive examination

of p32 as a potential biomarker for other cancers utilizing expanded TMAs is warranted.

In summary, TPN can target a subset of primary ovarian cancer cells freshly isolated

from the ascites fluid of patients with advanced ovarian cancer. These cell samples also

overexpress ID4, a novel ovarian oncogene recurrently amplified in high-grade serous ovarian

carcinomas. Examination of tumor tissue microarrays revealed that a large fraction of high-grade

ovarian tumors express p32. TPN-mediated delivery of *ID4*-specific siRNA could represent a

potential therapeutic strategy for clinical implementation.

8.4 Materials and Methods

Primary cells. Primary ovarian cancer cells were obtained from patients with advanced ovarian cancer at the Dana-Farber Cancer Institute under protocols approved by the Dana-Farber/Harvard Cancer Center Institutional Review Board (DFHCC IRB) as previously described[235]. Briefly, the ascites fluid from patients was obtained, processed, and tumor cells were isolated and enriched for their epithelial nature via EpCAM and HE4 immunostaining.

Tumor penetrating nanocomplex (TPN) preparation. TPNs were prepared as described previously [213]. TPN/siRNA treatments were performed on two consecutive days in either DF14 or OVCAR-4 cells, and lysates were harvested 48 h later.

Tissue Microarrays. A microarray of ovarian tumors was constructed from tumor biopsy samples from patients with late-stage (Stage III or IV) high-grade serous ovarian adenocarcinomas who underwent cytoreductive surgery at the Dana Farber (n = 131). A quadruplicate set of biopsy cores of 0.8 mm in diameter was obtained from each patient.

Immunohistochemistry. Formalin-fixed, paraffin-embedded ovarian tumor sections were de-waxed, rehydrated, and incubated in hydrogen peroxide solution to block endogenous peroxidase. Antigen retrieval was performed in a pressure cooker in citrate buffer (pH 6.0). Histological staining with a rabbit polyclonal p32 antibody was carried out at 4 °C overnight (antibody dilution 1 µg/mL). A HRP-conjugated goat anti-rabbit antibody was applied for 1 h at room temperature, followed by DAB for 5 min for visualization.

Statistical analysis. Statistical analyses were performed using built-in statistical functions in GraphPad Prism (GraphPad Software) and appropriate statistical tests.

9 Discussion and future directions

9.1 In vivo tumor cell targeting with 'Click' nanoparticles

In *Chapter 2*, we demonstrated that "click" chemistry can be applied to target nanomaterials to tumors *in vivo*. Leveraging peptide discoveries from phage display, we showed that attachment of the cyclic tumor homing and tissue-penetrating peptide, LyP-1, to iron-oxide nanoparticles was able to direct their binding to p32-expressing tumor cells in cell culture and in tumor xenografts. Importantly, nanoparticles bearing the same valence of a control peptide with the same net charge and cyclic structure as LyP-1 (LyP-1CTL) did not bind p32. While the work focused on iron oxide nanoparticles, the attachment chemistry is bio-orthogonal and generalizable to virtually any peptide or nanomaterial scaffold. Therefore, expansion of "click" attachment to other systems for *in vivo* tumor targeting is a critical next step. Specifically, other cyclic tumor homing peptides such as RGD4C and iRGD can be attached to the end of azido-bearing 5kDa PEG polymers to enhance the circulation of nanomaterials including semiconductor quantum dots, gold colloids, polymeric nanoparticles, and peptides.

Despite their moderate circulation half-lives, the macroscopic intra-tumoral accumulation of LyP-1 click nanoparticles and PEG-azido-nanoparticles was similar, suggesting that tumor accumulation was on par with passive delivery and was not enhanced with LyP-1 targeting. This is consistent with other reports of long-circulating nanoparticles that passively accumulate in tumors *via* their hyper-porous vasculature over time *via* the enhanced permeability and retention (EPR) effect [204]. Because the receptor for LyP-1 is likely located in epithelial tumor cells and myeloid cells, it is not surprising that receptor binding would have difficulty amplifying the rate of tumor extravasation for targeted nanoparticles beyond what's achievable by EPR.

Histological examination revealed that untargeted nanomaterials remain closely localized to the immediate periphery of blood vessels, consistent with high co-localization with CD31 staining of tumors. By contrast, LyP-1 nanoparticles penetrated the interstitium and were taken up by p32-expressing tumor epithelial cells in the parenchyma. These results are in accordance with existing literature suggesting that targeting ligands alter the micro-distribution of nanoparticles, but do not increase macroscopic tumor accumulation [323]. Thus, there may also be unique transportation pathways within tumors that are exploited by this ligand after extravasation which are not available to untargeted materials. A future area of investigation is to characterize the intra-tumoral transportation pathways by which LyP-1-targeted nanomaterials undertake to access the parenchyma. Also, the unique localization of LyP-1 nanoparticles in avascular regions deep in the tumor parenchyma may be of interest for directing therapeutics into hypoxic regions of tumors, where most conventional therapies do not reach.

At 24 h following incubation, particles remain within punctuate compartments outside the nuclei, which are likely to be endosomal compartments. These nanoparticles likely cannot actively escape from endosomes as they lack devices to trigger lysis of the endosomal structures. An important step forward would be to engineer multi-functional Click nanoparticles that encompass diverse functionalities such as tumor-targeting, endosomal-escape, and release of therapeutic cargo on demand.

9.2 Tumor-penetrating nanomaterials for siRNA delivery

In *Chapter 3*, we described the development of a novel siRNA delivery technology leveraging newly discovered pathways of active tumor penetration through 'stimulated penetration and retention'. The delivery system consists of a multifunctional tandem peptide structure that contains a tumor-penetrating motif (LyP-1), a siRNA binding motif, and a cell-

penetration motif for transporting siRNA out of the endosomes and into the cytosol of tumor cells that aberrantly express the mitochondrial protein p32 on the surface. We found that a subset of tandem peptides bearing cell-penetration motifs such as Transportan (TP) delivered siRNA payloads into tumor cells in a p32 receptor-specific manner. Furthermore, systemically administered TP-LyP-1 nanocomplexes carrying fluorescently-labeled siRNA preferentially accumulated in tumor xenografts established from cell lines that overexpress p32.

To date, no delivery technologies exist that enables tissue-penetrating delivery of siRNA after either i.v. or i.p. administration. Current peptide- or viral- based approaches are either passively targeted, actively target intravascular receptors on endothelial cells in a non-tissue penetrating manner, or is limited to one particular cell type in non-cancer settings [151, 324]. As a result, these approaches have met with limited success in delivering siRNA to solid tumors. Our system offers the distinct advantage of being able to target siRNA to tumors *via* either i.p. or i.v. delivery. An immediate follow-up study is needed to elucidate the mechanism of action by which large nanoparticles with diameters of up to 100 nm can extravasate into systemic circulation subsequent to intraperitoneal administration. A thorough understanding of the *in vivo* pharmacokinetics and transportation pathways would allow us to formulate more sophisticated nanocarriers for systemic delivery of therapeutic and diagnostic agents.

Looking forward, this versatility could enable the adaptation for targeting other organ systems beyond the ovaries. We believe that i.v. administration is an exciting application of this work and the technology could find utility for patients with lung cancer since the pulmonary vessels are the first vasculature bbed nanoparticles would encounter. Currently, efforts are underway to test the efficacy of TPN delivery in genetically engineered mouse models of non-small cell lung cancer (NSCLC) as well as pancreatic ductal carcinomas (PDAC), both of which

are highly lethal diseases where numerous conventional chemotherapeutics failed to induce complete remission in a majority of patients.

Furthermore, this approach is synthetically modular, allowing incorporation of arbitrary tumor-penetrating domains leveraging stimulated penetration pathways. In the future, efforts to extend this delivery system to other homing ligands should greatly enhance its therapeutic impact. We have already begun evaluating tandem peptides bearing iRGD, another tumor-penetrating motif identified recently [117-119]. Preliminary data suggests that TP-iRGD tandem peptides carrying fluorescent siRNA payloads rapidly penetrated the parenchyma of OVCAR-8 tumor xenografts and distributed to tumor cells that express neuropilin-1 (NRP-1), a pattern similar to that of iRGD-targeted phage and nanoparticles. In the future, the functional delivery of siRNA cargo by TP-iRGD to suppress gene expression *in vivo* will be investigated.

In addition to the utility of the technology, what is *conceptually* novel about our approach is the finding that tandem peptide construction and complexation can fundamentally alter the function of one peptide domain while retaining properties of the second. The transportan (TP) domain, normally a ubiquitous cell penetrating ligand, is restricted to act upon cells that are entered through a specific receptor. Its cell penetrating property is thwarted whereas its ability to traverse endosomal membranes is retained. In addition, we employ its cationic charge to serve an additional siRNA complexation function. In contrast, the tumor-penetrating peptide LyP-1 retains its properties and they are enhanced by multivalency through complexation with siRNA.

In an orthotopic mouse model of disseminated ovarian cancer, a significant dose of nanocomplexes was able to reach the parenchymal epithelial ovarian tumor cells to silence the expression of a luciferase reporter. Looking forward, more potent carriers could be designed to reduce the amount of siRNA and/or peptide carrier required to suppress gene expression. Since

the tumor-penetrating domain (LyP-1) alone has an effect on cell viability at high doses (100 μM), a reduction in the dosage of siRNA and carrier without sacrificing either the potency of RNAi or specificity of p32-targeting would also decrease associated non-specific toxicities and off-target effects. This could be achieved by engineering more stable, long-circulating nanocomplexes that readily accumulate in tumors over time.

9.3 An integrated platform for credentialing cancer targets

Large-scale efforts to comprehensively characterize cancer genomes, such as The Cancer Genome Atlas (TCGA) and the International Cancer Genome Consortium (ICGC), have begun to uncover a list of loci that exhibit cancer specific copy number variations such as amplifications and deletions. Results from characterizations of glioblastomas and ovarian cancers show that most amplified regions encompass hundreds of genes. Looking forward, as data from other cancers become available, it will become increasingly difficult to dissect the functional roles of these genetic lesions, and identify from structural genomics data which genes are relevant cancer drivers that directly contribute to carcinogenesis.

The work presented in *Chapters 4 & 5* provides a much-needed and moderate-throughput approach to distill emerging cancer genome datasets down to viable therapeutic targets, by functionally validating cancer drivers *in vitro* and *in vivo*. Leveraging tumor-penetrating nanocomplexes (TPN) that enable tumor-targeted delivery of siRNA payloads into the tissue parenchyma, this integrated platform has the capacity to interrogate the functional consequences of suppressing any gene-of-interest *in vivo* through RNAi. Rapid integration between genomics efforts, loss-of-function approaches, and effective delivery technologies can validate therapeutic targets in as few as eight (8) weeks.

To fully investigate the efficacy of p32-mediated, *ID4*-dependent cancer cell killing, more comprehensive characterizations are needed. For example, the TPN technology could be validated in cell lines that either do not express p32 on the surface, do not harbor 6p22 amplifications or *CYCLOPS* genes, or whose survival do not depend on *ID4*-mediated signaling. Moreover, as the *in vivo* tumor response to RNAi therapy is likely dynamic and heterogeneous, detailed assessment of single-cell response to ID4 suppression in the context of whole tumors via immunohistochemistry will be necessary to optimize drug penetration and dosing.

Here, the *in vivo* validation studies were performed in orthotopic ovarian cancer xenografts in immunodeficient mice. We chose the orthotopic xenograft model to demonstrate its clinical utility because it offers three distinct advantages: *(1)* OVCAR-8 and A2780 cells harbor defined genetic abnormalities such as amplification of *ID4* and loss of copy number of *PSMC2*, *(2)* they express p32 on the cell surface which can be harnessed for nanocomplex targeting, *(3)* tumors can be established within several weeks, allowing rapid *in vivo* evaluation of potential therapies. While xenograft models provide a facile and robust tool for rapidly validating the role of cancer-associated genes, these animal models often do not fully recapitulate the pathogenesis and molecular characteristics of disease. For example, certain xenograft tumor models fail to reproduce interstitial fluid pressures measured in patients and do not accurately predict the chemotherapeutic response for certain drugs [94, 320]. Moreover, variations in the host can influence tumor neo-angiogenesis and the development of tumor stromal microenvironment. Therefore, as we gain further insight into the molecular events that occur during ovarian cancer pathogenesis, an important future step is to perform *in vivo* validation experiments in more accurate *in vitro* and *in vivo* models. These include cell culture models using fallopian tube-derived secretory epithelial cells (FTSEC) that are most likely the cells-of-origin for ovarian

cancer; genetically-engineered mouse models (GEMMs) of ovarian cancer and metastases that recapitulate genetic lesions such as loss of p53 and BRCA1/BRCA2 mutations; and in primary xenografts of human patient-derived ovarian cancer cells. Results from these studies will be important in evaluating the therapeutic efficacy of suppressing candidate cancer genes and paving the way for future clinical studies.

The cognate receptor (p32) for TPN is overexpressed in a large number and type of tumors, including specific localized expression in avascular regions of tumor hypoxia. Moreover, the ability of peptides bearing cryptic CendR domains to penetrate into the tissue parenchyma and deliver any associated cargo should also be generalizable across tumor types. We are currently applying the TPN technology to deliver nucleic acid therapeutics in GEMMs of non-small cell lung cancer (NSCLC) as well as pancreatic ductal adenocarcinoma (PDAC). The ability to suppress candidate oncogenes or restore tumor suppressor genes by TPN-mediated delivery will be transformative in cancer therapeutic development.

Cancer cells evolve under incredible selection pressures and accumulate a significant number of genetic alterations (mutations, amplifications, and deletions) over the course of tumor development. Therefore, siRNA therapeutics against a single gene or pathway is unlikely to be curative as redundant pro-survival and/or anti-apoptotic pathways emerge. Indeed, in preclinical therapeutic trials conducted, a proportion of mice undergoing TPN/si*ID4* treatments had tumors that were resistant to ID4 suppression or relapsed after the cessation of RNAi. Therefore, an important future area of investigation is to identify and overcome mechanisms by which ovarian cancer cells undertake to become resistant to RNAi therapy. A key advantage of our approach is the ability to quickly "mix-and-match" siRNAs targeting other genes without the need to re-synthesize or re-purify the delivery vehicle. Much like the recent successes seen with receptor

tyrosine kinase inhibitors for lung cancer and melanoma, this type of molecular approach can potentially revolutionize ovarian cancer therapy and improve patient outcomes.

In *Chapter 4*, we have identified *ID4* as a putative ovarian cancer-specific oncogene. ID4 belongs to a family of ID proteins, many of which (such as ID1) have been implicated in cancer growth and metastasis through regulating cell cycle checkpoints such as *CDKN1A*. While the precise threshold of lethality was not determined for ID4 knockdown in this work, it is an important area of future investigation. In other cancer models, the dose-response to *Myc* inhibition has been investigated. However, in most other studies on tumor regression, it is unclear what the exact "threshold" for lethality is for an individual oncogene, such as *ID4*. This is an ongoing, fertile field of research in cancer biology and oncogene addiction. In the future, more definitive studies are needed to uncover the mechanisms through which *ID4* act to transform cells and identify its downstream target genes.

9.4 Characterization of receptor-specific cell-penetrating peptides for siRNA delivery

In *Chapter 6*, we performed a quantitative and systematic characterization of the mechanism by which tumor-penetrating nanocomplexes (TPN) deliver siRNA in a cell type-specific manner. The winning combination of TP-LyP-1 tandem peptide and siRNA resulted in potent cellular uptake that is highly receptor-specific, efficient endosomal escape, and significant gene silencing. Combined with least square regression analysis, we were able to identify peptide charge and the valence of the targeting ligand as two converging key structural parameters that favor cell-selective siRNA delivery.

While these properties are identified within the context of the TPN system, the strategy of combining experimental investigations with computational analysis could be generalized to other

delivery systems, where multi-step processes are involved for an exogenous cargo to ultimately exert its effect. An exciting area for future investigation is the delivery of miRNA therapeutics, where factors such as cellular uptake, escape from endolysosomal entrapment, and binding to cognate mRNA sequences could all affect the overall potency of the miRNA. As efforts to develop miRNA carriers accelerate, a systematic approach could help identify key carrier properties that enable efficient cellular delivery.

One important area for future follow-up is the experimental validation of computational modeling results. To fully exploit the power of computational analysis, future tandem peptide carriers could be rationally designed to exhibit physiochemical characteristics that are predicted to enhance nanocomplex fitness. Individual amino acid substitutions to the TP-LyP-1 backbone should be examined to identify new peptides that can potently transduce siRNA payloads into cancer cells. Examination of other existing cell-penetrating domains that fit the design criteria should also be performed to expand the repertoire of TPN.

Here, several assumptions were made in the modeling framework. Due to the sequential nature of the steps involved in siRNA transduction and activation of RNAi, each step during the entire process was assumed to be independent from adjacent ones. As a result, the relative contribution of each step towards the overall RNAi efficiency was modeled using least square regression. Indeed, preliminary examination of the various functional properties revealed little inter-dependence (data not shown). A potential area for future investigation is the utilization of more sophisticated computational models that do not assume linearity, such as artificial neural networks, to reveal non-linear interactions between TPN functional properties.

In this work, the nanocomplexes are stabilized via hydrophobic interactions between *N*-terminal myristic acid domains. The myristic acid motif was selected based on existing evidence

that suggests the importance of fatty acids and lipids in imparting a stable structure to the self-assembled polyplexes. Future investigations should explore peptides conjugated with other fatty acid moieties, such as palmitoyl- and stearoyl-groups, to enhance the hydrophobic interactions within the nanocomplex and protection of the nucleic acid cargo. Furthermore, since nanocomplexes are generally cationic, electrostatic stabilization with anionic backbones such as hyaluronic acid could further promote stability. Current efforts are underway to characterize a combinational library of hydrophobic materials based on a biodegradable anionic hyaluronic acid backbone. Combinatorial mixtures of hyaluronic conjugates, tandem peptides, and siRNA will be generated into nanocomplexes at defined molar ratios. The effect of formulation on particle stability, siRNA release, endosomal escape, and receptor targeting will be examined to identify optimal formulations for therapeutic studies.

9.5 Improving the microdistribution of tumor-targeted theranostics

Nanotechnology is an emerging field that has tremendous potential in developing novel diagnostics and therapeutics for cancer. The unique size (tens to hundreds of nanometers) of nanoparticles enables them to not only operate at the length scale of biological machinery, but also attain remarkable biological and material properties that distinguish them from macroscopic counterparts. Through "top-down" engineering approaches, nanoparticles have been constructed out of materials with unique electromagnetic properties for imaging and remote actuation, and loaded with therapeutics such as small molecule drugs and nucleic acids [162, 325]. Already, several nanotechnology-based formulations have been approved for clinical use, including ultrasensitive iron-oxide contrast agents for MRI imaging and liposomal carriers that deliver chemotherapy preferentially to tumors while minimizing systemic toxicity. Recently, nanoparticles that target receptors overexpressed in tumors but not in normal tissues have gained

considerable interest. However, targeted therapeutics such as nanoparticles and antibodies suffer from poor tissue penetration owing to the presence of a binding site barrier. As a result, they accumulate mostly in tumor vessels and tumor cells in close proximity to vasculature, limiting the amount of therapeutics that ultimately reach cells located deep in the tumor parenchyma.

To overcome this transport barrier, much effort has been devoted to engineering monoclonal antibodies with precisely-tuned receptor affinities, allowing them to dissociate from the receptors after binding to improve intratumoral distribution. It has been established that antibodies with high receptor affinities typically exhibit a more heterogeneous pattern of tumor distribution owing to enhanced diffusion prior to antigen-mediated internalization. Taking a separate but complementary approach, the work presented in *Chapter 7* demonstrates a proof-of-concept methodology to systematically reduce receptor expression prior to administration of targeted ligands, thereby allowing the ligand to diffuse farther into the tumor tissue before being bound to its cognate receptor. As the mathematical modeling work showed, the balance of receptor turnover rate and efficiency of receptor knockdown is critical in influencing the ultimate intratumoral localization of therapeutics. Therefore, an important area for future investigation is to fully explore the effects of modulating p32 expression in combination with tuning the receptor affinity of TPN on tumor distribution. Characterizations of the kinetics of p32 receptor turnover and the amount of p32 receptors that is available for binding in various tumor subtypes will improve the current model for more accurate predictions.

FDG-PET imaging is the gold standard for assessing the metabolic status of glycolytically active tumors, including ovarian cancer. Clinically, the incorporation of anatomical imaging such as PET/CT has significantly improved the diagnostic accuracy for primary and metastatic ovarian cancer, with 87-100% sensitivity and 74-100% specificity.

However, FDG-PET detection of borderline tumors and non-glycolytically active early-stage adenocarcinomas (< 1cm in diameter) are poor. Moreover, non-specific accumulation of FDG in metabolically active tissues, including the bowel, activated inflammatory cells, and normal ovarian tissue could make differentiation of neoplasms from surrounding tissues difficult.

In this work, tumor cells treated with *p32*-specific siRNA showed an upregulation in glycolysis, increased glucose consumption, and increased lactate production. This phenotype was exploited for tumor imaging by FDG-PET. By transiently elevating glycolysis in cancer cells via RNAi, this technology has the potential to detect tumors that may be previously "PET-silent". The tumor-targeting aspect of this work may have the potential of reducing background tissue uptake, as tumor cells that overexpress p32 on the surface can preferentially take up TPN. Therefore, it may be possible to utilize p32-knockdown as a general means to amplify the tumor metabolic characteristics detected on PET scans. This may be important in clinical applications such as detecting small lymph node metastases and tumor recurrence.

Recently it has been proposed that fluorescent glucose analogs such as the near-infrared probes used in this work may not accurately depict the metabolic state of a cell [318]. Indeed, histological examination of tumor cross-sections containing the probe showed both intracellular as well as interstitial accumulation, inconsistent with the hypothesis that only glycolytically-active tumor cells can take up the injected probe. Therefore, future investigations should utilize glucose probes that are small in molecular weight (such as 2-NBDG), and studies should be performed to confirm that uptake is indeed due to glucose uptake via specific transporters such as GLUT-1, using either knock-out systems or competitive inhibitors of glucose transport.

9.6 TPN Delivery to human patient ovarian cancer cell samples

In *Chapter 8*, we showed that a subset of freshly isolated, primary ovarian cancer cells from patients with advanced, late-stage epithelial ovarian cancer can be targeted by TPN. A subset of human patient ovarian cell samples examined overexpressed p32 on the cell surface. DF14, a particular p32-expressing primary cell strain, also took up LyP-1-directed, siRNA-carrying TPN. Separately, a significant subset of primary ovarian cells also overexpressed ID4, an ovarian-specific oncogene that interrupts normal differentiation and proliferation pathways of the ovary and fallopian tube. Together, TPN delivery of *ID4*-specific siRNA to DF14 primary cells potently suppressed ID4 expression in a receptor- and siRNA sequence-dependent manner.

Given the findings suggesting the dual-presence of ID4-overexpression and p32-surface expression in a subset of advanced-stage, patient-derived, uncultured ovarian cancer cells, the TPN delivery technology could serve as a powerful therapeutic strategy in this subset of refractory advanced cancers that are resistant to conventional chemotherapy. One immediate and critical follow-up experiment is to investigate the effects of TPN-mediated RNAi inhibition of *ID4* on cellular survival and proliferation. Successful siRNA-inhibition of growth of primary cancer cells would represent a major step in shifting the ovarian cancer treatment paradigm towards personalized, nucleic acid-based therapies.

To further evaluate and substantiate the therapeutic value of ID4-inhibition in ovarian cancer patients, pre-clinical studies using mice bearing tumor xenografts derived from these primary cancer cells is of the utmost importance. To best mimic ovarian disease and the host response, immunocompetent mouse models should be considered. Following establishment of orthotopic human patient ovarian cancer xenografts, the effect of TPN delivery of *ID4*-specific siRNA should be investigated in a longitudinal therapeutic trial.

Combination therapies with other small molecule-, antibody-, or nucleic acid-based therapeutics are also worth exploring to maximize the synergistic effects on tumor killing. It has been recently established that depletion of ErbB3 in these primary cells interrupts a NRG1/ErbB-3 autocrine loop that is critical in maintaining cell viability [235]. Therefore, suppression of ErbB3-signalling by RNAi should also be examined. While the existing TPN system failed to significantly suppress ErbB3 expression *via* delivering a single siRNA sequence (data not shown), additional optimizations of siRNA potency should be performed.

Immunoblotting and flow cytometry analyses suggested that p32 is overexpressed in tumors and is also aberrantly localized to the cell surface. While the p32 protein lacks a canonical hydrophobic transmembrane-spanning region or a consensus site for GPI anchoring, it is thought that p32 localizes to the membrane through interacting with other membrane-anchored proteins. Indeed, this pattern of expression has been previously noted in other cell types, including Raji human lymphoma cells, neutrophils, and inflammatory cell populations [202, 326-330]. Here, we detected a linear correlation between total and cell-surface p32 in established human cancer cell lines, consistent with the observation that a fraction (~2-5%) of total p32 is "shuttled" to the cell surface. A future area of investigation is to further elucidate the domains within p32 that is responsible for LyP-1 peptide binding. As p32 expression has been found to fluctuate due to increased cell stress, approaches to upregulate p32 expression for enhanced tumor targeting should also be explored. Identification of p32's binding partners that anchors the protein to the plasma membrane will be crucial in enabling more detailed molecular studies.

Finally, examination of large cohorts of high-grade serous ovarian carcinomas through tissue microarrays (TMA) revealed that p32 overexpression occurs frequently in patients with advanced-stage ovarian cancer. It is still unclear whether the expression of this marker is an

indication of malignancy or predictor of clinical outcome, as p32 alone is insufficient to stratify this set of patients. Nevertheless, the high prevalence of p32 expression implies that a large fraction of patients could benefit from p32-targeted TPN/siRNA therapy. Examination of p32 status in expanded tissue arrays from patients with other types of cancers is a critical next step to evaluate its potential as a biomarker.

10 References

1. Hopkins, A.L. and C.R. Groom, *The druggable genome.* Nat Rev Drug Discov, 2002. **1**(9): p. 727-30.
2. Elbashir, S.M., et al., *Duplexes of 21-nucleotide RNAs mediate RNA interference in cultured mammalian cells.* Nature, 2001. **411**(6836): p. 494-8.
3. Fire, A., et al., *Potent and specific genetic interference by double-stranded RNA in Caenorhabditis elegans.* Nature, 1998. **391**(6669): p. 806-11.
4. Hannon, G.J. and J.J. Rossi, *Unlocking the potential of the human genome with RNA interference.* Nature, 2004. **431**(7006): p. 371-8.
5. Whitehead, K.A., R. Langer, and D.G. Anderson, *Knocking down barriers: advances in siRNA delivery.* Nat Rev Drug Discov, 2009. **8**(2): p. 129-38.
6. Bumcrot, D., et al., *RNAi therapeutics: a potential new class of pharmaceutical drugs.* Nat Chem Biol, 2006. **2**(12): p. 711-9.
7. Pecot, C.V., et al., *RNA interference in the clinic: challenges and future directions.* Nat Rev Cancer, 2011. **11**(1): p. 59-67.
8. Siegel, R., et al., *Cancer statistics, 2011: the impact of eliminating socioeconomic and racial disparities on premature cancer deaths.* CA Cancer J Clin, 2011. **61**(4): p. 212-36.
9. Jemal, A., et al., *Global cancer statistics.* CA Cancer J Clin, 2011. **61**(2): p. 69-90.
10. Carlson, K.J., S.J. Skates, and D.E. Singer, *Screening for ovarian cancer.* Ann Intern Med, 1994. **121**(2): p. 124-32.
11. Rosen, D.G., et al., *Potential markers that complement expression of CA125 in epithelial ovarian cancer.* Gynecol Oncol, 2005. **99**(2): p. 267-77.
12. Markman, M., *Concept of optimal surgical cytoreduction in advanced ovarian cancer: a brief critique and a call for action.* J Clin Oncol, 2007. **25**(27): p. 4168-70.
13. Covens, A.L., *A critique of surgical cytoreduction in advanced ovarian cancer.* Gynecol Oncol, 2000. **78**(3 Pt 1): p. 269-74.
14. Bristow, R.E., et al., *Survival effect of maximal cytoreductive surgery for advanced ovarian carcinoma during the platinum era: a meta-analysis.* J Clin Oncol, 2002. **20**(5): p. 1248-59.
15. Winter, W.E., 3rd, et al., *Prognostic factors for stage III epithelial ovarian cancer: a Gynecologic Oncology Group Study.* J Clin Oncol, 2007. **25**(24): p. 3621-7.
16. Dedrick, R.L., et al., *Pharmacokinetic rationale for peritoneal drug administration in the treatment of ovarian cancer.* Cancer Treat Rep, 1978. **62**(1): p. 1-11.
17. Markman, M., *Intraperitoneal chemotherapy.* Semin Oncol, 1991. **18**(3): p. 248-54.
18. Kyrgiou, M., et al., *Survival benefits with diverse chemotherapy regimens for ovarian cancer: meta-analysis of multiple treatments.* J Natl Cancer Inst, 2006. **98**(22): p. 1655-63.
19. Parmar, M.K., et al., *Paclitaxel plus platinum-based chemotherapy versus conventional platinum-based chemotherapy in women with relapsed ovarian cancer: the ICON4/AGO-OVAR-2.2 trial.* Lancet, 2003. **361**(9375): p. 2099-106.
20. Bissell, M.J. and D. Radisky, *Putting tumours in context.* Nat Rev Cancer, 2001. **1**(1): p. 46-54.
21. Druker, B.J., et al., *Effects of a selective inhibitor of the Abl tyrosine kinase on the growth of Bcr-Abl positive cells.* Nat Med, 1996. **2**(5): p. 561-6.

22. Shepherd, F.A., et al., *Erlotinib in previously treated non-small-cell lung cancer.* N Engl J Med, 2005. **353**(2): p. 123-32.

23. Bast, R.C., Jr., B. Hennessy, and G.B. Mills, *The biology of ovarian cancer: new opportunities for translation.* Nat Rev Cancer, 2009. **9**(6): p. 415-28.

24. Burger, R.A., et al., *Incorporation of bevacizumab in the primary treatment of ovarian cancer.* N Engl J Med, 2011. **365**(26): p. 2473-83.

25. Eskander, R.N. and L.M. Randall, *Bevacizumab in the treatment of ovarian cancer.* Biologics, 2011. **5**: p. 1-5.

26. Annunziata, C.M., et al., *Vandetanib, designed to inhibit VEGFR2 and EGFR signaling, had no clinical activity as monotherapy for recurrent ovarian cancer and no detectable modulation of VEGFR2.* Clin Cancer Res, 2010. **16**(2): p. 664-72.

27. Cesca, M., et al., *The effects of vandetanib on paclitaxel tumor distribution and antitumor activity in a xenograft model of human ovarian carcinoma.* Neoplasia, 2009. **11**(11): p. 1155-64.

28. Jacobs, I.J., et al., *Clonal origin of epithelial ovarian carcinoma: analysis by loss of heterozygosity, p53 mutation, and X-chromosome inactivation.* J Natl Cancer Inst, 1992. **84**(23): p. 1793-8.

29. *Integrated genomic analyses of ovarian carcinoma.* Nature, 2011. **474**(7353): p. 609-15.

30. Crum, C.P., et al., *The distal fallopian tube: a new model for pelvic serous carcinogenesis.* Curr Opin Obstet Gynecol, 2007. **19**(1): p. 3-9.

31. Levanon, K., C. Crum, and R. Drapkin, *New insights into the pathogenesis of serous ovarian cancer and its clinical impact.* J Clin Oncol, 2008. **26**(32): p. 5284-93.

32. Kurman, R.J. and M. Shih Ie, *The origin and pathogenesis of epithelial ovarian cancer: a proposed unifying theory.* Am J Surg Pathol, 2010. **34**(3): p. 433-43.

33. Kim, J., et al., *High-grade serous ovarian cancer arises from fallopian tube in a mouse model.* Proc Natl Acad Sci U S A, 2012. **109**(10): p. 3921-6.

34. TCGA-Network, *Comprehensive genomic characterization defines human glioblastoma genes and core pathways.* Nature, 2008. **455**(7216): p. 1061-8.

35. Peeper, D.S., et al., *A functional screen identifies hDRIL1 as an oncogene that rescues RAS-induced senescence.* Nat Cell Biol, 2002. **4**(2): p. 148-53.

36. Boehm, J.S., et al., *Integrative genomic approaches identify IKBKE as a breast cancer oncogene.* Cell, 2007. **129**(6): p. 1065-79.

37. He, L., et al., *A microRNA polycistron as a potential human oncogene.* Nature, 2005. **435**(7043): p. 828-33.

38. Garzon, R., et al., *MicroRNA expression and function in cancer.* Trends Mol Med, 2006. **12**(12): p. 580-7.

39. Griffiths-Jones, S., *miRBase: the microRNA sequence database.* Methods Mol Biol, 2006. **342**: p. 129-38.

40. Volinia, S., et al., *A microRNA expression signature of human solid tumors defines cancer gene targets.* Proc Natl Acad Sci U S A, 2006. **103**(7): p. 2257-61.

41. Calin, G.A., et al., *Frequent deletions and down-regulation of micro- RNA genes miR15 and miR16 at 13q14 in chronic lymphocytic leukemia.* Proc Natl Acad Sci U S A, 2002. **99**(24): p. 15524-9.

42. Liu, C., et al., *The microRNA miR-34a inhibits prostate cancer stem cells and metastasis by directly repressing CD44.* Nat Med, 2011. **17**(2): p. 211-5.

43. Hannon, G.J., *RNA interference.* Nature, 2002. **418**(6894): p. 244-51.

44.   Meister, G. and T. Tuschl, *Mechanisms of gene silencing by double-stranded RNA.* Nature, 2004. **431**(7006): p. 343-9.

45.   Meister, G., et al., *Human Argonaute2 mediates RNA cleavage targeted by miRNAs and siRNAs.* Mol Cell, 2004. **15**(2): p. 185-97.

46.   Liu, J., et al., *Argonaute2 is the catalytic engine of mammalian RNAi.* Science, 2004. **305**(5689): p. 1437-41.

47.   Martinez, J., et al., *Single-stranded antisense siRNAs guide target RNA cleavage in RNAi.* Cell, 2002. **110**(5): p. 563-74.

48.   Cheung, H.W., et al., *Systematic investigation of genetic vulnerabilities across cancer cell lines reveals lineage-specific dependencies in ovarian cancer.* Proc Natl Acad Sci U S A, 2011. **108**(30): p. 12372-7.

49.   Leachman, S.A., et al., *First-in-human mutation-targeted siRNA phase Ib trial of an inherited skin disorder.* Mol Ther, 2010. **18**(2): p. 442-6.

50.   DeVincenzo, J., et al., *A randomized, double-blind, placebo-controlled study of an RNAi-based therapy directed against respiratory syncytial virus.* Proc Natl Acad Sci U S A, 2010. **107**(19): p. 8800-5.

51.   Jopling, C.L., et al., *Modulation of hepatitis C virus RNA abundance by a liver-specific MicroRNA.* Science, 2005. **309**(5740): p. 1577-81.

52.   Fattal, E. and A. Bochot, *Ocular delivery of nucleic acids: antisense oligonucleotides, aptamers and siRNA.* Adv Drug Deliv Rev, 2006. **58**(11): p. 1203-23.

53.   Veber, D.F., et al., *Molecular properties that influence the oral bioavailability of drug candidates.* J Med Chem, 2002. **45**(12): p. 2615-23.

54.   Lipinski, C.A., *Drug-like properties and the causes of poor solubility and poor permeability.* J Pharmacol Toxicol Methods, 2000. **44**(1): p. 235-49.

55.   Gao, S., et al., *The effect of chemical modification and nanoparticle formulation on stability and biodistribution of siRNA in mice.* Mol Ther, 2009. **17**(7): p. 1225-33.

56.   Inoue, T., et al., *Modulation of scratching behavior by silencing an endogenous cyclooxygenase-1 gene in the skin through the administration of siRNA.* J Gene Med, 2007. **9**(11): p. 994-1001.

57.   Palliser, D., et al., *An siRNA-based microbicide protects mice from lethal herpes simplex virus 2 infection.* Nature, 2006. **439**(7072): p. 89-94.

58.   Wu, Y., et al., *Durable protection from Herpes Simplex Virus-2 transmission following intravaginal application of siRNAs targeting both a viral and host gene.* Cell Host Microbe, 2009. **5**(1): p. 84-94.

59.   Li, B.J., et al., *Using siRNA in prophylactic and therapeutic regimens against SARS coronavirus in Rhesus macaque.* Nat Med, 2005. **11**(9): p. 944-51.

60.   DeVincenzo, J., et al., *Evaluation of the safety, tolerability and pharmacokinetics of ALN-RSV01, a novel RNAi antiviral therapeutic directed against respiratory syncytial virus (RSV).* Antiviral Res, 2008. **77**(3): p. 225-31.

61.   Dominska, M. and D.M. Dykxhoorn, *Breaking down the barriers: siRNA delivery and endosome escape.* J Cell Sci, 2010. **123**(Pt 8): p. 1183-9.

62.   Stoorvogel, W., et al., *Late endosomes derive from early endosomes by maturation.* Cell, 1991. **65**(3): p. 417-27.

63.   Gibbings, D. and O. Voinnet, *Control of RNA silencing and localization by endolysosomes.* Trends Cell Biol, 2010. **20**(8): p. 491-501.

64. Ledley, F.D., *Nonviral gene therapy: the promise of genes as pharmaceutical products.* Hum Gene Ther, 1995. **6**(9): p. 1129-44.

65. Singh, N., et al., *Effect of nanoparticle conjugation on gene silencing by RNA interference.* J Am Chem Soc, 2010. **132**(24): p. 8241-3.

66. Nakhaei, P., et al., *RIG-I-like receptors: sensing and responding to RNA virus infection.* Semin Immunol, 2009. **21**(4): p. 215-22.

67. Akira, S., S. Uematsu, and O. Takeuchi, *Pathogen recognition and innate immunity.* Cell, 2006. **124**(4): p. 783-801.

68. Hornung, V., et al., *Sequence-specific potent induction of IFN-alpha by short interfering RNA in plasmacytoid dendritic cells through TLR7.* Nat Med, 2005. **11**(3): p. 263-70.

69. Judge, A.D., et al., *Sequence-dependent stimulation of the mammalian innate immune response by synthetic siRNA.* Nat Biotechnol, 2005. **23**(4): p. 457-62.

70. Marques, J.T. and B.R. Williams, *Activation of the mammalian immune system by siRNAs.* Nat Biotechnol, 2005. **23**(11): p. 1399-405.

71. Meylan, E. and J. Tschopp, *Toll-like receptors and RNA helicases: two parallel ways to trigger antiviral responses.* Mol Cell, 2006. **22**(5): p. 561-9.

72. Judge, A.D., et al., *Design of noninflammatory synthetic siRNA mediating potent gene silencing in vivo.* Mol Ther, 2006. **13**(3): p. 494-505.

73. Robbins, M., A. Judge, and I. MacLachlan, *siRNA and innate immunity.* Oligonucleotides, 2009. **19**(2): p. 89-102.

74. Jackson, A.L., et al., *Position-specific chemical modification of siRNAs reduces "off-target" transcript silencing.* RNA, 2006. **12**(7): p. 1197-205.

75. Jackson, A.L., et al., *Widespread siRNA "off-target" transcript silencing mediated by seed region sequence complementarity.* RNA, 2006. **12**(7): p. 1179-87.

76. Farh, K.K., et al., *The widespread impact of mammalian MicroRNAs on mRNA repression and evolution.* Science, 2005. **310**(5755): p. 1817-21.

77. Khan, A.A., et al., *Transfection of small RNAs globally perturbs gene regulation by endogenous microRNAs.* Nat Biotechnol, 2009. **27**(6): p. 549-55.

78. Grimm, D., et al., *Fatality in mice due to oversaturation of cellular microRNA/short hairpin RNA pathways.* Nature, 2006. **441**(7092): p. 537-41.

79. Sevick, E.M. and R.K. Jain, *Viscous resistance to blood flow in solid tumors: effect of hematocrit on intratumor blood viscosity.* Cancer Res, 1989. **49**(13): p. 3513-9.

80. Sevick, E.M. and R.K. Jain, *Geometric resistance to blood flow in solid tumors perfused ex vivo: effects of tumor size and perfusion pressure.* Cancer Res, 1989. **49**(13): p. 3506-12.

81. Helmlinger, G., et al., *Solid stress inhibits the growth of multicellular tumor spheroids.* Nat Biotechnol, 1997. **15**(8): p. 778-83.

82. Leunig, M., et al., *Angiogenesis, microvascular architecture, microhemodynamics, and interstitial fluid pressure during early growth of human adenocarcinoma LS174T in SCID mice.* Cancer Res, 1992. **52**(23): p. 6553-60.

83. Chaplin, D.J., et al., *Evidence for intermittent radiobiological hypoxia in experimental tumour systems.* Biomed Biochim Acta, 1989. **48**(2-3): p. S255-9.

84. Vaupel, P., F. Kallinowski, and P. Okunieff, *Blood flow, oxygen and nutrient supply, and metabolic microenvironment of human tumors: a review.* Cancer Res, 1989. **49**(23): p. 6449-65.

85. Heldin, C.H., et al., *High interstitial fluid pressure - an obstacle in cancer therapy.* Nat Rev Cancer, 2004. **4**(10): p. 806-13.

86. Stohrer, M., et al., *Oncotic pressure in solid tumors is elevated.* Cancer Res, 2000. **60**(15): p. 4251-5.

87. Netti, P.A., et al., *Enhancement of fluid filtration across tumor vessels: implication for delivery of macromolecules.* Proc Natl Acad Sci U S A, 1999. **96**(6): p. 3137-42.

88. Kinzler, K.W. and B. Vogelstein, *Landscaping the cancer terrain.* Science, 1998. **280**(5366): p. 1036-7.

89. Netti, P.A., et al., *Role of extracellular matrix assembly in interstitial transport in solid tumors.* Cancer Res, 2000. **60**(9): p. 2497-503.

90. Tang, Y., et al., *Extracellular matrix metalloproteinase inducer stimulates tumor angiogenesis by elevating vascular endothelial cell growth factor and matrix metalloproteinases.* Cancer Res, 2005. **65**(8): p. 3193-9.

91. Farokhzad, O.C. and R. Langer, *Nanomedicine: developing smarter therapeutic and diagnostic modalities.* Adv Drug Deliv Rev, 2006. **58**(14): p. 1456-9.

92. Maeda, H., et al., *Tumor vascular permeability and the EPR effect in macromolecular therapeutics: a review.* J Control Release, 2000. **65**(1-2): p. 271-84.

93. Iyer, A.K., et al., *Exploiting the enhanced permeability and retention effect for tumor targeting.* Drug Discov Today, 2006. **11**(17-18): p. 812-8.

94. Gutmann, R., et al., *Interstitial hypertension in head and neck tumors in patients: correlation with tumor size.* Cancer Res, 1992. **52**(7): p. 1993-5.

95. Torchilin, V., *Tumor delivery of macromolecular drugs based on the EPR effect.* Adv Drug Deliv Rev, 2011. **63**(3): p. 131-5.

96. Ran, S. and P.E. Thorpe, *Phosphatidylserine is a marker of tumor vasculature and a potential target for cancer imaging and therapy.* Int J Radiat Oncol Biol Phys, 2002. **54**(5): p. 1479-84.

97. Qian, X., et al., *In vivo tumor targeting and spectroscopic detection with surface-enhanced Raman nanoparticle tags.* Nat Biotechnol, 2008. **26**(1): p. 83-90.

98. Koivunen, E., et al., *Tumor targeting with a selective gelatinase inhibitor.* Nat Biotechnol, 1999. **17**(8): p. 768-74.

99. Soares, M.M., S.W. King, and P.E. Thorpe, *Targeting inside-out phosphatidylserine as a therapeutic strategy for viral diseases.* Nat Med, 2008. **14**(12): p. 1357-62.

100. Koivunen, E., B. Wang, and E. Ruoslahti, *Phage libraries displaying cyclic peptides with different ring sizes: ligand specificities of the RGD-directed integrins.* Biotechnology (N Y), 1995. **13**(3): p. 265-70.

101. Laakkonen, P., et al., *A tumor-homing peptide with a targeting specificity related to lymphatic vessels.* Nat Med, 2002. **8**(7): p. 751-5.

102. Dassie, J.P., et al., *Systemic administration of optimized aptamer-siRNA chimeras promotes regression of PSMA-expressing tumors.* Nat Biotechnol, 2009. **27**(9): p. 839-49.

103. Weissleder, R., et al., *Cell-specific targeting of nanoparticles by multivalent attachment of small molecules.* Nat Biotechnol, 2005. **23**(11): p. 1418-23.

104. Minchinton, A.I. and I.F. Tannock, *Drug penetration in solid tumours.* Nat Rev Cancer, 2006. **6**(8): p. 583-92.

105.   Nanda, S., *Pancreas: high stromal expression of alpha-smooth-muscle actin correlates with aggressive pancreatic cancer biology.* Nat Rev Gastroenterol Hepatol, 2010. **7**(12): p. 652.

106.   Chu, G.C., et al., *Stromal biology of pancreatic cancer.* J Cell Biochem, 2007. **101**(4): p. 887-907.

107.   Tong, R.T., et al., *Vascular normalization by vascular endothelial growth factor receptor 2 blockade induces a pressure gradient across the vasculature and improves drug penetration in tumors.* Cancer Res, 2004. **64**(11): p. 3731-6.

108.   Jain, R.K., *Normalizing tumor vasculature with anti-angiogenic therapy: a new paradigm for combination therapy.* Nat Med, 2001. **7**(9): p. 987-9.

109.   Jain, R.K., *Normalization of tumor vasculature: an emerging concept in antiangiogenic therapy.* Science, 2005. **307**(5706): p. 58-62.

110.   Curti, B.D., et al., *Interstitial pressure of subcutaneous nodules in melanoma and lymphoma patients: changes during treatment.* Cancer Res, 1993. **53**(10 Suppl): p. 2204-7.

111.   Morinaga, Y., et al., *Combination effect of AC-7700, a novel combretastatin A-4 derivative, and cisplatin against murine and human tumors in vivo.* Cancer Sci, 2003. **94**(2): p. 200-4.

112.   Horsman, M.R. and D.W. Siemann, *Pathophysiologic effects of vascular-targeting agents and the implications for combination with conventional therapies.* Cancer Res, 2006. **66**(24): p. 11520-39.

113.   Eikenes, L., et al., *Collagenase increases the transcapillary pressure gradient and improves the uptake and distribution of monoclonal antibodies in human osteosarcoma xenografts.* Cancer Res, 2004. **64**(14): p. 4768-73.

114.   Brown, E., et al., *Dynamic imaging of collagen and its modulation in tumors in vivo using second-harmonic generation.* Nat Med, 2003. **9**(6): p. 796-800.

115.   Olive, K.P., et al., *Inhibition of Hedgehog signaling enhances delivery of chemotherapy in a mouse model of pancreatic cancer.* Science, 2009. **324**(5933): p. 1457-61.

116.   Provenzano, P.P., et al., *Enzymatic targeting of the stroma ablates physical barriers to treatment of pancreatic ductal adenocarcinoma.* Cancer Cell, 2012. **21**(3): p. 418-29.

117.   Sugahara, K.N., et al., *Tissue-penetrating delivery of compounds and nanoparticles into tumors.* Cancer Cell, 2009. **16**(6): p. 510-20.

118.   Teesalu, T., et al., *C-end rule peptides mediate neuropilin-1-dependent cell, vascular, and tissue penetration.* Proc Natl Acad Sci U S A, 2009. **106**(38): p. 16157-62.

119.   Sugahara, K.N., et al., *Coadministration of a tumor-penetrating peptide enhances the efficacy of cancer drugs.* Science, 2010. **328**(5981): p. 1031-5.

120.   Emerich, D.F., et al., *Bradykinin modulation of tumor vasculature: II. activation of nitric oxide and phospholipase A2/prostaglandin signaling pathways synergistically modifies vascular physiology and morphology to enhance delivery of chemotherapeutic agents to tumors.* J Pharmacol Exp Ther, 2001. **296**(2): p. 632-41.

121.   Emerich, D.F., et al., *Bradykinin modulation of tumor vasculature: I. Activation of B2 receptors increases delivery of chemotherapeutic agents into solid peripheral tumors, enhancing their efficacy.* J Pharmacol Exp Ther, 2001. **296**(2): p. 623-31.

122.   Martinive, P., et al., *Reversal of temporal and spatial heterogeneities in tumor perfusion identifies the tumor vascular tone as a tunable variable to improve drug delivery.* Mol Cancer Ther, 2006. **5**(6): p. 1620-7.

123. Soker, S., et al., *Neuropilin-1 is expressed by endothelial and tumor cells as an isoform-specific receptor for vascular endothelial growth factor.* Cell, 1998. **92**(6): p. 735-45.

124. Narazaki, M. and G. Tosato, *Ligand-induced internalization selects use of common receptor neuropilin-1 by VEGF165 and semaphorin3A.* Blood, 2006. **107**(10): p. 3892-901.

125. Robinson, S.D., et al., *Alphav beta3 integrin limits the contribution of neuropilin-1 to vascular endothelial growth factor-induced angiogenesis.* J Biol Chem, 2009. **284**(49): p. 33966-81.

126. Akinc, A., et al., *A combinatorial library of lipid-like materials for delivery of RNAi therapeutics.* Nat Biotechnol, 2008. **26**(5): p. 561-9.

127. McNamara, J.O., 2nd, et al., *Cell type-specific delivery of siRNAs with aptamer-siRNA chimeras.* Nat Biotechnol, 2006. **24**(8): p. 1005-15.

128. Song, E., et al., *Antibody mediated in vivo delivery of small interfering RNAs via cell-surface receptors.* Nat Biotechnol, 2005. **23**(6): p. 709-17.

129. Bartlett, D.W., et al., *Impact of tumor-specific targeting on the biodistribution and efficacy of siRNA nanoparticles measured by multimodality in vivo imaging.* Proc Natl Acad Sci U S A, 2007. **104**(39): p. 15549-54.

130. Choung, S., et al., *Chemical modification of siRNAs to improve serum stability without loss of efficacy.* Biochem Biophys Res Commun, 2006. **342**(3): p. 919-27.

131. Wolfrum, C., et al., *Mechanisms and optimization of in vivo delivery of lipophilic siRNAs.* Nat Biotechnol, 2007. **25**(10): p. 1149-57.

132. Soutschek, J., et al., *Therapeutic silencing of an endogenous gene by systemic administration of modified siRNAs.* Nature, 2004. **432**(7014): p. 173-8.

133. Wilson, D.S. and J.W. Szostak, *In vitro selection of functional nucleic acids.* Annu Rev Biochem, 1999. **68**: p. 611-47.

134. Wheeler, L.A., et al., *Inhibition of HIV transmission in human cervicovaginal explants and humanized mice using CD4 aptamer-siRNA chimeras.* J Clin Invest, 2011. **121**(6): p. 2401-12.

135. Torchilin, V.P., *Recent advances with liposomes as pharmaceutical carriers.* Nat Rev Drug Discov, 2005. **4**(2): p. 145-60.

136. Allen, T.M. and P.R. Cullis, *Drug delivery systems: entering the mainstream.* Science, 2004. **303**(5665): p. 1818-22.

137. Felgner, P.L., et al., *Lipofection: a highly efficient, lipid-mediated DNA-transfection procedure.* Proc Natl Acad Sci U S A, 1987. **84**(21): p. 7413-7.

138. Felgner, P.L. and G.M. Ringold, *Cationic liposome-mediated transfection.* Nature, 1989. **337**(6205): p. 387-8.

139. Zimmermann, T.S., et al., *RNAi-mediated gene silencing in non-human primates.* Nature, 2006. **441**(7089): p. 111-4.

140. Leuschner, F., et al., *Therapeutic siRNA silencing in inflammatory monocytes in mice.* Nat Biotechnol, 2011. **29**(11): p. 1005-10.

141. Peer, D., et al., *Systemic leukocyte-directed siRNA delivery revealing cyclin D1 as an anti-inflammatory target.* Science, 2008. **319**(5863): p. 627-30.

142. Sato, Y., et al., *Resolution of liver cirrhosis using vitamin A-coupled liposomes to deliver siRNA against a collagen-specific chaperone.* Nat Biotechnol, 2008. **26**(4): p. 431-42.

143. Kleinman, M.E., et al., *Sequence- and target-independent angiogenesis suppression by siRNA via TLR3.* Nature, 2008. **452**(7187): p. 591-7.

144. Geisbert, T.W., et al., *Postexposure protection of guinea pigs against a lethal ebola virus challenge is conferred by RNA interference.* J Infect Dis, 2006. **193**(12): p. 1650-7.

145. Landen, C.N., Jr., et al., *Therapeutic EphA2 gene targeting in vivo using neutral liposomal small interfering RNA delivery.* Cancer Res, 2005. **65**(15): p. 6910-8.

146. Halder, J., et al., *Focal adhesion kinase targeting using in vivo short interfering RNA delivery in neutral liposomes for ovarian carcinoma therapy.* Clin Cancer Res, 2006. **12**(16): p. 4916-24.

147. Villares, G.J., et al., *Targeting melanoma growth and metastasis with systemic delivery of liposome-incorporated protease-activated receptor-1 small interfering RNA.* Cancer Res, 2008. **68**(21): p. 9078-86.

148. Merritt, W.M., et al., *Effect of interleukin-8 gene silencing with liposome-encapsulated small interfering RNA on ovarian cancer cell growth.* J Natl Cancer Inst, 2008. **100**(5): p. 359-72.

149. Tanaka, T., et al., *Sustained small interfering RNA delivery by mesoporous silicon particles.* Cancer Res, 2010. **70**(9): p. 3687-96.

150. Ahmed, A.A., et al., *SIK2 is a centrosome kinase required for bipolar mitotic spindle formation that provides a potential target for therapy in ovarian cancer.* Cancer Cell, 2010. **18**(2): p. 109-21.

151. Eguchi, A., et al., *Efficient siRNA delivery into primary cells by a peptide transduction domain-dsRNA binding domain fusion protein.* Nat Biotechnol, 2009. **27**(6): p. 567-71.

152. McNaughton, B.R., et al., *Mammalian cell penetration, siRNA transfection, and DNA transfection by supercharged proteins.* Proc Natl Acad Sci U S A, 2009. **106**(15): p. 6111-6.

153. Howard, K.A., et al., *RNA interference in vitro and in vivo using a novel chitosan/siRNA nanoparticle system.* Mol Ther, 2006. **14**(4): p. 476-84.

154. Pille, J.Y., et al., *Intravenous delivery of anti-RhoA small interfering RNA loaded in nanoparticles of chitosan in mice: safety and efficacy in xenografted aggressive breast cancer.* Hum Gene Ther, 2006. **17**(10): p. 1019-26.

155. Minakuchi, Y., et al., *Atelocollagen-mediated synthetic small interfering RNA delivery for effective gene silencing in vitro and in vivo.* Nucleic Acids Res, 2004. **32**(13): p. e109.

156. Urban-Klein, B., et al., *RNAi-mediated gene-targeting through systemic application of polyethylenimine (PEI)-complexed siRNA in vivo.* Gene Ther, 2005. **12**(5): p. 461-6.

157. Kunath, K., et al., *Integrin targeting using RGD-PEI conjugates for in vitro gene transfer.* J Gene Med, 2003. **5**(7): p. 588-99.

158. Hu-Lieskovan, S., et al., *Sequence-specific knockdown of EWS-FLI1 by targeted, nonviral delivery of small interfering RNA inhibits tumor growth in a murine model of metastatic Ewing's sarcoma.* Cancer Res, 2005. **65**(19): p. 8984-92.

159. Davis, M.E., et al., *Evidence of RNAi in humans from systemically administered siRNA via targeted nanoparticles.* Nature, 2010. **464**(7291): p. 1067-70.

160. Pooga, M., et al., *Cellular translocation of proteins by transportan.* FASEB J, 2001. **15**(8): p. 1451-3.

161. Pooga, M., et al., *Cell penetration by transportan.* FASEB J, 1998. **12**(1): p. 67-77.

162. Muratovska, A. and M.R. Eccles, *Conjugate for efficient delivery of short interfering RNA (siRNA) into mammalian cells.* FEBS Lett, 2004. **558**(1-3): p. 63-8.

163. Meade, B.R. and S.F. Dowdy, *Enhancing the cellular uptake of siRNA duplexes following noncovalent packaging with protein transduction domain peptides.* Adv Drug Deliv Rev, 2008. **60**(4-5): p. 530-6.

164. Kim, W.J., et al., *Cholesteryl oligoarginine delivering vascular endothelial growth factor siRNA effectively inhibits tumor growth in colon adenocarcinoma.* Mol Ther, 2006. **14**(3): p. 343-50.

165. Kumar, P., et al., *T cell-specific siRNA delivery suppresses HIV-1 infection in humanized mice.* Cell, 2008. **134**(4): p. 577-86.

166. Kumar, P., et al., *Transvascular delivery of small interfering RNA to the central nervous system.* Nature, 2007. **448**(7149): p. 39-43.

167. Crombez, L., et al., *A new potent secondary amphipathic cell-penetrating peptide for siRNA delivery into mammalian cells.* Mol Ther, 2009. **17**(1): p. 95-103.

168. Ezzat, K., et al., *PepFect 14, a novel cell-penetrating peptide for oligonucleotide delivery in solution and as solid formulation.* Nucleic Acids Res, 2011. **39**(12): p. 5284-98.

169. von Maltzahn, G., et al., *In vivo tumor cell targeting with "click" nanoparticles.* Bioconjug Chem, 2008. **19**(8): p. 1570-8.

170. Lee, S.M., et al., *Targeting bladder tumor cells in vivo and in the urine with a peptide identified by phage display.* Mol Cancer Res, 2007. **5**(1): p. 11-9.

171. Rajotte, D. and E. Ruoslahti, *Membrane dipeptidase is the receptor for a lung-targeting peptide identified by in vivo phage display.* J Biol Chem, 1999. **274**(17): p. 11593-8.

172. Porkka, K., et al., *A fragment of the HMGN2 protein homes to the nuclei of tumor cells and tumor endothelial cells in vivo.* Proc Natl Acad Sci U S A, 2002. **99**(11): p. 7444-9.

173. Ruoslahti, E., *Vascular zip codes in angiogenesis and metastasis.* Biochem Soc Trans, 2004. **32**(Pt3): p. 397-402.

174. Simberg, D., et al., *Biomimetic amplification of nanoparticle homing to tumors.* Proc Natl Acad Sci U S A, 2007. **104**(3): p. 932-6.

175. Reddy, G.R., et al., *Vascular targeted nanoparticles for imaging and treatment of brain tumors.* Clin Cancer Res, 2006. **12**(22): p. 6677-86.

176. Zhang, C., et al., *Specific targeting of tumor angiogenesis by RGD-conjugated ultrasmall superparamagnetic iron oxide particles using a clinical 1.5-T magnetic resonance scanner.* Cancer Res, 2007. **67**(4): p. 1555-62.

177. Giordano, R.J., et al., *Structural basis for the interaction of a vascular endothelial growth factor mimic peptide motif and its corresponding receptors.* Chem Biol, 2005. **12**(10): p. 1075-83.

178. Colombo, G., et al., *Structure-activity relationships of linear and cyclic peptides containing the NGR tumor-homing motif.* J Biol Chem, 2002. **277**(49): p. 47891-7.

179. Rozek, A., et al., *Structure-based design of an indolicidin peptide analogue with increased protease stability.* Biochemistry, 2003. **42**(48): p. 14130-8.

180. Ruoslahti, E. and M.D. Pierschbacher, *New perspectives in cell adhesion: RGD and integrins.* Science, 1987. **238**(4826): p. 491-7.

181. Green, J.J., et al., *Electrostatic ligand coatings of nanoparticles enable ligand-specific gene delivery to human primary cells.* Nano Lett, 2007. **7**(4): p. 874-9.

182. Sokolov, K., et al., *Real-time vital optical imaging of precancer using anti-epidermal growth factor receptor antibodies conjugated to gold nanoparticles.* Cancer Res, 2003. **63**(9): p. 1999-2004.

183. Huang, X., et al., *Cancer cell imaging and photothermal therapy in the near-infrared region by using gold nanorods.* J Am Chem Soc, 2006. **128**(6): p. 2115-20.

184. Kolb, H.C., M.G. Finn, and K.B. Sharpless, *Click Chemistry: Diverse Chemical Function from a Few Good Reactions.* Angew Chem Int Ed Engl, 2001. **40**(11): p. 2004-2021.

185. Lee, J.W., et al., *Synthesis of symmetrical and unsymmetrical PAMAM dendrimers by fusion between azide- and alkyne-functionalized PAMAM dendrons.* Bioconjug Chem, 2007. **18**(2): p. 579-84.

186. Wu, P., et al., *Multivalent, bifunctional dendrimers prepared by click chemistry.* Chem Commun (Camb), 2005(46): p. 5775-7.

187. Shi, Q., et al., *The immobilization of proteins on biodegradable polymer fibers via click chemistry.* Biomaterials, 2008. **29**(8): p. 1118-26.

188. Rozkiewicz, D.I., et al., *Transfer printing of DNA by "click" chemistry.* Chembiochem, 2007. **8**(16): p. 1997-2002.

189. Ciampi, S., et al., *Functionalization of acetylene-terminated monolayers on Si(100) surfaces: a click chemistry approach.* Langmuir, 2007. **23**(18): p. 9320-9.

190. Such, G.K., et al., *Ultrathin, responsive polymer click capsules.* Nano Lett, 2007. **7**(6): p. 1706-10.

191. Li, H., et al., *Functionalization of single-walled carbon nanotubes with well-defined polystyrene by "click" coupling.* J Am Chem Soc, 2005. **127**(41): p. 14518-24.

192. Cavalli, S., et al., *The chemical modification of liposome surfaces via a copper-mediated [3 + 2] azide-alkyne cycloaddition monitored by a colorimetric assay.* Chem Commun (Camb), 2006(30): p. 3193-5.

193. Fischler, M., et al., *Chain-like assembly of gold nanoparticles on artificial DNA templates via 'click chemistry'.* Chem Commun (Camb), 2008(2): p. 169-71.

194. Opsteen, J.A., et al., *"Clickable" polymersomes.* Chem Commun (Camb), 2007(30): p. 3136-8.

195. Antoni, P., et al., *A chemoselective approach for the accelerated synthesis of well-defined dendritic architectures.* Chem Commun (Camb), 2007(22): p. 2249-51.

196. Zeng, Q., et al., *Chemoselective derivatization of a bionanoparticle by click reaction and ATRP reaction.* Chem Commun (Camb), 2007(14): p. 1453-5.

197. Brennan, J.L., et al., *Bionanoconjugation via click chemistry: The creation of functional hybrids of lipases and gold nanoparticles.* Bioconjug Chem, 2006. **17**(6): p. 1373-5.

198. Sun, E.Y., L. Josephson, and R. Weissleder, *"Clickable" nanoparticles for targeted imaging.* Mol Imaging, 2006. **5**(2): p. 122-8.

199. Said Hassane, F., B. Frisch, and F. Schuber, *Targeted liposomes: convenient coupling of ligands to preformed vesicles using "click chemistry".* Bioconjug Chem, 2006. **17**(3): p. 849-54.

200. Laakkonen, P., et al., *Antitumor activity of a homing peptide that targets tumor lymphatics and tumor cells.* Proc Natl Acad Sci U S A, 2004. **101**(25): p. 9381-6.

201. Fogal, V., Zhang, L., and Ruoslahti, E., *Mitochondrial/cell surface protein p32/gC1qR as a molecular target in tumor cells and tumor stroma.* Cancer Research. **(Submitted)**.

202. Rubinstein, D.B., et al., *Receptor for the globular heads of C1q (gC1q-R, p33, hyaluronan-binding protein) is preferentially expressed by adenocarcinoma cells.* Int J Cancer, 2004. **110**(5): p. 741-50.

203. Montet, X., et al., *Multivalent effects of RGD peptides obtained by nanoparticle display.* J Med Chem, 2006. **49**(20): p. 6087-93.

204.	Unezaki, S., et al., *Direct measurement of the extravasation of polyethyleneglycol-coated liposomes into solid tumor tissue by in vivo fluorescence microscopy.* International Journal of Pharmaceutics, 1996. **144**(1): p. 11-17.

205.	Son, D.H., et al., *In vivo tumor targeting and radionuclide imaging with self-assembled nanoparticles: Mechanisms, key factors, and their implications.* Ejc Supplements, 2006. **4**(12): p. 47-47.

206.	Moghimi, S.M. and J. Szebeni, *Stealth liposomes and long circulating nanoparticles: critical issues in pharmacokinetics, opsonization and protein-binding properties.* Prog Lipid Res, 2003. **42**(6): p. 463-78.

207.	Moghimi, S.M., A.C. Hunter, and J.C. Murray, *Long-circulating and target-specific nanoparticles: theory to practice.* Pharmacol Rev, 2001. **53**(2): p. 283-318.

208.	Gu, F., et al., *Precise engineering of targeted nanoparticles by using self-assembled biointegrated block copolymers.* Proceedings of the National Academy of Sciences of the United States of America, 2008. **105**(7): p. 2586-2591.

209.	Shen, T., et al., *Monocrystalline iron oxide nanocompounds (MION): physicochemical properties.* Magn Reson Med, 1993. **29**(5): p. 599-604.

210.	Josephson, L., et al., *High-efficiency intracellular magnetic labeling with novel superparamagnetic-Tat peptide conjugates.* Bioconjug Chem, 1999. **10**(2): p. 186-91.

211.	Ruoslahti, E., S.N. Bhatia, and M.J. Sailor, *Targeting of drugs and nanoparticles to tumors.* J Cell Biol, 2010. **188**(6): p. 759-68.

212.	Henke, E., et al., *Peptide-conjugated antisense oligonucleotides for targeted inhibition of a transcriptional regulator in vivo.* Nat Biotechnol, 2008. **26**(1): p. 91-100.

213.	Ren, Y., et al., *Targeted tumor-penetrating siRNA nanocomplexes for credentialing cancer targets.* Science Translational Medicine, 2012: p. In Revision.

214.	Sugahara, K.N., et al., *Coadministration of a Tumor-Penetrating Peptide Enhances the Efficacy of Cancer Drugs.* Science, 2010.

215.	Wadia, J.S., R.V. Stan, and S.F. Dowdy, *Transducible TAT-HA fusogenic peptide enhances escape of TAT-fusion proteins after lipid raft macropinocytosis.* Nat Med, 2004. **10**(3): p. 310-5.

216.	Chen, Y.B., et al., *Increased expression of hyaluronic acid binding protein 1 is correlated with poor prognosis in patients with breast cancer.* J Surg Oncol, 2009. **100**(5): p. 382-6.

217.	Fogal, V., et al., *Mitochondrial/cell-surface protein p32/gC1qR as a molecular target in tumor cells and tumor stroma.* Cancer Res, 2008. **68**(17): p. 7210-8.

218.	Roth, L., et al., *Transtumoral targeting enabled by a novel neuropilin-binding peptide.* Oncogene, 2011.

219.	Park, J.H., et al., *Cooperative nanomaterial system to sensitize, target, and treat tumors.* Proc Natl Acad Sci U S A, 2010. **107**(3): p. 981-6.

220.	Gump, J.M. and S.F. Dowdy, *TAT transduction: the molecular mechanism and therapeutic prospects.* Trends Mol Med, 2007. **13**(10): p. 443-8.

221.	Pham, W., et al., *Enhancing membrane permeability by fatty acylation of oligoarginine peptides.* Chembiochem, 2004. **5**(8): p. 1148-51.

222.	Maurer-Stroh, S. and F. Eisenhaber, *Myristoylation of viral and bacterial proteins.* Trends Microbiol, 2004. **12**(4): p. 178-85.

223.	Agrawal, A., et al., *Functional delivery of siRNA in mice using dendriworms.* ACS Nano, 2009. **3**(9): p. 2495-504.

224.	Karmali, P.P., et al., *Targeting of albumin-embedded paclitaxel nanoparticles to tumors.* Nanomedicine, 2009. **5**(1): p. 73-82.

225.	Memarzadeh, S. and J.S. Berek, *Advances in the management of epithelial ovarian cancer.* J Reprod Med, 2001. **46**(7): p. 621-9; discussion 629-30.

226.	TCGA-Network, *Integrated genomic analysis of ovarian carcinoma.* Nature, in press, 2011.

227.	Hambley, T.W. and W.N. Hait, *Is anticancer drug development heading in the right direction?* Cancer Res, 2009. **69**(4): p. 1259-62.

228.	Jain, R.K., *Transport of molecules, particles, and cells in solid tumors.* Annu Rev Biomed Eng, 1999. **1**: p. 241-63.

229.	Gupta, B., T.S. Levchenko, and V.P. Torchilin, *Intracellular delivery of large molecules and small particles by cell-penetrating proteins and peptides.* Adv Drug Deliv Rev, 2005. **57**(4): p. 637-51.

230.	van den Berg, A. and S.F. Dowdy, *Protein transduction domain delivery of therapeutic macromolecules.* Curr Opin Biotechnol, 2011.

231.	Sieben, N.L., et al., *In ovarian neoplasms, BRAF, but not KRAS, mutations are restricted to low-grade serous tumours.* J Pathol, 2004. **202**(3): p. 336-40.

232.	Singer, G., et al., *Mutations in BRAF and KRAS characterize the development of low-grade ovarian serous carcinoma.* J Natl Cancer Inst, 2003. **95**(6): p. 484-6.

233.	Singer, G., et al., *Diverse tumorigenic pathways in ovarian serous carcinoma.* Am J Pathol, 2002. **160**(4): p. 1223-8.

234.	Gorringe, K.L., et al., *Copy number analysis identifies novel interactions between genomic loci in ovarian cancer.* PLoS One, 2010. **5**(9).

235.	Sheng, Q., et al., *An activated ErbB3/NRG1 autocrine loop supports in vivo proliferation in ovarian cancer cells.* Cancer Cell, 2010. **17**(3): p. 298-310.

236.	Lin, H.K., et al., *Skp2 targeting suppresses tumorigenesis by Arf-p53-independent cellular senescence.* Nature, 2010. **464**(7287): p. 374-9.

237.	Hamad, N.M., et al., *Distinct requirements for Ras oncogenesis in human versus mouse cells.* Genes Dev, 2002. **16**(16): p. 2045-57.

238.	Liu, J., et al., *A genetically defined model for human ovarian cancer.* Cancer Res., 2004. **64**(5): p. 1655-63.

239.	Rangarajan, A., et al., *Species- and cell type-specific requirements for cellular transformation.* Cancer Cell, 2004. **6**(2): p. 171-83.

240.	Boehm, J.S., et al., *Transformation of human and murine fibroblasts without viral oncoproteins.* Mol Cell Biol, 2005. **25**(15): p. 6464-74.

241.	Karst, A.M. and R. Drapkin, *Ovarian cancer pathogenesis: a model in evolution.* J Oncol, 2010. **2010**: p. 932371.

242.	Karst, A.M., K. Levanon, and R. Drapkin, *Modeling high-grade serous ovarian carcinogenesis from the fallopian tube.* Proc Natl Acad Sci U S A, 2011. **108**(18): p. 7547-52.

243.	Prabhu, S., et al., *Regulation of the expression of cyclin-dependent kinase inhibitor p21 by E2A and Id proteins.* Mol. Cell Biol., 1997. **17**(10): p. 5888-96.

244.	Ciarrocchi, A., et al., *Id1 restrains p21 expression to control endothelial progenitor cell formation.* PLoS One, 2007. **2**(12): p. e1338.

245.	Huang, Y.H., et al., *Claudin-3 gene silencing with siRNA suppresses ovarian tumor growth and metastasis.* Proc Natl Acad Sci U S A, 2009. **106**(9): p. 3426-30.

246.   Takeda, A., C. Goolsby, and N.R. Yaseen, *NUP98-HOXA9 induces long-term proliferation and blocks differentiation of primary human CD34+ hematopoietic cells.* Cancer Res., 2006. **66**(13): p. 6628-37.

247.   Faber, J., et al., *HOXA9 is required for survival in human MLL-rearranged acute leukemias.* Blood, 2009. **113**(11): p. 2375-85.

248.   Gilliland, D.G., *Molecular genetics of human leukemias: new insights into therapy.* Semin Hematol, 2002. **39**(4 Suppl 3): p. 6-11.

249.   Garraway, L.A. and W.R. Sellers, *Lineage dependency and lineage-survival oncogenes in human cancer.* Nat Rev Cancer, 2006. **6**(8): p. 593-602.

250.   Weir, B.A., et al., *Characterizing the cancer genome in lung adenocarcinoma.* Nature, 2007. **450**(7171): p. 893-8.

251.   Bass, A.J., et al., *SOX2 is an amplified lineage-survival oncogene in lung and esophageal squamous cell carcinomas.* Nat Genet, 2009. **41**(11): p. 1238-42.

252.   Tomlins, S.A., et al., *Recurrent fusion of TMPRSS2 and ETS transcription factor genes in prostate cancer.* Science, 2005. **310**(5748): p. 644-8.

253.   Yun, K., et al., *Id4 regulates neural progenitor proliferation and differentiation in vivo.* Development, 2004. **131**(21): p. 5441-8.

254.   Bedford, L., et al., *Id4 is required for the correct timing of neural differentiation.* Dev Biol, 2005. **280**(2): p. 386-95.

255.   Tokuzawa, Y., et al., *Id4, a new candidate gene for senile osteoporosis, acts as a molecular switch promoting osteoblast differentiation.* PLoS Genet, 2010. **6**(7): p. e1001019.

256.   Dell'Orso, S., et al., *ID4: a new player in the cancer arena.* Oncotarget, 2010. **1**(1): p. 48-58.

257.   Jeon, H.M., et al., *ID4 imparts chemoresistance and cancer stemness to glioma cells by derepressing miR-9*-mediated suppression of SOX2.* Cancer Res, 2011. **71**(9): p. 3410-21.

258.   Abramovich, C. and R.K. Humphries, *Hox regulation of normal and leukemic hematopoietic stem cells.* Curr Opin Hematol, 2005. **12**(3): p. 210-6.

259.   Nakamura, T., et al., *Cooperative activation of Hoxa and Pbx1-related genes in murine myeloid leukaemias.* Nat Genet, 1996. **12**(2): p. 149-53.

260.   Ono, R., et al., *Mixed-lineage-leukemia (MLL) fusion protein collaborates with Ras to induce acute leukemia through aberrant Hox expression and Raf activation.* Leukemia, 2009. **23**(12): p. 2197-209.

261.   Kobayashi, A. and R.R. Behringer, *Developmental genetics of the female reproductive tract in mammals.* Nat Rev Genet, 2003. **4**(12): p. 969-80.

262.   Han, H.D., et al., *Targeted gene silencing using RGD-labeled chitosan nanoparticles.* Clin Cancer Res, 2010. **16**(15): p. 3910-22.

263.   Curnis, F., A. Sacchi, and A. Corti, *Improving chemotherapeutic drug penetration in tumors by vascular targeting and barrier alteration.* J Clin Invest, 2002. **110**(4): p. 475-82.

264.   MacDiarmid, J.A., et al., *Sequential treatment of drug-resistant tumors with targeted minicells containing siRNA or a cytotoxic drug.* Nat Biotechnol, 2009. **27**(7): p. 643-51.

265.   Nijhahwan, D., et al., *Cancer Vulnerabilities Unveiled by Genomic Loss.* In preparation, 2012.

266. Lindblad-Toh, K., et al., *Loss-of-heterozygosity analysis of small-cell lung carcinomas using single-nucleotide polymorphism arrays.* Nat Biotechnol, 2000. **18**(9): p. 1001-5.

267. Hollstein, M., et al., *p53 mutations in human cancers.* Science, 1991. **253**(5015): p. 49-53.

268. Druker, B.J., et al., *Efficacy and safety of a specific inhibitor of the BCR-ABL tyrosine kinase in chronic myeloid leukemia.* N Engl J Med, 2001. **344**(14): p. 1031-7.

269. Soda, M., et al., *Identification of the transforming EML4-ALK fusion gene in non-small-cell lung cancer.* Nature, 2007. **448**(7153): p. 561-6.

270. Paez, J.G., et al., *EGFR mutations in lung cancer: correlation with clinical response to gefitinib therapy.* Science, 2004. **304**(5676): p. 1497-500.

271. Davies, H., et al., *Mutations of the BRAF gene in human cancer.* Nature, 2002. **417**(6892): p. 949-54.

272. Kaelin, W.G., Jr., *The concept of synthetic lethality in the context of anticancer therapy.* Nat Rev Cancer, 2005. **5**(9): p. 689-98.

273. Solimini, N.L., J. Luo, and S.J. Elledge, *Non-oncogene addiction and the stress phenotype of cancer cells.* Cell, 2007. **130**(6): p. 986-8.

274. Luo, J., N.L. Solimini, and S.J. Elledge, *Principles of cancer therapy: oncogene and non-oncogene addiction.* Cell, 2009. **136**(5): p. 823-37.

275. Hershko, A. and A. Ciechanover, *The ubiquitin system.* Annu Rev Biochem, 1998. **67**: p. 425-79.

276. Besche, H.C., A. Peth, and A.L. Goldberg, *Getting to First Base in Proteasome Assembly.* Cell, 2009. **138**(1): p. 25-28.

277. Kaneko, T., et al., *Assembly Pathway of the Mammalian Proteasome Base Subcomplex Is Mediated by Multiple Specific Chaperones.* Cell, 2009. **137**(5): p. 914-925.

278. Richardson, P.G., et al., *Bortezomib or high-dose dexamethasone for relapsed multiple myeloma.* N Engl J Med, 2005. **352**(24): p. 2487-98.

279. Frei, E., 3rd, *Gene deletion: a new target for cancer chemotherapy.* Lancet, 1993. **342**(8872): p. 662-4.

280. Ashworth, A., *A synthetic lethal therapeutic approach: poly(ADP) ribose polymerase inhibitors for the treatment of cancers deficient in DNA double-strand break repair.* J Clin Oncol, 2008. **26**(22): p. 3785-90.

281. Fong, P.C., et al., *Inhibition of poly(ADP-ribose) polymerase in tumors from BRCA mutation carriers.* N Engl J Med, 2009. **361**(2): p. 123-34.

282. Goldberg, M.S., et al., *Nanoparticle-mediated delivery of siRNA targeting Parp1 extends survival of mice bearing tumors derived from Brca1-deficient ovarian cancer cells.* Proc Natl Acad Sci U S A, 2011. **108**(2): p. 745-50.

283. Goldberg, M.S. and P.A. Sharp, *Pyruvate kinase M2-specific siRNA induces apoptosis and tumor regression.* J Exp Med, 2012. **209**(2): p. 217-24.

284. Luo, B., et al., *Highly parallel identification of essential genes in cancer cells.* Proc. Natl Acad. Sci. USA, 2008. **105**(51): p. 20380-5.

285. Boehm, J.S., et al., *Transformation of human and murine fibroblasts without viral oncoproteins.* Mol. Cell Biol., 2005. **25**(15): p. 6464-74.

286. Subramanian, A., et al., *Gene set enrichment analysis: a knowledge-based approach for interpreting genome-wide expression profiles.* Proc. Natl Acad. Sci. USA, 2005. **102**(43): p. 15545-50.

287. Ren, Y., et al., *Identification and characterization of receptor-specific cell-penetrating peptides for siRNA delivery*. ACS Nano, 2012: p. Submitted.

288. Gump, J.M., R.K. June, and S.F. Dowdy, *Revised role of glycosaminoglycans in TAT protein transduction domain-mediated cellular transduction*. J Biol Chem, 2010. **285**(2): p. 1500-7.

289. Zorko, M. and U. Langel, *Cell-penetrating peptides: mechanism and kinetics of cargo delivery*. Adv Drug Deliv Rev, 2005. **57**(4): p. 529-45.

290. Tan, M., et al., *Selective inhibition of ErbB2-overexpressing breast cancer in vivo by a novel TAT-based ErbB2-targeting signal transducers and activators of transcription 3-blocking peptide*. Cancer Res, 2006. **66**(7): p. 3764-72.

291. Jiang, T., et al., *Tumor imaging by means of proteolytic activation of cell-penetrating peptides*. Proc Natl Acad Sci U S A, 2004. **101**(51): p. 17867-72.

292. Vocero-Akbani, A.M., et al., *Killing HIV-infected cells by transduction with an HIV protease-activated caspase-3 protein*. Nat Med, 1999. **5**(1): p. 29-33.

293. Frankel, A.D. and C.O. Pabo, *Cellular uptake of the tat protein from human immunodeficiency virus*. Cell, 1988. **55**(6): p. 1189-93.

294. Elliott, G. and P. O'Hare, *Intercellular trafficking and protein delivery by a herpesvirus structural protein*. Cell, 1997. **88**(2): p. 223-33.

295. Derossi, D., et al., *The third helix of the Antennapedia homeodomain translocates through biological membranes*. J Biol Chem, 1994. **269**(14): p. 10444-50.

296. Hu, Y., et al., *Cytosolic delivery of membrane-impermeable molecules in dendritic cells using pH-responsive core-shell nanoparticles*. Nano Lett, 2007. **7**(10): p. 3056-64.

297. Sonawane, N.D., F.C. Szoka, Jr., and A.S. Verkman, *Chloride accumulation and swelling in endosomes enhances DNA transfer by polyamine-DNA polyplexes*. J Biol Chem, 2003. **278**(45): p. 44826-31.

298. Belsley, D.A., *Regression diagnostics : identifying influential data and sources of collinearity*. Wiley series in probability and statistics. 2004, Hoboken, N.J.: Wiley-Interscience. xv, 292 p.

299. Ren, Y., et al., *Receptor down-regulation improves the microdistribution of tumor-targeted theranostics*. In preparation, 2012.

300. Sinek, J., et al., *Two-dimensional chemotherapy simulations demonstrate fundamental transport and tumor response limitations involving nanoparticles*. Biomed Microdevices, 2004. **6**(4): p. 297-309.

301. Arap, W., R. Pasqualini, and E. Ruoslahti, *Cancer treatment by targeted drug delivery to tumor vasculature in a mouse model*. Science, 1998. **279**(5349): p. 377-80.

302. Park, J.W., et al., *Anti-HER2 immunoliposomes for targeted therapy of human tumors*. Cancer Lett, 1997. **118**(2): p. 153-60.

303. Thurber, G.M., M.M. Schmidt, and K.D. Wittrup, *Factors determining antibody distribution in tumors*. Trends Pharmacol Sci, 2008. **29**(2): p. 57-61.

304. Jain, R.K. and T. Stylianopoulos, *Delivering nanomedicine to solid tumors*. Nat Rev Clin Oncol, 2010. **7**(11): p. 653-64.

305. Adams, G.P., et al., *High affinity restricts the localization and tumor penetration of single-chain fv antibody molecules*. Cancer Res, 2001. **61**(12): p. 4750-5.

306. Friedman, L.M., et al., *Synergistic down-regulation of receptor tyrosine kinases by combinations of mAbs: implications for cancer immunotherapy*. Proc Natl Acad Sci U S A, 2005. **102**(6): p. 1915-20.

307. Frykholm, G., et al., *Heterogeneity in antigenic expression and radiosensitivity in human colon carcinoma cell lines.* In Vitro Cell Dev Biol, 1991. **27A**(12): p. 900-6.

308. Rudnick, S.I., et al., *Influence of affinity and antigen internalization on the uptake and penetration of Anti-HER2 antibodies in solid tumors.* Cancer Res, 2011. **71**(6): p. 2250-9.

309. Fogal, V., et al., *Mitochondrial p32 protein is a critical regulator of tumor metabolism via maintenance of oxidative phosphorylation.* Mol Cell Biol, 2010. **30**(6): p. 1303-18.

310. Saga, T., et al., *Targeting cancer micrometastases with monoclonal antibodies: a binding-site barrier.* Proc Natl Acad Sci U S A, 1995. **92**(19): p. 8999-9003.

311. Ackerman, M.E., D. Pawlowski, and K.D. Wittrup, *Effect of antigen turnover rate and expression level on antibody penetration into tumor spheroids.* Mol Cancer Ther, 2008. **7**(7): p. 2233-40.

312. Thurber, G.M., M.M. Schmidt, and K.D. Wittrup, *Antibody tumor penetration: transport opposed by systemic and antigen-mediated clearance.* Adv Drug Deliv Rev, 2008. **60**(12): p. 1421-34.

313. Thurber, G.M., S.C. Zajic, and K.D. Wittrup, *Theoretic criteria for antibody penetration into solid tumors and micrometastases.* J Nucl Med, 2007. **48**(6): p. 995-9.

314. Rhoden, J.J. and K.D. Wittrup, *Dose dependence of intratumoral perivascular distribution of monoclonal antibodies.* J Pharm Sci, 2012. **101**(2): p. 860-7.

315. El Emir, E., et al., *Predicting response to radioimmunotherapy from the tumor microenvironment of colorectal carcinomas.* Cancer Res, 2007. **67**(24): p. 11896-905.

316. Orlova, A., et al., *Tumor imaging using a picomolar affinity HER2 binding affibody molecule.* Cancer Res, 2006. **66**(8): p. 4339-48.

317. Vander Heiden, M.G., L.C. Cantley, and C.B. Thompson, *Understanding the Warburg effect: the metabolic requirements of cell proliferation.* Science, 2009. **324**(5930): p. 1029-33.

318. Tseng, J.C., et al., *Incongruity of Imaging Using Fluorescent 2-DG Conjugates Compared to (18)F-FDG in Preclinical Cancer Models.* Mol Imaging Biol, 2012.

319. Choi, Y., et al., *A hantavirus causing hemorrhagic fever with renal syndrome requires gC1qR/p32 for efficient cell binding and infection.* Virology, 2008. **381**(2): p. 178-83.

320. Gura, T., *Systems for identifying new drugs are often faulty.* Science, 1997. **278**(5340): p. 1041-2.

321. Sausville, E.A. and A.M. Burger, *Contributions of human tumor xenografts to anticancer drug development.* Cancer Res, 2006. **66**(7): p. 3351-4, discussion 3354.

322. Fiebig, H.H., A. Maier, and A.M. Burger, *Clonogenic assay with established human tumour xenografts: correlation of in vitro to in vivo activity as a basis for anticancer drug discovery.* Eur J Cancer, 2004. **40**(6): p. 802-20.

323. Kirpotin, D.B., et al., *Antibody targeting of long-circulating lipidic nanoparticles does not increase tumor localization but does increase internalization in animal models.* Cancer Res, 2006. **66**(13): p. 6732-40.

324. Kumar, M.S., et al., *Impaired microRNA processing enhances cellular transformation and tumorigenesis.* Nat Genet, 2007. **39**(5): p. 673-7.

325. Dhar, S., et al., *Targeted delivery of cisplatin to prostate cancer cells by aptamer functionalized Pt(IV) prodrug-PLGA-PEG nanoparticles.* Proc Natl Acad Sci U S A, 2008. **105**(45): p. 17356-61.

326.   Ghebrehiwet, B., et al., *gC1q-R/p33, a member of a new class of multifunctional and multicompartmental cellular proteins, is involved in inflammation and infection.* Immunol Rev, 2001. **180**: p. 65-77.

327.   Braun, L., B. Ghebrehiwet, and P. Cossart, *gC1q-R/p32, a C1q-binding protein, is a receptor for the InlB invasion protein of Listeria monocytogenes.* EMBO J, 2000. **19**(7): p. 1458-66.

328.   Ghebrehiwet, B. and E.I. Peerschke, *Structure and function of gC1q-R: a multiligand binding cellular protein.* Immunobiology, 1998. **199**(2): p. 225-38.

329.   Ghebrehiwet, B., et al., *Identification of functional domains on gC1Q-R, a cell surface protein that binds to the globular "heads" of C1Q, using monoclonal antibodies and synthetic peptides.* Hybridoma, 1996. **15**(5): p. 333-42.

330.   Eggleton, P., et al., *Identification of a gC1q-binding protein (gC1q-R) on the surface of human neutrophils. Subcellular localization and binding properties in comparison with the cC1q-R.* J Clin Invest, 1995. **95**(4): p. 1569-78.

11 Appendix

Experimental contributions for each chapter:

Chapter 2: A versatile surface chemistry – In vivo tumor cell targeting with 'Click' nanoparticles. Yin Ren and Geoff von Maltzahn contributed equally. Yin Ren synthesized and characterized nanoparticles. Geoff von Maltzahn designed the concept and conducted *in vivo* experiments.

Chapter 3: Development of targeted tumor-penetrating nanomaterials for siRNA delivery. Yin Ren designed and characterized tandem peptides, performed *in vitro* gene knockdown and *in vivo* tumor homing and penetration experiments.

Chapter 4: Targeted tumor-penetrating siRNA nanocomplexes for credentialing cancer targets. Yin Ren and Hiu Wing (Tony) Cheung contributed equally. Tony Cheung conducted the genomic analyses, shRNA screen, ID4 transformation and mechanism experiments. Yin Ren performed *in vitro* validation with TPN and *in vivo* animal therapeutic trials.

Chapter 5: Partial Genomic Loss Reveals Specific Cancer Vulnerabilities. Deepak Nijhawan and Travis Zack contributed equally. Yin Ren performed TPN therapeutic experiments.

Chapter 6: Characterization of receptor-specific cell-penetrating peptides for siRNA delivery. Yin Ren conducted structural and functional chacracterizations of TPN. Sabine Hauert performed least square regression modeling. Yin Ren and Sabine Hauert analyzed the computational results.

Chapter 7: Receptor down-regulation improves the microdistribution of tumor-targeted theranostics. Yin Ren performed *in vitro* and *in vivo* p32 knockdown experiments. Sabine Hauert performed stochastic modeling experiments. John Rhoden assisted with image quantification.

Chapter 8: Delivery of siRNA to primary ovarian cancer cell samples. Joyce Liu and Karen Yuan established primary human cell strains. Yin Ren performed p32 expression analysis and TPN transfections in primary cells. Ronny Drapkin and Alison Karst performed IHC staining of p32 in ovarian cancer TMAs.

Curriculum Vitae

450 Memorial Drive, Apt. C221   Cell: 734-819-0957
Cambridge, MA 02139   Email: yinren@mit.edu

EDUCATION

Harvard Medical School, *Boston, MA*   *2006-Present*
M.D. Candidate, Harvard-MIT Division of Health Sciences & Technology

Massachusetts Institute of Technology, *Cambridge, MA*   *2008-2012*
Ph.D. Candidate in Medical Engineering
   Advisor: Sangeeta N. Bhatia, MD, PhD

Massachusetts Institute of Technology, *Cambridge, MA*   *2006*
Bachelors of Science, Electrical Engineering; Minor, Biomedical Engineering.

PROFESSIONAL EXPERIENCE

Massachusetts Institute of Technology, *Cambridge, MA*   *2008-2012*
Doctoral Candidate, Laboratory of Multiscale Regenerative Technologies
- Developed novel nanomaterials for tumor-penetrating delivery of nucleic acid therapeutics.
- Established an integrated platform for the discovery and validation of cancer targets.
- Developed surface chemistries for tumor targeting with cyclic peptides.
- Experienced in grant and patent writing, lab management and mentoring new trainees.

Massachusetts Institute of Technology, *Cambridge, MA*   *2003 – 2006*
Undergraduate research assistant, Micro/Nanofluidic BioMEMS Laboratory
- Designed three-dimensional microfluidic channels for protein pre-concentration.

Massachusetts General Hospital, *Boston, MA*   *2004 – 2005*
Research assistant, Physics Division, Department of Radiation Oncology
- Implemented circuitry for the Integrated Radiotherapy Imaging system (IRIS).

University of Michigan Hospitals, *Ann Arbor, MI*   *2005*
Research assistant, Division of Radiation Physics, Department of Radiation Oncology
- Developed a programmable robot to model respiratory motions for radiation treatment.

PUBLICATIONS

Journal Articles
1. **Ren, Y***, Cheung, HW*, von Maltzahn, G, Agrawal, A, Cowley, GS, Weir, BA, Boehm, JS, Tamayo, P, Mesirov, JP, Karst, AM, Drapkin, R, Root, DE, Lo, J, Fogal, V, Ruoslahti, E, Hahn, WC, and Bhatia, SN, "Targeted tumor-penetrating siRNA nanocomplexes for credentialing cancer targets" *Science Translational Medicine,* **2012**, *In Revision*
2. **Ren, Y,** Hauert, S, Lo, J, and Bhatia, SN, "Identification and characterization of receptor-specific cell-penetrating peptides for siRNA delivery", *Submitted to ACS Nano.*

3. **Ren, Y,** Hauert, S, Rhoden, J, Trulove, J, Wittrup, KD, Nahrendorf, M, Bhatia, SN, "Receptor down-regulation improves the microdistribution of tumor-targeted theranostics", *In Preparation.*

4. Nijhahwan, D*, Zack, T*, **Ren, Y,** Strickland, M, Laemothe, R, Shumacher, S, Tsherniak, A, Shehata, S, Besche, H, Cowley, GS, Weir, BA, Goldberg, AL, Mesirov, JP, Root, DE, Bhatia, SN, Beroukhim, R, Hahn, WC, "Cancer Vulnerabilities Unveiled by Genomic Loss", *In Preparation.*

5. Cheung, HW*, Cowley, GS*, Weir, BA*, Boehm, JS*, Rusin, S, Scott, JA, East, A, Ali, LD, Lizotte, PH, Wong, TC, Jiang, G, Hsiao, J, Mermel, CH, Getz, G, Barretina, J, Gopal, S, Tamayo, P, Gould, J, Tsherniak, A, Stransky, N, Luo, B, **Ren, Y**, Drapkin, R, Bhatia, SN, Mesirov, JP, Garraway, LA, Meyerson, M, Lander, ES, Root, DE, Hahn, WC. "Systematic investigation of genetic vulnerabilities across cancer cell lines reveals lineage-specific dependencies in ovarian cancer", *Proc Natl Acad Sci U S A.,* **2011**, 108, 12372-12377.

6. Goldberg, MS*, Xing, D*, **Ren, Y,** Orsulic, S, Bhatia, SN, and Sharp, PA, "Nanoparticle-mediated delivery of siRNA targeting Parp1 extends survival of mice bearing tumors derived from Brca1-deficient ovarian cancer cells", *Proc Natl Acad Sci U S A.,* **2011**, 108, 745-750.

7. Aptekar, JW, Cassidy, MC, Johnson, AC, Barton, RA, Lee, M, Ogier, AC, Vo, C, Anahtar, MN, **Ren, Y,** Bhatia, SN, Ramanathan, C, Cory, DG, Hill, AL, Mair, RW, Rosen, MS, Walsworth, RL, and Marcus, CM , "Silicon nanoparticles as hyperpolarized magnetic resonance imaging agents." *ACS Nano,* **2009**, 3, 4003–4008.

8. von Maltzahn, G*, **Ren, Y***, Park, J-H, Min, D-H, Kotamraju, V R, Jayakumar, J, Fogal, V, Sailor, MJ, Ruoslahti, E, Bhatia, SN, "In vivo tumor cell targeting with "click" nanoparticles." *Bioconjug Chem.*, **2008**, 19, 1570-1578. (10 most-accessed articles of 2008)

(*These authors contributed equally*)

Book Chapters and Reviews

Ren, Y, and Lilly, LS, "Pericardial Disease, in Pathophysiology of Heart Disease: A Collaborative Project of Medical Students and Faculty." L. Lilly (ed.), Lippincott Williams & Wilkins, 2010.

PATENTS

Ren, Y, and Bhatia, SN, "Targeted Delivery of nucleic acids" (US Patent Application Publication No. 2011/0256088 A1, April 2011)

PRESENTATIONS AND TALKS

American Association for Cancer Research – Noncoding RNAs and Cancer, Miami Beach, FL, Jan 2012.
Ren, Y, "Targeted tumor-penetrating siRNA nanocomplexes provide a platform for credentialing cancer targets", Oral Presentation.

Koch Institute for Integrative Cancer Research Annual Retreat, Sturbridge, MA, Oct 2011.
Ren, Y "Treatment of ovarian cancer with tumor-homing siRNA nanocomplexes", Oral presentation.

Biomedical Engineering Society (BMES) National Conference, Austin, TX, Oct 2010.
Ren, Y, "Treatment of ovarian cancer with tumor-homing siRNA nanocomplexes", Oral presentation.

Koch Institute Focus Seminar Series, Cambridge, MA, Nov 2009
Ren, Y,"Targeted siRNA delivery to ovarian cancer", Oral presentation.

National MD/PhD Student Conference, Keystone, CO, July 2008.
Ren, Y, "*In vivo* tumor cell targeting with 'click' nanoparticles", Poster.

American Association of Physicists in Medicine, Seattle, WA, July 2005.
Sharp, GC, Jeung, A, **Ren, Y**, Povzner, S, Berbeco, RI, Mostafavi, H, Chen, G, Jiang, S, "Respiratory-Gated Dual Fluoroscopic Imaging for Positioning and Verification", Poster.

AWARDS AND HONORS

Repligen Koch Institute for Integrative Cancer Research Fellowship (2010-2011)
Medical Scientist Training Program Fellowship (2006-Present)
Honorable Mention, National Science Foundation Graduate Research Fellowship (2007)
First Place out of sixty teams, MIT "6.270" Autonomous Robot Design Competition (2004)
Honorable Mention, MIT Dewitt Prize for Science Writing for the Public (2005)
Letter of Commendation for placing in top 5% in undergraduate classes (2004)

SERVICE

Voting member, *HST MD Admissions Committee, Harvard Medical School*	*2008-2012*
Member, *HST Faculty Awards Committee, MIT*	*2008-2009*

MENTORING AND TEACHING

Graduate Resident Tutor, *Macgregor House, MIT*	*2009-Present*
Non-resident Premedical Tutor, *Lowell House, Harvard University*	*2009-2010*
Research mentor, *Undergraduate Research Opportunity Program, MIT*	*2007-2009*
Resident advisor, *Vanderbilt Hall, Harvard Medical School*	*2007-2008*
Lab Assistant, *Circuits and Electronics, MIT*	*2004-2005*
Volunteer teacher, *Educational Studies Program, MIT*	*2003-2004*

ACTIVITIES

MIT Keys to Empowering Youth Workshop Volunteer (2009-2011)
Photos exhibited at Harvard Student Art Show (2010)
Harvard Medical School First-year Urban Neighborhood Campaign (FUNC) volunteer (2006-2008)
Society co-captain in the annual HMS Society Olympics (2007)
Team captain of HST intramural soccer and basketball teams (2006-2008)